Analysis of Smart Photovoltaic Module for Effective Use of Solar Energy

Yousef Alharbi

BSc, MSc

School of Engineering

Lancaster University

A thesis submitted for the degree of

Doctor of Philosophy

1 October 2025

Declaration

I, Yousef Alharbi, confirm that the work presented in this thesis is entirely my own. It was conceived, developed, and written independently, and has not been submitted, in whole or in part, to any other university or institution for the award of a degree. This research was conducted at Lancaster University, United Kingdom, between October 2021 and October 2025.

Yousef Alharbi

Analysis of Smart Photovoltaic Module for Effective Use of Solar Energy

Yousef Alharbi MSc, BSc

School of Engineering, Lancaster University

A thesis submitted for the degree of Doctor of Philosophy. October 2025

Abstract

The main objective of this thesis is to present a comprehensive investigation of residential PV grid-connected inverters and propose novel, practical topologies to address the unbalanced power generation between PV modules. This thesis proposed a modular inverter (MI) derived from a power electronic converter topology. The suggested single-stage modular Cuk inverter (MCI) in this thesis is designed by connecting multiple low voltage (LV) MIs in series and linking the output terminals to the distribution network. The recommended topology does not require a large DC-link decoupling capacitor, which is common in conventional central inverters. The decentralized features of the proposed MCI enhance the controllability of the residential PV system. The suggested MCI topology is designed based on the Cuk converter. Therefore, it offers continuous input and output current features, which enable the use of small-sized filter components. MCI topology operates over a broad range of voltages, which makes it suitable for supplying local loads or charging battery storage. The control system of the proposed topology consists of two control systems. In PV-to-grid mode, the input control loop at the PV side is designed to mitigate ripples in the input current, which commonly reduces the efficiency of the MPPT algorithm. On the other hand, the outer control system at the grid side is responsible for maintaining a sinusoidal waveform matched with the grid current. The Simulink simulation results illustrate the effectiveness of the proposed MI in mitigating the unbalanced power production of residential PV systems. Also, a scaled-down prototype experiment has been developed to validate mathematical and simulation analysis.

The thesis presents another distributed MPPT approach for mitigating unbalanced power production in residential PV applications. The proposed strategy aims to replace the conventional bypass diodes inside the PV module with an effective power converter to utilize the full power of the PV module under the partial shading (PS) effect. The suggested

cascaded boost-based design is recommended to increase the power generation of the PV module and effectively tackle the unbalanced power production in PV residential systems. The design employs a boost converter to extract power from the three submodules (SM) of the PV model, and the outputs of the three boost converters are cascaded to step up the voltage to meet the grid side requirements. The voltage source inverter (VSI) is used at the grid side to effectively invert the DC power from the PV model side to alternating power. The proposed cascaded topology provides extra protection for the PV module by integrating a one-directional diode to prevent the reverse current from harming the PV module in faulty system scenarios. A practical experiment has been conducted to examine the effectiveness of the proposed topology.

In the last part of the thesis, a module predictive control (MPC) strategy for a two-stage single-phase inverter using a single-ended primary-inductor converter (SEPIC) converter has been developed for residential PV applications. This control approach predicts the input inductor current, the DC link capacitor voltage, and the AC grid current of the double-stage inverter, comparing them with the reference values to perform the control actions. It consists of two parts: the DC MPC controller, which regulates the PV input current and decouples the double-line frequency ripples in the DC link capacitor, and the AC MPC controller, which optimally operates the single-phase VSI while synchronizing with the grid current. The cost function of the MPC approach maintains a smooth input current, which enables the efficient operation of the MPPT. The system-level PR controller ensures that the proposed cascaded output current operates at grid frequency to maintain a stable operation of the PV system. The validity of the proposed MPC method is examined through both experimental and simulation studies.

The findings of this research project demonstrate that the proposed structure enhances the understanding of unbalanced irradiation levels in PV systems and their adverse impact on power production. Robust evidence is provided through the evaluation of the proposed solutions using both a simulation platform and experimental validation. The results indicate a significant improvement in power output after mitigating irregular irradiance levels between PV components.

Publications

The key contributions of this Ph.D. thesis are divided into journal and conference papers. The five articles—comprising two literature review papers and two original research papers—constitute the core components of this doctoral thesis and are listed as follows:

Journal Papers

1. Alharbi, Y.; Darwish, A. Control of Cuk-Based Microinverter Topology with Energy Storage for Residential PV Applications. Energies 2023, 16, 2293. https://doi.org/10.3390/en16052293.
2. Alharbi, Y.; Darwish, A.; Ma, X. A Comprehensive Review of Distributed MPPT for Grid-Tied PV Systems at the Sub-Module Level. Energies 2023, 16, 5468. https://doi.org/10.3390/en16145468.
3. Alharbi, Y.; Darwish, A.; Ma, X. Cascaded Multi-Input Single-Output Boost Inverter for Mismatch Mitigation at PV Submodule Level. Electricity 2024, 5, 93-111. https://doi.org/10.3390/electricity5010006.
4. Alharbi, Y.; Darwish, A.; Ma, X. A Review of Model Predictive Control for Grid-Connected PV Applications. Electronics 2025, 14, 667. https://doi.org/10.3390/electronics14040667.
5. Alharbi, Y.; Darwish, A. "Optimized Design and Control of SEPIC-based Grid-Connected PV CHB Inverter" **(in progress)**.

Conference Papers

1. Y. Alharbi, A. D. Badawy, and X. Ma, "A Hybrid Controller for Novel Cascaded DC-DC Boost Converters in Residential DC Microgrids," 2024 29th International Conference on Automation and Computing (ICAC), Sunderland, United Kingdom, **2024**, pp. 1-6.

Acknowledgements

My heartfelt appreciation goes to my primary supervisor, Dr. Ahmed Badawy, for his invaluable guidance, insightful advice, and continuous support throughout my studies. I would also like to extend my sincere thanks to my co-supervisor, Dr. Xiandong Ma, for his helpful discussions and valuable input.

I am deeply grateful to my beloved mother, respected father, dear son, supportive wife, and my brothers and sisters for their encouragement and unwavering love throughout this journey.

Finally, I am truly grateful to everyone who supported me in any way during my studies.

Table of Contents

List of Figures

List of Tables

List of Abbreviations and Acronyms

AC	Alternating current
ADC	Analog to Digital Converter
BES	Battery Energy System
BW	Bandwidth
CAN	Controller Area Network
CCM	Continuous Current Mode
D	Duty Ratio
DC	Direct Current
DSP	Digital Signal Processor
ESR	Equivalent Series Resistance
EU	Europe
FCS	Finite Control Set
FRT	Fault Ride Though
GaN	Gallium Nitride
HF	High Frequency
HV	High Voltage
IGBT	Insulated Gate Bipolar Transistor
IMPP	Current at Maximum Power Point
Kw	Kilowatts

LHP	Left Half Plane
LV	Low Voltage
MPC	Module Predictive Control
MPP	Maximum Power Point
MPPT	Maximum Power Point Tracking
Np	Number of PV modules in Parallel
Ns	Number of PV modules in Series
P&O	Perturb and Observe
PCC	Point of Common Coupling
PF	Power Factor
PM	Phase Margin
PR	Proportional Resonant
PV	Photovoltaic
PWM	Pulse Width Modulation
q	Electron Charge
RESs	Renewable Energy Sources
SEPIC	Single-Ended Primary-Inductor Converter
THD	Total Harmonic Distortion
T cell	Temperature of PV Cell
VMPP	Voltage A at Maximum Power Point

VSI	Voltage Source Inverter
fg	Grid Frequency
fs	Switching Frequency
ft	Sampling Frequency

Chapter 1

Introduction

1.1. Background

The development of grid-connected PV power generation systems has experienced a remarkable and significant wave over the past few decades. As a result, the efficiency of clean energy resources has been significantly improved, while greenhouse gas emissions have been mitigated [1]. Additionally, the increasing advancement in renewable energy technologies has led to stabilizing renewable energy prices, particularly with the significant increase in residential demand and the introduction of new types of electrical demand, such as electric vehicles (EVs) [2]. Figure 1.1 illustrates the details of the amount of power generated by the region in the last 10 years. It shows significant increases in renewable power generation because of rapid advancements and innovations in its related technology. As a result, the PV system's efficiency and robustness have been improved over time.

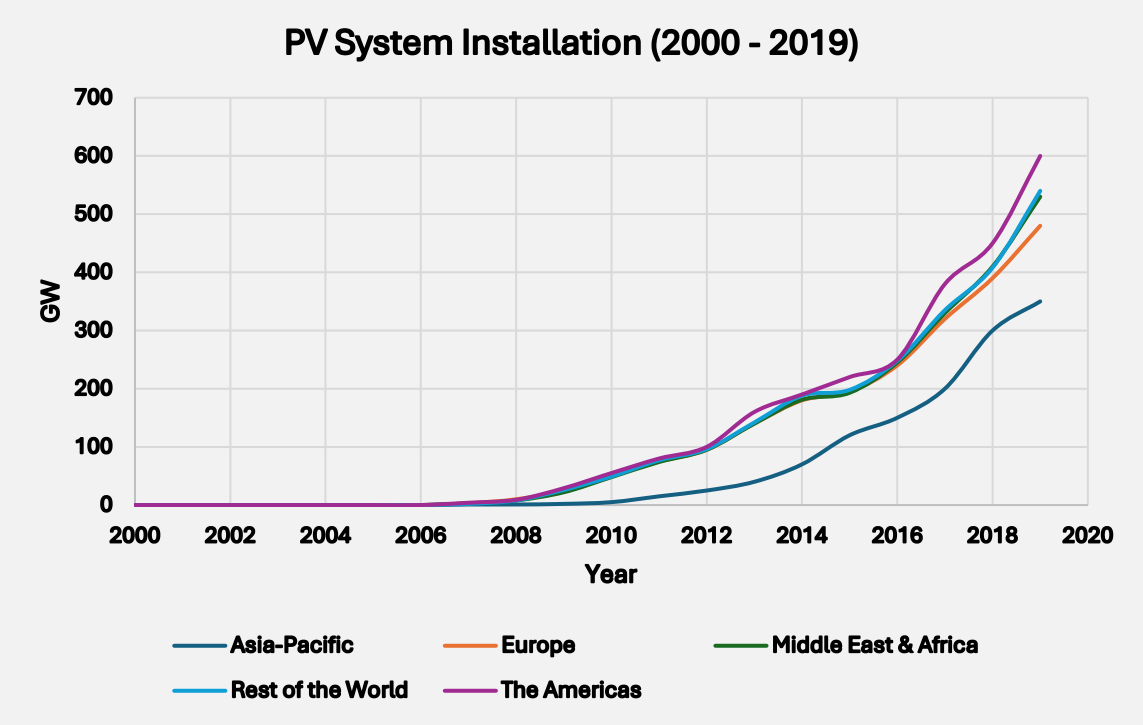

Figure 1.1 The development of PV installations in various regions [2].

The growth in energy demand has increased interest in investigating unconventional power resources [3]. Renewable energy resources are essential for meeting the growing electrical energy demand. Among the various options, solar energy has gained interest due to its clean and abundant nature. A fundamental element of grid-tied photovoltaic (PV) systems is the DC-AC inverter, which is designed to convert DC power from the PV side to alternating power and send it to the distribution network without causing voltage or frequency issues. The unequal power generation of PV modules in PV systems, which occurs due to factors such as partial shading and degradation of PV modules, results in reduced generation capability [4]. A relatively novel solution to address the concerns arising from power mismatch between PV modules is the individual extraction of maximum power from each PV module [5].

Grid-connected distributed PV systems form a significant part of the PV systems in Europe. This is a result of the long-established leadership that European nations maintain in this innovative technological area. In many European countries, effective feed-in tariff frameworks have been implemented, allowing consumers to become prosumers who can produce and consume their energy. Several countries have introduced different financial incentives to encourage end users to invest in renewable energy, especially for PV applications. The increasing development of such technologies can help users meet local electrical demand and support the electrical network [6]. Figure 1.2 illustrates the percentage of grid-connected distributed PV systems, grid-connected centralised PV installations, and off-grid PV systems. It also demonstrates that over 95 percent of the PV system applications are connected to the electrical grid.

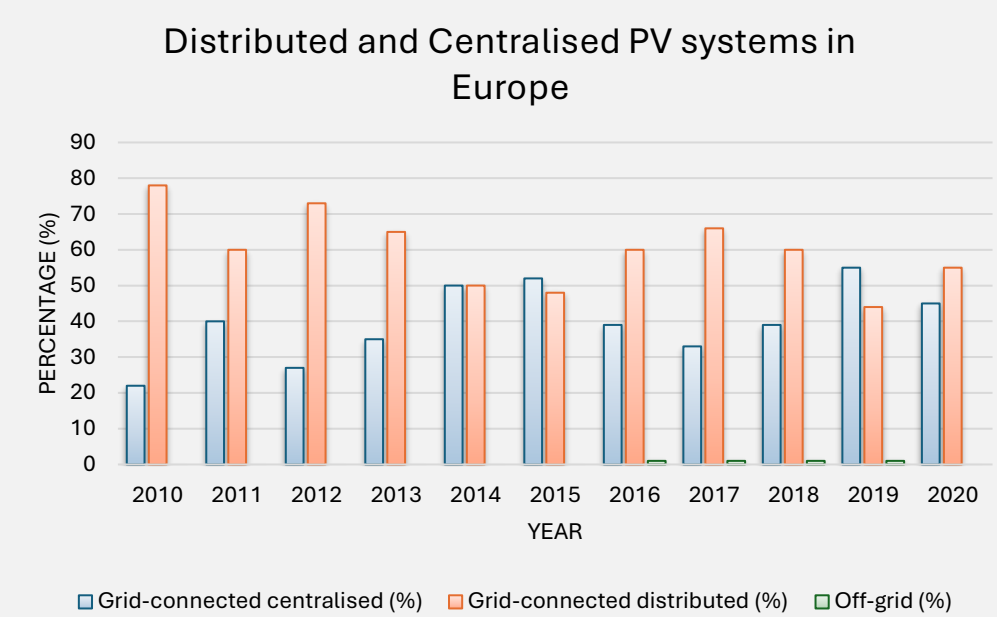

Figure 1.2 Yearly distribution of distributed and centralised PV systems in Europe.

Residential PV application prices decreased sharply between 2012 and 2019, reaching their minimum value at 2 USD/W. The significant reduction in PV system prices is due to advancements in PV systems and related technological developments, and the decrease is expected to continue as related technologies improve. This can lead end users to invest in PV residential applications and make profits [7].

Installation costs of residential and ground-mounted PV systems have decreased significantly in the last 10 years, with the lowest point recorded in 2019, as shown in Figure 1.3. This significant price reduction refers to many factors, including technological advances, manufacturing process improvements, and the considerable investment in these energy solutions. The number of residential and commercial users continuously increases due to the development of renewable energy technology [6-7].

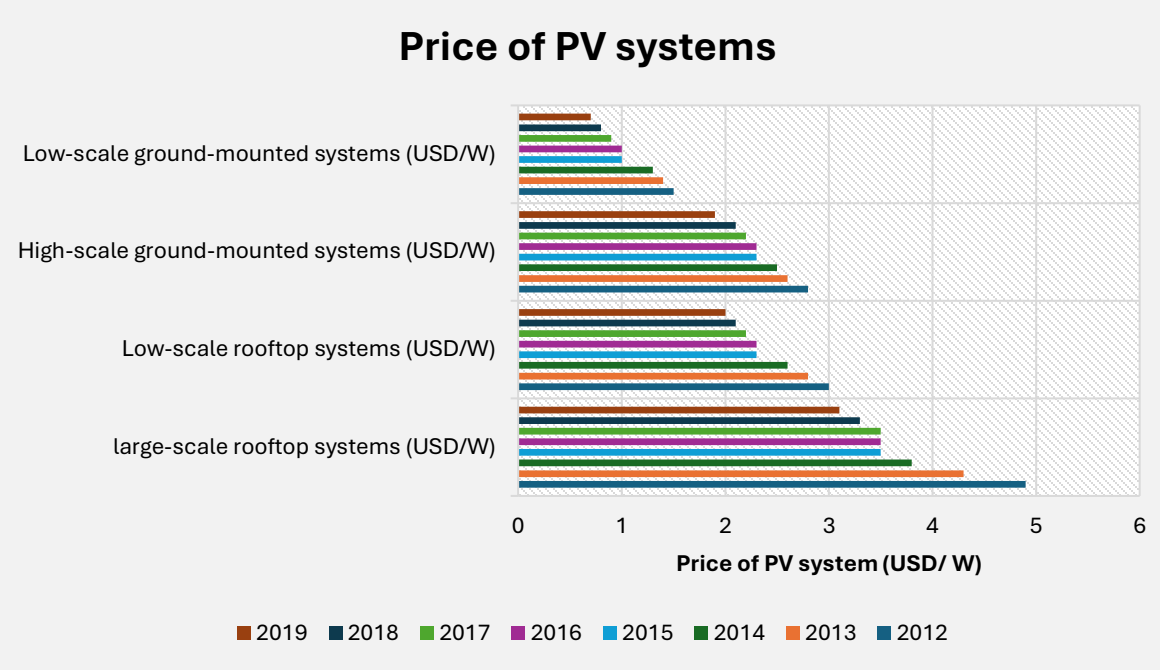

Figure1.3. The price of PV systems between 2012 and 2019 for high and low-range residential PV systems [6].

1.2 Grid-Tied Power Inverter Topologies

Grid-tied DC–AC inverters have been developed to facilitate the delivery of power generated from PV systems to the utility grid network. DC–AC inverter should meet grid standards. These standards include maintaining power quality, the decoupling of the AC components presented at the input side and providing practical protection strategies. The DC-AC inverter is a critical component of grid-connected PV systems, accounting for approximately twenty percent of the total PV system cost; thus, reducing the cost per watt of the inverter can significantly decrease the overall installation expenses of the PV generators [8]. Therefore, numerous researchers are concentrating their efforts on the innovation of optimised and cost-efficient inverter designs. The inverter in use can function either as a VSI or a current source inverter (CSI). In the case of VSIs, the input DC voltage is modulated by inverter switches using one of the modulation strategies, such as pulse width modulation (PWM). Then, the modulated signal at the VSI output passes through the filter circuit to remove the harmonics [9]. Figure 1.4 presents a typical structure of a grid-tied PV system for residential applications.

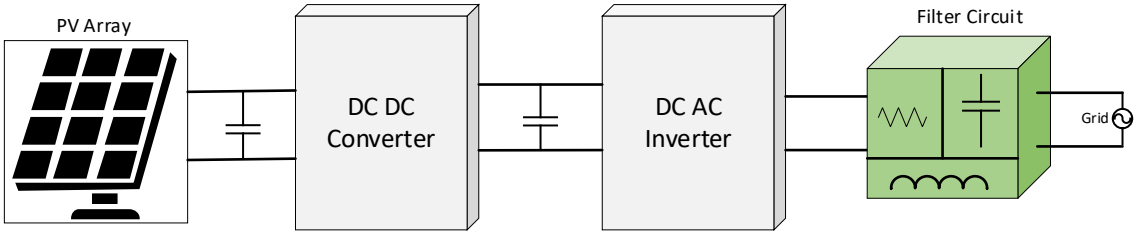

Figure 1.4 A standard grid-tied residential PV design.

One of the main issues with the VSI is the discontinuous input current, which necessitates the use of a large decoupling capacitor at the input side of the PV system to smooth the input current and enable the tracking system to capture accurate maximum power point (MPP). Using a large capacitor at the input side of the PV system is not preferable because it affects the reliability of the residential PV system and can also increase installation costs [10]. On the other hand, the CSI can maintain a continuous input current at the input of the PV system. The CSI does not require an input filtering capacitor, which makes it a proper choice for several PV applications. However, the control systems of most CSIs are commonly more complex than those of VSIs [11].

CSI topologies are commonly more complex than VSI, which makes this type less common in PV applications. Another issue of CSI is the need for a precise parameterization process in the design stage [12]. The additional stage at the input side of the PV system results in a complex system design for CSI because the input switch controls the PV system's input current, which flows through the inductor. Thus, the output current and voltage of the CSI are not directly related to the input current. This can lead to the introduction of a right-hand zero in the frequency domain of the CSIs, which can affect the bandwidth and require a professional design procedure. Figure 1.5 illustrates the fundamental configurations of both VSI and CSI [13].

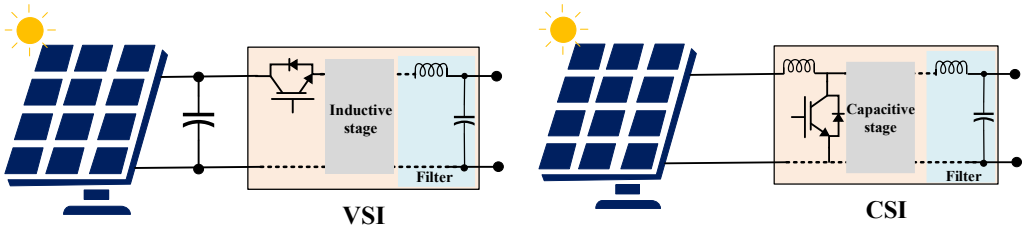

(a) VSI (b) CSI

Figure 1.5 A standard configuration for DC/AC inverters.

Integrating PV modules or panels with the electrical grid is critical and requires the appropriate selection of inverter systems [14]. Figure 1.6 illustrates various connection technologies, which will be briefly outlined in the subsequent subsections.

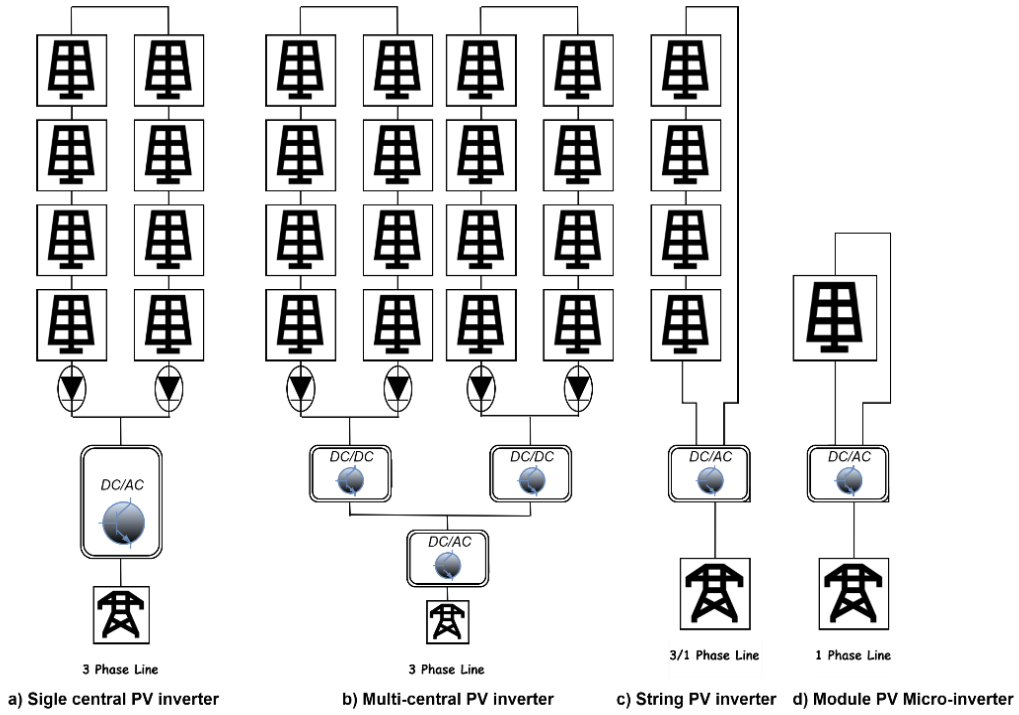

Figure 1.6 The classification of grid-connected PV systems based on the DMPPT.

1.2.1 Grid-Tied Central Inverter

Grid-tied central inverter technology is one of the oldest PV technologies for grid-connected and standalone large PV projects. Central inverter technology is designed to connect large PV applications to the electrical grid. Its configuration is based on connecting a mixture of series and parallel PV modules and linking them to the grid. The series configuration is commonly referred to as a string, and it is used to step up the LV of PV modules to meet the requirements of the electrical grid [15]. Therefore, central inverters commonly do not require extra booting consideration in the design stage. The PV modules in central PV system are often connected in series, and each string is equipped with a string diode, which prevents the adverse effect of reversing current flowing from other strings during faulty operation scenarios. The parallel connection of central inverters is usually implemented to provide sufficient output power and meet the power requirements of PV projects. PS is a primary challenge for central inverters and leads to a massive reduction in power output. Self-shading

is another issue with this technology, where part of the PV system poses a shading issue to neighboring PV modules. This concern is usually mitigated by adjusting the space between the PV modules in the central PV project [16].

The MPPT algorithms are used to extract the maximum power from the large PV system at the plant level. Thus, only one MPPT system is required, resulting in a more straightforward implementation. Although central inverter technology offers several advantages, especially for large PV projects, it also presents many serious concerns. Despite their benefits, central inverters present several significant limitations; one of the main troubles is the mismatch losses due to unequal power generation from the PV modules under shading conditions [17]. Additionally, the central PV inverter lacks a scalability feature; thus, increasing the system scale requires redesigning the PV project and probably replacing some components. Central PV inverters utilise string diodes to enhance the protection of the PV project; however, this approach leads to increased power losses and reduced system efficiency. A malfunction of any part of the PV project can result in the loss of the entire power generation of the PV system [18].

A DC-AC inverter failure stops the operation of the entire PV project, resulting in a loss of PV power generation. It also poses a serious concern regarding the frequency and voltage of the electrical grid. The multicentral PV inverter configuration is presented to address issues related to central PV inverters [19]. The multicentral PV inverter topology improves the reliability of central PV systems and enables the implementation of MPPT systems at the sub-plant level. As a result, the mismatch issue was reduced, and the power production of the PV system was enhanced. The multicentral PV topology design is based on dividing the conventional central PV project into sub-plants, where each sub-plant utilizes a separate power electronic inverter. This PV configuration is commonly used for medium to large-scale PV systems with power exceeding a megawatt. Multicentral PV inverters are often designed to connect the PV sub-plant in parallel, providing sufficient voltage output and enhancing the reliability of the PV project. Failing one inverter does not stop the entire PV system, which mitigates the possible problems associated with the utility grid [20]. Figure 1.6 (a) shows the topology of a single central PV inverter, while Figure 1.6 (b) illustrates the configuration of the multicentral PV inverter connection.

Conventional central inverters with three-phase VSI are commonly used for large PV projects, as illustrated in Figure 1.7. A single VSI controls the total output power of the PV project. Therefore, malfunctioning a single VSI switch results in a complete shutdown of the central PV system. The power converter switches are usually sensitive to overvoltage and current, which is common in large PV applications. Moreover, the switches in the central PV inverter handle high power; thus, the temperature of the switch can cause the electronic switch to burn out [21]. These factors can significantly reduce the central PV inverter reliability and increase power losses. Divide the PV system into small subsystems and enable the implementation of distributed MPPT approaches, resulting in enhanced energy harvesting and mitigating mismatch concerns [22].

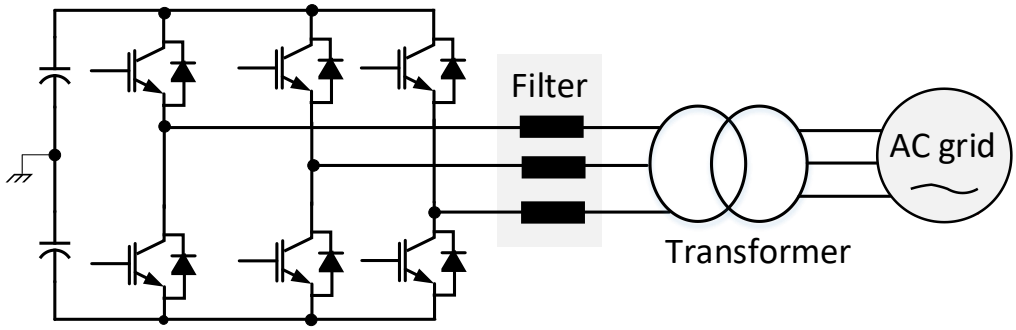

Figure 1.7 The three-phase VSI as a representative example of central inverters.

1.2.2 String Level Inverter

The string PV inverter technology is introduced to overcome the limitations of conventional central and multi-central PV inverters. The string PV inverter technology configuration is shown in Figure 1.6 (c). The PV strings in the PV string inverter are built by connecting several PV modules in series, where each PV string is usually linked with a DC-DC converter. These DC-DC converters are connected to a common DC-AC inverter for grid integration. The cascaded nature of the PV modules in string PV inverters provides sufficient stepping-up capability; thus, boosting the output voltage of PV string inverters is unnecessary [23]. Maintaining the voltage level at the grid side is crucial, especially when integrating a large PV project. Therefore, several large PV projects require increasing the output voltage of the PV string inverters; thus, the DC-DC converter side considers stepping up the output voltage in the design stage [24].

Grid-connected PV string inverters address several issues associated with conventional central PV inverters. Designing string PV inverters involves linking each PV string with a DC-DC converter. Thus, the string diode is eliminated, and power losses are minimized [25]. Moreover, the mismatch issues commonly occurring between PV strings in central PV inverters are reduced significantly, and each PV string captures the maximum available power via its own MPPT system. Unlike conventional central PV technology, string inverters provide better robustness for the PV system. In the event of a single PV string failure, the operation of the entire PV system is not significantly affected. The total power is distributed between PV strings, which can enable the capture of the maximum power from each PV string individually. As a result, both efficiency and power production capability improved [26].

1.2.3 Module Level Inverter

The central and string inverter technologies, which are often used for large and medium PV applications, rely on cascading several PV modules to enhance the PV system's step-up capability and meet the distributed network's output voltage. The maximum available power of conventional PV inverters is typically achieved at the PV plant or sub-plant level. At the same time, MPPT systems operate to capture the power of the entire PV project or PV string. This strategy is practical and effective in normal operation; however, under a mismatch scenario, a significant amount of power can be lost due to the mismatch effect [27]. Residential PV applications are more vulnerable to mismatch issues, especially PS. Mismatch issues pose a significant problem for the LV PV systems and can significantly reduce the power production of rooftop PV systems. One proposed strategy to mitigate the mismatch issue is to integrate a parallel diode with PV modules to isolate the mismatched part of the PV system. This method can reduce concerns about mismatches and prevent hotspots. However, separating the shaded PV section from the PV system means losing the power generated from that part [28].

The PV system with a module-level inverter utilizes a separate power converter for each PV module in the system, enabling maximum energy capture and ensuring that the PV modules operate at their respective MPPs. Therefore, each PV module can operate with a micro-inverter, which can be classified as a single-stage or a double-stage inverter. Since micro-

inverters are integrated at the PV module level, the semiconductor components can be designed with lower voltage and current ratings, enhancing overall system efficiency. Furthermore, the functionality and reliability of the entire system are enhanced during faults that affect one or more micro-inverters as the remainder of the system continues to operate [29].

Although the number of semiconductor components in PV module inverters is higher than in central and string inverter topologies, the installation net cost of PV module inverters is lower because the conventional string and central inverters use high-rate semiconductor devices and large-value filter components. Moreover, the PV module inverter offers more flexible features regarding generating reactive power and supporting the distribution grid [30]. In PV module inverter systems, a DC-DC optimizer is employed to effectively capture the maximum amount of power from each PV module, which helps to meet the local demands of the end users. There are two standard configurations of PV module inverters, one is based on connecting the DC-DC optimizers in series and linking the output to a standard DC-AC inverter. The second configurations rely on the parallel connection of the DC-DC optimizers. The series configuration of DC-DC optimizers can provide better efficiency compared to parallel connection, which makes it preferable in several LV PV applications [31]. Figure 1.6 (d) represents the module-integrated DC–AC micro-inverter.

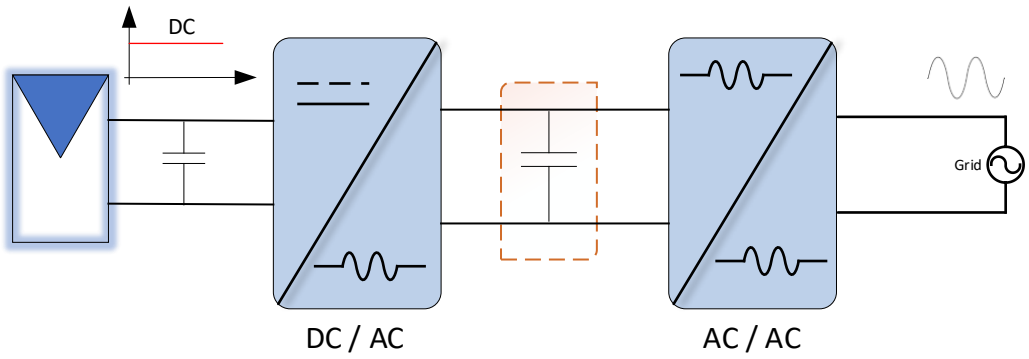

(a) DC-link

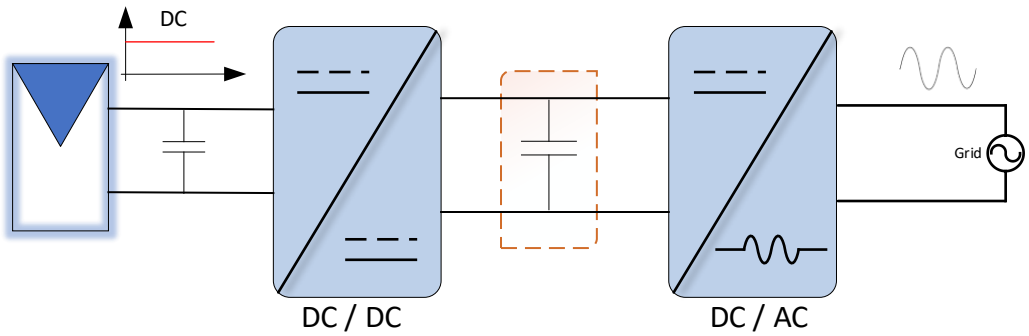

(b) Pseudo DC-link

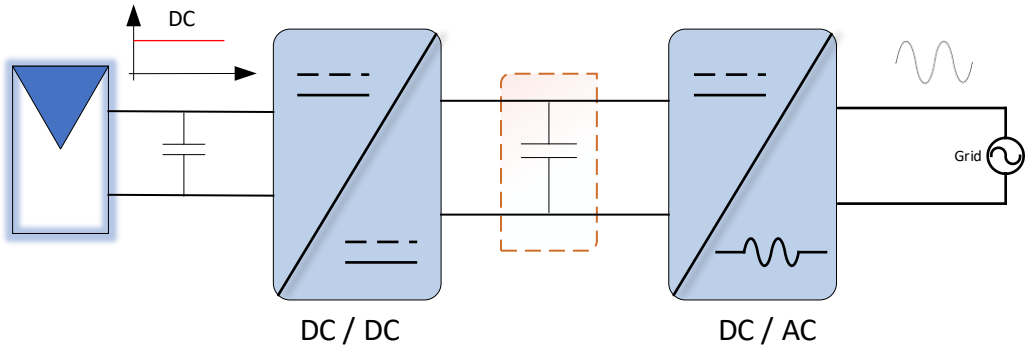

(c) High-frequency link.

Figure 1.8 Inverter structures for two-stage DC-AC modules.

In recent decades, there has been a significant and rapid increase in the integration of module-based inverters into residential PV applications. This growing technology is often categorized into several types: DC-link inverters, Pseudo DC-link inverters, and Frequency changer inverters [32]. DC-link inverters subdivide the inverter into two different stages: the DC-DC conversion stage and the DC-AC inversion stage, as illustrated in Figure 1.8 (a). The initial stage is typically responsible for regulating the DC side and optimizing MPPT algorithms, while the second stage addresses issues related to AC power quality. The primary challenges associated with this inverter topology include harmonic distortion at the output and switching losses. The DC-link inverter associated challenges can be mitigated through the implementation of soft-switching strategies. A decoupling capacitor is commonly placed after the DC-DC converter, where it remains isolated from the AC grid part, which can enhance the overall design and functionality of the DC-link inverter [33].

The second possible design of the integrated inverters is the Pseudo DC-link inverter. Among its special advantages are its operation at line frequency and the straightforward design of its

controllers. In this module-based PV inverter, the DC-DC converter regulates the input current to generate a rectified sine wave at the decoupling capacitor, as shown in Figure 1.8 (b). The DC-link voltage oscillates at double line frequency and generates a rectified sine wave. In the DC-AC inversion stage, the rectified sine wave at the DC link capacitor is converted into a sinusoidal output waveform operating at the line frequency [34]. This type of model-based PV inverter provides high performance and requires fewer components. However, it poses some concerns, especially to a distribution network. The Pseudo DC-link lacks galvanic isolation, which can pose a risk to end users. Also, maintaining the voltage level is challenging in this type of PV module inverter [35].

The third category of inverters integrated with PV modules is known as the High-Frequency link inverter, which is illustrated in Figure 1.8(c). A notable advantage of this category is that the power conversion process is simplified into just two stages. Usually, this type is used in the processing of AC power, thus operating without an intermediate direct current link capacitor. In the DC-AC conversion phase, the High-Frequency modulator adjusts the DC from the PV side into a high-frequency alternating current. Then, this high-frequency AC is converted into a sinusoidal waveform that operates at the line frequency [36].

1.3 Semiconductor Technology for PV Grid Applications

Si-based transistors, including metal-oxide-semiconductor field-effect transistors (MOSFETs) and insulated-gate bipolar transistors (IGBTs), are the dominant switches used in power electronic circuit design. This technology is mature, and the power loss estimation techniques are well-developed. Over the last few decades, Silicon-based materials have been the focus of power electronic researchers aiming to enhance the implementation of power electronic converters and mitigate associated power losses. However, the performance improvement is limited by the physical characteristics of silicon materials [37]. As a result, researchers have shifted their focus toward investigating other materials that offer better specifications. Wide-bandgap (WBG) devices, with their superior physical specifications over conventional silicon materials, have gained attention in power electronic design and are believed to be the next generation of power electronic converters. Gallium nitride (GaN) and Silicon Carbide (SiC)-based materials have emerged as the most common types of WBG devices used in the power electronic market [38].

In recent years, WBG devices have gained significant attention in power electronic converters due to their ability to provide superior efficiency and reduce power losses. The development of WBG devices has encouraged power electronic researchers to study the characteristics of this new technology and compare it with conventional Si-based technology to improve the efficiency of power converters. GaN and SiC switches are commonly used in modern power electronic converters [39]. In the low- and medium-voltage ranges, WBG transistors offer superior features to silicon-based switches due to the high electron mobility of these semiconductor materials. However, the current literature on WBG switches lacks detailed comparative investigations of the associated losses in conventional silicon transistors and GaN HEMT switches. WBG semiconductor materials provide several advantages over traditional silicon-based technology, including higher blocking voltage, better efficiency, and operation at higher switching frequencies [40].

GaN-based transistors have been introduced to the semiconductor devices market over the last decade and are considered promising devices for future power electronic circuits. GaN devices offer several advantages over conventional silicon-based switches. They can handle higher blocking voltage in the ON state compared to Si and SiC switches. High power efficiency is a critical requirement for power electronic converters, ideally approaching 99%, and GaN transistors have demonstrated an overall efficiency increase of three to four percent compared to conventional switches. However, GaN semiconductor technology faces several challenges as a developing technology, and one main issue is accurately estimating the associated losses to calculate the efficiency of GaN transistors [41].

The standard approach for estimating the performance of power electronic converters is based on calculating the ON state resistance (Ron) and breakdown voltage. These two parameters are commonly used to calculate the losses of different power-switching devices and perform a comparison analysis. The conventional MOSFET transistors are limited by the physical characteristics of the silicon element, as they are silicon-based technology [42]. A new semiconductor material with improved physical specifications is required to optimise power converter circuits and minimise power losses. In the last few years, new semiconductor devices with wide-band energy have been introduced. The ON-state resistance of these devices is relatively low, which allows a high breakdown voltage. GaN-

based devices are among the most promising technologies in switch-mode converters, offering several advantages, including improved operating temperature, high thermal conductivity, high blocking voltage, and high switching frequencies [43]. Table 1.1 presents a detailed comparison of the three most common semiconductor technologies used in power converters across various applications.

Table 1.1: Semiconductor technology features used for power converters [43].

Features/Tech	*Conduction losses*	*Switching losses*	*Thermal losses*	*Voltage Range*	*Installation cost*	*Efficiency*
Silicon (Si)	High	High	High	Moderate	Low	Low
Gallium Nitride (GaN)	Low	Low	Low	Low	High	High
Silicon Carbide (SiC)	Moderate	Low	Low	High	Moderate	Moderate

1.4 Main Challenges and Study Objectives

The objective of this research project is to enhance the performance of low-level grid-connected PV systems. The main complications of low-level grid-connected PV systems are low conversion efficiency, high installation cost, and irregular power generation. These complications should be addressed to increase energy harvesting of residential PV grid-connected applications.

- Low conversion efficiency can be a significant concern for PV systems. The efficiency of the power electronic inverter usually depends on the materials used and the manufacturing process. Therefore, one objective of this project is to propose a new power converter topology with enhanced efficiency.
- The lifetime of the power electronic inverter should be increased, and the inverter should be capable of coping with different environmental conditions. That can improve the functionality of the PV module. Several factors, including the decoupling

capacitor, operating temperature, and used materials, can affect the lifetime of the power electronic inverter.

- The input voltage of a single PV module is relatively low compared to the distribution grid voltage, which poses another challenge for the DC-AC module inverter. Therefore, the DC-AC model inverter must be able to boost the PV module voltage to match the grid voltage. Proposing a practical method that compares viable solutions and recommends the most optimal design, which converts a low input DC voltage to a high output voltage with improved efficiency, is crucial.

- The PV side input power comes in DC form, while the grid side power is AC. Thus, the DC-AC power electronic inverter must decouple the input direct power at the PV side from the alternating power at the grid side. Introducing a new practical decoupling technique is important in DC-AC design.

Mismatch loss due to PS and other mismatch factors is a significant concern in rooftop PV systems, which can result in substantial power loss. Implementing the distributed MPPT at the PV module and PV sub-module level can significantly mitigate mismatch concerns. This dissertation will focus on designing and investigating new, practical module- and sub-module-based power inverter topologies to maximize energy and reduce mismatch issues. It will also compare the proposed topology to different available topologies and suggest the most promising option based on efficiency and functionality.

1.5 Thesis Outlines

The thesis consists of six chapters. Each chapter of the thesis begins with a general introduction and overview of the chapter's contents to provide the reader with a better understanding of the chapter. Then, it introduces the methodology and describes the proposed system. Followed by an analysis of the results and concluded with a chapter summary.

Chapter 1 demonstrates the recent advances in technologies for grid-connected PV systems and the motivations of this study. It introduces the different PV inverter technologies, starting with the old central inverter and ending with PV module conversion technologies. Also, it presents a brief introduction to the rules for employing new semiconductor technologies,

including GaN and SiC devices to power electronic converters. The chapter ends with introducing the main challenges faced by LV PV applications and the objective of this thesis.

Chapter 2 Briefly explains the PV single-diode model, which is commonly used to understand the behavior of PV systems. It then provides detailed explanations about the effect of a low irradiation level on the PV system and its relationship to the system's output power. The chapter also addresses concerns about mismatch and the operation of PV cells string under mismatch conditions. Then, it presents an overview of the different sources of mismatch problems in the PV system, including permanent and temporary mismatches. Furthermore, the chapter presents the common mitigation approaches that are commonly used to mitigate mismatch concerns in PV system applications. The chapter concludes by offering a comprehensive overview of implementing distributed MPPT approaches at the PV sub module level to reduce mismatch issues.

Chapter 3 presents a novel Cuk-based PV MI designed for grid-connected PV applications. It begins with an overview of residential grid-connected configurations, including series and parallel model-based inverters. Then, it introduces the proposed Cuk-based inverter topology and how it is integrated with the electrical grid. Moreover, the different operation modes of the proposed MI , including DC-DC, DC-AC, and AC-DC modes, are described, followed by a presentation of the experimental validation process for various operating scenarios. A comparison study is presented to evaluate the proposed MCI against the conventional central Cuk inverter, demonstrating the effectiveness of the proposed method in mitigating mismatch issues. The chapter concludes with a summary of the findings of the proposed strategy.

Chapter 4 starts with a comprehensive introduction to grid-tied rooftop PV applications. Then, it introduces the proposed multi-input single-output topology, aiming to tackle the mismatch issues inside a single PV module. The chapter illustrates the circuit configuration of the proposed PV sub-module inverter, which is designed to employ the distributed MPPT strategy at the PV SM level. Next, the chapter demonstrates the small-signal model of the boost converter to derive the control system for the proposed topology. Additionally, it presents experimental validation, which confirms the effectiveness of the suggested method in addressing the mismatch problem at the PV SM level. The chapter concludes by providing

a comparative discussion, illustrating the capability of the proposed strategy to enhance the power production of a single PV module.

Chapter 5. It presents a comprehensive introduction to MPC and its application for grid-connected power electronic configurations. It begins with providing an overview of the state-of-the-art in this advanced control technology. Then, it introduces the two common types of MPC strategy: continuous MPC and predefined MPC. Additionally, it provides a brief explanation of the MPC components used for controlling power electronic circuits and introduces some limitations of the MPC technology, such as the computational burden and operating at variable switching frequencies. After that, it proposed an MPC-based strategy to decouple the 2nd-order harmonic effectively in the decoupling capacitor of the SEPIC-based single-phase inverter. Also, a novel duty ratio-based MPC method is presented at the end of this chapter to overcome the variable switching concern.

Chapter 6 presents a summary of the thesis and future research directions. It highlights the primary contributions of this project and their relevance to the research objectives. The chapter concludes by demonstrating the outcomes of the thesis and recommendations for future studies.

Chapter 2

State of the Art Review

2.1 PV Model

A PV or solar cell is a photosensitive semiconductor device and is the fundamental element of a PV module. The function of a solar cell is the reverse of a light-emitting diode (LED); instead of emitting light when current flows, a solar cell absorbs light and generates an electrical current. Like a diode, solar cells consist of a P-N junction. However, the PV cell's P-N junction is sensitive to light [44]. The typical PV cell module is illustrated in Figure 2.1. The incoming photons from the light will enhance the movement of electrons and act as a current source. Part of the current will pass through the diode and have the same equation as the standard diode. The remaining portion of the current will represent the PV cell current. The voltage across the diode varies according to the semiconductor material used in its manufacturing process. The current generated by the solar cell can vary according to the percentage of the sun's radiation [45]. The relationship between the cell current and voltage, also known as the V-I characteristic of the solar cell, can be calculated using the following equations.

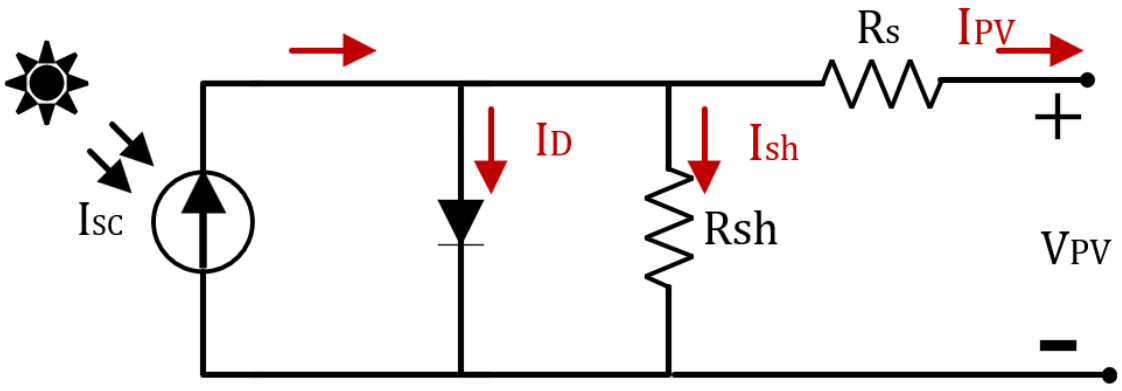

Figure 2.1: The standard equivalent circuit of the PV cell.

$$I_{PV} = I_{sc} - I_D - I_{sh} \quad (2.1)$$

$$I_D = I_o * (\exp\left(\left[\frac{Vcell}{nV_T}\right]\right) - 1) \quad (2.2)$$

$$I_{PV} = I_{sc} - I_o * \exp\left(\left[\frac{Vcell}{nV_T}\right]\right) - 1) - \frac{V_{PV} - I_{PV} \cdot R_S}{R_{sh}} \quad 2.3$$

Where I_{sc} is the short-circuit current, V_{cell} is PV cell voltage, V_T is the thermal voltage, which equals 25.85 mV at 25°, n is the ideality factor, and is the saturation current.

The PV cell characteristics can be obtained by plotting the cell voltage against the cell current. Figure 2.2 illustrates the relationships between V-cells and I-cells at different irradiation levels when the cell temperature is assumed to be constant. There is a direct correlation between insulation level and power output. Also, the plot shows the behavior of the PV cell in the reverse direction. On the right side of the plot, the PV cell acts as the current source and generates power; however, in some scenarios, the PV cell can be shifted to the left side, where it acts as a sink [46].

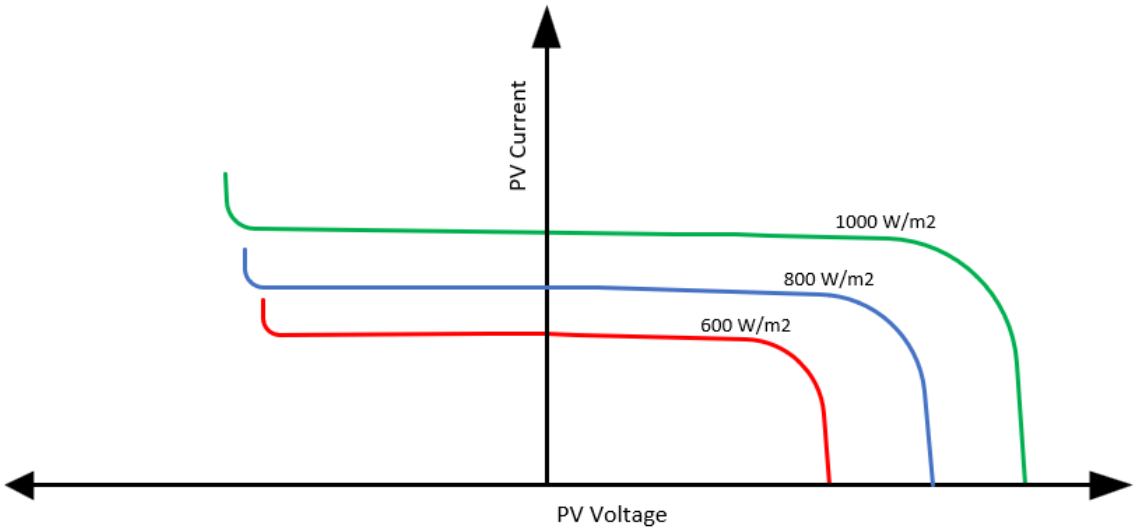

Figure 2.2 The IV curves for three distinct PV cells with different insulation levels.

The short-circuit current (I_{SC}) is considered when the current voltage I-V curve intersects the current axis of the I-V plot. Each PV cell has a unique I_{SC}, depending on the level of irradiation. The open-circuit voltage of the PV cell can be calculated when the I-V curve crosses the voltage axis of the I-V plot. Raising the cell temperature is one of the main factors that can negatively affect the open-circuit voltage of the PV cell. The open-circuit voltage drops as the temperature increases, which reduces cell power generation. The open voltage can vary from one cell to another, according to the PV cell temperature [47].

The voltage of a single PV cell can range from 0.5 V to 0.7 V, according to the material used in the manufacturing process. The PV cell voltage is relatively small and cannot meet the required output voltage. Thus, a series of PV cells is connected in series to increase the output voltage to the appropriate level [48]. Connecting the PV cell in series can be a viable solution to solve the LV output issue of the PV cell; however, it can pose some concerns regarding power production. One main problem is that the behaviour of PV cells can be different if the environmental conditions are not uniform across all PV cells, which can reduce power output and raise some safety concerns. This issue arises from a mismatch between PV cells, which can also occur between PV modules and SMs [49].

The first PV cell on the right of Figure 2.3 is assumed to have a lower irradiation level than cells two and three. The I-V characteristics of both the shaded PV cell and the other two PV cells are illustrated on the left side of Figure 2.3. The PV cell with a low irradiation level suffers from severe reverse voltage, which can cause a hot spot or, worse, cell damage. The conventional strategy to shift the reverse voltage to the positive side is to apply a parallel bypass diode to the shaded PV cell. An individual MPPT at the PV cell level is required to utilize the power from all PV cells of the PV module. However, the installation cost can significantly increase. Cascading a group of PV cells is crucial to step up the voltage of the PV cells. Thus, applying the MPPT to a group of PV cells can be more practical.

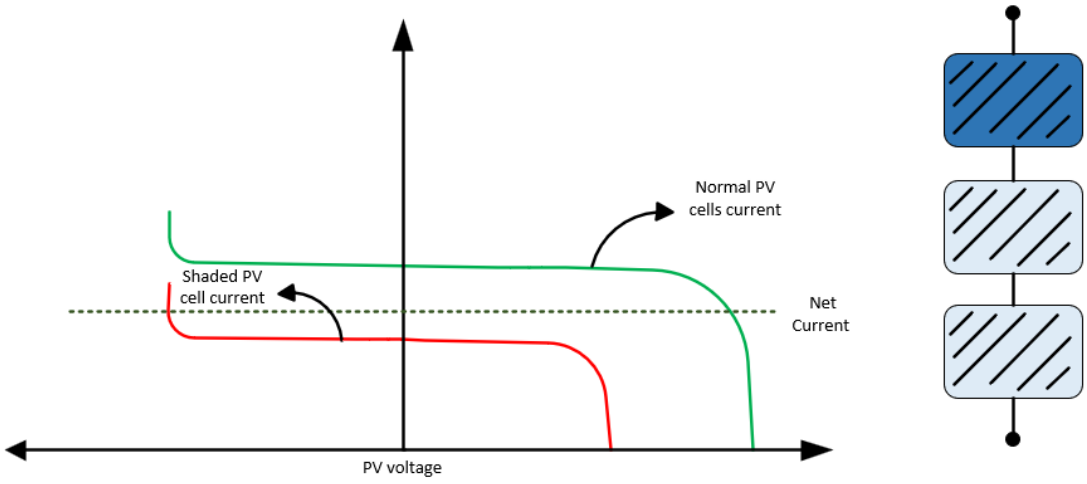

Figure 2.3 The partial shade effect on PV cells.

The PV cells are commonly linked in series, and the *I* string represents the behaviour of the series connection. In some cases, especially when PV cell power generation is reduced significantly, it will have a negative voltage and consume power instead of generating energy. The conventional PV junction box uses a bypass diode to shift the negative voltage to the positive side. This can address the concern of negative voltage in the PV module. However, the power generated by the faulty PV cells is lost. Applying the Distributed MPPT can be a viable solution to mitigate the mismatch issue. However, using it at the PV cell level is not practical nowadays because the PV cell voltage is relatively low [50].

2.2 Mismatch in PV Systems

Mismatch problems in different PV systems are commonly classified into two groups based on the type of mismatch fault. The Temporary mismatch category includes transient faults whose impact is not continuous with time. Partial and complete shading are the most common contributing factors to temporary mismatch issues. Dust is another type of temporary mismatch issue, which usually significantly reduces PV module power generation. Several approaches have been introduced to regularly clean PV modules to enhance the PV system's power generation [51].

The second group of mismatches in the PV system is associated with permanent faults. Most permanent mismatch faults are related to the manufacturing process of PV modules. The soldering stage during PV module construction is not perfect, resulting in a mismatch between PV cells within a PV module. Additionally, the environment in which the PV module is constructed contains small impurities that negatively impact its performance. Moreover, the aging of the PV module can lead to a permanent mismatch problem. Permanent defects can decrease the PV system's efficiency and power output by 10% [52]. Figure 2.4 illustrates the different sources of mismatch problems and some examples of each type.

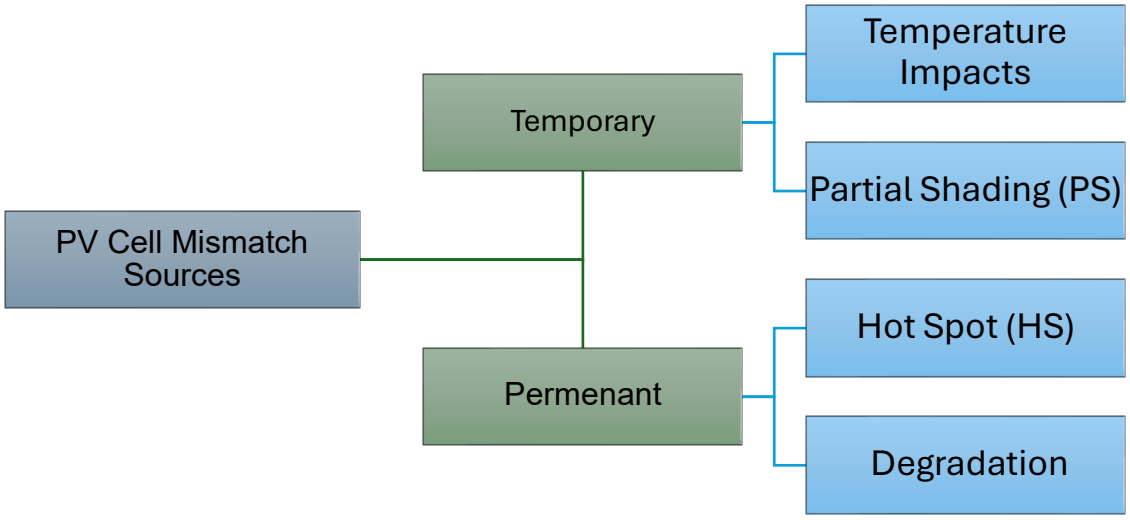

Figure 2.4 The PV mismatch faults and examples for each classification.

2.2 1 Temperature Impacts

Raising the PV module temperature is a major issue for most PV applications because it reduces the performance of the PV system. Temperature variation affects the characteristics of the PV module, resulting in changes to the current, voltage, and power curves of the module. The clear impact of increasing the PV module temperature is on the open circuit voltage. It results in a significant reduction in the open-circuit voltage, which minimizes the PV module's output voltage [53]. The behavior of the PV module varies according to the PV module's operating temperature. The MPPs of PV modules with different temperatures are not equal, resulting in a mismatch between PV modules. The PV modules' Standard Test Condition (STC) is 25 °. However, the actual operating temperatures of the PV modules are different. Figure 2.5 shows the adverse effect of increasing temperature on the performance of PV modules [54].

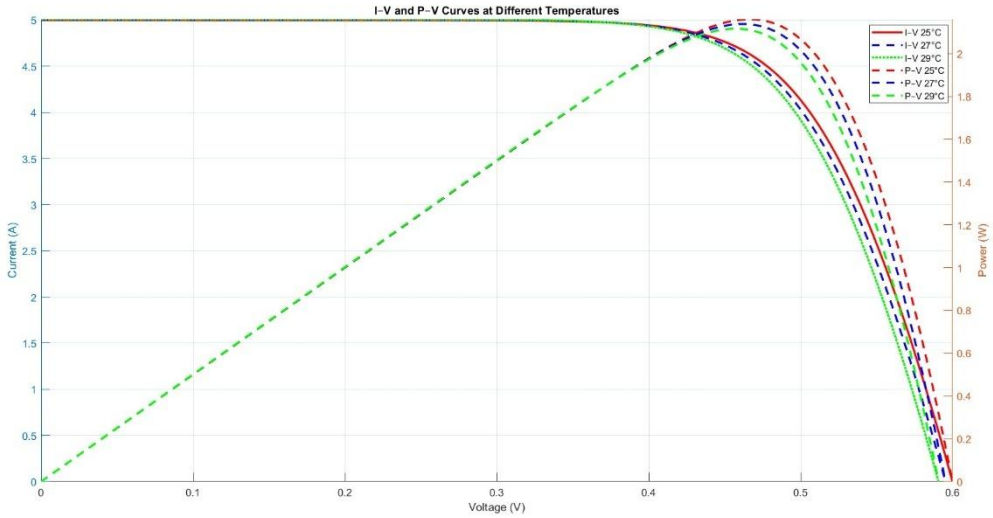

Figure 2.5 The High temperatures' impact on the PV system operation.

2.2.2 Partial shading

The intensity of solar irradiance often determines the performance of PV modules and can be a primary factor in deciding their output power. The high irradiance level on the surface of the PV module results in increased power generation for PV systems. The PS can cause uneven solar irradiation on the PV module surface, which results in different power generation of the PV SMs. The unequal power generation from the PV SMs can reduce power production and negatively impact the performance of the PV module [55]. The PS is commonly categorized into two types: uniform shading, where the entire PV module is blocked from receiving sunlight. The second type is non-uniform shading, and only a specific portion or section of the PV module is impacted by shading. These types commonly lead to a significant reduction in PV power generation and minimize the overall efficiency of the PV system [56].

The performance of the shaded part of the PV model differs significantly from that of the unshaded part. As a result, the interaction between the shaded and unshaded sections becomes complicated. The maximum power from the PV module is directly proportional to the percentage of irradiation on the PV module surface; thus, the shaded portion of the PV module generates less power than the section that receives a high rate of irradiation. The PV SMs are commonly linked in series to overcome the low-voltage nature of PV cells.

However, the series connection constrains the entire PV module by the PV SM with the lowest power generation. This condition can lead to a mismatch between the PV SMs, which can significantly reduce the power generation and efficiency of the PV system [57].

PS can arise from various factors, including moving clouds, birds or bird droppings, high buildings, and shading from trees [58]. An illustration of a real example of the PS on a PV module is shown in Figure 2.6.

Figure 2.6 The shading impact on residential PV models.

2.2.3 Hot Spot (HS)

A part of the PV module can experience a temperature rise, leading to a serious issue in the PV system known as an HS. The impact of the HS on the PV model is usually temporary; however, in some cases, it can have a permanent effect on the PV module. PS can cover a portion of the PV module, causing the shaded PV cell to become reverse-biased and result in temperature rise [59]. Once the PS effect is finished, the PV module is expected to function normally under normal conditions. However, in some cases, the adverse impact of the HS can arise, leading to a reduction in the PV module performance. The HS issue can arise from

shortages during the PV module manufacturing process, leading to a permanent problem and damage to the PV module [60].

The HS can pose a serious risk to the PV system users and reduce the PV system's performance. Thus, an effective monitoring system is introduced to mitigate this problem and maintain the optimal operation of the PV system [61]. The output power from a high-temperature PV module differs from that of a standard PV module. As a result, the faulty PV module becomes an energy sink rather than a power generator. In such a scenario, the PV system can experience a reduction in power generation. Moreover, the excess heat generated by a defective PV module can cause considerable damage to the PV module. The energy losses associated with HS issues in PV systems can exceed 5% of the total PV system generation [62]. Furthermore, the HS poses serious risks, including the potential for burning the PV module, as illustrated in Figure 2.7.

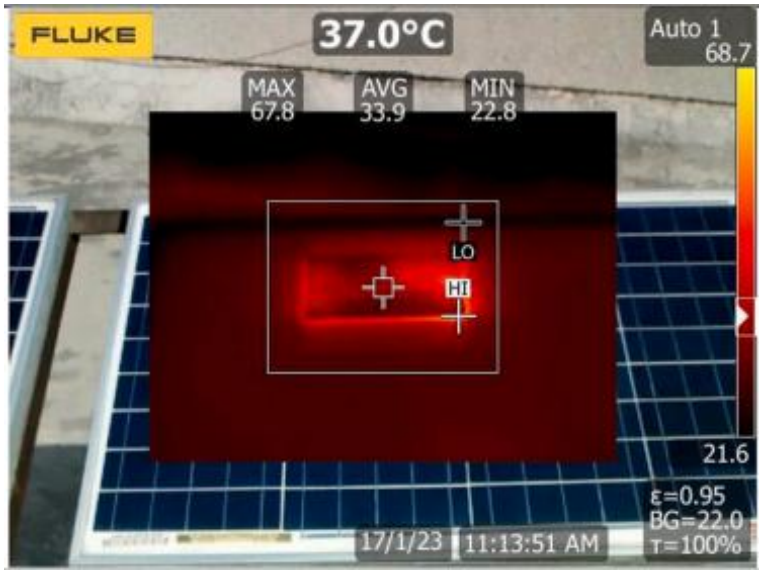

Figure 2.7 The influence of hot spots on the PV modules [62].

2.2.4 PV Degradation

Degradation of PV modules can negatively affect the overall performance of the PV system. Several factors can contribute to degrading the PV modules, including a reduction in the quality of the power converters, internal weaknesses within the PV modules, and increased humidity levels [63]. Recent PV applications utilized advanced technology to identify the types of degradation in the PV modules. A monitoring camera is a common approach for

identifying the cause of PV module degradation, as visual assessment is insufficient for precisely determining the source of degradation. One common degradation factor is the presence of microcracks on the surface of PV modules, which can be detected using specialized tools [64].

The color of the PV cell surface changes with time, which can significantly reduce the PV module's performance and the PV model's power generation. Several factors, including the material used in the manufacturing process, often cause a color change [65]. Usually, the color of the PV module changes to brown, blocking the irradiance from reaching the PV cell surface. Furthermore, humidity contributes to the degradation of PV modules and can cause delamination. The delamination issue is a common cause of mismatch in PV systems. Additionally, it raises a range of concerns, including light decoupling and potential fire risks [66]. An illustration of an aged PV module is shown in Figure 2.8.

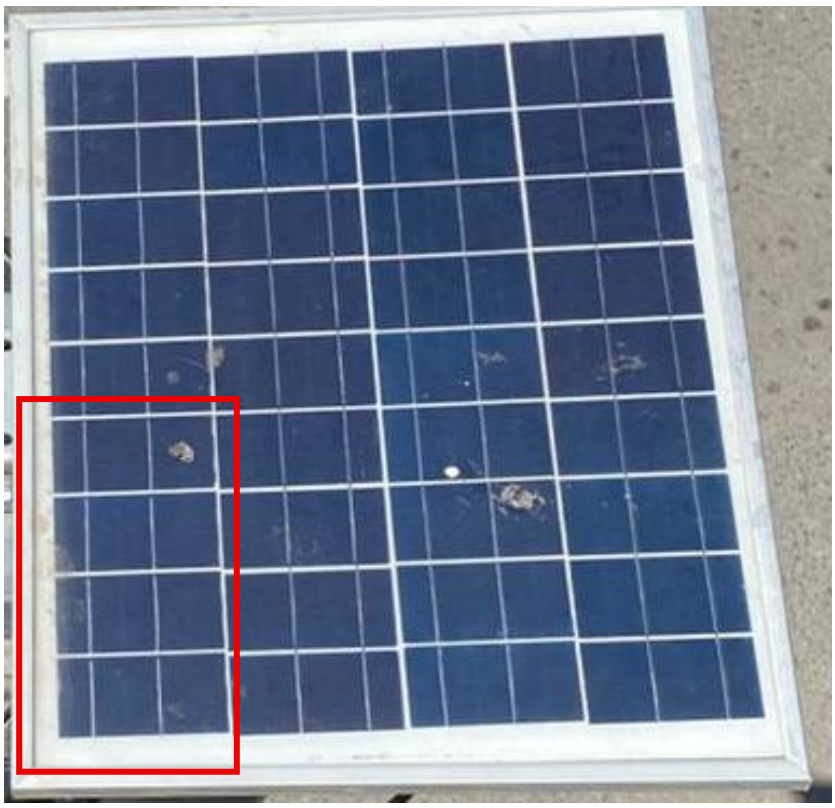

Figure 2.8 A 12-year-old PV module.

2.3 Mismatch Reduction Strategies in PV Systems

The mismatch issues between PV modules are one of the primary factors that contribute to power losses in PV systems. Connecting the PV modules in series is crucial for most PV applications to overcome the LV nature of the PV modules and meet the distribution network's standards requirements. However, linking the PV modules in series can cause several challenges regarding the performance and power quality of the PV system [67]. The nonuniform irradiance profile is commonly associated with most PV system applications, reducing power generation and minimising PV system efficiency. Thus, several mitigation approaches have been proposed to enhance the efficiency of PV systems and increase their power production effectively. Mismatch mitigation strategies are commonly divided into two main types: bypassing methods, where the defective PV part is isolated from the PV system, and distribution strategies, which aim to capture the power generated by the mismatched portion [68]. The chart presented in Figure 2.9 illustrates the various optimization strategies employed to address the mismatch issue.

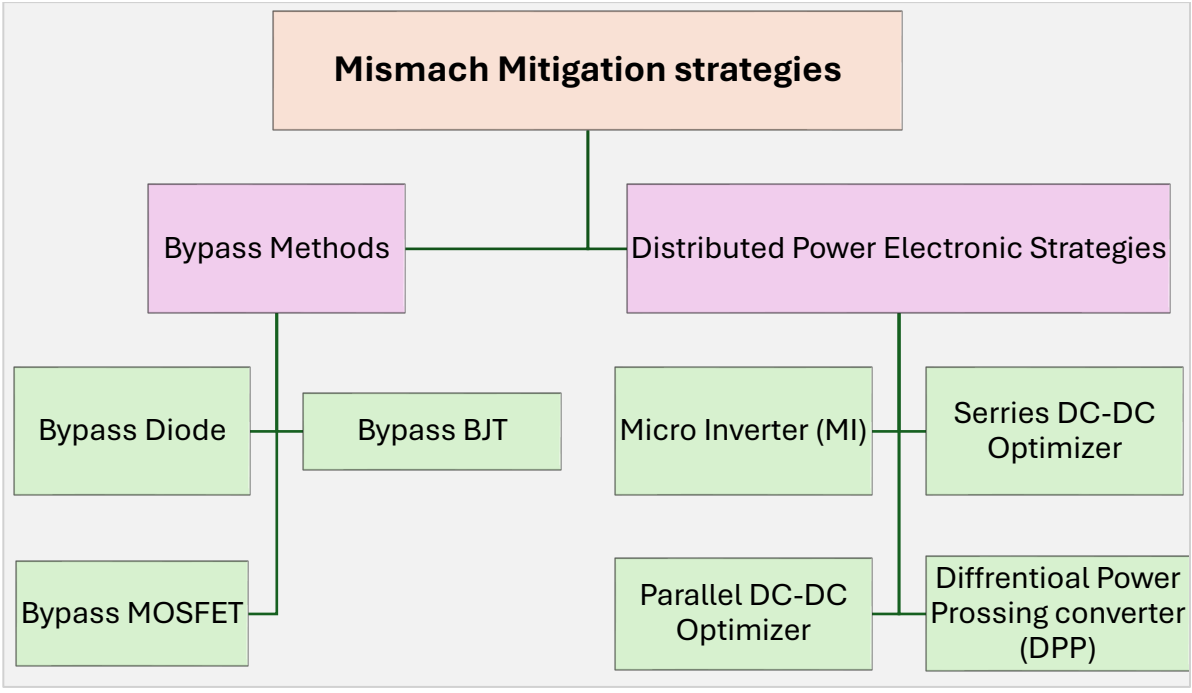

Figure 2.9 The mitigation approaches used for the mismatch issue.

2.3.1Bypass Methods

The conventional strategy for reducing the negative impact of the mismatch between PV modules is to bypass the net current of the PV system and isolate the shaded PV module from the overall system. The bypass strategy can mitigate the concern of mismatch and protect the rest of the PV system from defective PV modules. Although this method can effectively minimize the impact of the mismatch problem, the power generation from a faulty PV module is lost due to isolation from the PV system. A viable solution to this challenge is the individual harvesting of energy from each PV module, which solves the mismatch issue while enhancing the power harvesting of the PV system [69].

2.3.1.1 Bypass Diode

In this methodology, a bypass diode is installed in parallel with the PV module to reduce the adverse effects associated with mismatch issues and to address the reverse voltage problems that arise due to mismatch concerns. Implementing the bypass diode is one of the most traditional and straightforward methods for minimizing mismatch issues between PV modules. The presence of reverse voltage leads to power dissipation, which can cause an increase in the temperature of the PV module. Therefore, the bypass diode creates an alternate pathway for the current, mitigating HS concerns [70]. The I-V curve of a series string of PV modules will be different under the PS effect when a bypass diode is added in parallel to each PV module. This change can result in multiple MPPs, which can confuse the tracking algorithms that determine the maximum output power [71]. The multiple MPPs issue arising from employing the bypass strategy is illustrated in Figure 2.10.

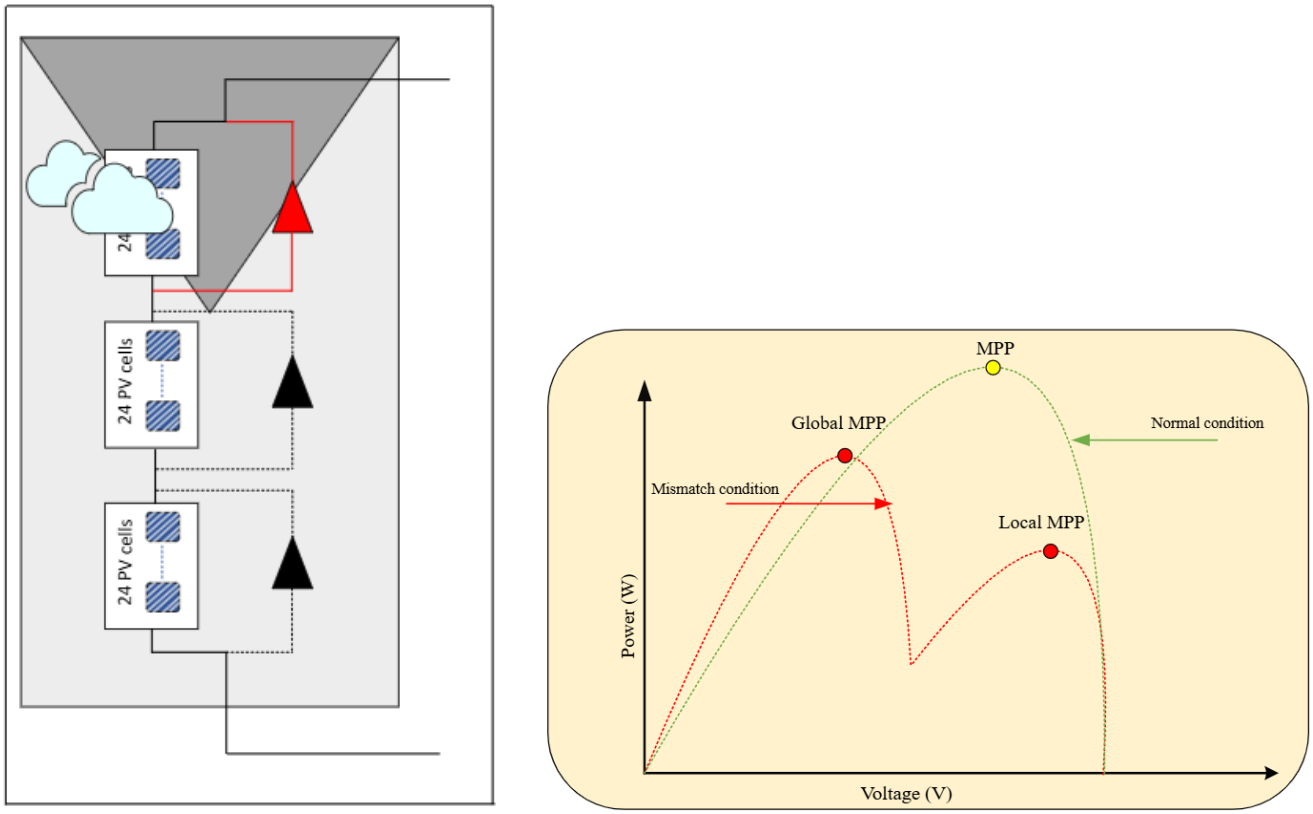

(a) Typical PV model structure

(b) The voltage-current (V-I) characteristics curve.

Figure 2.10: The Bypassing diode method strategy.

2.3.1.2 Bypass BJT

Another bypass technique used to mitigate the negative impact of mismatch problems between PV modules is employing a BJT to bypass the PV system current. The main objective of this strategy is to generate a path for current when the power generation of the PV system is unequal. Two MOSFET switches are responsible for controlling the BJT without introducing an extra control process. The gate-source voltage of MOSFET (1) is the same as the PV module voltage; therefore, this switch will remain on. Similarly, the gate-source voltage of MOSFET (2) is equal to the drain-source voltage of MOSFET (1). Under the regular operation of the PV system, the current passes through the MOSFET (1) and then the PV module. When the PV system is affected by partial shading, the gate-source voltage of MOSFET (1) becomes 0; hence, MOSFET (1) will turn off. MOSFET (2) will turn on, allowing the current to pass through the BJT. The difference between this approach and the conventional bypass diode is that this strategy overcomes the problem of negative voltage

because it can share negative voltage with the internal resistance of the series MOSFET switch [72]. The BJT method employed for reducing unbalanced power generation is illustrated in Figure 2.11 (a).

2.3.1.3 Bypass MOSFET

This strategy is based on connecting a MOSFET switch in series with the PV module, and one diode is connected in parallel with this string. The MOSFET bypassing method is similar to the BJT's strategy but involves one fewer electronic switch. The MOSFET switch turns on when the mismatch problem does not occur, allowing the current to flow through it. Similarly, when a part of the PV system is shaded, the MOSFET switch turns on, allowing current to flow through the parallel diode. Internal resistance can cause an extra loss to the PV system operating in normal conditions. However, this becomes an advantage when the PV system is affected by partial shading, as it resolves the reverse voltage issue [73]. This strategy is illustrated in Figure 2.11(b).

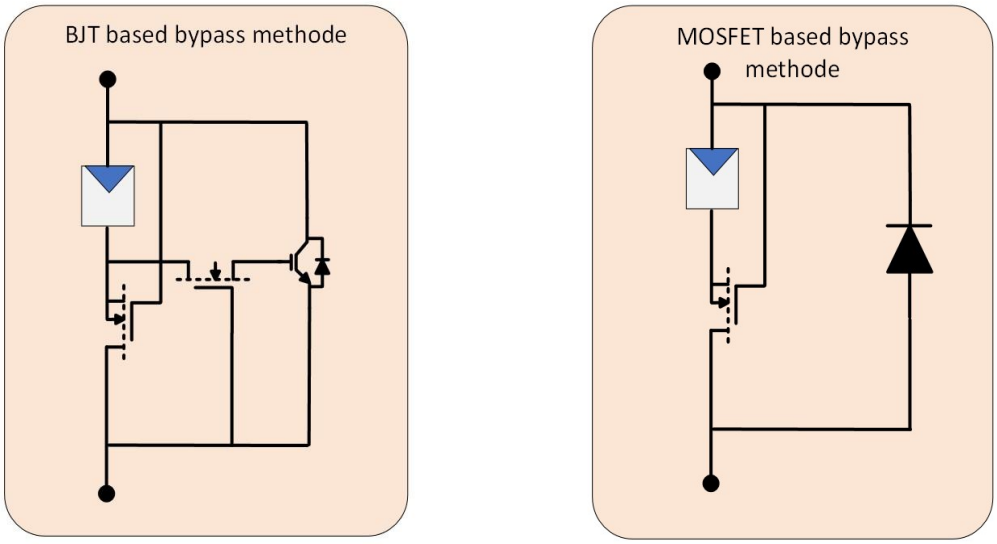

(a) BJT bypass strategy (b) MOSFET bypass technique.

Figure 2.11 The untraditional bypass strategies.

2.3.2 Distributed Power Electronics Strategies

Harvesting the power from each PV module separately can mitigate the PV system's mismatch concerns and increase PV power production. The distributed MPPT system within

each PV module is utilized to extract the PV module's maximum power. Distributed MPPT is commonly used in PV systems to effectively mitigate mismatch issues and maximize power output from the PV system. The Distributed MPPT methodology can be effectively implemented at various levels of the PV system architecture, which ranges from the PV array level down to the individual PV cell level [74].

The PV system is regulated to operate at MPP to extract the optimal energy from the PV system, as illustrated in Figure 2.12. Different tracking algorithms are introduced to accurately determine the MPPs [75]. The tracking process becomes challenging under the mismatch effect because more than one maximum power point is produced. Also, in regular operation, the input voltage of the PV system must be regulated to operate at relatively small ripples. Maintaining a constant input voltage is crucial in the PV system to effectively manage the maximum power tracking system. The voltage ripple can mislead the tracking algorithm of the PV system; thus, it must remain strictly below a threshold of 8.5%. Additionally, the accuracy of the MPPT tracking system must exceed 98% to capture the maximum power [76]. As a result, a noticeable improvement in PV system efficiency can be achieved, and PV system reliability can be enhanced.

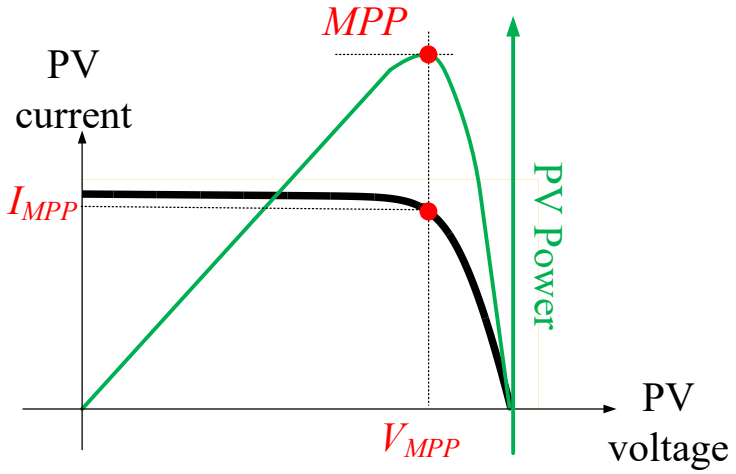

Figure 2.12 Typical current-voltage and power-voltage characteristics for a PV module.

2.4 PV Sub-Module Microinverters.

Implementing distributed MPPT approaches at the PV SM level leads to increased power harvesting of residential PV applications. The mismatch issue between the PV SMs within the same PV module can be mitigated by implementing the power distribution approaches at the PV SM level. Three MPPT systems employed within a single PV module enhance the PV system's performance and increase power harvesting [77]. One approach is to utilize cascaded DC-DC optimizers to mitigate the mismatch problem and improve the efficiency of residential PV systems. However, using this approach can result in a noticeable increase in installation cost because it requires more components than other methods. Also, designing the controlling system for cascaded DC-DC optimizers is a complex process [78]. Differential Power Processing (DPP) DC-DC converters are another strategy that is used to mitigate mismatch issues between PV SMs. The primary goal of DPP converters is to adjust the photocurrent between the PV SMs under the impact of mismatch issues. Nevertheless, this strategy requires a complex controlling process, and the installation costs are relatively high [79].

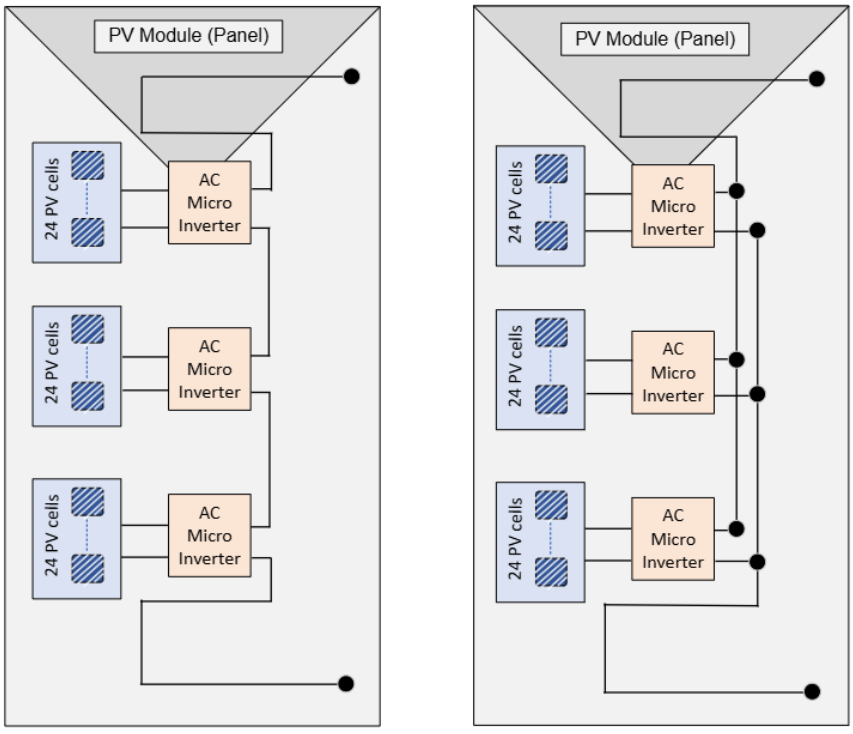

(a) Series-linked MI (b) Parallel linked MI

Figure 2.13 Sub-Module grid-tied microinverter.

A sub-module microinverter (SMMI) is an effective strategy for efficiently harvesting the maximum power from each PV SM in a PV system. Employing this method not only tackles the mismatch issue between PV SMs but also improves the efficiency of the PV system. This advanced approach enables converting the DC power at the PV side into alternating power to meet grid party requirements. The SMMI is designed to connect the PV module output directly to the utility grid without adding a central DC–AC inverter [80]. A definition of both series and parallel grid-connected microinverters at the PV SM level will be detailed in the subsequent sections. Figure 2.13 illustrates the configurations of both series and parallel grid-connected microinverters at the PV SM level.

2.4.1 PV Sub-Module Series Converters

The objective of the PV SM DC-DC optimiser is to enhance the energy harvest of the PV module in cases of unbalanced power generation between PV SMs. It aims to utilize a power electronic converter topology to address mismatch issues at the PV SM levels effectively. In the design stage, compact, economically priced components are used to build the suggested DC-DC optimiser [81]. The synchronous buck converters are connected in a cascading manner to achieve a higher output voltage, therefore eliminating the need for additional step-up power converter circuits. The control mechanism of the SM DC-DC optimiser is relatively straightforward, as it does not require communication between the controllers of the SMs during mismatch scenarios [82]. Figure 2.14 presents a schematic representation of the SM DC-DC optimizer.

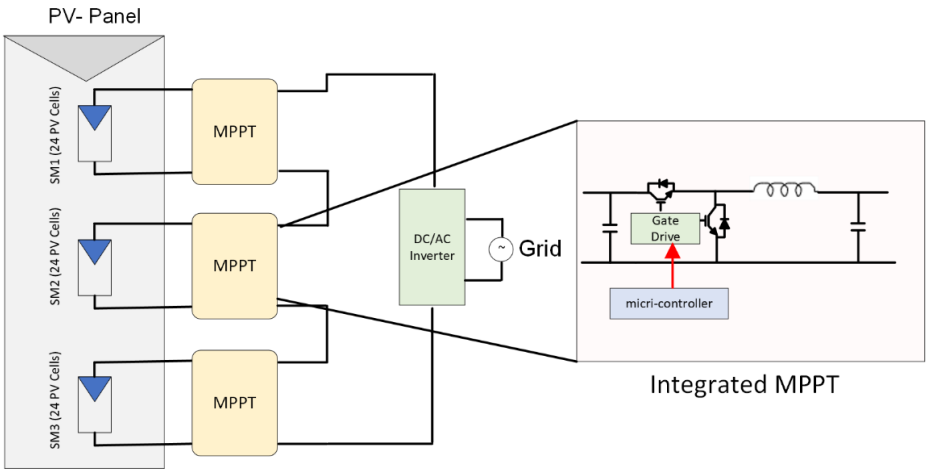

Figure 2.14 A graph of the buck-based PV SM combined with an MPPT system.

Regarding the MPPT control, the output power of each PV SM is regulated through the perturb and observe (P&O) algorithm. The implementation of a DC-DC optimiser strategy effectively addresses the issues arising from multiple maximum points, which are often associated with conventional bypass diodes in conditions of uneven power generation [83]. Given that the three SMs are connected in series, the string current can be considered a constant value. Therefore, the controlling parameter utilized to confirm the MPP is the voltage corresponding to each PV SM. This situation presents a direct optimisation challenge, which seeks to maximise power by adjusting the duty cycle of each DC-DC optimizer [84]. The flow chart represented in Figure 2.15 illustrates the MPPT algorithm employed for tracking the optimal MPP for each PV SM.

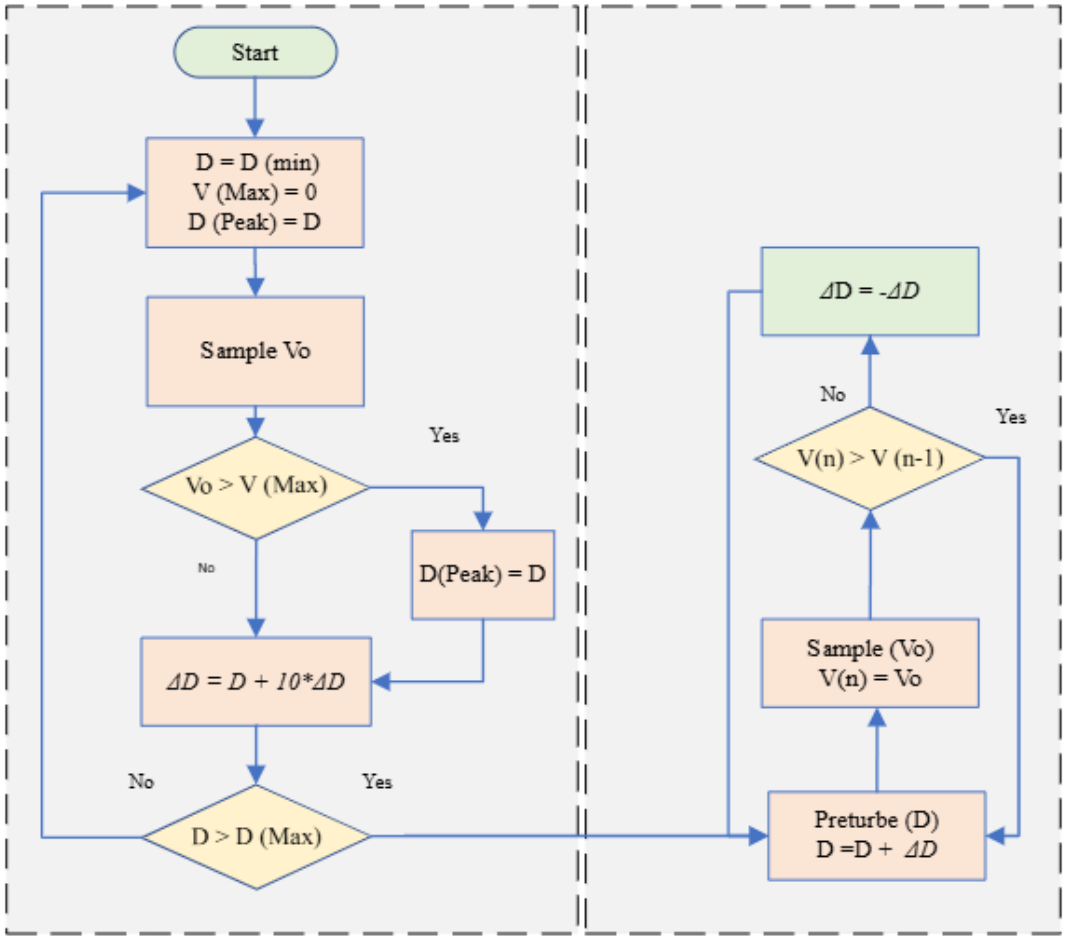

(a) Local maximum algorithm (b) Traditional P&O algorithm

Figure 2.15 The flowchart diagram of the MPPT algorithms of the buck-based PV SM converter.

The PV SM series converter is a common strategy for employing a distributed MPPT system at the PV SM level. In this method, the primary objective of DC-DC power converters is to reduce the size of power electronic components and minimize installation costs. One inductor and one sensor are used to effectively capture the output power of each PV SM independently. As a result, the net power of the PV module increases, and the mismatch is reduced at the PV SM level. To enhance the stepping-up capability of the PV system, the PV modules can be connected in series. The conventional P&O tracking approach is employed in this design to capture the maximum power from the PV module. The main disadvantage of this strategy is that a single traditional MPPT algorithm is utilized for all three PV SMs of the PV module. Therefore, the effectiveness of energy harvesting and the overall performance of the PV system are negatively affected [85]. Figure 2.16 illustrates the circuit configuration of the proposed topology that relies on a single inductor and a single current sensor.

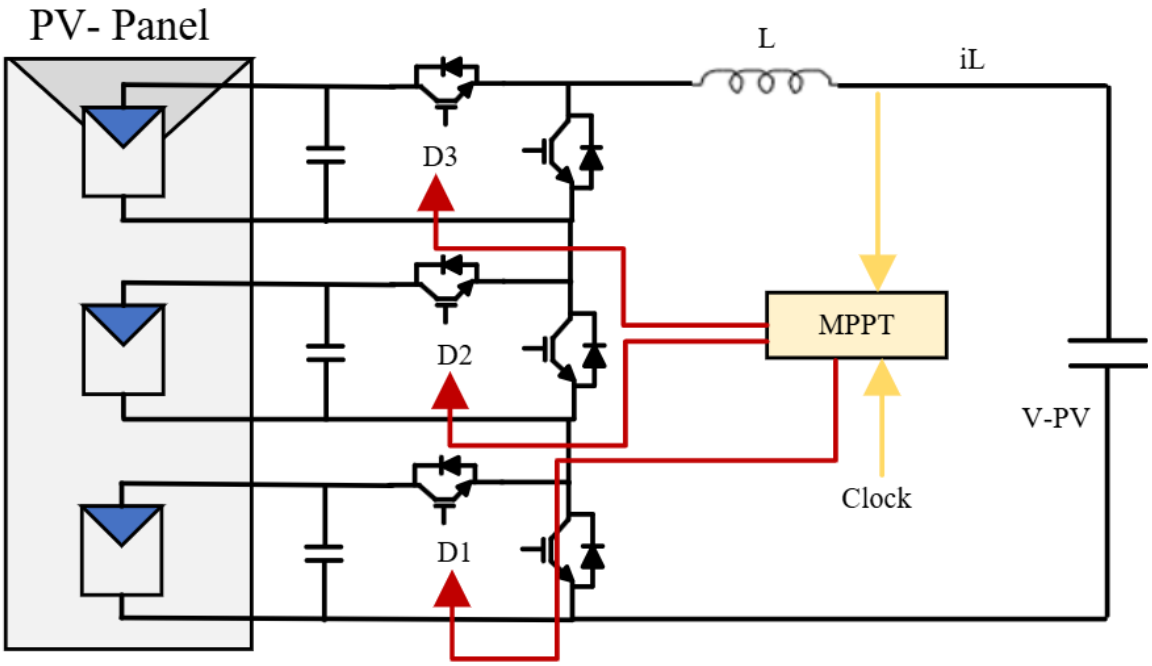

Figure 2.16 Structure of the improved buck-constructed MPPT method

To regulate the MPP of each PV SM, an adaptive P&O algorithm has been employed to obtain the current of the PV module and determine the path for the subsequent cycle. The current of the PV module is measured and matched with the current of each SM, serving as the reference current for the subsequent tracking interval. The duty-cycle ratio applied for

the operation of the SM converters is determined as the proportion between the SM current and the PV module current during a single tracking cycle [85]. Figure 2.17 illustrates the flowchart of the adaptive MPPT algorithm implemented in this research; the clock parameter is a critical factor that determines which SM should be prioritized for tracking.

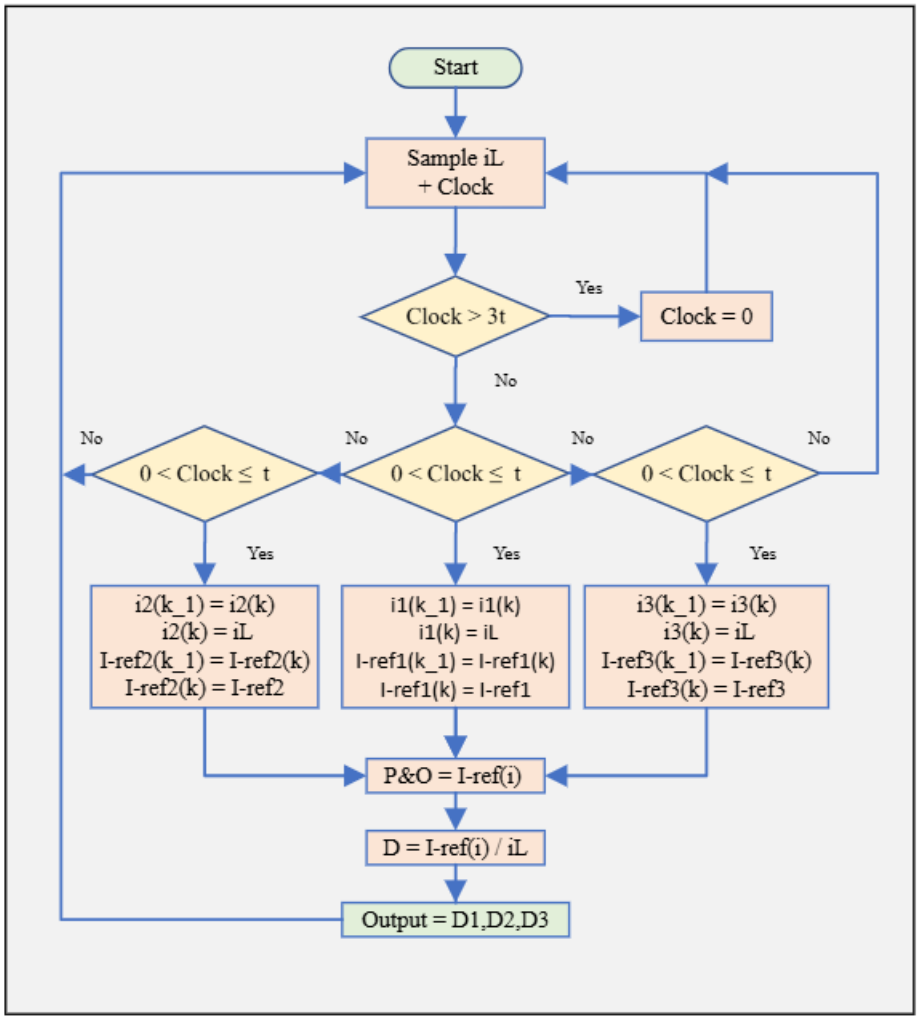

Figure 2.17 The diagram of the MPP algorithm in accordance with the current generated by the PV SM.

2.4.2 PV Sub-Module Parallel Converters

The low-voltage output nature of solar cells makes boost converter topologies more practical for several PV applications. Typically, boost converters are utilized in parallel arrangements to boost the LV to the appropriate grid voltage level [86]. A multiple synchronous boost converter is a general type of parallel design for this purpose. This specific topology is designed to address the mismatch issues associated with series-connected PV SM while

significantly enhancing the energy harvesting from PV modules. The proposed converter operates by connecting the SM power converters in parallel, thus allowing for the individual capture of the maximum available power of each SM, which optimizes energy harvesting and minimizes power losses. Furthermore, the external configuration of the PV modules is arranged in series to achieve a practical output voltage [87]. Figure 2.18 demonstrates the circuit configuration of the SM parallel integrated converter.

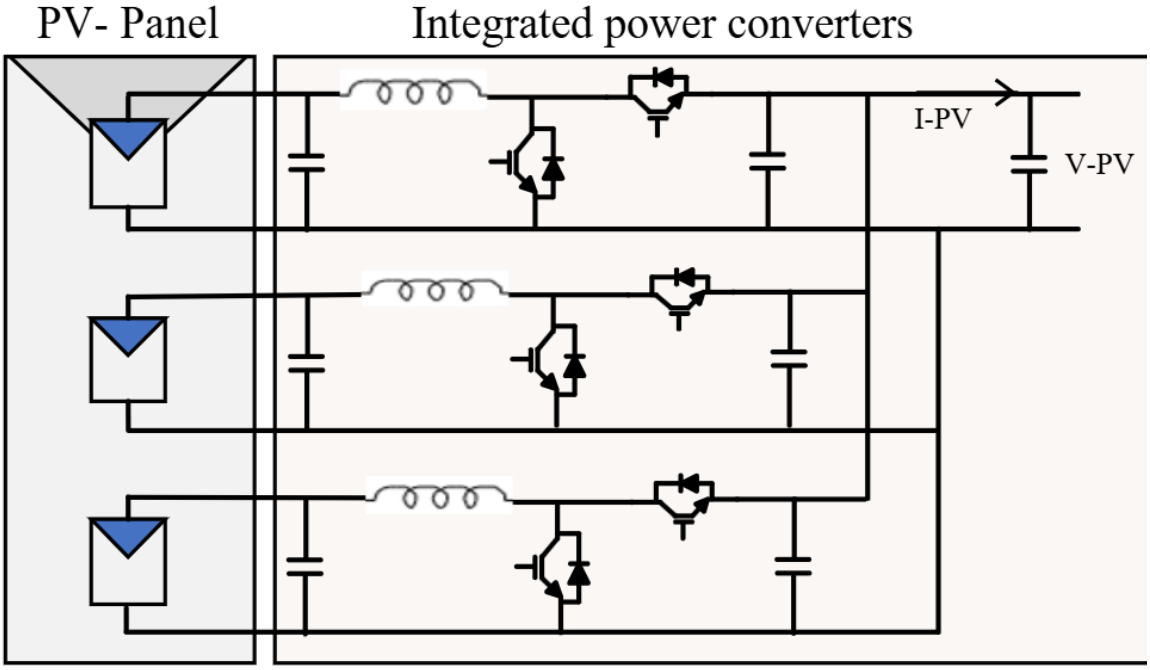

Figure 2.18 Sub-model structure of parallel boost converters for the individual PV model.

A single MPPT microcontroller has been implemented to control the three PV SMs of the grid-connected PV system, as the three converters are configured in parallel. The P&O tracking algorithm has been utilized to capture the maximum available power from each PV SM. The output voltage of the PV module serves as a reference value, which is compared with the voltages of the SMs to determine the appropriate direction for the following tracking cycle. During each cycle of the tracking process, the voltages of the three SMs are subjected to perturbation and subsequently compared with the output voltage [87]. The flow chart of the MPPT control algorithm is illustrated in Figure 2.19.

The initial phase of the MPPT algorithm involves initializing the parameters required for the tracking system. Subsequently, the algorithm begins measuring the output voltage and the

voltages of the three separate SMs. The indices associated with the SMs determine which specific SM voltage is subject to control. Continuous perturbation of the three SM voltages is initialized, with subsequent recording of the variations in the output voltage of the PV module. The variations in the output voltage of the PV module are assessed in relation to changes in the SMs voltages. The direction of the tracking cycle for each SM is established based on the changes in the output voltage resulting from the perturbation of the respective SM voltage. If the output voltage demonstrates a positive change, the tracking algorithm will maintain its direction; conversely, if the change is negative, the direction of the tracking process will be adjusted accordingly [87].

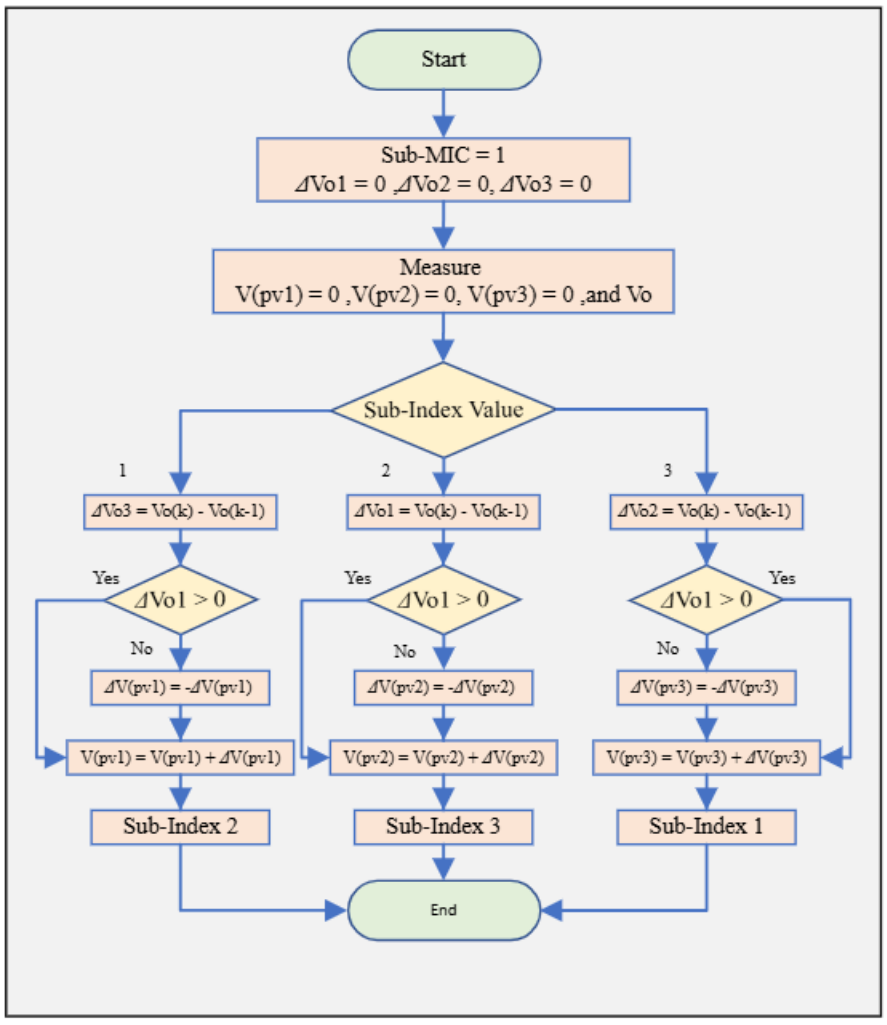

Figure 2.19 The MPPT algorithm of PV sub-modules of parallel boost converters.

2.4.3 PV Sub-Module Differential Power Processing (DPP)

The DPP topology is used to implement an optimization strategy that equalizes the current of the PV module and effectively mitigates the mismatch challenges arising between PV SMs [88]. This investigation utilizes the DPP PV-PV topology by integrating a bidirectional buck-boost converter to effectively reduce the current mismatch between PV SMs, resulting in enhanced energy extraction and minimizing power losses. The primary objective of the proposed configuration is to efficiently balance the current across the PV SMs in scenarios of unequal power generation [89]. Figure 2.20 illustrates the DPP PV-PV architecture employed to reduce mismatch issues between the PV SMs.

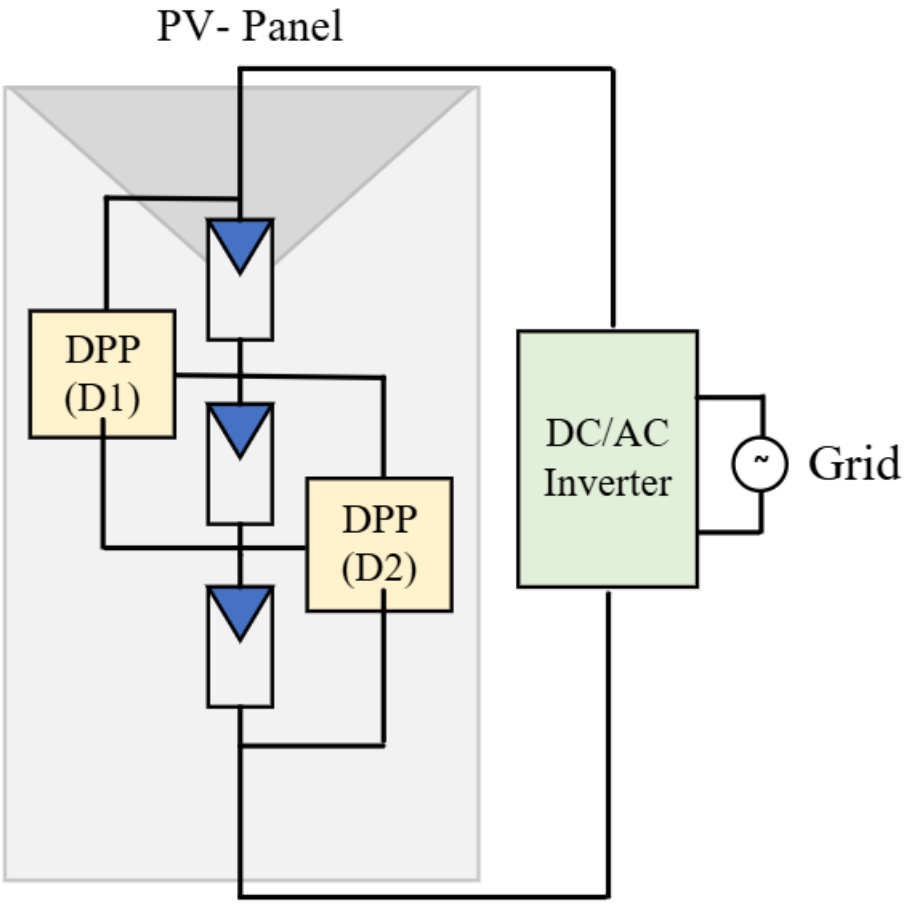

Figure 2.20 The schematic representation of the DPP.

The P&O algorithm monitors and redirects the current between PV SMs to effectively obtain the MPP. Given that the DPP converter operates at a relatively high frequency, it is assumed that the voltage of the PV module remains constant. As a result of this assumption, the current

from the PV module determines the direction of the subsequent tracking cycle. The proposed configuration implements two loops for MPP tracking. The fast control loop controls the operation of the DPP buck-boost converters, whereas the slower loop regulates the DC–AC grid-tied inverter [89]. Figure 2.21 illustrates the flowchart representing the control loop of the DPP buck-boost converters.

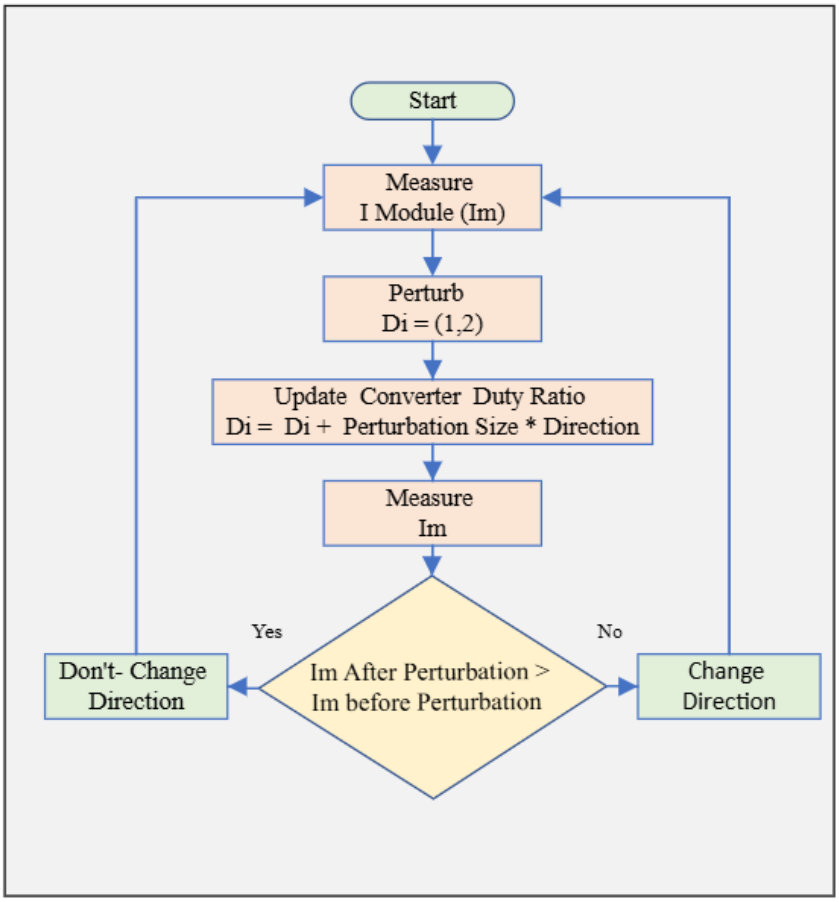

Figure 2.21 The algorithm employed for operating the DPP at PV SM.

Adjusting the duty cycle ratio of the DC-DC converters is based on measuring the current of the PV module. As a result, the duty ratio of the DPP converter is regulated by assessing the perturbation sample. The change in the current of the PV SM will be detected and recorded as the duty ratio applied to the DPP converters experiences systematic variation. The current value of the PV module is then compared with the initial value. If the current of the PV module before perturbation exceeds the current after perturbation, the tracking direction will change; conversely, if this condition is not met, the tracking direction will remain unchanged [89].

2.5 Future of the Grid-Tied MI

The issue of both partial and complete shading effects on PV systems can be characterized as unpredictable and, in many cases, unavoidable. PS can arise from various factors, including tree and building shadows, cloud covers, or bird droppings [90]. Therefore, the electrical properties of the shaded parts of the PV system become different from those of the unshaded sections. The level of irradiation on the PV modules directly relates to the total electrical power produced. Therefore, PV modules receiving a higher level of irradiation can generate greater power than those subjected to lower irradiation levels. Finally, the performance of the PV system is constrained by the PV modules that experience the lowest irradiation levels, resulting in a mismatch between the PV modules [91]. Thus, new novel MPPT algorithms aiming to equalize the current of the PV modules are expected in future studies.

The Mismatch issues between the PV modules and the PV SMs adversely affect the overall performance of PV systems. The series configuration of the PV modules limits the entire system to the PV module with the lowest power generation. Implementing MPPT distribution approaches aims to harvest the maximum power from each PV module or SM independently, leading to optimizing power extraction and mitigating mismatch issues. Thus, several power electronic topologies have been proposed to apply the distributed MPPT system at the finest PV level to enhance PV power production [92]. A new, optimized power electronic topology is expected in future studies that can improve PV system efficiency and maximize power production in grid-connected PV applications. Optimized power converter circuits are crucial for addressing the limitations of the current design, enabling the use of more compact components. Moreover, employing WBG devices like GaN and SiC can achieve considerable improvement in the PV system's efficiency, which can improve the power harvesting from the PV system. Thus, future topologies are expected to utilize these advanced technologies for addressing mismatch issues in PV systems.

As mismatch issues are a significant challenge in PV systems and are associated with most losses, proposing an optimized mitigation strategy becomes necessary in the design stage. The mismatch between PV modules is a result of unequal power generation in the series architecture, leading to a significant decrease in total power generation. Several factors can

cause a mismatch in PV systems; however, PS is often the most common contributor to this issue. The internal characteristics of the PV components vary according to the environmental conditions; therefore, each part of the PV system can behave differently. In a PV module, usually, three PV SMs are connected internally and integrated with bypass diodes. Thus, applications of distributed MPPT require breaking this connection and replacing the bypass diode with optimized power electronic converters [93]. Therefore, the PV module manufacturers should reassess the existing electrical configuration of the PV module inside the junction box. The new expected design should enable the integration of optimized power converters to facilitate the implementation of distributed MPPT at the PV SM level.

Enhancing the operations of the PV system at the PV SM level and integrating optimized power electronic converters can improve energy harvesting of the different types of PV systems. The PS effect can be significant, and it is often the source of mismatch problems. Applying the distributed MPPT strategy at the PV SM can effectively reduce the PS effect in the different PV systems and lead to the harvesting of maximum available power [94]. Optimized and practical power electronic circuits are mandatory in future studies to further enhance PV system efficiency and effectively increase power production from PV systems. Integrating the optimized power electronic converters has the potential to address mismatch problems and increase energy harvesting.

2.6 Chapter Summary

This chapter begins with an explanation of PV cell modeling and the relationship between irradiation intensity and PV power production. Then, it presents a comprehensive overview of the mismatch problem in PV systems and the challenges that lead to this issue. These challenges include dust accumulation, PV module degradation, and manufacturing tolerances. It also highlights the negative impact of the mismatch problem on power and energy production. Then, it discusses the different mitigation strategies that are used to address the mismatch problem in PV systems, including bypassing and distributing approaches. Moreover, common techniques for implementing distributed MPPT at the PV SM level are reviewed in terms of converter configurations, control methods, advantages, and drawbacks. Finally, it finished by providing some practical suggestions for future studies.

Chapter 3

Modular Cuk Inverter (MCI)

This chapter presents an MI design to address PS issues at the PV module level. The proposed grid-tied inverter is created by connecting several MCIs in series, linking their outputs to the grid, allowing each PV module to optimize power extraction through independent MPPT. Boosting the voltage from PV modules to meet grid requirements is important; therefore, the series configuration of the MCI design offers a key advantage to stepping up the voltage output at the grid side. Utilizing the Cuk inverter helps maintain consistent input current, reduces capacitor size at the PV module side, and improves PV system efficiency. The MCI also operates without an auxiliary decoupling circuit, which separates DC power on the PV side from pulsating grid power.

This chapter explains the MCI's operational modes and control strategies, which ensure optimal functioning when the PV system is powered by PV modules, integrated with a battery system, or linked to the utility grid. The MCI controller has two control loops to ensure system robustness. Additionally, mathematical analyses evaluate the performance of the PV system in various operational modes during PV generation and battery charging processes. The effectiveness of the MCI is validated through experimental studies using a 1 kW prototype controlled by a Texas Instruments TMS320F28335 DSP.

3.1 Background

Several strategies are introduced to enhance the efficiency of the PV system, tackle power mismatch concerns, and maximise power generation [95]. Employing the distributed MPPT system for each PV module is one common approach to improving PV system efficiency and increasing power production. Distributing the MPPT systems can lead to the capture of the maximum power from each PV module independently, thus improving overall power production and reducing mismatch issues between PV modules. The consequences of mismatch issues arising from differences in voltage, current, and consequently power are more straightforward to evaluate in small-scale PV systems compared to medium and large-scale PV projects [96-97].

1. Mismatch at the PV module level

The mismatch in power generation between PV modules is a significant problem in residential PV systems, which can significantly reduce power generation or cause severe damage to the PV modules. Applying the distributed MPPT system at the PV module level is a practical approach to overcoming mismatch concerns between PV modules and increasing power production [98]. This mitigation method can maximise the power of the PV system by incorporating each PV model with a unique MPPT system. A suggested method for the mismatch issue proposes integrating each PV module in the PV system with a DC-DC converter. The power converter of a PV module in the PV system incorporates a unique MPPT system, which improves the overall power harvesting capability of the PV system. Furthermore, the efficiency of the PV system is raised, and the voltage stress is reduced by as much as 33% [99]. As a result, smaller and more cost-effective components can be used. However, it is crucial to note that the overall efficiency of the PV system is constrained by the efficiency of the converters utilised.

2. PV Microinverter for PV systems

The efficiency of residential PV systems can be improved, and the impact of PS can be mitigated by utilizing microinverters at the PV module level. Implementing the MPPT system at the PV module level enhances power system production. In instances of PV module malfunctioning, the PV system performance can be negatively affected; however, the energy output of the unshaded PV modules remains normal. The DC–AC inverter of each PV module can maximize energy harvested within the PV system and address concerns related to mismatch. Moreover, implementing a microinverter at the PV module level can improve the scalability of residential PV applications and enable increasing the size of the PV system [100].

PV MI technology has become a topic of interest among power electronics researchers due to its noticeable advantages, including improved PV system performance and reduced mismatch issues between PV modules [101]. The MI converts the DC power of a single PV module into AC power to effectively interface with the distribution network. Therefore, proposing an effective single-stage DC-AC inverter can lead to a considerable improvement in the functionality of PV systems. The traditional two-stage DC–AC inverters usually use a

buck-boost converter, which generates discontinuous input currents, resulting in a reduction of the PV system efficiency and a negative effect on the MPPT algorithm. The LV MIs represent an effective alternative because they can enhance the efficiency of PV systems, particularly for residential and some medium-scale PV projects. Employing MIs at the PV module level can result in a fifteen percent increase in output power [102]. Moreover, the robustness of the PV system can be significantly enhanced using this technology because the PV system can operate effectively even with the malfunctioning of one MI.

3. PV MI for a three-phase system

A three-phase isolated differential inverter using the single-ended primary-inductor converter (SEPIC) DC/DC converter has been suggested, demonstrating improvements in power quality and the management of negative sequence harmonic components (NSHC)[103]. However, the analysis has not considered the operational characteristics of the converter from the viewpoint of PV modules. One proposed approach details the operation of the differential Flyback three-phase inverter, which utilizes parallel-connected inputs [104]. The study demonstrates that current stresses are distributed efficiently between the parallel PV modules and converters. Furthermore, another method describes a series-connected PV MI that employs cascaded H-bridge converters. Although this study incorporates an MPPT control system that is intended to optimize energy capture from the PV modules, it fails to investigate the effects of the discontinuous current generated by the H-bridge converters on both the control system's performance and the PV modules themselves. Additionally, the study has neglected the impact of second-order harmonic components in single-phase operation [105].

3.2 Parallel MI

In a parallel-connected MI system, illustrated in Figure 3.1(a), each DC-AC MI is able to operate independently of the other MIs. Therefore, the malfunction of a single MI will not impact the performance of the remaining units within the PV system, as it is a current-controlled converter. Typically, in residential PV applications, stepping up the MIs voltage is necessary to boost the voltage from the PV side, which usually ranges from approximately 12 to 27 DC volts to around 220 to 230 AC root mean square (RMS) volts. The significant

voltage step-up ratio required in this configuration to match the grid output voltage can minimise the efficiency of the PV system and increase the associated installation costs [106].

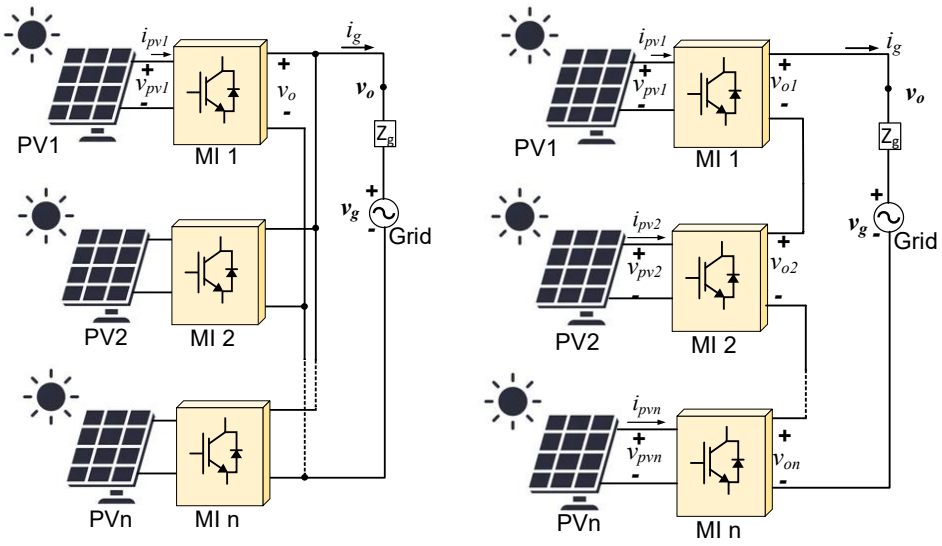

(a) System with parallel-connected module interconnections

(b) System featuring series-connected module interconnections.

Figure 3.1 LV PV Module Interconnections.

The utilization of transformers with high turn ratios in parallel-connected PV module applications is a common practice to meet the high voltage requirements on the grid side. However, this approach can lead to an increase in both the weight and the overall cost of the PV system. As a result, transformer-less configurations and high-frequency transformers (HFTs) are recommended to tackle these challenges. Additionally, the non-isolated configurations of PV applications that require a significant step-up ratio can result in increased expenses for residential PV system implementations, primarily due to the higher size and number of capacitors needed for the design. In terms of the system efficiency, the boost converters must elevate the output voltage to a considerably high level, which can cause considerable stress on the switches and negatively impact the efficiency of the PV system [107].

3.3 Series MI

The series-connected PV MIs are built by connecting each LV MI with its adjacent peer. The cascaded PV MI architecture is connected to the electrical grid, which can enable sending

the extra energy to it. As illustrated in Figure 3.1(b), this arrangement represents a range of interconnected MIs operating together. In this practical configuration, the need for a high step-up conversion ratio is reduced because the series connection inherently enhances the system's ability to meet the voltage requirements at the distribution grid [108].

The series-connected PV MI technology offers several advantages, including the use of small components and improved PV system efficiency. The stress on the power converter switches is significantly minimised, which improves the efficiency of the PV system and extends the lifetime of the switches. The scalability of the grid-connected PV system is enhanced because a separate control system controls each PV MI. The energy harvesting capability of the PV system is enhanced because each PV module has its own separate MPPT algorithm. As a result, the series-connected MI technology ensures optimal performance of the PV system under different environmental conditions [109].

3.4 Modular Cuk Inverter (MCI)

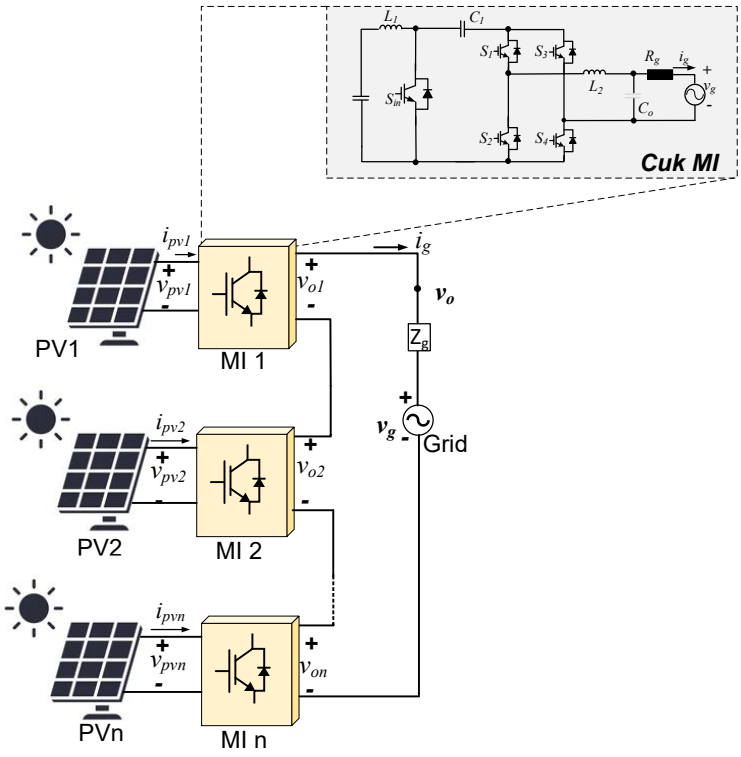

Figure 3.2 The suggested series-connected Cuk-based LV MI

The Cuk-based MI is specifically designed for series-connected rooftop PV systems. As illustrated in Figure 3.2, the proposed modular MCI architecture illustrates connections between adjacent inverters. Utilising the Cuk converter topology as the inverter for each PV module optimizes power extraction from the PV modules and enhances the efficiency of the overall PV system. Each PV module operates with an independent MPPT algorithm, which effectively addresses mismatch issues at the PV module level and significantly increases energy harvesting from the PV system. This configuration utilises a series connection to meet the voltage requirements at the grid side, enabling the achievement of a high-voltage step-up ratio.

3.4.1 Operation of the MCI

The single-phase PV MCI system interfaces with the electrical grid via the grid impedance, represented as $Z_g = r_g + jL_g$, where r_g denotes the resistance of the grid and L_g represents the inductance of the grid. The overall voltage generated by the converter is the total of the individual voltages corresponding to the series-connected modular converters. Therefore, these total voltages, denoted as v_o, can be framed as follows:

$$v_o = Vsin(wt + \theta) \tag{3.1}$$

In this context, V denotes the magnitude of the output voltage, while θ represents the phase shift relative to the grid voltage, and ω indicates the angular frequency of the grid. Throughout this chapter, V_g will be utilized to describe the magnitude of the grid voltage. When the MIs deliver active power P to the grid at a power factor of cos φ, the parameters V, Θ, and the magnitude of the single-phase output current Ig can be stated as follows:

$$I_g = \frac{2P}{V_g \cos(\varphi)} \tag{3.2}$$

$$\theta = \tan^{-1}\left[\frac{r_g I_g \sin(\varphi) + \omega L_g I_g \cos(\varphi)}{V_g + r_g I_g \cos(\varphi) - \omega L_g I_g \sin(\varphi)}\right] \tag{3.3}$$

$$V = \left[\frac{V_g + r_g I_g \cos(\varphi) - \omega L_g I_g \sin(\varphi)}{\cos(\theta)}\right] \tag{3.4}$$

Under normal operating conditions, the k_{th} MI in phase j produces a voltage given by:

$$v_{kj} = \frac{v_j}{n} \tag{3.5}$$

Where n denotes the total number of MIs.

3.4.2 Operation Modes of MCI

Modern residential energy systems need to incorporate energy storage systems (ESSs) to facilitate the storage of excess energy generated during off-peak times, allowing for its utilisation during peak demand periods. The MCI can include singular battery units associated with each MI, as illustrated in Figure 3.3.

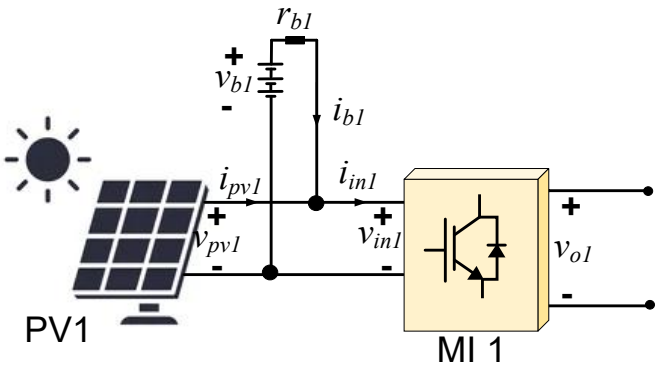

Figure 3.3 PV MI integrated with battery packs.

The suggested MCI can work in four different operational modes, which depend on the configuration of the relays illustrated in Figure 3.4 (a). Each MI is linked to three single-pole-double-throw (SPDT) relays, namely S_{pv}, Sb_1, Sb_2, and Sb_3. These relays facilitate the connection of the MI to the PV module, the battery pack, or both simultaneously. The output terminals of the MI are interfaced with the AC side through the SPDT relay labeled S_g. A comprehensive description of the four modes is provided in the subsequent subsections.

a) PV Modules to AC Grid (DC - AC)

The operational mode of the residential PV system, which facilitates the conversion of power from the PV modules to the electrical grid, is illustrated in Figure 3.4(b). In this configuration, all relays remain disconnected, except for S_{pv} and S_g. In this operational state, the active power P is defined by the maximum power output feasible from the PV modules, as regulated by the MPPT controllers. The values for voltage and current are calculated by equations 3.2 and 3.4. This operational mode is advantageous for supporting the grid during

daylight hours, when the PV modules can generate maximum output power. In this mode, the MCI functions as a DC/AC inverter.

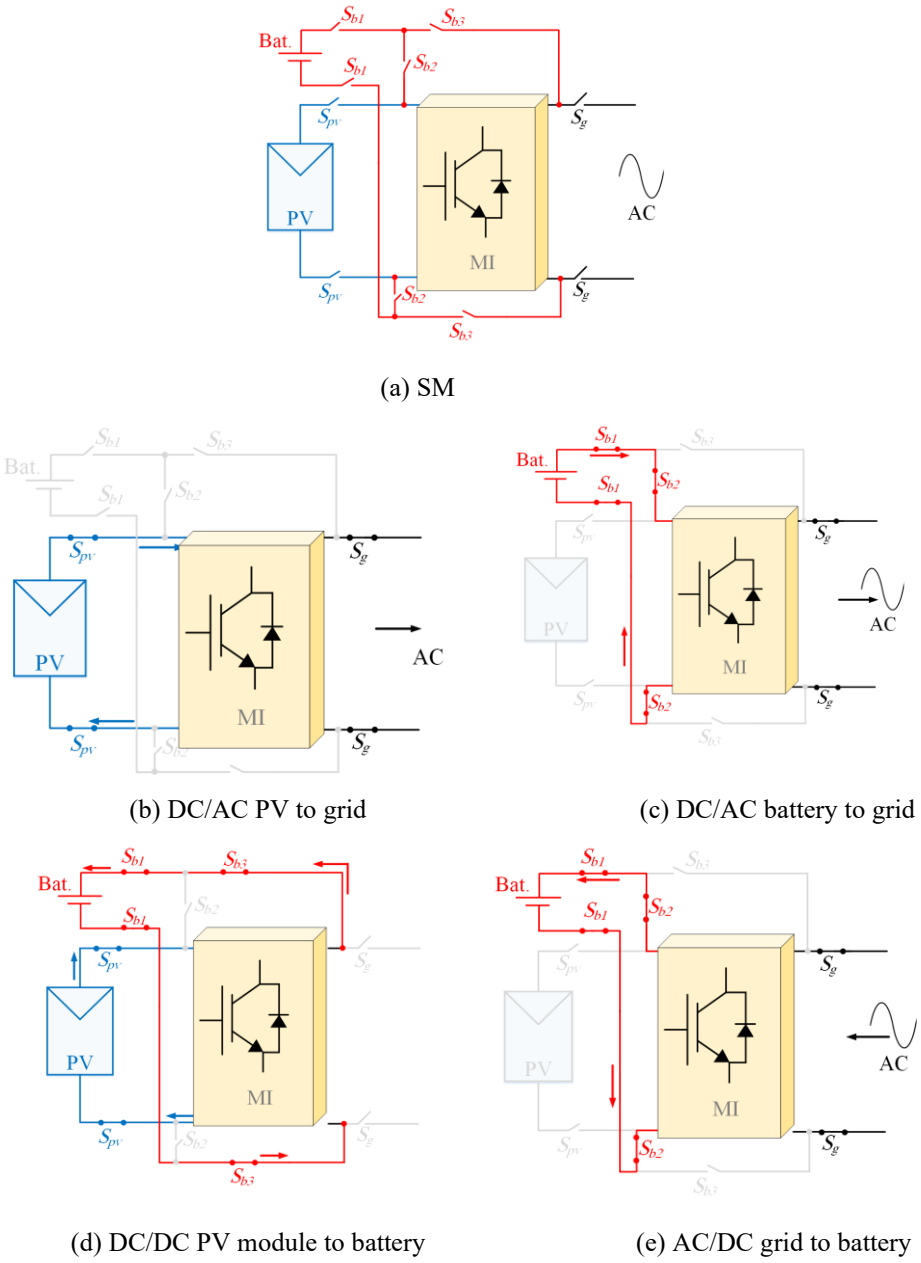

Figure 3.4 PV MCI integrated with battery packs operation modes.

b) Battery to AC Grid (DC - AC)

In the event that the power output of the PV modules is inadequate to support the grid, the battery is capable of supplying the necessary energy by activating relays S_{b1} and S_{b2} while deactivating relay S_{pv}. Figure 3.4 (c) illustrates the circuit configured in this manner. The

active power, P, is confirmed by the optimal discharge current from the battery, which aims to maximize both its practical capacity and operational lifespan. During this mode, the MCI continues to function as a DC/AC inverter.

c) PV Modules to Battery (DC - DC)

In instances where the electrical grid does not require active power assistance from the PV modules during daylight hours, the batteries can be charged using the PV modules by establishing connections through relays S_{b1} and S_{b3} with relay S_{pv}, while disconnecting relay S_g, as represented in Figure 3.4 (d). Under these circumstances, power will be supplied from the PV modules to facilitate battery charging while the AC grid terminals remain isolated. In this operational mode, the MCI functions as a DC-DC converter.

d) AC Grid to Battery (AC - DC)

The battery will be recharged using the electrical grid during nighttime hours by linking relay S_g with S_{b1} and S_{b2}, as demonstrated in Figure 3.4(e), while ensuring that all other relays remain in the open position. In this arrangement, the MI functions as an AC/DC rectifier, allowing power to flow from the electrical grid to the batteries through the MI.

3.4.3 Cuk MI Operation, Modeling, and Control

In order to effectively employ the MCI under the specified modes, the appointed MI must maintain several necessary characteristics. Firstly, it should be capable of supporting different output voltages that can be either above or below the input voltages derived from the PV modules, battery, or electrical grid. Additionally, it must ensure isolation between the input and output sides to comply with demonstrated safety standards. This objective can be accomplished if the selected MI facilitates the integration of a high-frequency transformer (HFT). Given that the PV modules and battery systems necessitate functioning at stable voltages and currents, the input current to the MI must remain steady and stable while the output current and voltage operate in a sinusoidal form corresponding to the grid's frequency of 50/60 Hz. Furthermore, the MCI must be equipped to store the second-order harmonics within appropriate storage elements to enhance system efficiency, as illustrated in Figure 3.5.

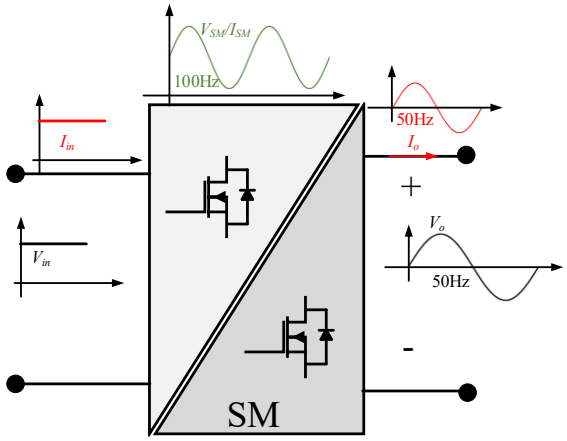

Figure 3.5 Modular Cuk Inverter

For these reasons, the Cuk inverter illustrated in Figure 3.6 represents the most suitable option for the proposed modular system, as it meets all the specified requirements. The proposed MCI includes five semiconductor switches, an isolating transformer characterized by a turn's ratio of N_s/N_p, two inductors labeled L_1 and L_2, two essential capacitors C_1 and C_2, along with an optional capacitor C_o.

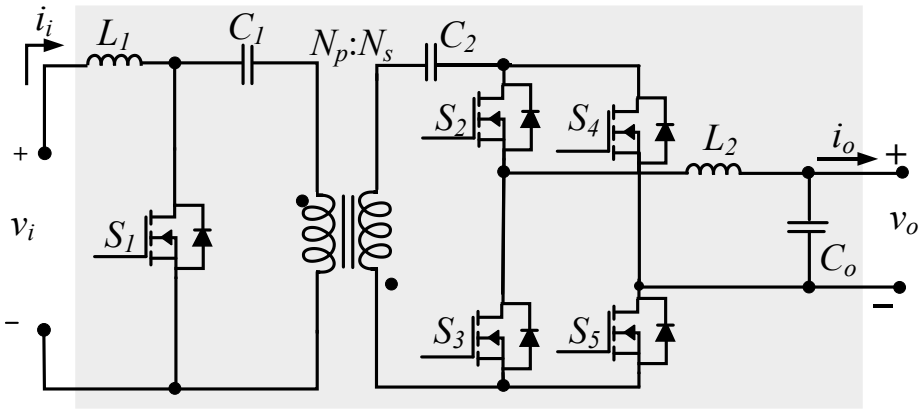

Figure 3.6 Isolated Cuk-based MI

a) DC - DC Mode

The operation of the DC/DC converter will be essential when the PV modules are employed to charge the respective battery packs. As illustrated in Figure 3.7, the MI operates in two different states:

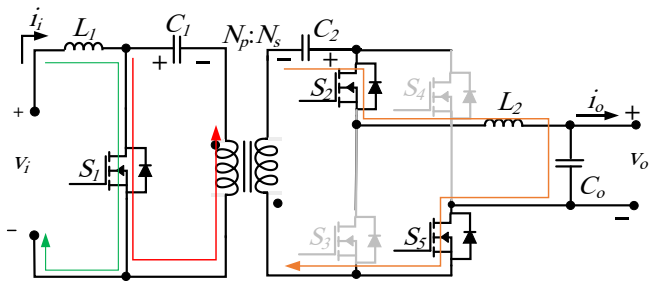

(**a**) St_{dc1}

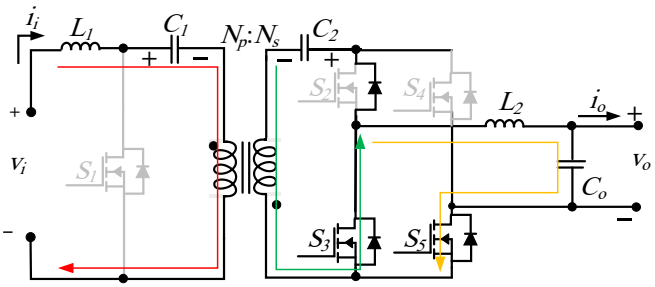

(**b**) St_{dc2}

Figure 3.7 MCI as a DC/DC mode converter.

b) DC - DC Operation

i. During the time interval specified as St_{dc1} $(0 \leq t < ton)$, switches S_1, S_2, and S_5 are simultaneously activated. The input current, denoted as i_i, is increasing to charge the inductor L_1. Concurrently, capacitors C_1 and C_2 are discharging into the output load connected to L_2, facilitating its charging process. The duration of this phase is defined as ton = d_{Xts}, where d represents the duty cycle ratio and ts indicates the switching time of the MI. This condition is illustrated in Figure 3.7 (a).

ii. In the interval defined as St_{dc2} (where $ton \leq t < ts$), switch S_1 is deactivated, resulting in the flow of current i_i into capacitors C_1 and C_2, which facilitates their charging process. Alongside, switches S_3 and S_5 are activated to create a pathway for the current in inductor L_2, resulting in a reduction in the currents of the inductors. This state is illustrated in Figure 3.7 (b).

c) DC - DC Modeling and Control

The MI operates in two separate operational states for its DC/DC conversion. Therefore, the state-space representation is derived by averaging the two operational states over time. In

this scenario, the state vector of the MI can be defined as follows*: xdc(t) = [ii(t) vCt(t) iL2 (t) vo(t) io (t)]* , with the output *ydc(t) = ii(t),* representing the current flowing to the battery. The average model is subsequently formulated as indicated in equation (3.6)

$$\dot{x}(t) = A_{dc}x(t) + B_{dc}\begin{bmatrix} v_i \\ v_b \end{bmatrix}$$

$$A_{dc} = \begin{bmatrix} 0 & \frac{1-d}{NL_1} & 0 & 0 & 0 \\ \frac{1-d}{NC_t} & 0 & 0 & 0 & \frac{-d}{C_t} \\ 0 & \frac{-d}{L_2} & 0 & \frac{-1}{L_2} & 0 \\ 0 & 0 & \frac{1}{C_o} & 0 & \frac{-1}{C_o} \\ 0 & 0 & 0 & \frac{1}{L_2} & 0 \end{bmatrix} \quad B_{dc} = \begin{bmatrix} \frac{1}{L_1} & 0 \\ 0 & 0 \\ 0 & 0 \\ 0 & 0 \\ 0 & \frac{-1}{L_2} \end{bmatrix} \tag{3.6}$$

In this context, $i_i(t)$ represents the input current, whereas $v_o(t)$ denotes the output voltage. Additionally, $iL_2(t)$ indicates the current flowing through the output inductor, and $i_o\ (t)$ signifies the output current from the MI. The state $v_{Ct}(t)$ can be articulated as $N_vC_1(t) + vC_2(t)$, where N signifies the turns ratio, calculated as N_s/N_p, and C_t is defined as $C_1C_2/(C_1 + N_2C_2)$.

The converter's transfer function is as follows:

$$G_{dc}(s) = \frac{i_o}{V_i} = C_{dc}(sI - A_{dc})^{-1}B_{dc} \tag{3.7}$$

$$C_{dc} = [0 \quad 0 \quad 0 \quad 0 \quad 1] \tag{3.8}$$

The control system for the battery charging process utilizing PV modules, based on maximum PV power, is illustrated in Figure 3.8. The reference input current, denoted as i_i*, is derived from the MPPT controller, while the actual current is regulated through a straightforward hysteresis controller. For the sake of simplicity, the output current of the battery is assumed to remain unmanaged, under the assumption that the power generated by the PV modules will not exceed the nominal power capacity of both the maximum input and the battery pack.

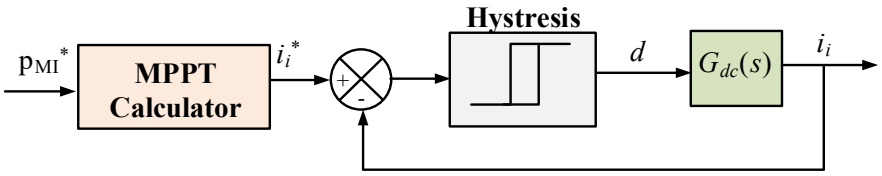

Figure 3.8 MCI Controller utilized during the DC/DC conversion process to facilitate battery charging.

d) DC- AC Mode

The operation of the DC/AC system with three distinct states is initiated when either the PV module or the battery delivers real power to the grid. In contrast to the DC/DC mode, this additional state offers an enhanced level of control over both the input and output parameters simultaneously. This capability is important to maintain a constant input current while producing sinusoidal output voltages and currents, as illustrated in Figure 3.5. The three operational states are represented in Figure 3.9 and can be explained as follows:

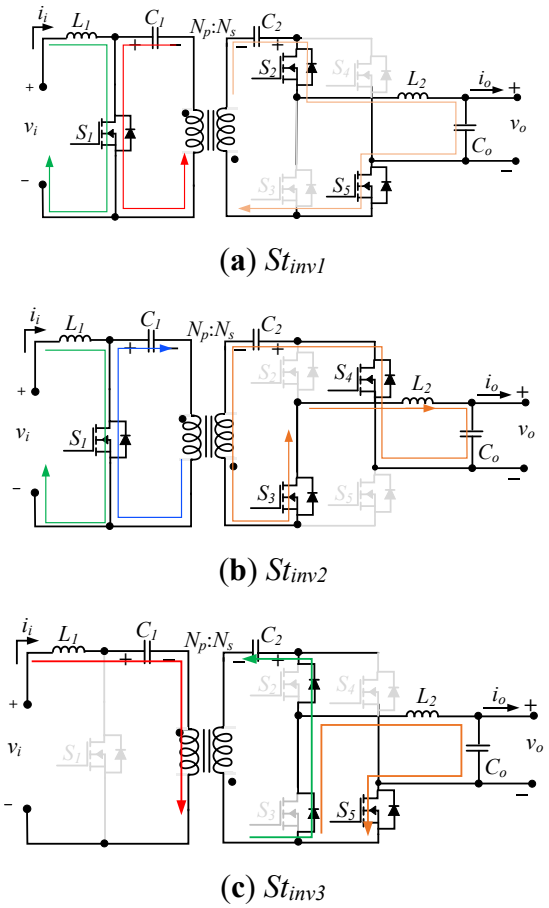

(a) St_{inv1}

(b) St_{inv2}

(c) St_{inv3}

Figure 3.9 MCI DC/AC inversion when i_o is positive.

e) DC - AC Operation

i. During the interval St_{inv1} ($0 \leq t < t_{on1}$), the switch S_1 is activated, resulting in an increase in the input current i_i and the charging of inductor L_1. The capacitors C_1 and C_2 discharge into the output load via switches S_2 and S_5 during the positive half-cycle of current i_o, and through switches S_3 and S_4 during the negative half-cycle. As described in Figure 3.9 (a), in this state, inductor L_2 is charged. The duration of this phase is defined as $t_{on1} = d_{1.ts}$.

ii. In the subsequent interval St_{inv2} ($to_{n1} \leq t < t_{on1} + t_{on2}$), switch S_1 remains in the on position. However, capacitors C_1 and C_2 are charged by activating switches S_3 and S_4 during the positive half-cycle of i_o, or switches S_2 and S_5 during the negative half-cycle. In this scenario, while L_2 continues to charge, L_1 is also in a charging state. Therefore, this phase enables decoupling between the input and output sections, as illustrated in Figure 3.9 (b). The duration for this state is represented as $t_{on2} = d_{2.ts}$.

iii. During the final interval St_{inv3} ($ton1 + ton2 \leq t < ts$), switch S_1 is deactivated, permitting capacitors C_1 and C_2 to remain charged by the input current i_i. If the current i_o is in its positive half cycle, switches S_3 and S_5 will be activated to create a path for the current to flow through L_2, leading to a decrease in the currents through the inductors (refer to Figure 3.9 (c). A similar situation occurs during the negative half cycle of i_o when switches S_2 and S_4 are activated.

f) DC-AC Modeling and Control

The MI operates within three different states in DC-AC mode. As a result, the state-space model will be formulated by computing the average of the three states over time. The average model is expressed in equation (3.9).

$$\dot{x}(t) = A_{inv}\, x(t) + B_{inv} \begin{bmatrix} v_i \\ v_g \end{bmatrix}$$

$$A_{inv}=\begin{bmatrix} 0 & \frac{d_1+d_2-1}{NL_1} & 0 & 0 & 0 \\ \frac{1-d_1-d_2}{NC_t} & 0 & \frac{d_2-d_1}{NC_t} & 0 & 0 \\ 0 & \frac{d_1-d_2}{L_2} & 0 & \frac{-1}{L_2} & 0 \\ 0 & 0 & \frac{1}{C_o} & 0 & \frac{-1}{C_o} \\ 0 & 0 & 0 & \frac{1}{nL_g} & 0 \end{bmatrix} \quad B_{inv}=\begin{bmatrix} \frac{1}{L_2} & 0 \\ 0 & 0 \\ 0 & 0 \\ 0 & 0 \\ 0 & \frac{-1}{L_g} \end{bmatrix} \tag{3.9}$$

The transfer function of the inverter is defined as

$$G_{inv}(s)=\frac{i_o}{V_i}=C_{inv}(sI-A_{inv})^{-1}B_{inv} \tag{3.10}$$

$$C_{inv}=[0 \quad 0 \quad 0 \quad 0 \quad 1] \tag{3.11}$$

The control method at the PV module level for PV systems, when MCI functions as a single-phase inverter and facilitates power transmission from the PV modules to the AC electrical grid, is illustrated in Figure 3.10. The reference value of the input current is received from the MPPT algorithm of the PV module. The actual current is then compared with the reference value to get the error, which is regulated by a typical hysteresis controller. Moreover, the output grid current is controlled by a separate proportional-resonant (PR) controller, which ensures synchronization with the grid current frequency, denoted as $\omega o = 2\pi f$. The controlling system operates under the assumption that the irradiance and other environmental factors of all PV modules are the same. An alternative system-level control will be required to effectively manage scenarios involving PS and ensure power distribution between the different MIs according to their respective maximum power points.

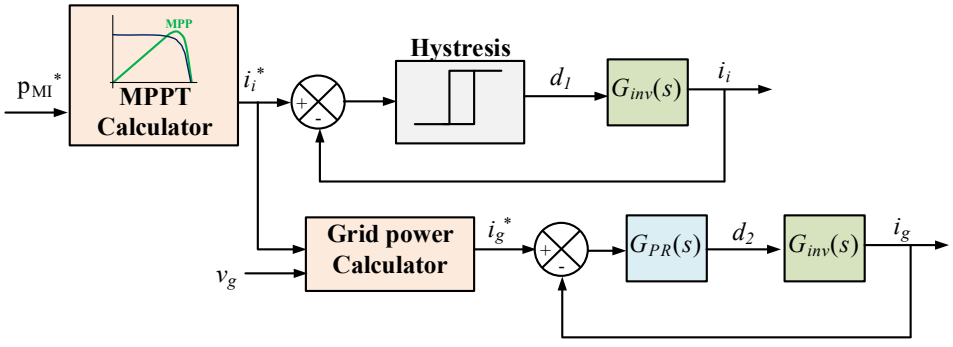

Figure 3.10 MCI Controller for converting DC PV module's power to AC for integration with the grid.

The control at the PV module level, while the MCI continues to function as a single-phase inverter with power being transmitted from the battery packs to the AC electrical grid, is illustrated in Figure 3.11. In this scenario, there is no specified MPP for operation, which allows for flexibility in the discharging currents of the batteries. However, it is advisable to select the reference current based on the nominal current value suggested by the manufacturer in order to optimize the lifespan of the batteries.

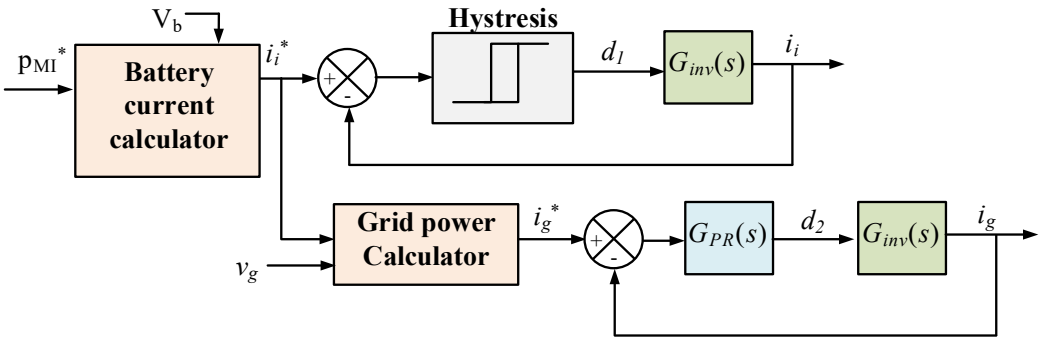

Figure 3.11 MCI Controller for converting DC battery power to AC for integration with the grid.

g) AC-DC Mode

The MCI is designed to function as an AC/DC rectifier when it becomes necessary to charge the battery packs from the AC power grid. In a manner equivalent to the operation of the inverter, the incorporation of an additional state within the modulation scheme offers an enhanced degree of freedom for the independent regulation of both the input grid current and the output current to the battery. This capability ensures that the current flowing to the battery remains stable over time. The three operational states are illustrated in Figure 3.12 and are described in detail as follows:

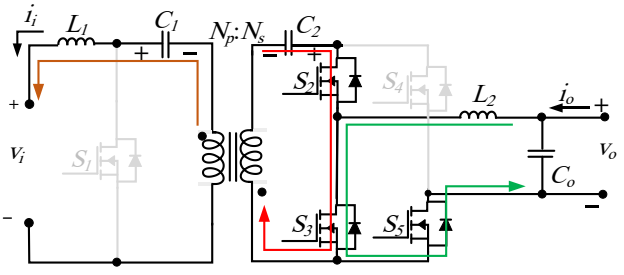

(a) St_{rec1}

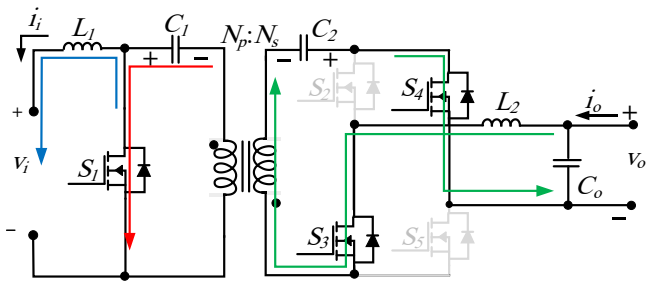

(b) St_{rec2}

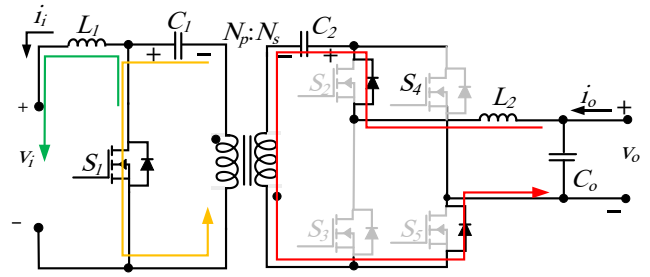

(c) St_{rec3}

Figure 3.12 Cuk SM functions as an AC/DC rectifier when io is positive.

i. Over the period specified as St_{rec1} $(0 \leq t < t_{on1})$, switch S_1 remains in the off position, battery current i_i is increasing while inductor L_1 experiences charging. Concurrently, capacitors C_1 and C_2 discharge into the battery via switches S_2 and S_3. The grid current flows through either S_3 and S_5 or S_2 and S_4. As illustrated in Figure 3.12 (a), inductor L_2 is charged during this phase, which lasts for a duration defined by $t_{on1} = d_{1.}t_s$.

ii. In the subsequent phase, St_{rec2} $(t_{on1} \leq t < t_{on1} + t_{on2})$, switch S_1 is activated, leading to a reduction in the battery's current. Simultaneously, capacitors C_1 and C_2 are discharged by engaging switches S_3 and S_4, as illustrated in Figure 3.12 (b). During this interval, the grid-side current is on the rise, while the battery's current continues to decline. The duration of this phase is defined as $t_{on2} = d_{2.}t_s$.

iii. Finally, in St_{rec3} $(t_{on1} + t_{on2} \leq t < t_s)$, switch S_1 remains activated, maintaining the decrease in battery current. At this stage, capacitors C_1 and C_2 are charged by deactivating all other switches, which allows the grid current to pass through the diodes of S_2 and S_5. In this state, both inductors, L1 and L2, discharge, resulting in a reduction of their respective currents, as illustrated in Figure 3.12(c).

h) AC DC Modeling and Control

The MI functions within three separate states in AC-DC mode. Therefore, the state-space model will be established by averaging the three states over a given time. The resulting average model is represented in equation (3.12)

$$\dot{x}(t) = A_{rec}x(t) + B_{rec}\begin{bmatrix} v_i \\ v_g \end{bmatrix}$$

$$A_{rec} = \begin{bmatrix} 0 & 0 & \frac{-n}{L_g} & 0 & 0 \\ 0 & 0 & \frac{1}{nL_2} & \frac{1-d_1}{L_2} & 0 \\ \frac{1}{C_o} & \frac{-1}{C_o} & 0 & 0 & 0 \\ \frac{1-2d_2-d_1}{C_t} & 0 & 0 & 0 & \frac{-d_1}{NC_t} \\ 0 & 0 & 0 & \frac{d_1}{NL_1} & 0 \end{bmatrix} \quad B_{rec} = \begin{bmatrix} 0 & \frac{1}{L_g} \\ 0 & 0 \\ 0 & 0 \\ \frac{-1}{L_1} & 0 \end{bmatrix} \qquad 3.12$$

The transfer function of the rectifier is defined as

$$G_{rec}(s) = \frac{i_i}{V_g} = C_{rec}(sI - A_{rec})^{-1}B_{rec} \qquad 3.13$$

$$C_{rec} = [0 \quad 0 \quad 0 \quad 0 \quad 1] \qquad 3.14$$

Figure 3.13 illustrates the control mechanisms at the PV module level when the MCI is functioning as a single-phase rectifier to charge battery packs from the AC electrical grid. The reference modulation power index PMI* is used to compute the reference grid current i_o*. Then, the actual current is regulated through a PR controller. In addition, the battery reference current is decided by assessing the battery's voltage and state of charge and then regulated via a hysteresis controller.

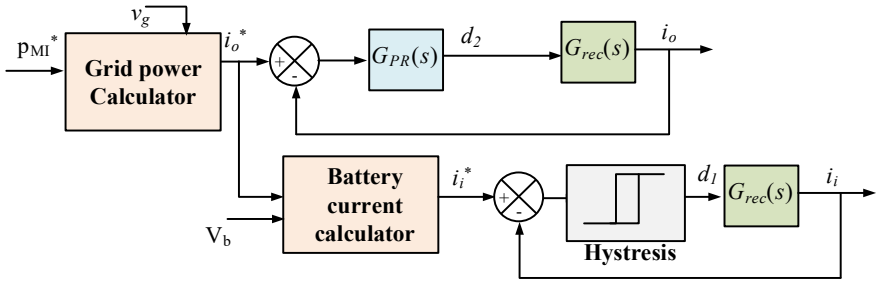

Figure 3.13 MCI Controller as an AC/DC converter for battery charging.

Figure 3.14 illustrates the power command for the MCI system. During the interval T_1, the MCI demonstrated equal power distribution among the four MIs, starting from zero power and gradually increasing. Throughout T_2, the MIs achieved a maximum power output of 250 W. The interval T_3 simulates the effects of partial shading, wherein the upper two MIs continued their output at 250 W, while the remaining two experienced a reduction to 30%, ending in a total power output decline to 65%.

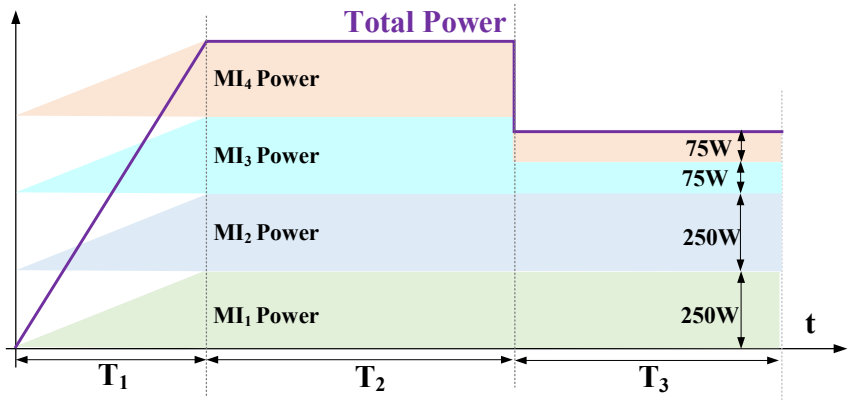

Figure 3.14 Power sharing between the four MIs when converting PV to grid DC/AC.

The Sisotool toolbox within MATLAB/Simulink is used to tune the K_p and K_r gains for the transfer function of the PR controller, aiming to obtain optimal gains that balance stability and bandwidth, as illustrated in Figure 3.15. The Sisotool toolbox in MATLAB/Simulink provides the Bode plot of the investigated power converter system. Although phase margin is commonly evaluated with respect to -180°, the phase in the illustrated Bode plot is displayed around +180° due to phase wrapping. Since +180° and −180° differ by 360°, this representation does not affect the calculated phase margin or the stability assessment.

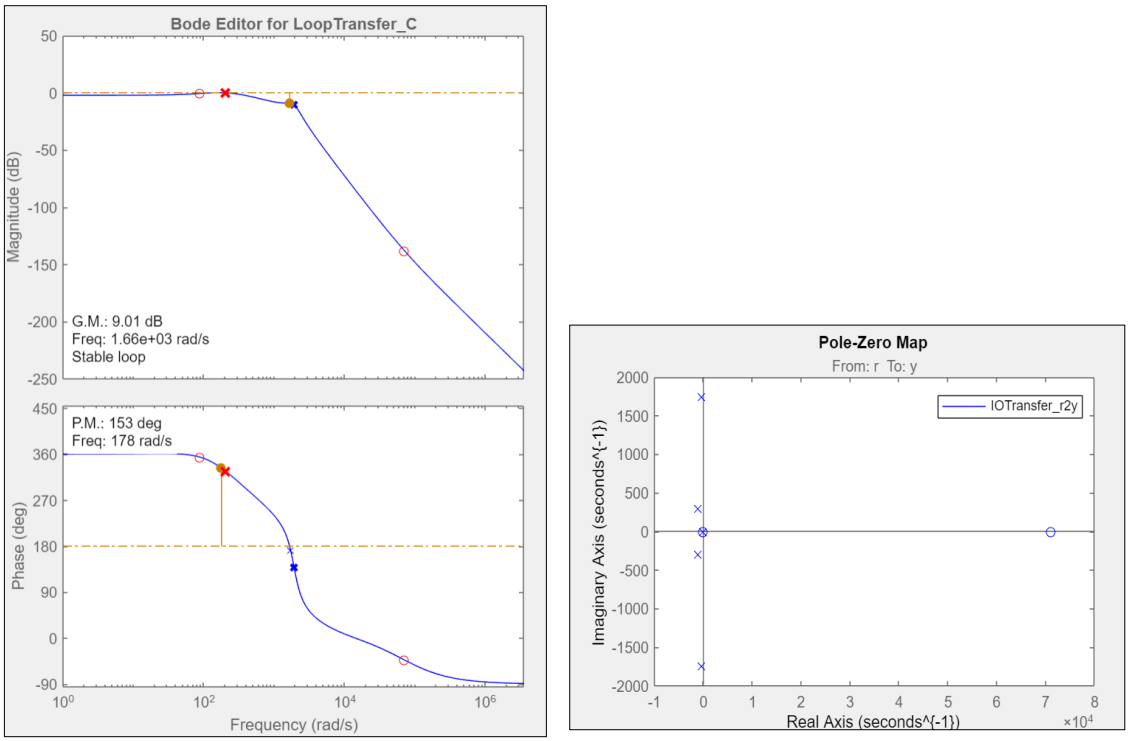

(a)Bode plot (b)Pole-zero Map

Figure 3.15 Control systems throughout PV to grid conversion: k_p = 2.5 and k_r = 5

3.4.4 MCI Simulation Study

Figure 3.16 presents the block diagram implemented in the MATLAB/SIMULINK program to examine the performance of the proposed Cuk-based modular inverter. This diagram has been used to evaluate the different operation modes, including DC-AC conversion mode, where power is sent from the PV modules to the AC grid, and DC-DC mode, in which PV modules charge the battery. Two different scenarios are conducted using the parameters listed in Table 3.1.

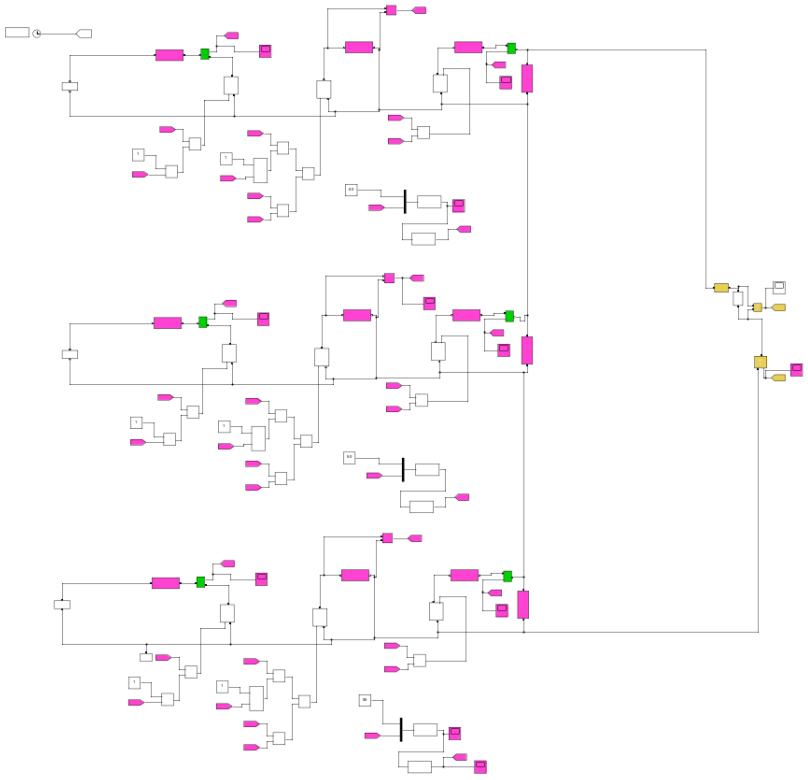

Figure 3.16 The block diagram built in MATLAB/Simulink for MCI

The simulation results for examining system operation when PV sends power to the AC grid are illustrated in Figure 3.17. The simulation outputs for DC- DC operation mode, in which PV modules charge the batteries, are shown in Figure 3.18.

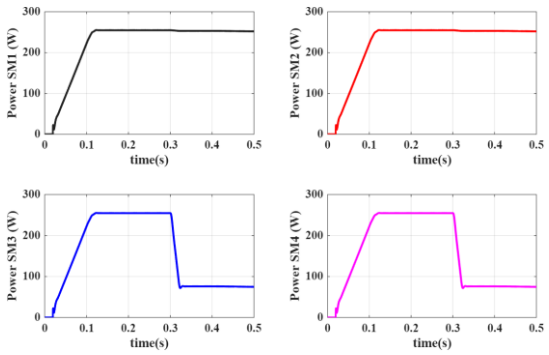

(a) The input power

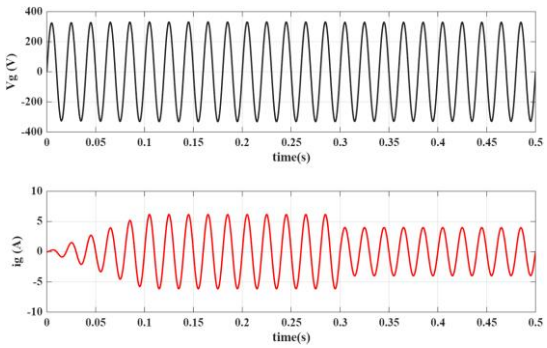

(b) Grid voltage and current

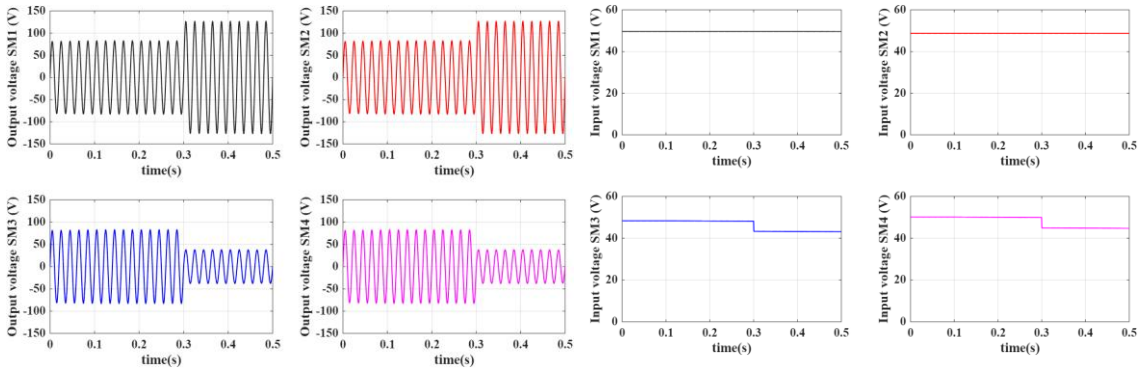

(c) the four SMs output voltage

(d) The input voltage of four SMs

Figure 3.17 The simulation results during DC-AC operation mode

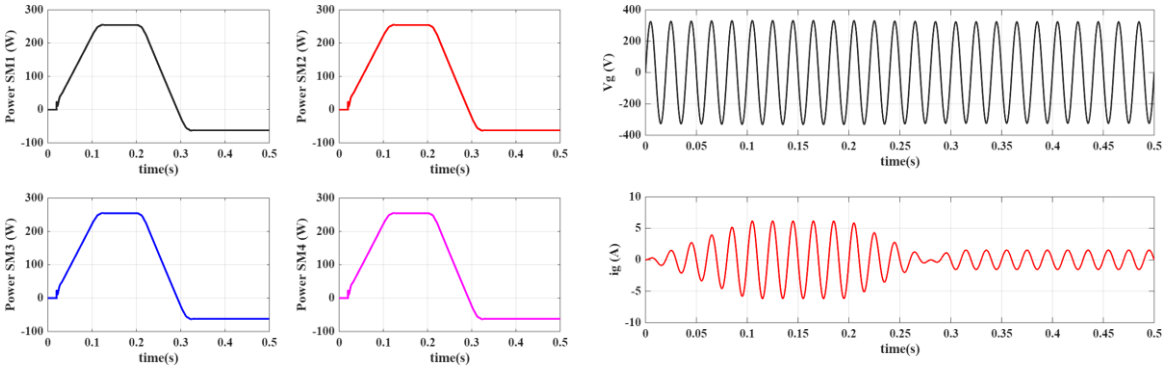

(a) The input power

(b) Grid voltage and current

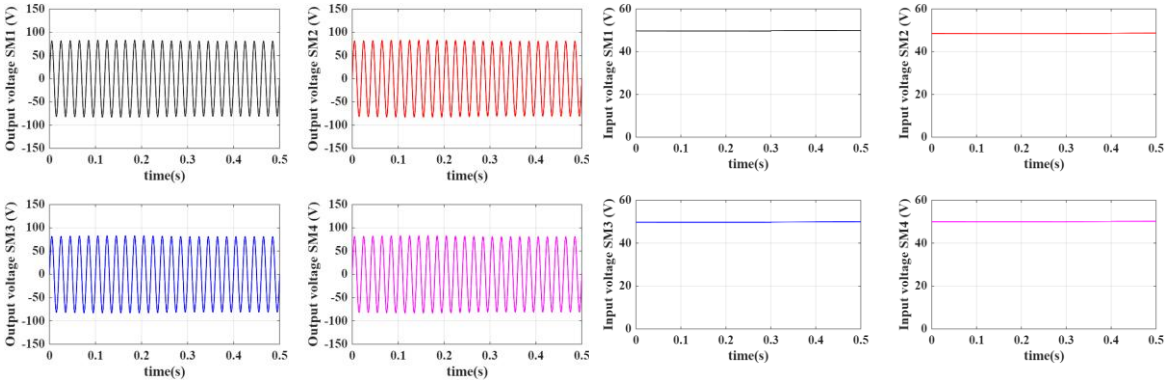

(c) the four SMs output voltage

(d) The input voltage of four SMs

Figure 3.18 The simulation result for Battery/Grid discharging and charging

3.4.5 MCI Experimental Validation

The configuration of the experimental setup for the MCI is illustrated in Figure 3.19, which was managed by a TMS32028335 DSP, as detailed in Table 3.1. DC voltage sources were

employed to simulate the PV modules under their respective operational modes. Each PV MI was linked to a battery part consisting of 12 series-connected lithium-ion battery cells, generating an approximate voltage of 50 V. The battery configuration is shown in Figure 3.20. The safety of the experimental setup is crucial. Thus, battery packs have been regulated by the energy management unit system EMUS battery management system (BMS), which regularly monitors the voltage, temperature, and current of each battery cell through a specified module circuit.

The cell modules communicated their measurements of voltage, current, and temperature to the central controller via the controller area network (CAN) communication bus. Subsequent subsections will demonstrate experimental case studies examining the proposed MCI's functionality.

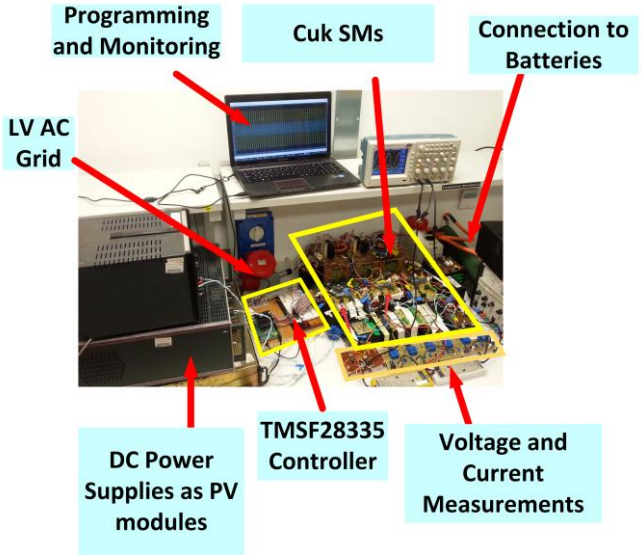

Figure 3.19 MCI Experimental setup.

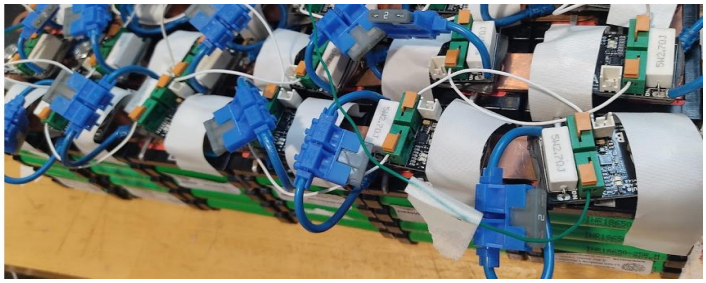

Figure 3.20 Battery packets.

Table 3.1. MCI model Parameters

Parameters	Value
Number of modules	$n = 4$
MI rated power	$p_{MI} = 250\ W$
MI inductors	$L_1 = L_2 = 0.5$ mH
MI capacitors	$C_1 = C_2 = 80$ µF - $C_o = 1$ µF
MI Switching frequency	$f_s = 50$ kHz
Transformer turns' ratio	$N = 1$
Battery Parameters	Li-ion 18650: 4.1 V, 2.5 Ah
Charged battery voltage	V_{bat} = 12s x 4.1 V ≈ 49V
Grid voltage	325 V peak
Grid impedance	$L_g = 1$ mH, $r_g = 0.5\Omega$
Grid frequency	$f = 50$ Hz

a) PV Model to Grid Scenario

The comprehensive system, including the PV module and system-level controllers, is illustrated in Figure 3.21. The reference power values for each PV module have been pre-established and computed. The reference current for the Kth MI was regulated by the duty-cycle ratio denoted as d_{1k}. In parallel, the duty-cycle ratio d_{2k} managed both the output voltage and current through the PR controller, with the controller gains designated as k_p and k_r. It is important to note that the duty-cycle ratios d_{1k} and d_{2k} for various MIs are not uniform if the MIs operate under dissimilar points due to mismatches such as PS. These individual MI controllers functioned effectively when all MIs were associated with the same operational point. On the other hand, in the event of mismatches, a system-level controller became essential to balance the output voltages and currents among the different MIs. Positioned at the top right, the system-level controller produced a central duty-cycle ratio, D_2, applicable to all MIs, which was subsequently integrated with the individual duty-cycle ratios, d_{2k}.

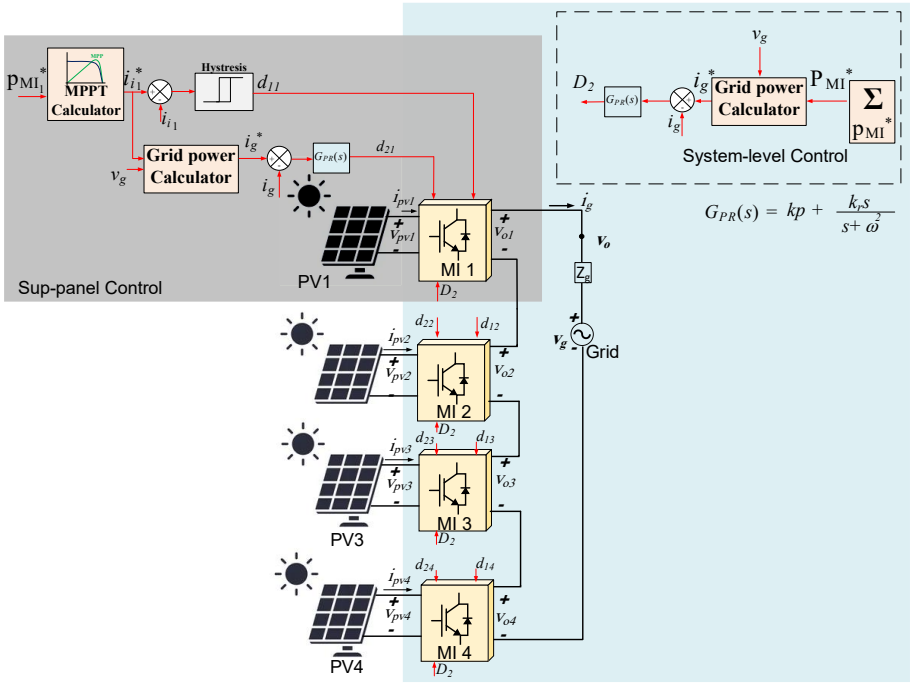

Figure 3.21 CMI sub-panels and controllers for managing PV/grid DC to AC conversion.

The decentralized control method increased the power harvesting capacity successfully during each operational interval, as depicted in Figure 3.22. The real power regulation was achieved at a different level, as demonstrated in Figure 3.22(a), where the power output increased from 0 W to 250 W for all MIs. Subsequently, at t = 0.3 s, the power associated with MI_3 and MI_4 was reduced to 30% to imitate PS conditions. The input of each *MI* was controlled by d_{1k}, while the output side was regulated via $d_{2k} + D_2$; the input current remained unaffected, allowing the storage of the 2nd-order harmonics in the internal Cuk capacitor. Figure 3.22(b) presents the grid voltage alongside the output grid current; it is evident that the current exhibits a direct correlation with the power output. The output voltages of the *MIs* were uniform when the power outputs of the individual *MIs* were equivalent. Under PS conditions, *MIs* generating higher output produced voltage levels, as all MIs shared a common output current. The output voltages of the *MIs* are displayed in Figure 3.22(c). Additionally, the input voltages from the power supplies used to simulate the PV module voltages are collectively presented in Figure 3.22(d).

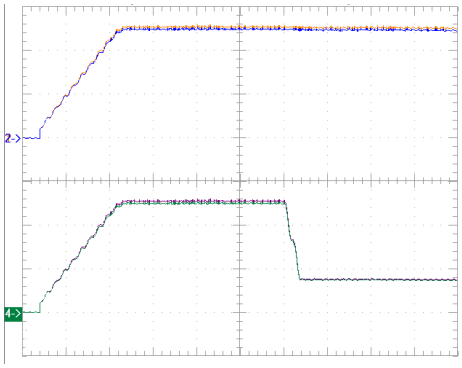

(a) Powers: Top (Ch1 & Ch2): MI_1 & MI_2, Bottom (Ch3 and Ch4): MI_3 & MI_4 50 ms/div – 100 W/div

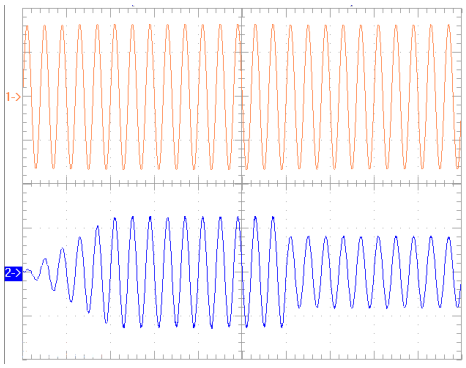

(b) Top (Ch1): Grid voltage at PCC & Bottom (Ch2): Grid current 50 ms/div – 200 V/div – 5 A/div

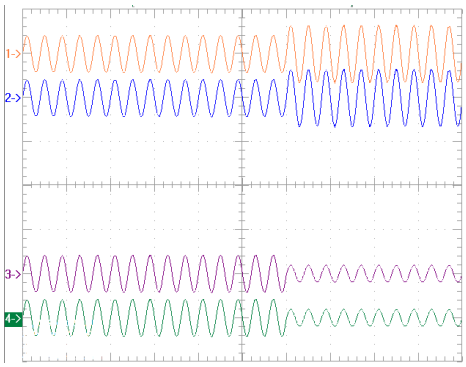

(c) Output voltages: Top (Ch1 & Ch2): MI_1 & MI_2, Bottom (Ch3 and Ch4): MI_3 &MI_4 50 ms/div – 200 V/div

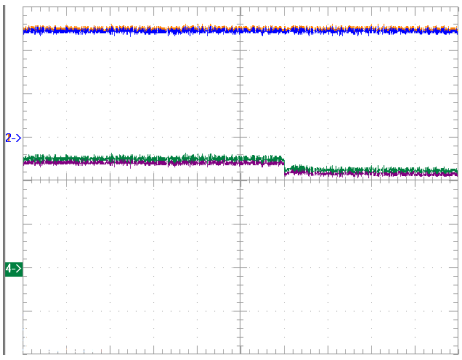

(d) Input (power supplies) voltages: Top (Ch1 & Ch2): MI_1 & MI_2, Bottom (Ch3 and Ch4): MI_3 &MI_4 50 ms/div – 20 V/div

Figure 3.22 Results from experiments on the MIs throughout PV to grid DC/AC conversion.

b) Battery to Grid Scenario

The control system utilized for discharging the battery packs into the AC grid is illustrated in Figure 3.23. This system is equivalent to the PV/grid controller; however, it does not incorporate the MPPT controller since the batteries do not possess a maximum power point. The charging control system is illustrated in Figure 3.24, wherein the MCI system functions as a rectifier when the power command experiences a directional reversal. Figure 3.25 presents a case study detailing both the discharging and subsequent charging of the battery pack.

During the period from t = 0 to t = 0.1 seconds, the battery packs were gradually discharged into the AC grid until each *MI* achieved its rated capacity of 100%, which corresponds to 250 Watts. At t = 0.3 seconds, the power command was reversed, stimulating the battery packs to charge at a rate of 25%. Figure 3.25 (a) illustrates the power levels of each *MI*, while Figure 3.25 (b) demonstrates the grid current. Figure 3.25 (c) provides an overview of the terminal AC voltage for each *MI*, and Figure 3.25 (d) outlines the battery terminal voltages throughout the discharging and charging phases.

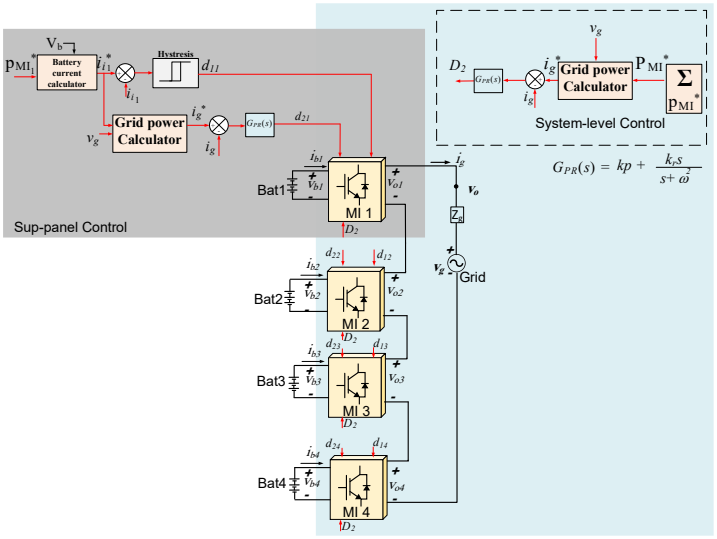

Figure 3.23 CMI system-level controllers for DC/AC conversion of battery and grid systems.

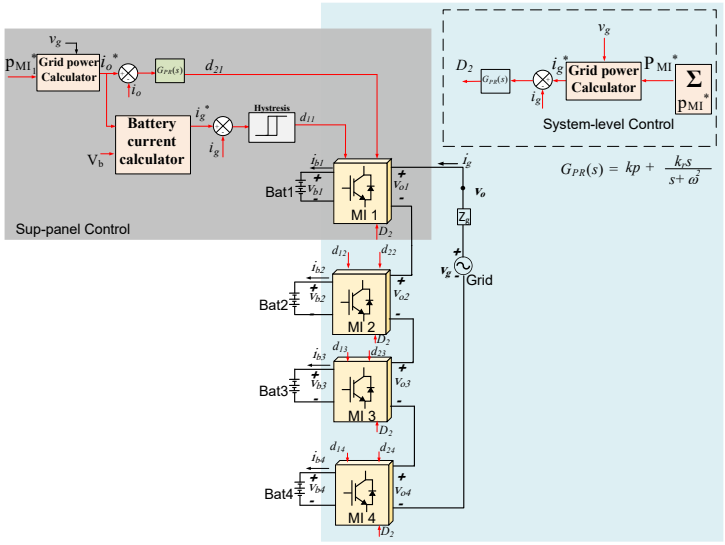

Figure 3.24 CMI system-level controllers for the rectification of grid and battery AC/DC power.

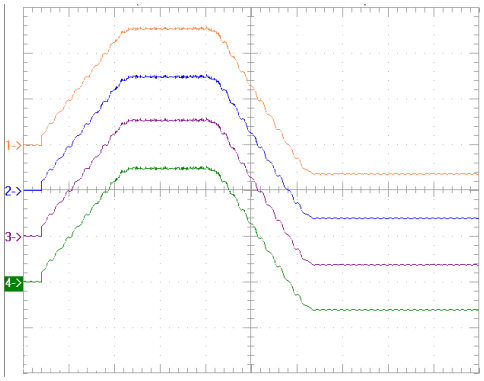

(a) Powers: Top (Ch1 & Ch2): MI_1 & MI_2, Bottom (Ch3 and Ch4): MI_3 & MI_4 50 ms/div – 100 W/div

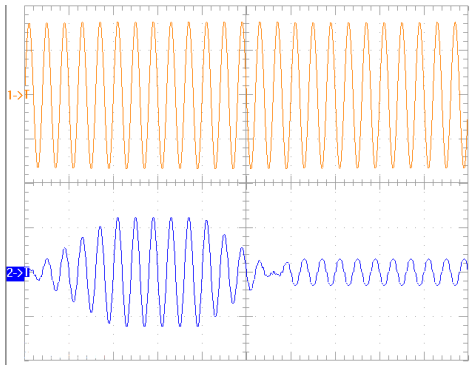

(b) Top (Ch1): Grid voltage at PCC & Bottom (Ch2): Grid current 50 ms/div – 200 V/div – 5 A/div

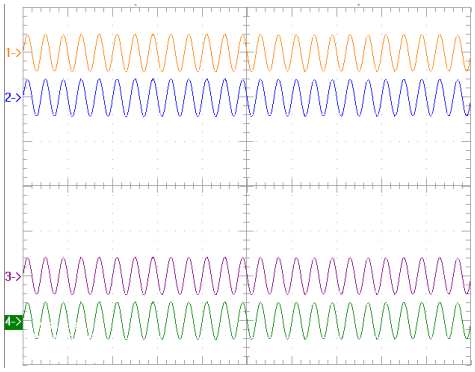

(c) Output voltages: Top (Ch1 & Ch2): MI_1 & MI_2, Bottom (Ch3 and Ch4): MI_3 &MI_4 50 ms/div – 200 V/div

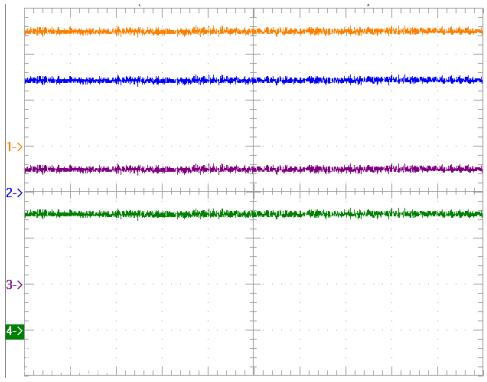

(d) Input (power supplies) voltages: Top (Ch1 & Ch2): MI_1 & MI_2, Bottom (Ch3 and Ch4): MI_3 &MI_4 50 ms/div – 20 V/div

Figure 3.25 Experiment findings of the MIs for Battery/Grid discharging and charging.

3.5 Central Cuk Inverter (CCI) versus MCI

Unlike the traditional central inverter, the MCI presents several advantages in terms of improved PV system performance and enhanced energy harvesting. This section presents a comparative investigation of the CCI and the MCI, focusing on device stress and power losses. Figure 3.26 outlines the contrast between the CCI and the MCI inverter. The CCI utilizes a total of five switches. In contrast, the modular-based Cuk inverter is characterized by several switches that can be expressed as $n_t = 5_n$, where n denotes the number of PV modules.

The configuration of the PV system, employing a CCI, where the PV modules are organized in a combination of parallel and series, is described in Figure 3.26(a). In this configuration, n_p represents the number of parallel strings within the PV array, while n_s denotes the number of PV modules connected in series. The current rating can be determined by multiplying the number of parallel strings by the current at the MPP. The MCI, as presented in Figure 3.26(b), demonstrates that each PV module is linked to a separate inverter, facilitating the reduction of both voltage and current fluctuations. Consequently, this leads to a decrease in the dimensions of the components utilized in the design.

The number of switches and the corresponding power losses for central and modular Cuk inverters have been determined through the mathematical analysis presented in [110], utilizing a consistent power level of 32 kW. The equations employed for the calculation of power losses in central-based inverters and modular-based inverters are summarized, respectively, in Table 3.2 and Table 3.3.

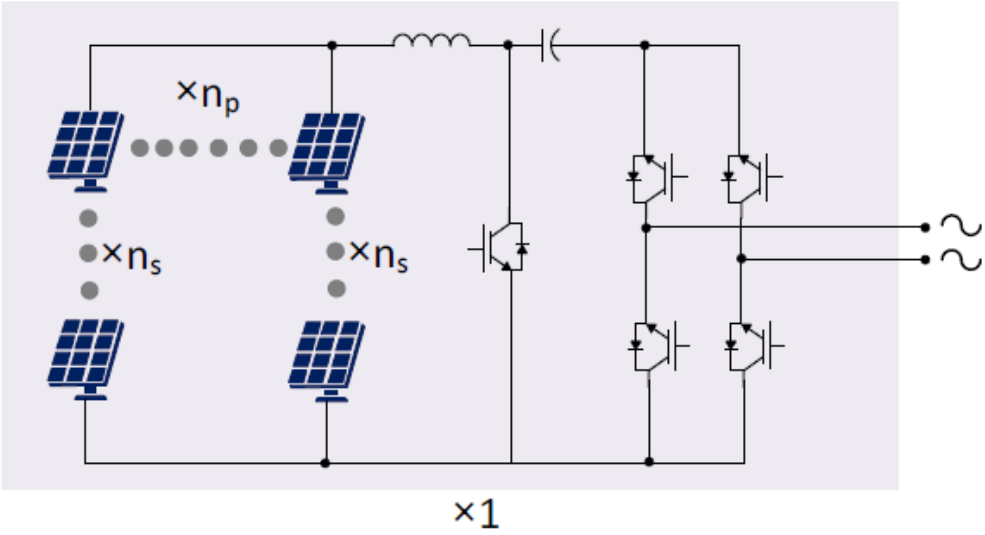

(**a**) Central MCI

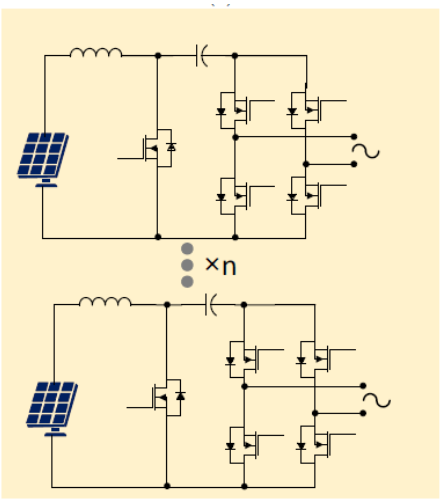

(**b**) Modular MCI

Figure 3.26 Central versus MCI.

Table 3.2. Power losses and stress on switches in the Central Cuk Inverter (CCI).

Vsw	Isw	Input switch losses	Output switches' losses
$V_g + n_s V_{mpp}$	$n_p I_{mpp}$	$n_p^2 r_{DS(on)} I_{mpp}^2 + \frac{3(V_g + n_s V_{mpp}) I_{mpp}}{2} (t_{on} + t_{off}) + n_p V_f I_{mpp} + n_p^2 r_{DS} I_{mpp}^2$	$r_{DS(on)} I_o^2 + \frac{(V_g + n_s V_{mpp}) I_o}{2} (t_{on} + t_{off}) + V_f I_o + r_{DS} I_o^2$

Table 3.3 Power losses and stress on switches in Modular Cuk Inverter MCI.

Vsw	Isw	Input switch losses	Output switches' losses
$V_g/n + n_s V_{mpp}$	$n_p I_{mpp}$	$n_p^2 r_{DS(on)} I_{mpp}^2 + \frac{n_p(V_g/n + n_s V_{mpp}) I_{mpp}}{2} (t_{on} + t_{off}) + n_p V_f I_{mpp} + n_p^2 r_{DS} I_{mpp}^2$	$r_{DS(on)} I_o^2 + \frac{(V_g/n + n_s V_{mpp}) I_o}{2} (t_{on} + t_{off}) + V_f I_o + r_{DS} I_o^2$

The number of switches increased when the PV modules increased in the modular Cuk inverter; however, the rating of the switches in the MI reduced, which led to minimizing the installation cost and the on-resistance of the switches. The stress on the device, power losses, number of switches, and the associated costs of the switches are detailed in Table 3.4. A detailed numerical calculation is presented for the different topologies of the PV module. Power losses in the modular configuration are reduced by increasing the number of modular inverters, as the stress on the switches decreases. Moreover, the calculations demonstrate a reduction in the installation cost by utilizing the MI topology. In MI design, the low internal

resistance MOSFET switches can be used instead of traditional IGBT switches, which results in reduced installation costs and improved efficiency. However, the significant increase in the number of switches can lead to a decrease in the efficiency of the MI.

The MI configuration is more complex than a conventional central system inverter topology, and more switches are required in the design stage. However, power conversion efficiency has significantly improved, and energy harvesting has been maximized because each PV module can operate independently in terms of MPPT during unequal power generation conditions. Furthermore, the fault detection process in modular design is swift and accurate when one of the inverters malfunctions.

Table 3.4. A Comparative analysis of central-based and modular-based topologies.

Array connection	Voltage Stress (V)	Current Stress (A)	Switches	Switches losses (W)	Efficiency	Number of Switches	Switches Cost (£)
Central Ns: 15 Np: 16	1030	136	IRG5U200SD 12B IGBT	736	≈ 90 %	5	≈ 1429
Modular N: 2 Ns: 5 Np: 8	398	68	IGW75N60H3 FKSA1 IGBT	2560	≈ 92 %	10	≈ 233
Modular N: 4 Ns: 4 Np: 5	270	42.5	IRF300P227	1227	≈ 96 %	20	≈ 167
Modular N: 8 Ns: 3 Np: 3	180	28	IRFP250NPBF	1900	≈ 94 %	40	≈ 133

The parameters for PV modules will be selected according to the lookup table, and the current generated by each PV module will be adjusted based on its respective voltage. In the scenario of PS, the digital signal processor (DSP) calculates the voltages of the PV module and subsequently predicts a transition of the MPP to a new value, along with its associated current.

3.6 Chapter Conclusion

This chapter presented a new grid-connected inverter with energy storage systems (ESS) using a Cuk converter. The MCI connects several PV modules to different battery storage systems, enabling both power delivery to the AC grid and charging of the battery from it. The control strategies for the different operation modes for the proposed MI, including DC-AC inversion, AC-DC rectification, and DC-DC conversion, are explained. The controller maintains a stable input current operation while ensuring synchronization of the output current with the 50/60 Hz grid frequency. The 2nd-order harmonics in the DC-AC inversion mode were decoupled effectively, resulting in improved system efficiency and increased power generation. The MI reduces mismatch issues between PV modules and enhances power conversion efficiency. The bidirectional feature of the proposed MI enables adequate energy storage during periods of low demand. Experimental results demonstrate the functionality of the suggested modular topology in providing optimal operation under two different operating conditions. The proposed MI configuration demonstrates a practical approach for mitigating mismatch issues and increasing power harvesting of the PV system. However, further investigation is needed to suggest more effective control methods and minimize design complexity.

Chapter 4

Multi-Input Single-Output Cascaded Boost Inverter

This chapter presents a new multiple-input single-output PV inverter to mitigate mismatch issues between PV SMs within a PV module and improve the power harvesting of residential PV systems. The PV cell generates relatively low power; thus, extracting the power from each PV cell is often impractical. Therefore, PV modules are built by connecting tens of PV cells to generate higher power. Implementing a power distribution method for a string of PV cells can be a more practical approach that can effectively maximize power production. Often, PV modules have three or four groups of PV cell strings, and traditional bypass diodes are connected to each of these PV cell strings. Replacing the bypass diodes with an effective power converter can mitigate the mismatch issue at the PV SM level and lead to further enhancement of PV system performance. Employing cascaded boost power electronic converters represents a viable strategy for addressing the mismatch between PV SMs. Utilizing the boost converter to extract the maximum power from each PV SM individually is associated with an increase in passive components; however, it offers the benefit of improving the overall performance of the power system and substantially increasing the energy collected from the PV module. The proposed topology is designed to maximize the extraction of available power from a group of PV cells within a single PV module. Given that most PV modules are typically divided into three SMs, the proposed topology focuses on effectively harvesting the maximum available power from the three groups of PV cells within the PV module.

The control strategy expressed in this chapter utilizes the distributed MPPT method to optimize power extraction from each PV cell string within a PV module. The distributed MPPT technique is employed to extract the maximum power from each PV SM, enhancing the power harvesting of the PV system. The strategy presented in this chapter aims to mitigate the mismatch issues between PV SM, which commonly lead to a significant reduction in PV module power output in residential PV systems. The strategy aims to replace the

conventional method, which is based on isolating the impacted PV SM, with a more practical approach to tackle mismatch issues within a PV module.

4.1 Background

A conventional residential grid-tied PV system typically includes solar PV modules, power electronic DC-DC converters, a Battery Energy Storage System (BESS), and grid-connected DC-AC inverters. Figure 4.1 provides an illustrative example of a grid-tied residential PV system. Filter circuits are frequently employed on the grid side to mitigate harmonics resulting from the conversion process [111]. Electrical power generated by the PV modules is sent to DC-DC power converters, where optimal power generation is obtained. The primary aim of MPPT controllers is to extract the maximum obtainable power from the PV module and subsequently either charge the BESS or send the excess energy into the grid. PV modules typically consist of groups of PV cells, with PV modules with three SMs being among the most common types. Residential PV systems can experience a range of faults that adversely impact their performance and reduce power output. One of the most critical issues in PV systems is the mismatch between PV modules, with PS being a significant contributing factor to this problem [112].

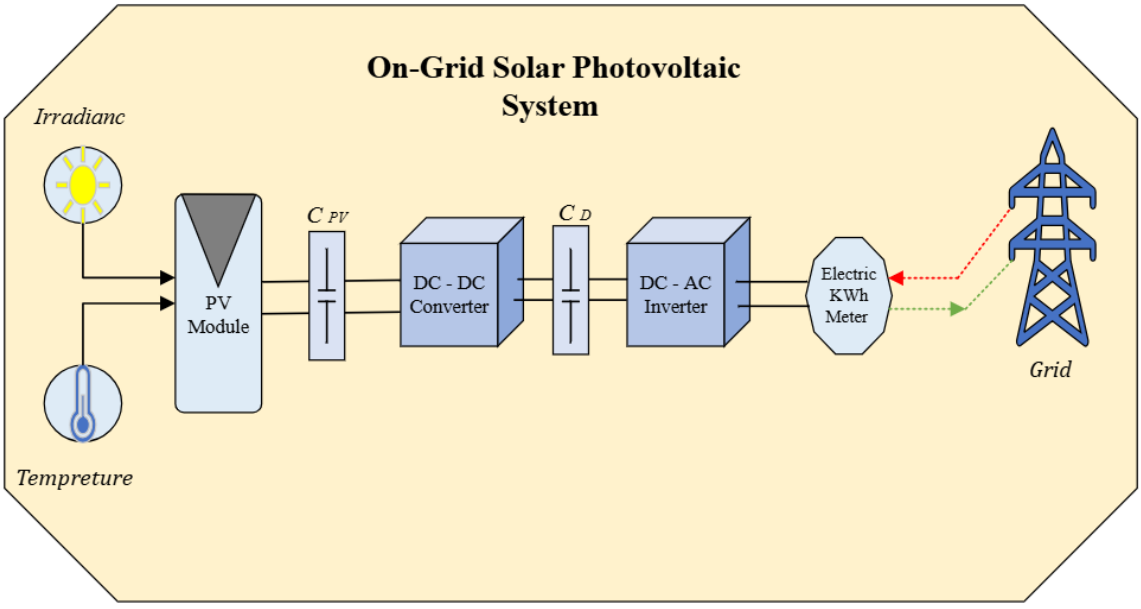

Figure 4.1 Schematic representation of a standard grid-tied residential PV system.

Inverter designers must meet grid interconnection regulations when considering incorporating a PV system with the AC distribution grid. Energy providers establish specific guidelines and standards for grid-connected applications not only to formalize the interconnection process but also to prevent complications that can arise from the distribution side of the grid. Therefore, the stability of the entire electrical network must be protected when connecting the PV applications to the electrical grid [113].

Maintaining safe operation is essential for designing the PV system inverter to protect both end users and system equipment in the event of grid-tied system malfunctions. The isolation feature is commonly considered in the design of the grid-connected application to protect the system during faulty conditions. Currently, the isolation operation for the grid-connected applications is not mandatory for interconnection with the electrical grid; however, the power converter designers often take this essential factor into account to enhance and extend the overall safety of the PV system [114]. The power electronic devices in the PV system are commonly responsible for critical functions that enable the grid-connected system to operate efficiently. Furthermore, the current generated on the grid side must demonstrate a pure sinusoidal waveform, as this characteristic is crucial for practical interaction with the distribution grid [115].

4.2 Distributed Multi-Input Single-Output Structure

The multi-input single-output microinverter presents a promising solution for addressing the mismatch issue within a single PV module. Given that the energy produced by an individual PV cell is relatively low, it is often impractical to extract the maximum power from each cell independently. Instead, it is more beneficial to obtain the maximum power from a group of PV cells. Commonly, a PV module is divided into groups of PV cells known as PV SMs, and the effective capture of maximum power from each group can enhance the overall energy output of the PV system. To mitigate the mismatch challenges that occur between the various PV SMs, the implementation of a cascaded boost power electronic converter can be a suitable solution.

Although these cascaded boost converters can require an increased number of passive components, they possess the potential to enhance the performance of the power system and

significantly optimize the energy harvesting capabilities of the PV module. The proposed topology aims to extract the maximum available power from a cluster of PV cells within a single PV module. Given that most PV modules are grouped into three SMs, the proposed topology aims to efficiently harvest the maximum available power from these three groups of PV cells within the PV module.

The control strategy for the proposed configuration relies on implementing the distributed MPPT method to optimize power extraction from each PV SM independently. The distributed MPPT system is employed to capture the MPP of each PV SM. The maximum power output of each PV SM is achieved through the regulation of its output voltage. Figure 4.2 illustrates the PV module built of 72 PV cells.

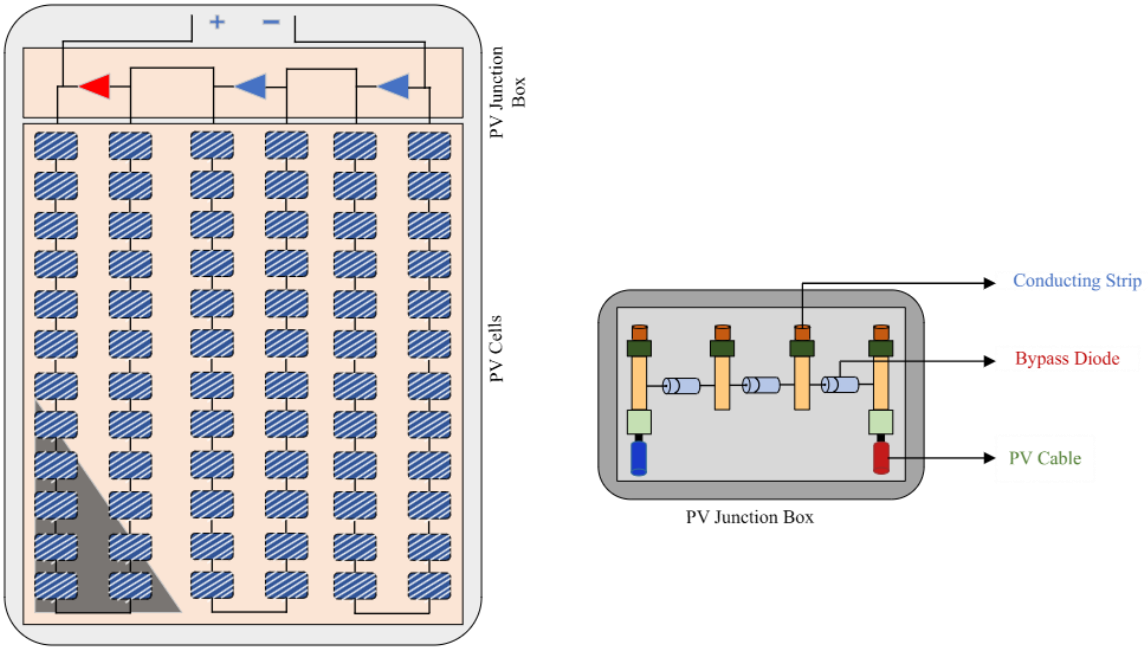

Figure 4.2 A representative 72-PV-cell module circuit diagram: (a) the series configuration of the 72 solar cells and (b) the integrated junction box of the 72-cell PV module.

4.2.1 Proposed System Description.

Figure 4.3 illustrates the proposed cascaded boost converters utilized for employing distributed MPPT at the PV SM level. Given that the output voltage of the PV SM can be relatively low and that the boost converter has a limited range for voltage amplification, the

design cascades the three boost converters to improve the overall boosting capability of the proposed configuration. A VSI is implemented at the utility side to convert the DC power generated by the PV module into sinusoidal AC power, which is suitable for grid integration. Additionally, the cascaded topology is connected to the utility grid via a forwarding diode to prevent reverse currents from affecting the PV side under faulty scenarios. A DC link capacitor is also employed between the PV side and the grid side to provide decoupling functionality, store the second-order harmonic, and mitigate the effects of THD.

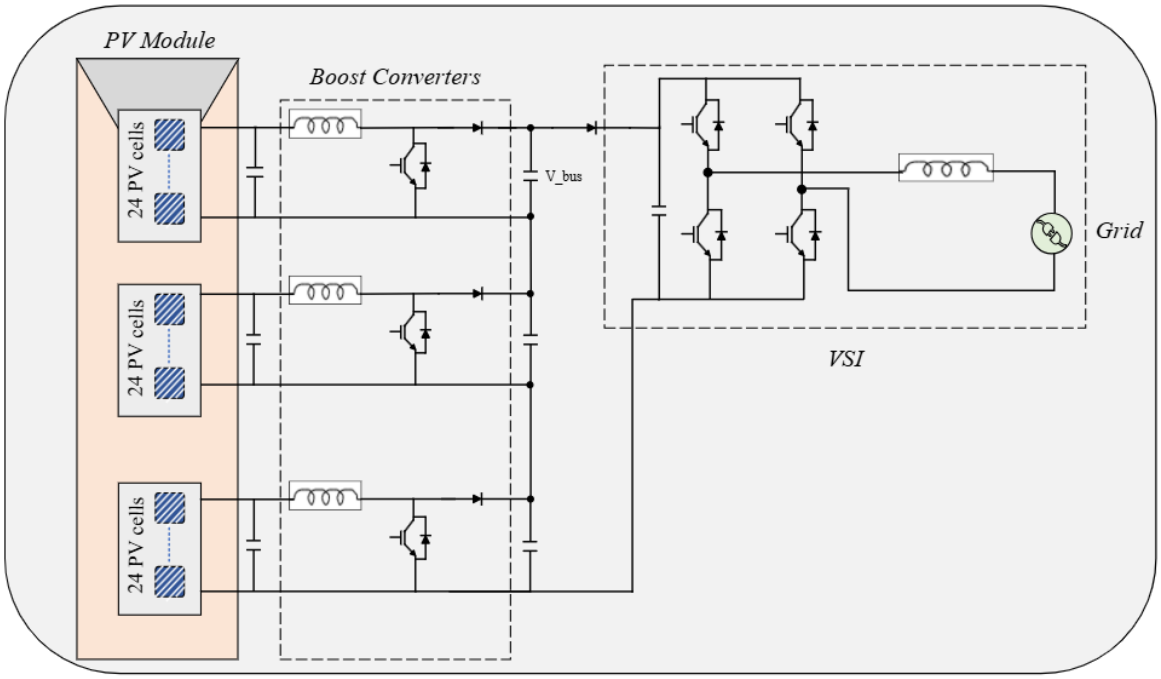

Figure 4.3 The proposed multi-input single-output boost-based inverter.

The residential PV system is often constructed from several PV modules, and the required number of PV modules is determined based on the local energy demands of end-users [116]. The suggested approach in this chapter aims to mitigate the mismatch issue at the PV SM level, which can enhance the PV system performance and increase power production. The scalability of the PV system is improved, and increasing the size of the PV system will not present challenges because the mismatch issue is internally reduced at the PV SM level. Moreover, the proposed design also considers protecting the PV system in the event of a fault. The proposed topology implements a blocking diode between the PV module and the electrical grid, preventing reverse current from flowing back into the PV module.

4.2.2 State Space Model

Modelling by averaging over a switching cycle is a commonly used practical approach for capturing the behaviour of power converters [117]. This strategy averages the model of the power converter over a single switching cycle, which helps to capture the internal dynamics of switching power converters. Power electronic systems commonly reveal nonlinear behaviour, and modelling these systems can be complex; therefore, the linearization of these systems around a specific operating point can be a viable solution to the nonlinearity challenge. Once the linear module of the power converter is derived, the system state variables are perturbed by small values, facilitating the creation of the small-signal model. The small-signal model is generally practical and capable of accurately copying the dynamic behavior of the actual power converter model. A small-signal model of the boost converter is derived to study the proposed method for mitigating the mismatch issue at the PV SM level.

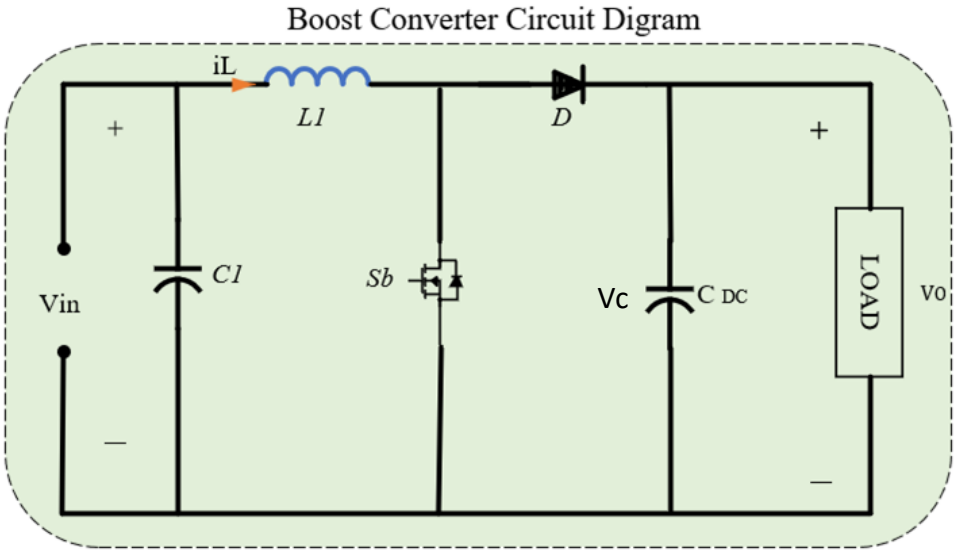

Figure 4.4 Typical asynchronous boost converter.

The boost converter model is demonstrated from the circuit described in Figure 4.4. It is assumed that the converter component operates under ideal conditions, therefore ignoring any internal losses associated with the component. The system equations are formulated employing the general averaging method, as detailed below:

Upon activation of switch Q, the state equation is modified as follows:

$$L\frac{di}{dt} = V_{in} \quad (4.1)$$

$$C_{DC}\frac{dv}{dt} = -\frac{V_C}{R} \quad (4.2)$$

Upon deactivation of switch Q, the state equation is modified as follows:

$$L\frac{di}{dt} = V_{in} - V_C \quad (4.3)$$

$$C_{DC}\frac{dv}{dt} = i_L - \frac{V_C}{R} \quad (4.4)$$

While in the *ON* state:

$$X' = A_{ON}X + B_{ON}V_{IN} \quad (4.5)$$

$$V_O = C_{ON}X \quad (4.6)$$

While in the *OFF* state:

$$X' = A_{OFF}X + B_{OFF}V_{IN} \quad (4.7)$$

$$V_O = C_{OFF}X \quad (4.8)$$

Upon deriving the state space equations for the boost converter, the matrices corresponding to the *ON* and *OFF* states are demonstrated as follows:

1) *ON* state

$$A_{ON} = \begin{bmatrix} 0 & 0 \\ 0 & -\frac{1}{\mathrm{RC}} \end{bmatrix} \qquad B_{ON} = \begin{bmatrix} \frac{1}{L} \\ 0 \end{bmatrix}, \qquad \text{and } C_{ON} = [0\ \ 1]X \quad (4.9)$$

2) *OFF* state

$$A_{OFF} = \begin{bmatrix} 0 & -\frac{1}{L} \\ \frac{1}{C} & -\frac{1}{RC} \end{bmatrix}, \qquad B_{OFF} = \begin{bmatrix} \frac{1}{L} \\ 0 \end{bmatrix} \qquad \text{and } C_{OFF} = [0\ \ 1]X \quad (4.10)$$

Where $X = [i_l\ \ v_c]$

The equations presented below are employed to derive the average model:

$$X' = [A_{ON}D + A_{OFF}(1-D)]X + [B_{ON}D + B_{OFF}(1-D)]V_{IN} \quad 4.11$$

$$V_O = [C_{ON}\,D + C_{OFF}(1-D)]X \quad 4.12$$

The average model:

$$A_{AV} = \begin{bmatrix} 0 & \frac{(D-1)}{\mathrm{L}} \\ \frac{1-\mathrm{D}}{\mathrm{C}} & -\frac{1}{RC} \end{bmatrix}, \qquad B_{AV} = \begin{bmatrix} \frac{1}{L} \\ 0 \end{bmatrix} \qquad \text{and } C_{AV} = [0\ \ 1]X \quad 4.13$$

The equation below can be employed to obtain the steady-state values of I_L and V_O:

$$SS = -inv(A_{AV}) * B_{AV} * V_{IN} \quad 4.14$$

A minor disturbance is introduced to the state variable to obtain the small signal module, wherein ~ denotes the minor perturbation to the variables:

$$\begin{bmatrix} i_L + \widetilde{il} \\ v_C + \widetilde{v_c} \end{bmatrix} = \begin{bmatrix} 0 & -\frac{-(1-D-\tilde{d})}{L} \\ \frac{(1-D-\tilde{d})}{C} & 0 \end{bmatrix} \begin{bmatrix} i_L + \widetilde{il} \\ v_C + \widetilde{v_c} \end{bmatrix} + \begin{bmatrix} \frac{1}{\mathrm{L}} \\ 0 \end{bmatrix} [V_{IN} + \widetilde{v_{in}}]$$

$$[Vo + \widetilde{v_o}] = [0\ \ 1] \begin{bmatrix} i_L + \widetilde{il} \\ v_C + \widetilde{v_c} \end{bmatrix} \quad 4.15$$

$$\tilde{x} = \left[\begin{bmatrix} 0 & -\frac{-(1-D)}{L1} \\ \frac{(1-D)}{C} & 0 \end{bmatrix} + \begin{bmatrix} 0 & \frac{\tilde{d}}{L} \\ \frac{-\tilde{d}}{C} & 0 \end{bmatrix} \right] \left[\begin{bmatrix} i_L \\ v_C \end{bmatrix} + \begin{bmatrix} \widetilde{il} \\ \widetilde{v_c} \end{bmatrix} \right] \quad 4.16$$

$$\tilde{x} = \begin{bmatrix} 0 & \frac{-(1-D)}{L} \\ \frac{(1-D)}{C} & 0 \end{bmatrix} \begin{bmatrix} \widetilde{il} \\ \widetilde{v_c} \end{bmatrix} + \begin{bmatrix} \frac{1}{\mathrm{L}} & \frac{\mathrm{Vo}}{L} \\ 0 & -\frac{\mathrm{IL}}{\mathrm{C}} \end{bmatrix} \begin{bmatrix} Vin \\ \tilde{d} \end{bmatrix} \quad 4.17$$

After the computation of the new A and B matrices, the transfer function can be derived employing the equation presented below:

$$TF = C_{AV} * inv(s * eye(3) - A_{AV}) * B \quad 4.18$$

$$TF = \frac{V_o\,R\,D_{OFF} - L\,R\,I_L s}{C\,L\,R\,s^2 + L\,s + R\,D_{OFF}^2} \quad 4.19$$

4.2.3 Selection of Passive Components

The suggested topology utilizes the boost converter due to the comparatively low output voltage of the PV SM. In this type of converter, the output voltage is expected to exceed the input voltage of the PV system. The input voltage derived from the PV SM is supposed to be under conditions of maximum irradiation. It is assumed that each PV SM functions at the highest power available; therefore, the voltage of the PV SM will be denoted as V_{MPP}. Based on steady-state analysis, the duty ratio corresponding to the output voltage of each PV SM can be defined as follows:

$$D = 1 - \frac{V_{in}}{V_O} \tag{4.20}$$

$$D = 1 - \frac{VMPP_{SM}}{Vo_{SM}} \tag{4.21}$$

In this context, where D represents the duty cycle, $V_{MPP_{SM}}$ the output voltage of each boost converter corresponds to the voltage at the MPP.

Figure 4.5 shows both the circuit configuration and the current waveforms of the investigated PV boost converter. In the context of a grid-connected inverter, the value of the DC bus capacitor is determined based on both the input and output power, enabling it to mitigate second-order harmonic distortion within the proposed configuration. A current-based derivation method can be applied to determine the most suitable capacitance value for the decoupling capacitor. An appropriate selection of capacitor value ensures the delivery of pure DC power from the PV input while maintaining a sinusoidal current waveform on the grid side. Following a similar manner, the DC_{BUS} capacitor value can be chosen with the assumption of a pure DC output from cascaded boost converters. The shape of the grid current waveform is sinusoidal, indicating that the current through the inductor represents the grid current. However, it is essential to note that the direction of the DC bus capacitor current is phase-shifted.

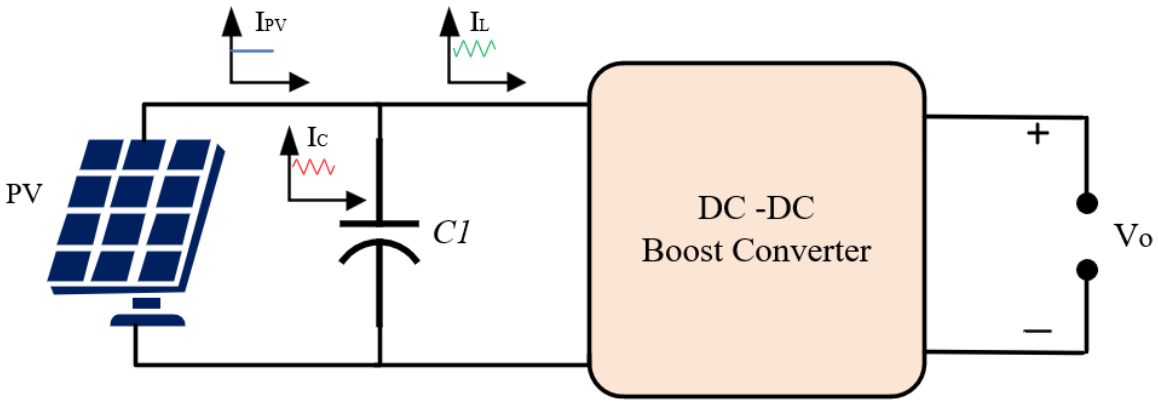

Figure 4.5 The circuit and current waveforms associated with the PV system.

The parameters for the presented boost converters have been determined based on continuous conduction mode (CCM) as illustrated below:

$$L\frac{di}{dt} = V_{MPP_{SM}} \quad 4.22$$

$$L = \frac{\Delta t\, V_{MPP_{SM}}}{\Delta i} \quad 4.23$$

$$CV = \int Capacitor\ Stored\ Energy \quad 4.24$$

$$C_{PV}\,\Delta V_{PV} = \frac{1}{2}\left(\frac{\Delta i}{2} * \frac{T_{SW}}{2}\right) \quad 4.25$$

$$C_{PV} = \frac{\Delta i}{8\Delta_{PV} f_{sw}} \quad 4.26$$

The configuration of the suggested three-input single-output power electronic converter is determined by calculating the output voltage at the common DC bus. The output voltages from the three cascaded boost converters are computed to determine the output voltage at the DC bus, where *n* represents the number of PV SMs.

$$V_{Bus} = \sum_{X=0}^{n} \frac{V_{PV\ SM_X}}{1-D_{PV\ SM_X}} \quad 4.27$$

4.2.4 Open-Loop Dynamics and Systematic Investigation

The voltage and current levels at the MPP of the PV SM step-up converter are determined based on a standard PV module. Regarding the design of the passive components of the boost

converter, during the ON state, the inductance can be demonstrated from the peak-to-peak fluctuations of the inductor current. The chosen inductance for the PV step-up converter is calculated with an emphasis on minimizing the peak-to-peak ripple value. The output capacitor of the PV step-up converter is selected following a compromise that balances the capacitor size with the permitted peak-to-peak voltage ripples.

Following the calculation of the transfer function for the boost converter, the parameters L, $C_{PV,}$ and C bus are determined under CCM with the assumption that the system operates under a condition of balanced energy. The chosen values are presented in Table 4.1. The developed small-signal averaged model of the boost converter reveals the existence of two poles and a non-negative zero. For the system to reach internal absolute stability, both poles must reside within the left half of the s-plane. The presence of a non-negative zero can lead to phase margin reduction and generate undershoot during transient conditions; however, the process of zero cancellation can adversely impact the system's overall stability.

Table 4.1 The System Parameter

Parameter	**Value**
V_{MPP}	12 V
I_{MPP}	7A
L	2.4m H
C_{PV}	47 µF
R_L	10 Ω
F_s	5 kHz

$$TF = \frac{-1.49*10^5 S+5.32*10^7}{s^2+2128s+2.22*10^6} \quad 4.28$$

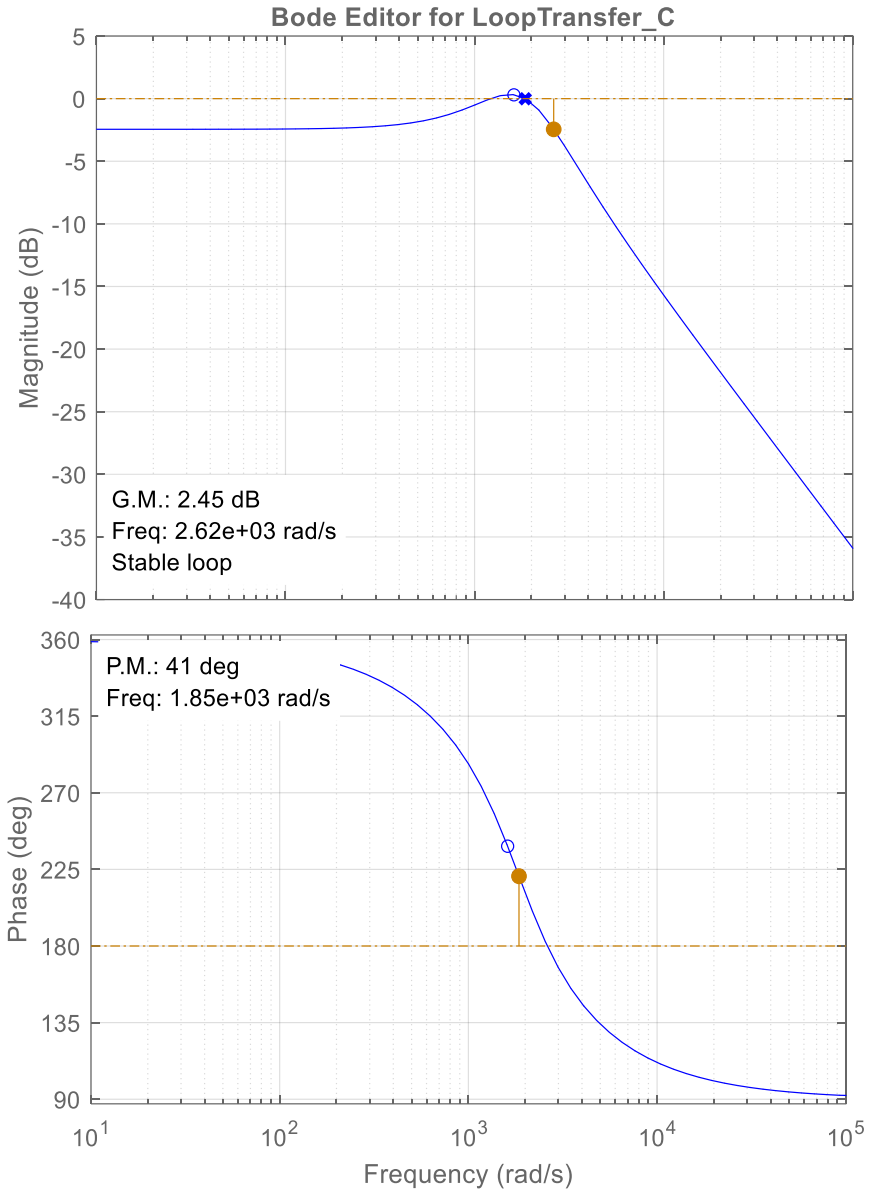

Figure 4.6 The Bode plot for the output voltage of the open-loop system for a multi-input boost inverter.

Therefore, the most effective strategy to minimize the impact of the non-negative zero is to speed up its response by placing it at a greater distance from the origin (0,0) because faster zeros are less damaging compared to their slower ones. Figure 4.6 presents the Bode plot of the boost converter in the absence of controllers. The frequency response indicates that the system maintains stability, with both the gain margin and phase margin having positive values. However, the systems appear to be critically stable, given that the gain margin is near the negative part of the Bode plot. Figure 4.7 illustrates the step response graph of the boost

converter, which reveals a significant undershoot during the transient time. The presence of considerable undershoot is attributable to the non-negative zero in the transfer function of the boost converter. Obtaining the appropriate controller for the boost converter is crucial to addressing this concern and moving the system to a stable side.

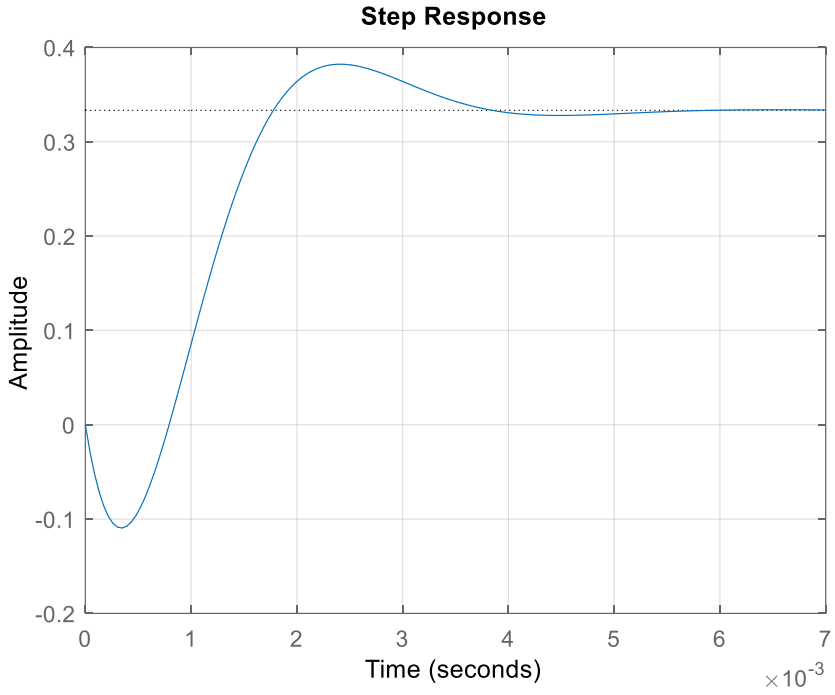

Figure 4.7 The step response of the open-loop system for a multi-input boost inverter.

4.2.5 Design the Controller for the Proposed System

The derived open-loop system transfer function shows two complex poles placed at −261 rad/s and a singular positive zero located at 1610 rad/s. According to the principles of control theory, the stability of the system is inherently linked to the positioning of its poles [118]. The controlling system can enhance the stability of the investigated system by relocating these poles to the left-hand side of the s-plane. The positive zeros generally do not result in a complete loss of system stability; however, they can lead to significant challenges, such as strong undershooting and a reduction in the phase margin of the system. A common approach to mitigate the adverse effects of positive zeros is to accelerate their response. The fast zeros, defined as those located farther from the origin (0,0), are preferable because they impose

considerably fewer negative impacts in comparison to their slower counterparts. The SISO tool within SIMULINK/MATLAB has been employed to identify and fine-tune the parameters of the proposed system's controller. The integration of the controller enhances the stability of the system and optimizes performance by relocating the system's poles into the stable left-hand side.

The poles and zeros corresponding to the parameters presented in Table 4.1 are represented in Figure 4.8. The value of the k_i gain for the controller is consistently set at 0.6, whereas the k_p gain is varied within the range of [0.2 to 0.5] to examine the dynamics of the proposed system. Remarkably, a k_p gain of 0.25 within the proportional integral derivative (PID) controller has the most suitable dynamic response for the system. The SISO tool available in SIMULINK/MATLAB has been employed to derive and adjust the parameters of the PR controller. The findings indicate that the optimal k_p and k_r gains for the PR controller, which ensure adequate stability and bandwidth, are 3 and 5, respectively.

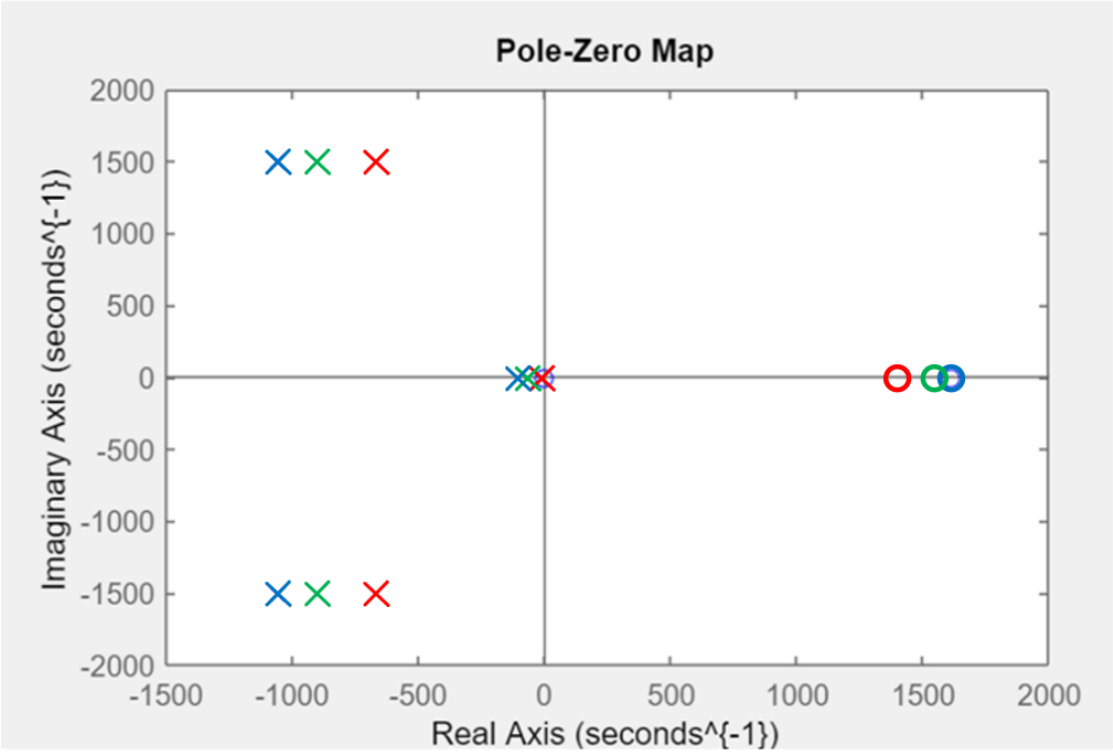

Figure 4.8 The Pole-Zero Map depicts the relocated poles of the system.

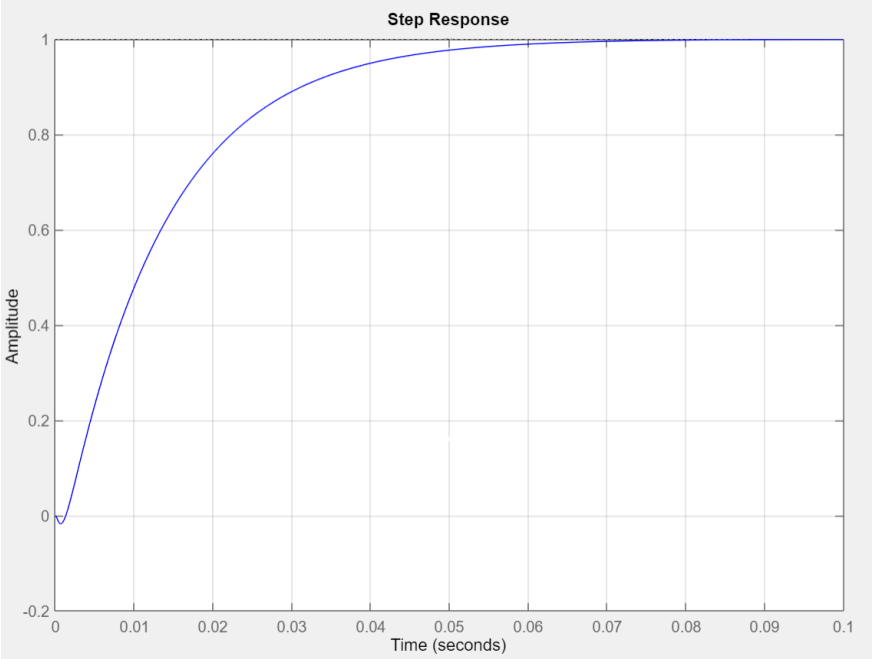

Figure 4.9 The step response for the output voltage of the PV SM boost converter with controller.

The PID controlling systems are widely recognized as practical controllers and one of the most dominant controllers used in power electronic converters; they have been applied to the input side of the proposed configuration. The MPPT algorithm is used to obtain the current at the MPP under specific temperatures and irradiation conditions, which serves as a reference value for the controller. The actual current is compared to the reference current to calculate the error, which is passed to the PID controller block. The PID controller will manage the difference between the reference current and the actual current for each boost converter and perform control actions accordingly. The controlling system in this chapter maintains the input current from the PV SM at a constant DC level while reducing the associated current ripple. Therefore, the accuracy of the MPPT system can be enhanced, and the efficiency of the PV system can be improved. Figure 4.9 illustrates the improvement in the dynamic system response and step response characteristics by implementing the appropriate controller for the proposed system.

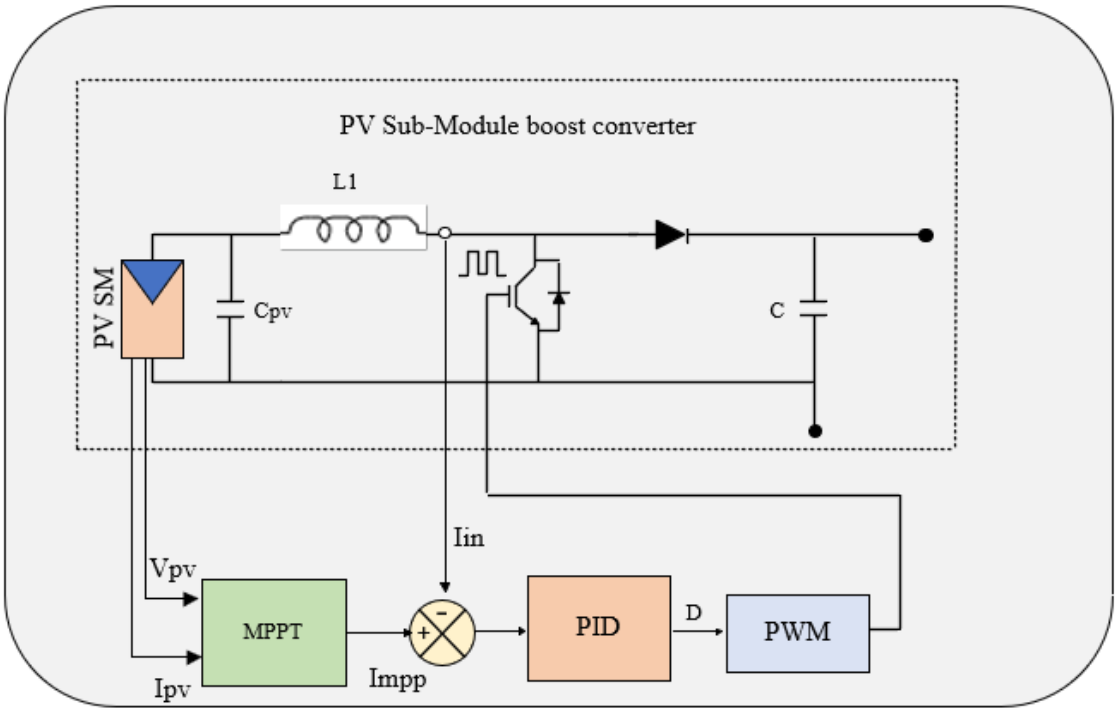

Figure 4.10 The schematic representation of the boost converter control system.

The current closed-loop control system employed to regulate the PV SM is illustrated in Figure 4.10. The I_{MPP} of the PV SM is used as a reference current for the controller at the subsystem level. The primary objective of the controller is to regulate the current at the input side of the PV SM while simultaneously mitigating the adverse effects associated with the total harmonics of the grid power. By eliminating or mitigating the distortion caused by the total harmonics in the PV system, the performance of the MPPT algorithm can be enhanced, which improves the entire efficiency of the PV system. The MPPT tracking system determines the I_{MPP} of the SM based on the subsystem irradiation level and temperature. When this current is used as the reference input for the compensator, it is compared with the real input current of the boost converter to perform the control process.

The net output voltage at the inverter terminal of the suggested PV system can be expressed as follows:

$$V_o = Vsin(wt + \theta) \qquad 4.29$$

In this context, V represents the amplitude of the voltage, while V_g is defined as the magnitude of the grid voltage, and * denotes the reference value of the grid current. If the proposed system supplies an active power P to the grid with a power factor of cos(α), the expression for the single-phase output current can be stated as follows:

$$Ig = \frac{2P}{V_g \cos(\alpha)} \tag{4.24}$$

The conventional strategy for regulating alternating current involves transforming the rotating current into direct current, followed by a control process that utilizes a traditional PID control method, and then converts it back into controlled alternating signals after performing control actions. The PID-based method has been implemented for many years in power system design and is suitable for various applications; however, it requires multiple design stages, which can reduce the efficacy of the control process. The proportional resonant (PR) is another control method for regulating rotating current, and it has been used in several applications for power system applications. The effectiveness of the PR control strategy in regulating the rotating signal has been demonstrated, making it a practical alternative to the conventional control method for inverters. In this study, the PR controller is utilized to control the grid current, which regulates a sinusoidal current waveform on the grid side. The PR controller monitors and compares the grid current with the target value to determine the error between the two signals. This error is then processed through the PR controller, which completes the control action and tracks the sinusoidal reference grid signal. The block diagram representing the PR controller for the suggested electrical configuration is illustrated in Figure 4.11.

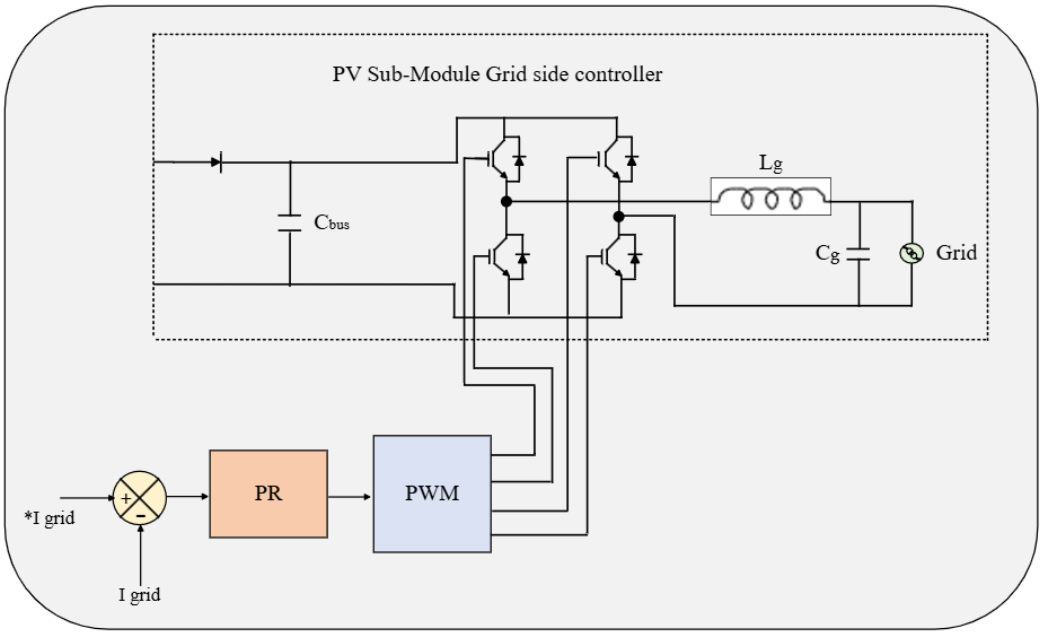

Figure 4.11. The grid current controller for the proposed microinverter.

In this context, k_p denotes the proportional gain, while k_r and w_o refer to the resonant gain and frequency, respectively. The classic PID controller is often suitable for systems characterized by constant values, such as DC-DC converters, because it is effective in eliminating steady-state errors and ensuring a fast response. However, the PID controller cannot accurately track sinusoidal waveforms because it designed to regulate constant values. On the other hand, the PR controller is capable of delivering infinite gain at a specified frequency; thus, it is a suitable choice for application in grid-connected systems. The grid section of the proposed system incorporates an *LC* filter to enhance system efficiency, as illustrated in Figure 4.12. Additionally, the Bode plot corresponding to the PR controller utilized in this analysis is presented in Figure 4.13.

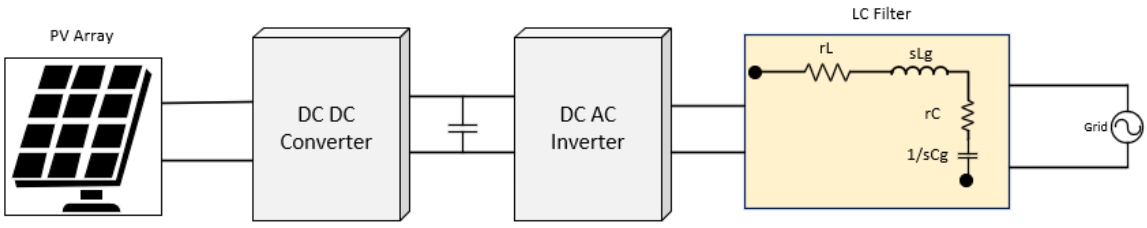

Figure 4.12 Single-phase grid-tied PV system with filter circuit.

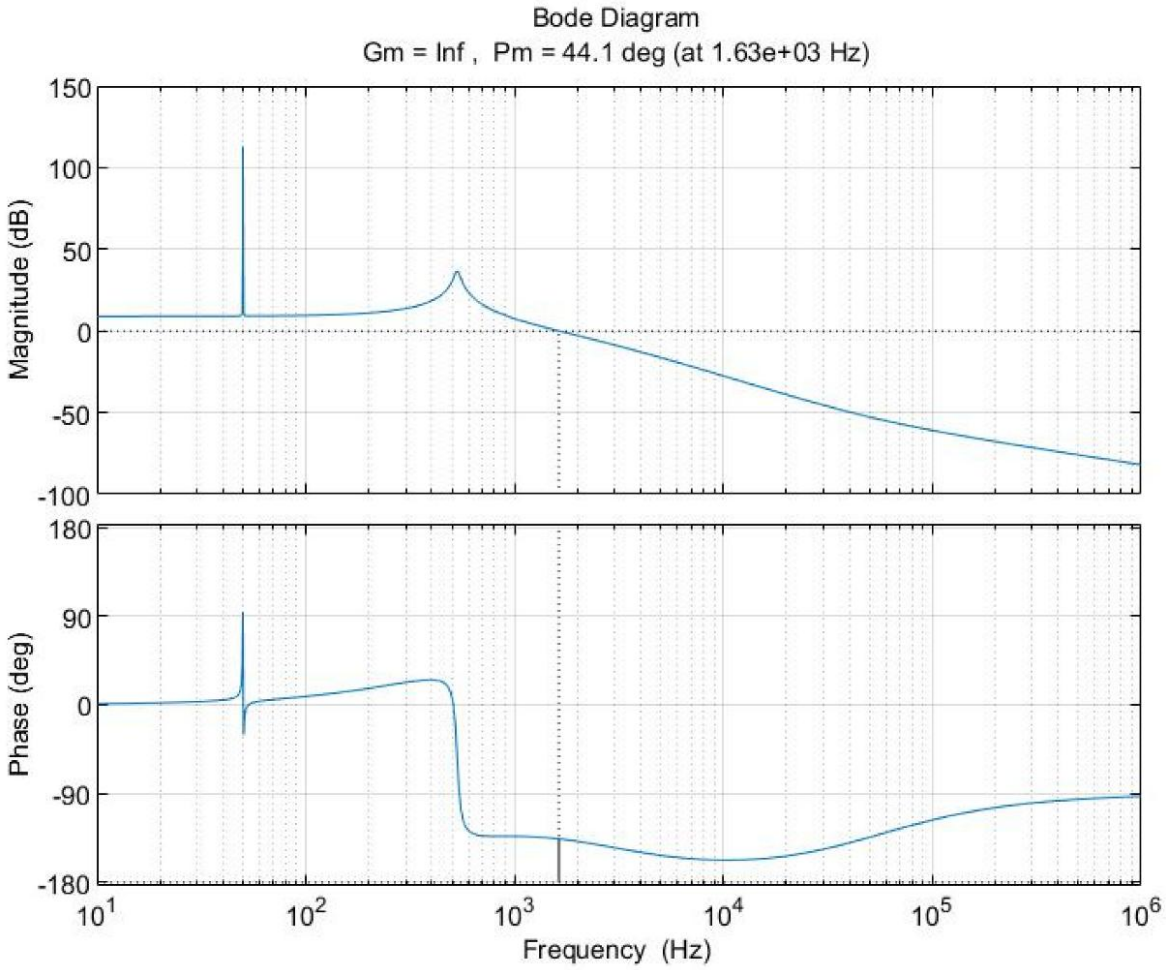

Figure 4.13 Bode plot for PR controller.

The Laplace transform function of the LC filter is represented by the subsequent equations:

$$\frac{V_O}{V_{in}} = \frac{r_{cg}+\frac{1}{sC_g}}{r_{LS}+r_{cg}+sL_g+\frac{1}{sC_g}} \tag{4.25}$$

$$\frac{V_O}{V_{in}} = \frac{sC_{rg}+1}{s^2L_gC_g+sC_g(r_{lg}+r_{cg})+1} \tag{4.26}$$

4.3 Simulation study

The open-loop condition of the MISO converter has been investigated using the MATLAB/Simulink environment to evaluate its performance. A passive load is employed in the model, and Table 4.2 lists the components used in the simulation. Ideal components

are assumed in the simulation module; therefore, the internal resistance of both active and passive components is neglected.

The MATLAB model of the MISO inverter is illustrated in Figure 4.14. The input power from the three SMs is shown in Figure 4.15. The grid voltage and grid current are presented in Figures 4.16 and 4.17, respectively. In addition, the voltage across the decoupling capacitor is illustrated in Figure 4.18.

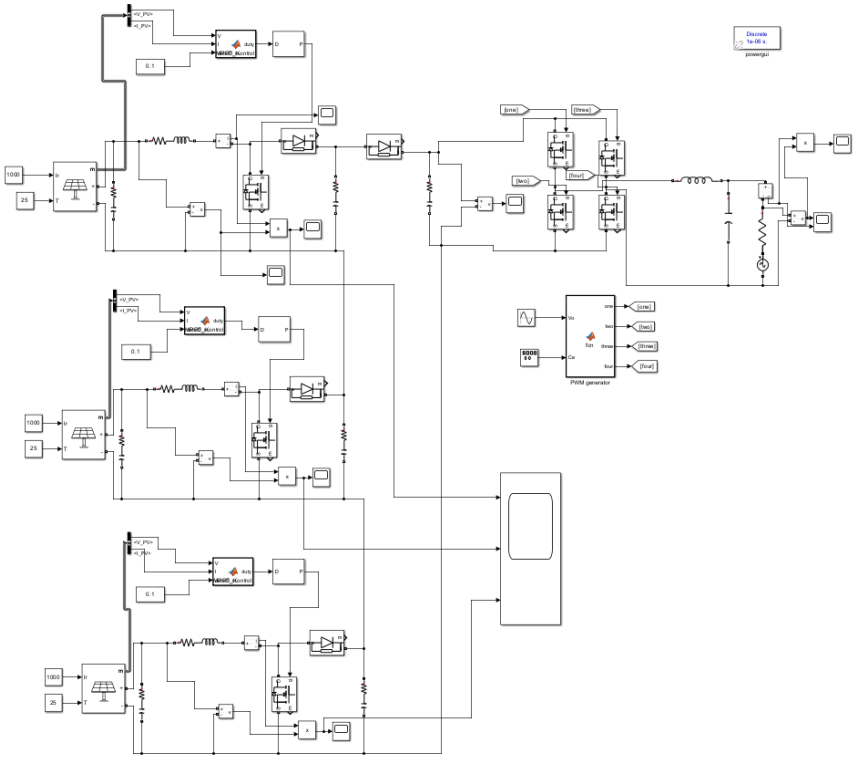

Figure 4.14 The MATLAB/Simulink block diagram

Table 4.2 Simulation Parameters

Parameter	Value
V_{MPP}	1.2 V
I_{MPP}	8A
L	1.5 m H
C_{PV}	2200 µF
R_L	100 Ω
F_s	25 kHz

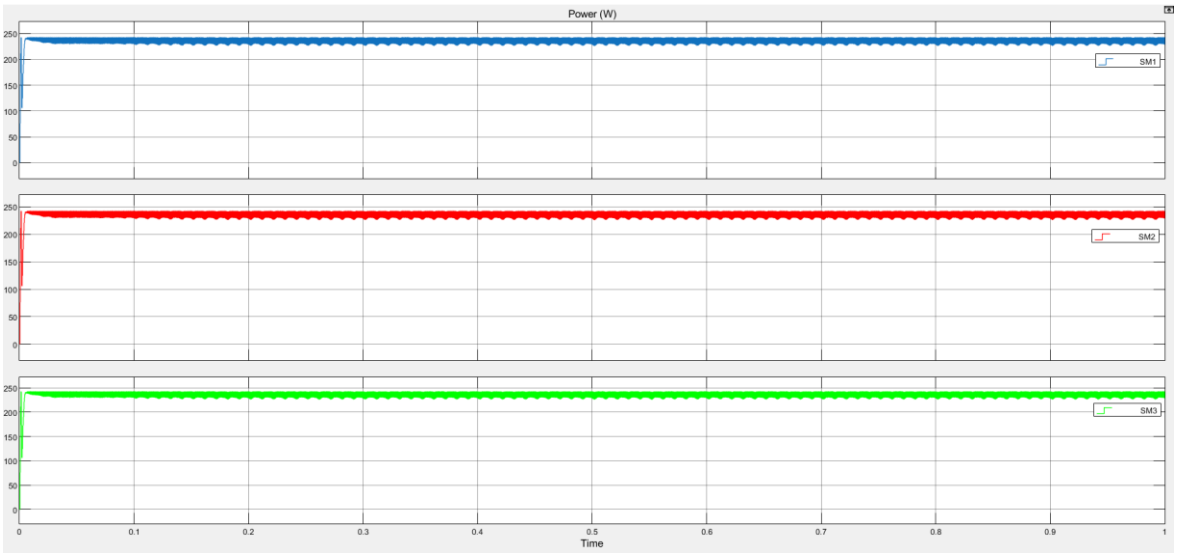

Figure 4.15 The input power from the three SMs.

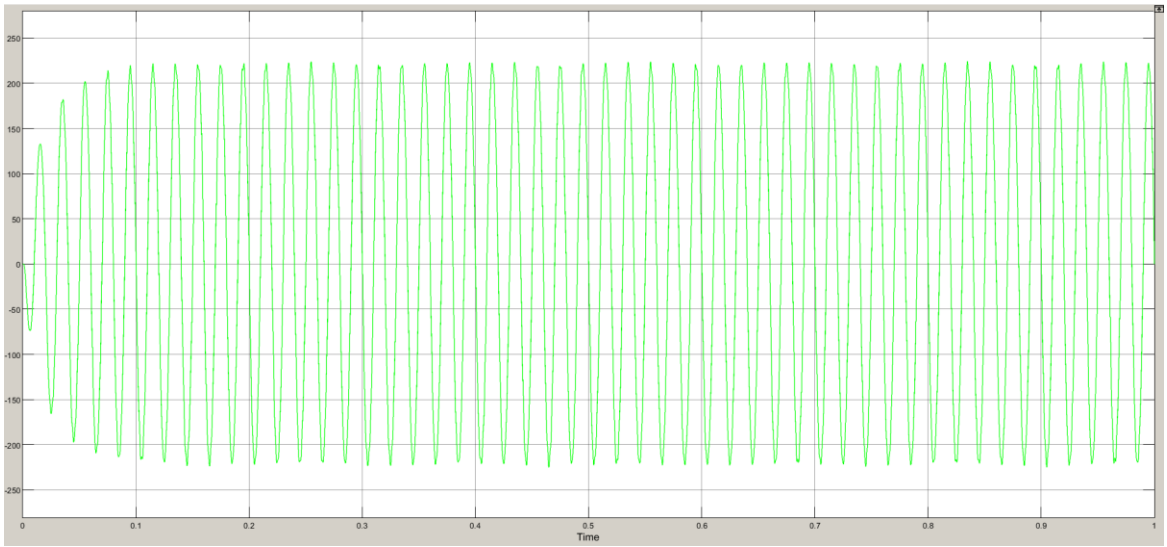

Figure 4.16 The output voltage at the grid side.

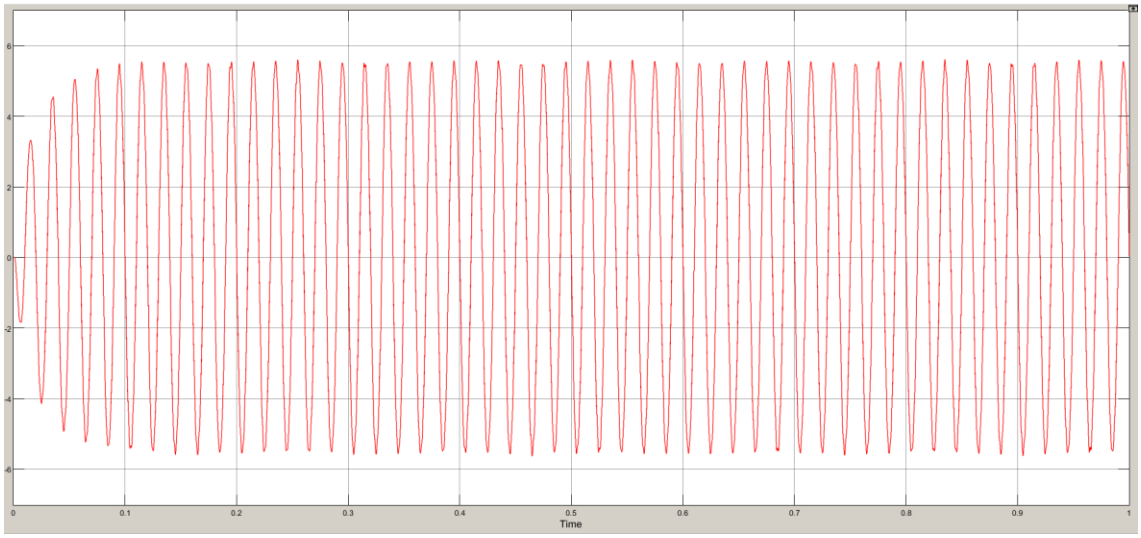

Figure 4.17 The output current at the grid side.

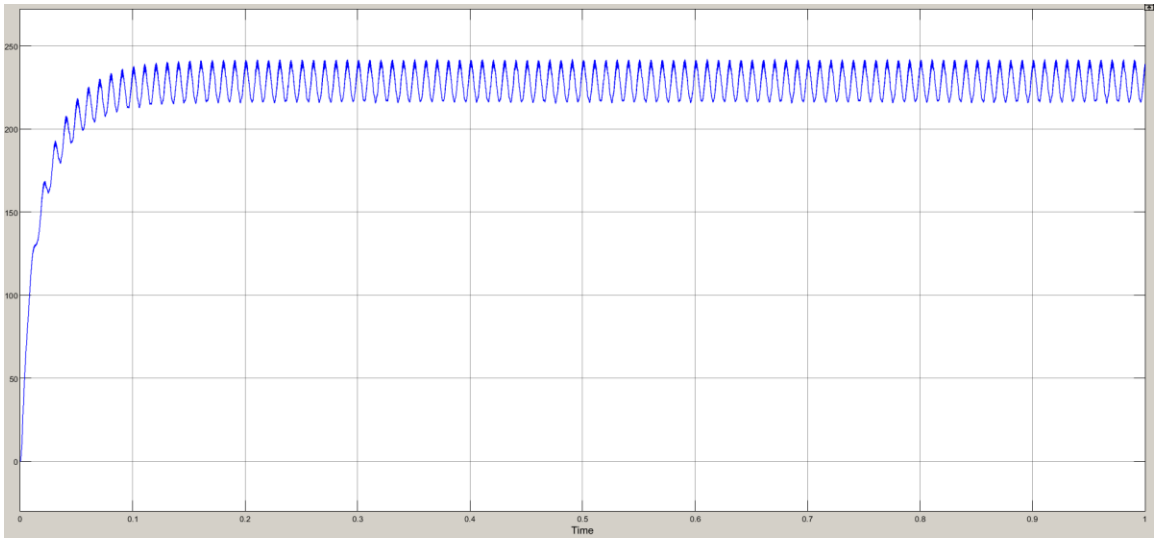

Figure 4.18 The voltage at the decoupling capacitor

4.4 Experimental Results

The experimental configuration designed to extract the maximum available power from the three PV SMs within a single PV module is illustrated in Figure 4.19. Each PV SM is rated at 250 W, resulting in a net maximum available power rating of 750 W for the entire PV module. The system utilizes the Texas Instruments DSP (TMS320F28335) as the control unit, which manages signals for gate points for the proposed three boost converters at the input side. Three DC power supplies are used as PV SMs to investigate the operation of the proposed system. Each of the three PV SMs is connected to an individual boost converter to

mitigate mismatch issues at the SM level and enhance PV module performance. The output from the PV module interfaces with the utility grid via an autotransformer, which reduces the utility grid voltage from 240 V to 100 V. The DC output generated by the PV module is converted to low-voltage AC (LV AC) for validation of the proposed system topology.

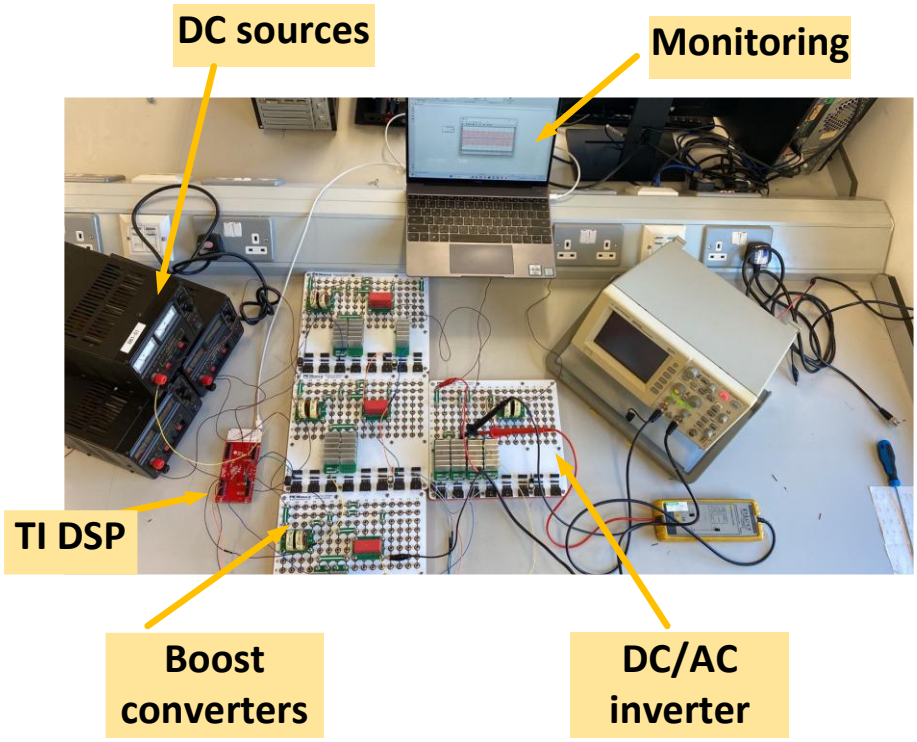

Figure 4.19. The experimental configuration of the proposed microinverter.

The outcomes of the experiments conducted on the proposed topology for utilizing the distributed MPPT at the PV SM level are illustrated in Figure 4.20. Specifically, Figure 4.20 (a) presents the overall input power of the system. Figure 4.20 (b) illustrates the output voltage and current when power is transmitted into the grid via the autotransformer at a unity power factor. Figure 4.20 (c) represents the DC-link voltage maintained between the PV SMs and the DC/AC inverter. Lastly, Figure 4.20 (d) displays the input currents of the PV SMs.

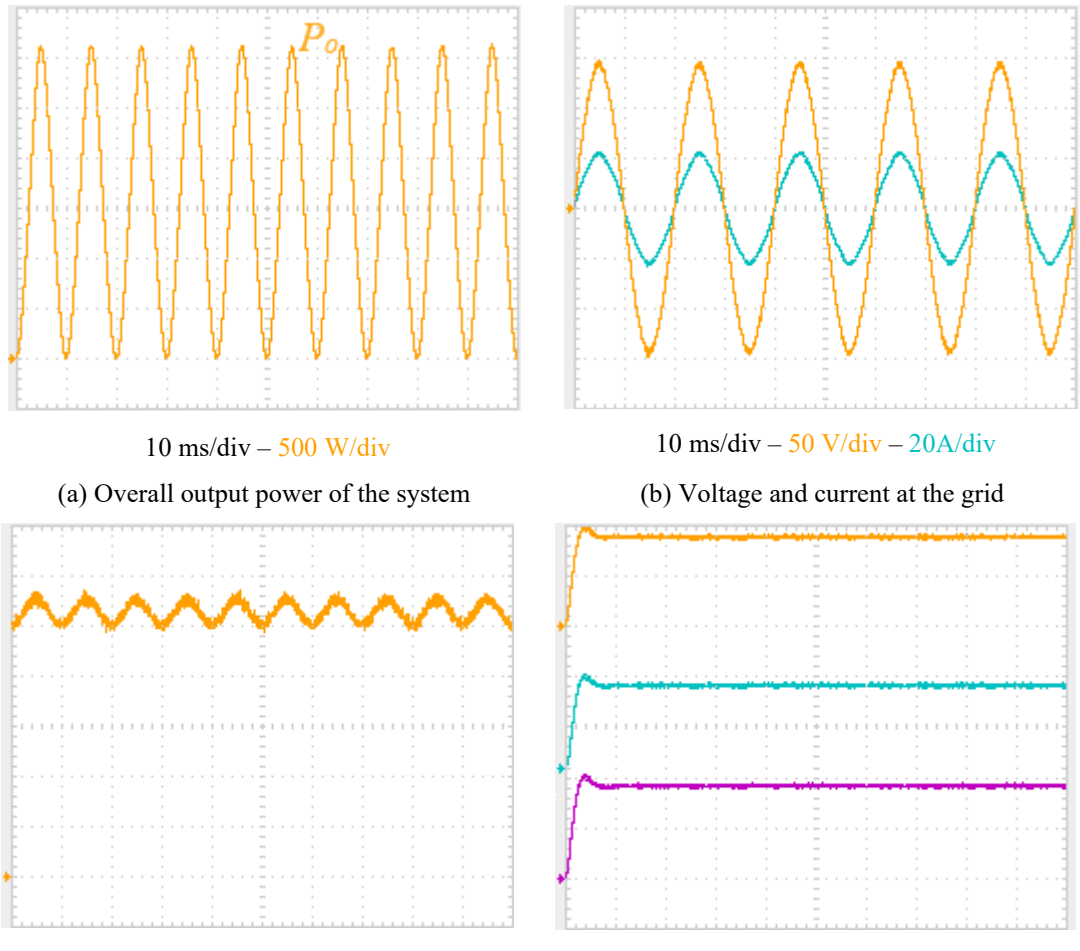

10 ms/div – 500 W/div

(a) Overall output power of the system

10 ms/div – 50 V/div – 20A/div

(b) Voltage and current at the grid

10 ms/div – 50 V/div

(c) Voltage at the DC-link

10 ms/div – 4A/div

(d) Input current of the SMs

Figure 4.20 Experimental findings of the proposed microinverter.

The stability of the proposed system is assessed by suddenly reducing the output power by 50%. Figure 4.21 illustrates the response of the grid current to a change in output power, which leads to a reduction in its peak value. Further, the input current of the three SMs also decreases as a consequence of the decrease in the system's output power.

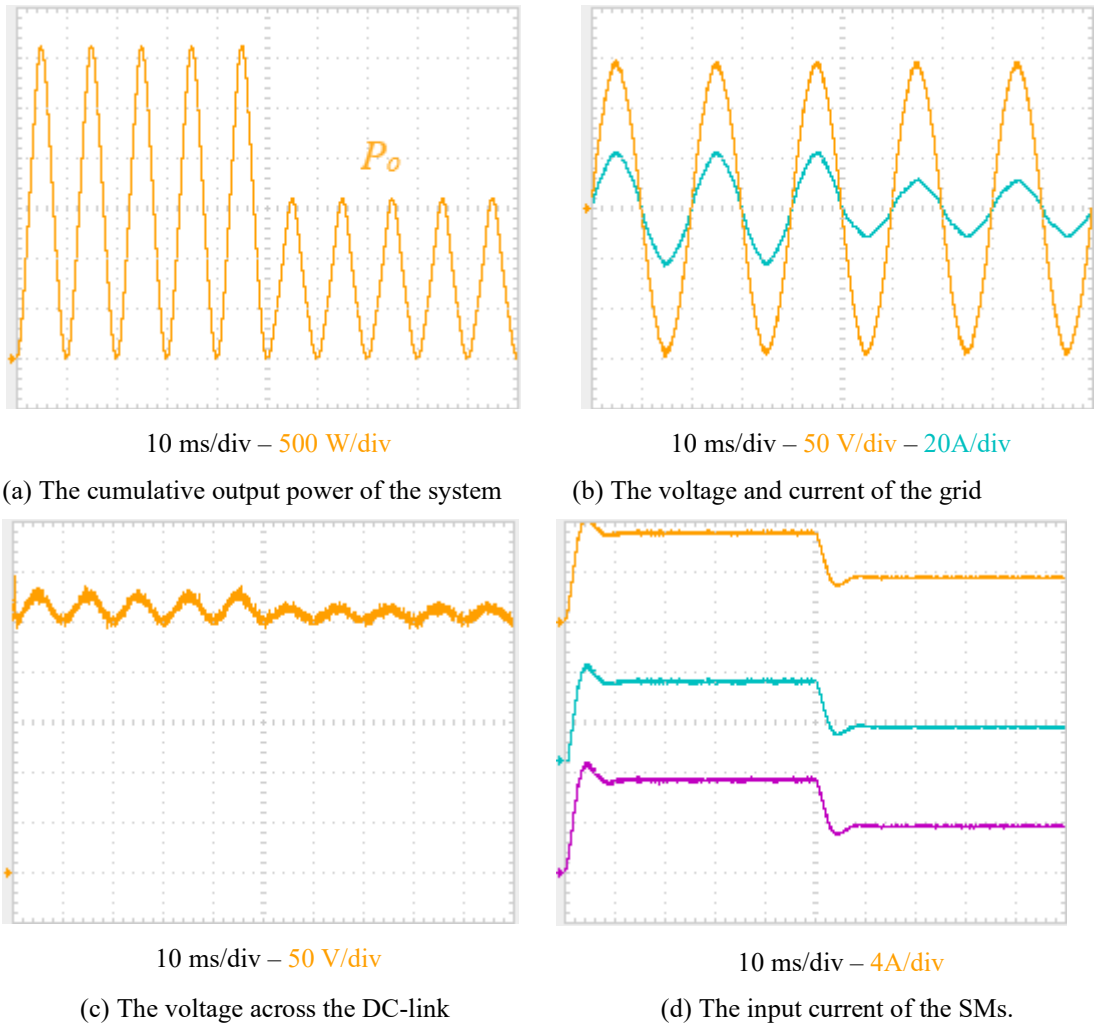

10 ms/div – 500 W/div

(a) The cumulative output power of the system

10 ms/div – 50 V/div – 20A/div

(b) The voltage and current of the grid

10 ms/div – 50 V/div

(c) The voltage across the DC-link

10 ms/div – 4A/div

(d) The input current of the SMs.

Figure 4.21 The experimental findings indicate a 50% reduction in output power.

The findings demonstrate that implementing the proposed three-input, single-output inverter at the PV SM level can facilitate the extraction of available power from each group of PV cells and mitigate mismatch issues within a PV module. The MPPT system is employed for each PV string of PV cells individually, enhancing the power production of the residential PV system. In contrast to the traditional approach, which isolates shaded PV SM from the overall PV system, the proposed configuration includes the shaded part of the PV model and harvests its power.

4.5 Comparative Study

The different mismatch issues, including partial and complete shading, can lead to a considerable reduction in the power output of a single PV module. In the context of PV systems, shading issues are often unavoidable and can adversely impact the entire performance of the PV system. The study presented in this chapter demonstrates that employing the distributed MPPT at the PV SM level for an LV PV system can enhance power generation and reduce mismatch effects. The output voltage produced by a single PV cell is comparatively low, which requires linking multiple PV cells in series to achieve a higher output voltage. This approach can address the issue of LV associated with an individual PV cell; however, it is worth noting that the PV system becomes sensitive to mismatch issues, which can minimize the power generation of the PV system.

Table 4.3 Comparison between applying MPPT at the PV model and the SM level

MPPT in Rooftop PV system			
PV Module Level		**PV Sub Module Level**	
Advantages	**Drawbacks**	**Advantages**	**Drawbacks**
Easy Design	High losses	High power production	Complex implementation
Low Cost	No power recovery	Low mismatch issue	Higher installation cost
High reliability	Multiple MPPs	Single MPP	
	Complex MPPT Process	Strate MPPT Process	

The power generation associated with the proposed topology is illustrated in Figure 4.22 and explained as follows. During the initial phase at T1, the power generation of the three PV SM is distributed uniformly, beginning at zero and progressively increasing until it reaches its maximum output at T2. Each PV SM generates 80 W, resulting in a cumulative output of 240 W for the entire PV module. In the following interval, the shading covers one PV SM. Under conventional methods, power generation from a shaded PV SM is completely lost. On the other hand, within the proposed topology configuration, power generation is captured separately, allowing for the utilization of electrical output power from the shaded PV SM.

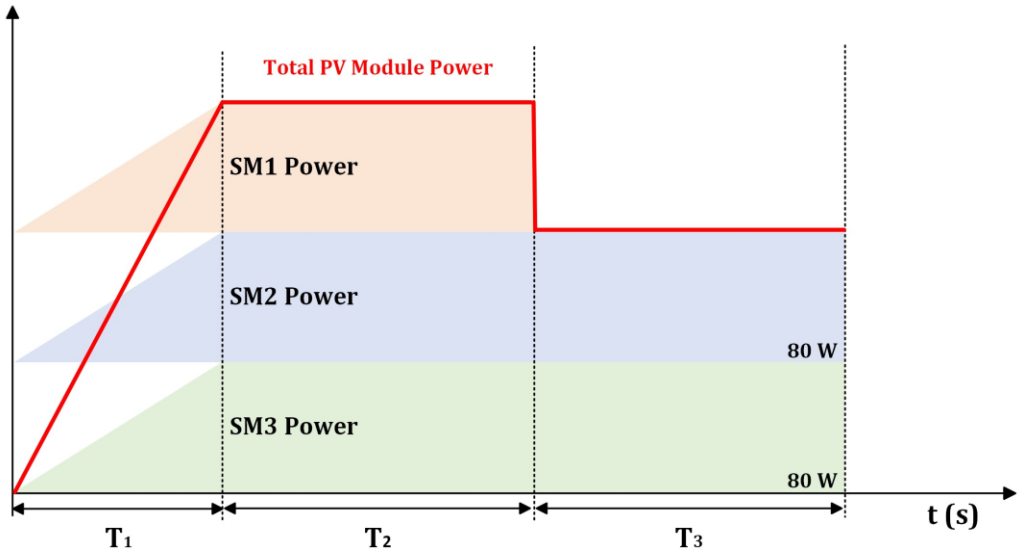

(a) Conventional

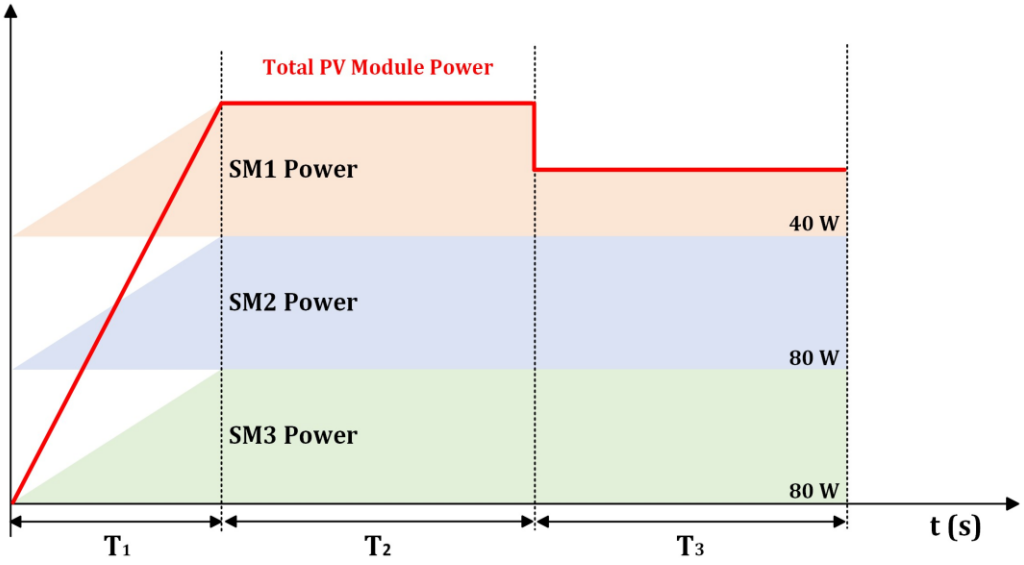

(b) Suggested

Figure 4.22 The output power generated by an individual PV model.

The proposed architecture is designed to extract energy from the shaded region of the PV module, which mitigates mismatch issues and enhances the power production of the PV system. It employs a power electronic boost converter for each PV SM to capture the maximum available power from each grouping of PV cells. The selection of the boost converter is attributed to its ability to step up the LV at the PV side of the grid-connected PV

system. Although the boost converter is employed to increase the input voltage to a higher level on the output side, its amplification capability is restricted to a specified output range. The output voltage produced by the boost converters is connected in series to satisfy the voltage specifications required by the utility grid. Furthermore, the proposed configuration is designed to optimize power extraction from the PV side while also enabling the conversion of direct power to alternating power.

The suggested topology in this chapter is designed for the forthcoming residential PV system, as currently available grid-connected systems utilize traditional PV modules that incorporate bypass diodes within their PV SMs. Although prototypes for PV cell optimizers remain undeveloped, relevant companies have initiated the implementation of distributed MPPT at the PV SM level.

4.6 Chapter Conclusion

This chapter has introduced a new microinverter topology that integrates three DC-DC boost converters with a single-phase inverter, which is designed to overcome mismatch challenges between PV SMs. The ability of the presented structure to extract optimal power from individual PV SM has been demonstrated through its series input, which eliminates the need for a high step-up voltage ratio. The two control systems introduced in this chapter ensure compliance with grid current standards and reduce input current ripple, which confirms their effectiveness in enhancing energy harvesting and mitigating the mismatch issue at the PV SM level. The simulation outcomes and experimental results confirm the ability of the proposed system to operate efficiently under both standard and mismatch conditions. In conclusion, the proposed microinverter topology offers a practical method that increases PV system power production and reduces mismatch problems between PV SMs by utilizing distribution MPPT at the PV SM level. Future investigations can focus on innovating control strategies and further minimizing system complexity to effectively capture the maximum available power from LV residential and commercial PV systems.

Chapter 5

Advanced Control Mechanisms

This chapter begins by presenting the latest developments in MPC technology for grid-connected PV systems. MPC offers several advantages in controlling power electronic converters, including the ability to handle nonlinearities and to effectively control multivariable systems due to the absence of a modulator. It presents a comparative analysis of continuous control (CC) MPC and predetermined control (PC) MPC, as well as their implementations for power electronic converters, with a specific focus on grid-tied inverters, control model structure, inverter architectural designs, and control objectives. Additionally, it proposes a new control strategy for the PC MPC that regulates the input and grid-side current while improving the performance of the grid-tied PV system. Furthermore, this study aims to predict the voltage across the decoupling capacitor for a single-phase SEPIC inverter to effectively eliminate the adverse effects of double-line ripples. This MPC approach not only reduces the ripples associated with input and output currents but also facilitates a fixed switching frequency feature.

5.1 State of the Art of MPC in Power Electronics

Over the past few decades, the integration of different renewable energy sources with existing electrical infrastructures has attracted significant attention from researchers in the field of power systems [119]. Grid-tied renewable energy systems enable the integration of various energy sources and loads into a single electrical system, which is typically connected to the main electrical grid. Power flow management in such systems is obtained by balancing generated power with electricity demand. Given the various forms of power generated by renewable energy sources, the power conversion process appears as an essential element of the electrical system [120]. Nowadays, solar and wind energy are recognized as the most prevalent and well-established renewable sources [121].

A) MPC for Power Converter

The MPC technique offers several benefits in controlling power electronics converters, including the ability to accurately capture system dynamics, making it a superior alternative

to conventional PID controllers. Digital processors have recently experienced significant improvements, which facilitate the implementation of MPC controllers to control power converter circuits in grid-connected systems. MPC technology offers several advantages in controlling switching circuits, such as fast response to system dynamics, precise searching, and simple implementation, which can make it the optimal solution for nonlinear regulation of power electronic converters [122]. MPC is a model-based predictive control system that utilizes a minimization function to regulate power converter variables in order to follow targeted values. The MPC mechanism is based on using a discrete-time model of the converter to assess the outcomes of the optimization function and select the optimal switching state that achieves the minimum error. During the prediction phase, MPC utilizes the discrete-time model to predict future values, which are subsequently compared with existing control variables to confirm the appropriate control action. The optimal switching state obtained by the minimization functions is used to operate the power converter circuit [123].

Power control plays a crucial role in grid-connected PV applications. The primary aim of regulating the AC power at the grid side is to ensure that the controlled variables align with the specified target values. Several control approaches can be employed to control the grid's real and reactive power using either stationary or d-q reference frames [124]. The prediction control strategy based on a stationary frame is utilized for regulating the active and reactive power of a grid-connected system, incorporating a feature for the cancellation of steady-state errors. A direct MPC controller is commonly proposed to handle the active and reactive power within a grid-connected system. This controlling mechanism directly modulates grid power by identifying the optimal switching state that minimizes error [125].

B) MPC Categories

MPC for power converters is often classified into two categories: CC-MPC and PC-MPC [126]. In the instance of CC MPC, a signal modulator is required to generate the switching states of the power converter. On the other hand, PC MPC operates on the assumption that the switching states are pre-established and integrated into the control stage. The application of PC MPC is dominant in power electronic circuits, primarily due to its requirement for a finite number of switching states to conduct the optimization function. The absence of a

modulation stage in PC MPC enables direct implementation of control actions to the power converters, which facilitates the control process [127]. In contrast to CC MPC, the incorporation of additional terms into the optimization cost function in PC MPC does not require a reconfiguration of the control system. However, a significant drawback of PC MPC is the difficulty in maintaining a constant switching frequency because of the absence of a modulator. Various strategies have been proposed to mitigate the issue of variable switching frequency by introducing additional control actions [128]. Figure 5.1 (a) describes the block diagram of CC MPC, illustrating that modulation occurs after the control action. Figure 5.1(b) represents the PC MPC approach, where both control action and modulation processes are assessed and resolved in a single stage. In this context, X^* denotes the system input, u represents the modulator input, y indicates the system output, and X represents the feedback signal.

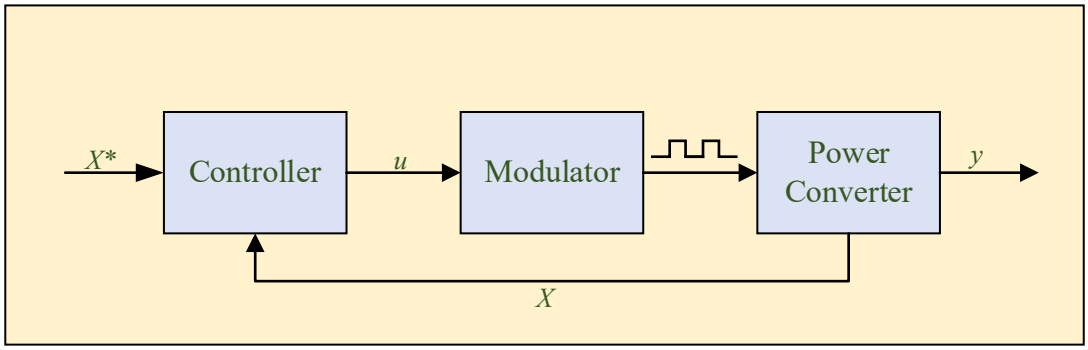

(a) CC Structure

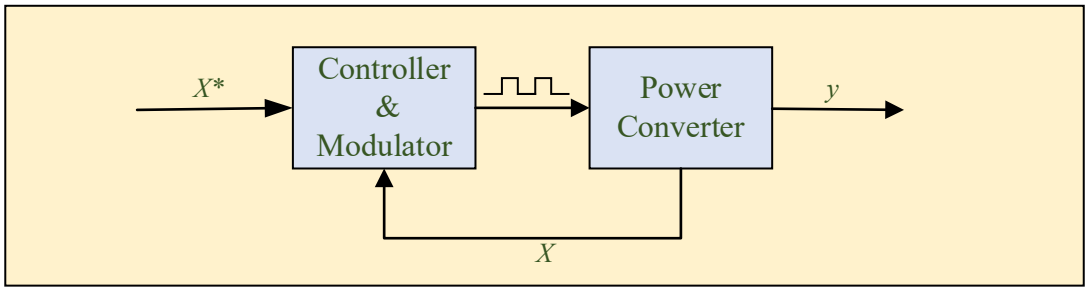

(b) PC Structure

Figure 5.1. MPC Controller Schemes

5.1.1 MPC Components for Power Converters

The MPC approach is often designed with some key components that are appropriately adjusted to match the needs of the targeted controlled system. The MPC components are

usually employed to effectively control power electronic converters and ensure optimal performance and efficiency. This section provides a comprehensive overview of the most commonly used MPC components employed to build the MPC for power converters [129].

a) Power Converter Model

The MPC approach relies on obtaining accurate discrete models of power converters. Accurately modeling power electronic converters enables the capture of the dynamic behavior of the power converter, which facilitates the straightforward implementation of the MPC controller. Deriving a precise discrete model is essential for implementing the MPC controller in the investigated system. The optimal switching state that achieves minimal error in the future is selected based on the MPC cost function of the power converter [130].

Power converter mathematical models of most power converters are characterized as continuous-time modules. In such systems, components like inductors and capacitors describe the dynamics of the power converter circuit. Therefore, the differential equations for inductor current and capacitor voltage are derived to describe most power converter circuits. The MPC approach requires a discrete-time model of the power converter to perform controlling actions and predict future values [131]. Therefore, for compatibility with discrete-time control methodologies, the continuous-time models must be converted into discrete-time representations. Various methods are available to change from continuous-time to discrete-time models [132].

Among these, the first-order forward Euler method stands out as one of the most widely approved techniques for discretizing power converter models. Two critical factors to consider when employing this method include the necessity for a sufficiently high sampling frequency to effectively approximate the continuous model and the absence of any filtering circuits within the system [133].

The fundamental equation of the first-order Euler method is presented below:

$$\frac{dx}{dt} = \lim_{t=0} \frac{x_{k+1} - x_k}{T} \tag{5.1}$$

By employing this technique, the estimated value for the subsequent time interval can be determined as follows:

$$x_{k+1} = x_k + T\left(\frac{dx}{dt}\right) \quad (5.2)$$

b) The MPC Cost Function

The MPC cost function can be employed in different forms, ranging from simple to complex, based on the requirements of the controlled system. Control designers often have the freedom to select the MPC cost function; however, the efficiency of the control system is significantly affected when a complex cost function is used [134]. Usually, the MPC cost function is expressed as a minimization problem that aims to minimize the error in the cost function. In the minimization function of the MPC control system, absolute or quadratic error values are commonly used to perform controlling actions, which can lead to an increased switching frequency. In the context of multi-objective cost functions, the error terms for different objective variables are cumulated, and the weighting factor is used according to the control system needs [135]. The equations provided below define the MPC cost function together with the methodologies for error calculation:

$$g = |x^* - x_n| \quad (5.3)$$

$$g = [x^* - x_n]^2 \quad (5.4)$$

$$\min\left(f_g[x^*, x_{pn}, S_n]\right) \qquad ,n = 1, \ldots\ldots, i \quad (5.5)$$

In this context, *g* represents the function used to minimize the cost function, *x** denotes the desired or target value, *x* indicates the measured actual value, and S_n denotes the state of switches.

c) The Objective Variables

In MPC, objective variables are generally represented within the cost function. The primary goal of this cost function is to ensure that the controlled variables follow their corresponding reference values. In the context of power converter applications, the inductor current is one of the most common controlled variables. It is common practice to employ cost functions with quadratic errors, which can effectively maintain the quality of current waveforms while minimizing the ripples in the current [136].

Voltage is another objective variable that is often regulated by the MPC technologies for power electronic applications. The voltage across the capacitors in the different power

converter topologies, which characterizes a part of the dynamics of power converters, is often selected as a key control variable in several converter designs [137]. The grid current and the output voltage are usually considered primary control objectives for grid-connected inverters when designing the MPC control system. The MPC methods are employed to regulate these variables, which can lead to a decrease in the complexity of control implementation while improving overall control performance [138]. Figure 5.2 illustrates the process of applying MPC control strategies to power converters.

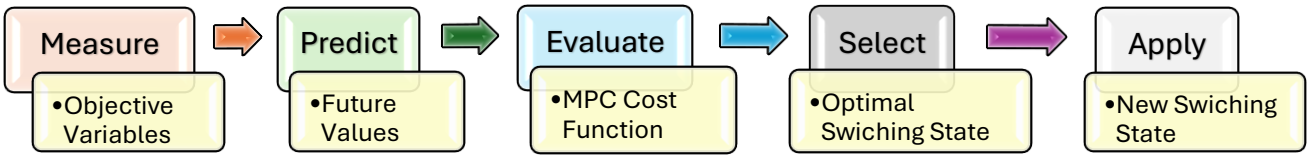

Figure 5.2. MPC process for power converters.

d) Parametrization of the MPC

Designing an MPC algorithm for power converter circuits requires considering the sampling frequency and the prediction horizon to construct the MPC control system accurately. In PC MPC methodologies, the absence of a modulator results in the switching operation occurring at different time intervals, leading to variable switching frequencies. Therefore, the stability of the grid-tied system, along with the quality of the modulated signal, is inherently linked to the duration of the sampling period [139].

The sampling time is directly proportional to the performance of the MPC controllers. Theoretically, the minimum required sampling frequency is twice that of the switching frequency; however, in practical applications, a higher sampling frequency is generally preferred to maintain the quality of the modulated signal. An appropriate discretization in the time domain can be achieved by maintaining a sampling-to-switching frequency ratio of approximately ten [140].

The computational complexity associated with MPC increases with extended prediction horizons and an increased number of control variables. Therefore, it is crucial to utilize

shorter prediction horizons when formulating MPC for power converters. However, specific applications require longer prediction horizons to capture system behavior accurately and correctly represent converter dynamics [141]. The computational complexity of the MPC algorithms is a concern for fast dynamic systems, including power converter systems. Therefore, proposing a new practical strategy for minimizing the computational burden while maintaining the stability of the investigated power converter topology is critical [142]. Table 5.1 provides an overview of general techniques employed to reduce the prediction horizon in MPC technology.

Table 5.1 Lowering Horizon Approaches

Reducing Horizon Method	**Computation Complexity**	**MPC Evaluation**	**Prediction Steps**	**Optimization strategy**	**Ref.**
Move Blocking	Medium	Online	Short & Long	Horizon division	[142]
Extrapolation	Medium	Online	Long	hysteresis bounds	[143]
Even Based	High	Offline	Long	Optimal Pulse Pattern	[144]

e) Tunning the Waiting Factor

The cost function of the MPC can include several control variables, which result in improved flexibility of the control system. However, the controlled variables have different levels of importance. Therefore, introducing the weighting factor becomes crucial to rank the variables according to their importance [145]. The objective variables of the MPC cost function can have a similar rank in some applications; thus, including the weight factor is unnecessary. On the other hand, when the terms have different characteristics, introducing weighting factors is essential to prioritize the most critical variables [146].

The weighting factors are not regularly necessary in the MPC system for the power converter topologies; however, they can significantly affect the control system functionality, particularly when the variables in the cost function vary in their level of importance. Ranking methods are commonly employed to assign weights for the different variables in the MPC cost functions for the power converter [147]. Several advanced strategies are available to

efficiently and accurately tune the weight factors [148]; however, their application in power converters is uncommon due to the internal complexity and time-consuming nature of these processes. On the other hand, analytical techniques for determining weighting factors offer a more direct and efficient option for controlling power converter systems [149].

The MPC optimization algorithms commonly include switching states, which are used for generating the gate signals for power converters. The microcontroller operates the MPC optimization algorithm to identify the optimal switching state that minimizes error. Algorithm (I) illustrates the standard PC MPC process, which is commonly used for regulating grid-connected power converters [150].

Algorithm (I): PV MPC Algorithm

Function MPC Power converter

1: measure (control variables)

2: $S_p = [\ Possible\ Swiching\ State]$

3: $for\ j = 1, 2 \ldots . DO$

4: Compute (inductor current equations), and(capacitor voltage equations)

5: Evaluate (Cost functions)

6: $if\ g < g_{\ Optimal}$

7: $j_{optimal} = j$

8: $g_{\ Optimal} = g$

9: end if

10: end for

11: $Current\ Switch\ State = State(\ j_{optimal})$

12: $End\ Function$

5.2 The Reduction of 2nd Order Harmonics with the MPC controller

In the two-stage grid-connected PV inverters, two power electronic circuits are commonly used. The DC-DC converter regulates the DC side of the PV system, maintaining a minimum current and voltage ripple, which helps in accurately obtaining the maximum power. The traditional strategy is based on employing one of the standard MPPT algorithms to determine the optimal voltage or current that achieves maximum available power from the PV system. The power switch operates according to the duty ratio from the MPPT algorithm [151]. The input power of the grid-tied PV system is DC power, while the output power is alternating power, which results in generating a double line frequency harmonic in the system. The decoupling capacitor is typically designed to store double-line frequency harmonics and ensure pure DC input power, as well as maintain an AC output power at the grid side. The DC-AC single-phase inverter adjusts the sign of the voltage output by controlling the switches of the H-bridge. In the two-level voltage inverter, three possible outputs can be obtained to generate alternating power at the grid side [152]. Figure 5.3 shows the typical two-stage grid-connected PV inverter based on single-ended primary-inductor converter (SEPIC) converter.

An MPC technique is employed for controlling the investigated grid-connected SEPIC

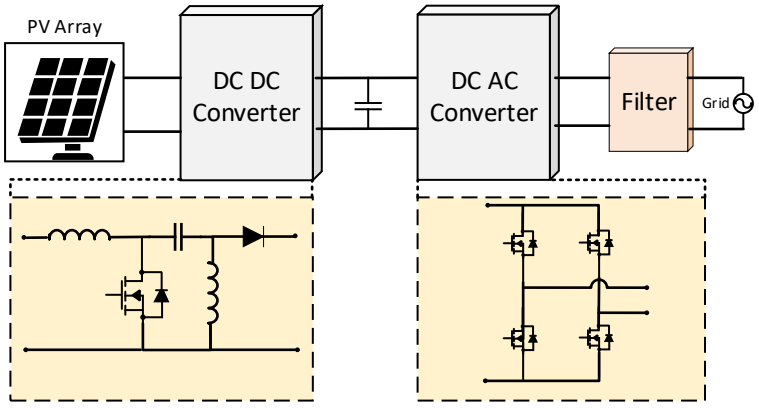

Figure 5.3 The two stages of SEPIC based inverter with VSI.

inverter, which includes two different control loops. The primary MPC controller is designed to regulate the DC power obtained from the PV source while simultaneously controlling the voltage across the decoupling capacitor. This dual MPC regulation enables optimal power extraction from the PV system while storing second-order harmonics in the decoupling

capacitor. Therefore, the conversion efficiency is significantly improved, and power extraction is increased. The control system is designed to regulate the controlled variables and ensure they follow the reference values, which helps in operating the PV system effectively.

The second controller is responsible for regulating the grid current and meeting the grid side requirements. Integrating a new system with the electrical grid can introduce new disturbances and lead to operating the system at different voltage and current levels, which can negatively impact the overall stability of the electricity grid. Regulating the grid-connected system to operate at the grid voltage and frequency is crucial for ensuring stable operation and protecting the grid-connected system against potential complications.

5.2.1 DC-DC SEPIC Converter Module

The differential equations at the DC-DC SEPIC converter side of i_{lx} and v_o can be calculated as follows:

$$\frac{d_{ilx}}{d_t} = \frac{1}{L_x}[\, vin - (vc_k + v_o).(1 - S_x)] \quad 5.6$$

$$\frac{d_{vc_o}}{d_t} = \frac{1}{C_o}[\, i_D.(1 - S_X) - i_o] \quad 5.7$$

Where i_{lx} is the inductor current from the PV side of the SEPEC-based inverter, v_o is the DC link capacitor voltage, S_X is the main switch of the SEPIC converter, i_D the current throws the diode, and v_{co} is the middle capacitor voltage.

Euler's forward method is employed to predict both the input inductor current and the middle capacitor voltage of the SEPIC converter in the future states as:

$$i_{lx}(k+1) = \frac{T_S}{L_X}[\, vin - (vc_k + v_o).(1 - S_x)] + i_{lx}(k) \quad 5.8$$

$$v_{co}(k+1) = \frac{T_S}{C_O}[\, i_D(1 - S_X) - i_o] + v_{co}(k) \quad 5.9$$

5.2.2 DC-AC VSI Inverter Module

The following equation can be used to obtain the conventional model of the output voltage for the grid-connected single-phase inverter:

$$v_{out} = L\frac{di}{dt} + R * i_{out} + v_{grid} \quad 5.10$$

The discrete-time model is crucial for designing the MPC control systems, and the Euler Forward method can be the most common discretization technique due to its effectiveness and simple implementation. The discrete-time model of the general output current equation is derived as follows:

$$i_{out}(K+1) = \left[\left(1 - \frac{RL}{T_S}\right) i_{out}(k) + \frac{T_S}{L}\left(v_{out}(K) - v_{grid}(k)\right)\right] \quad 5.11$$

Where $i_{out}(K+1)$ is the predicted value of the inverter current, $i_{out}(K)$ is the present value of the grid inverter, L is the inductor value, R is the equivalent value of the series resistance, $v_{out}(K)$ is the output voltage of the inverter, and $v_{grid}(k)$ is the grid voltage.

5.2.3 Second Order Harmonic Module

The voltage and current at the grid side can be expressed as:

$$Vg = vg\sin(wt - \emptyset) \quad 5.12$$

$$Ig = ig\ sine(wt) \quad 5.13$$

Then, the instantaneous power pumped to the utility network, $P_{g,}$ can be expressed as a product of the voltage and grid current as:

$$P_g = V_g . I_g \quad 5.14$$

$$Pg = P_{DC} + P_{AC} \quad 5.15$$

$$P_{DC} = \frac{v_g i_g \cos(\emptyset)}{2} \quad 5.16$$

$$P_{AC} = \frac{v_g i_g}{2}\mathrm{Sin}\left(2wt - \emptyset - \frac{\pi}{2}\right) \quad 5.17$$

The voltage and grid current in (5.10) and (5.11) can be used to determine the double-line oscillating part of the grid-connected PV inverter. The second part of the net cost function is used for regulating the voltage at the DC link capacitor. This voltage can be controlled to suppress the double-line ripples propagating to the input side of the PV inverter.

$$P_{AC}(t) + C_t v_{ct}\frac{dvc(t)}{dt} = 0 \quad 5.18$$

$$C_t v_{ct} \frac{dvc(t)}{dt} = \frac{vg.ig}{2} \text{Cos}\,(2wt - \emptyset - \frac{\pi}{2}) \quad 5.19$$

The oscillating part of the grid power contains the double line AC component; thus, the capacitor voltage can be expressed as:

$$v_{ct(t)} = VC_{DC} + VC_{AC}\, Sin(2wt + \delta) \quad 5.20$$

5.2.4 Cost Functions Formulation

The MPC in a power electronic converter is usually a minimization optimization strategy to reduce the error between the actual value and the predicted value of the state variable. Calculating the error values for the input current is based on the cost function of the SEPIC converter, which is described as follows:

$$g_a = |\, i_{lx}^*(k) - i_{lx}(k+1) \,| \quad 5.21$$

The proposed MPC strategy in this study is not only concerned with the error in the inductor input current of the SEPIC-based PV inverter but also aims to control the DC link capacitor voltage to maintain the efficiency of the MPPT and trap the double line frequency ripples. Thus, the next part is used to penalise the difference between the actual and predicted values of the DC link capacitor voltage.

$$g_b = |\, v_{co}^*(k) - v_{co}(k+1) \,| \quad 5.22$$

The grid current is penalised in the suggested MPC method, which ensures optimal system operation and improves the controller's performance. The third part of the MPC cost function is responsible for regulating the grid current, as illustrated below:

$$g_c = |\, i_{out}^*(k) - i_{out}(k+1) \,| \quad 5.23$$

The introduced MPC strategy consists of more than one term; thus, a weighting factor (λ) is required. λ is needed to prioritize between the different terms in the cost function. The heuristic approach presented in [153] was employed in this study to determine the optimal value of the weighting factor.

Hence, the total cost function can be written as follows:

$$g_T = ga + \lambda_a\, g_b + \lambda_b\, g_c \quad 5.24$$

The investigated control system for the SEPIC-based single-phase inverter includes two MPC loops. The controller on the input side utilizes the input current at the MPP as its reference. The inner controller predicts future output values by considering possible switching states and subsequently selects the optimal state that achieves minimum error. This determination regulates the ON/OFF state of the main switch in the SEPIC converter. The outer controller operates on the same predictive basis; however, it simultaneously manages the diagonal switches of the single-phase VSI according to the polarity of the output voltage. Furthermore, the MPC cost function is extended with an additional parameter, aiming to effectively decouple the second-order harmonic observed in single-phase inverter systems. A block diagram outlining the MPC control structure is illustrated in Figure 5.4.

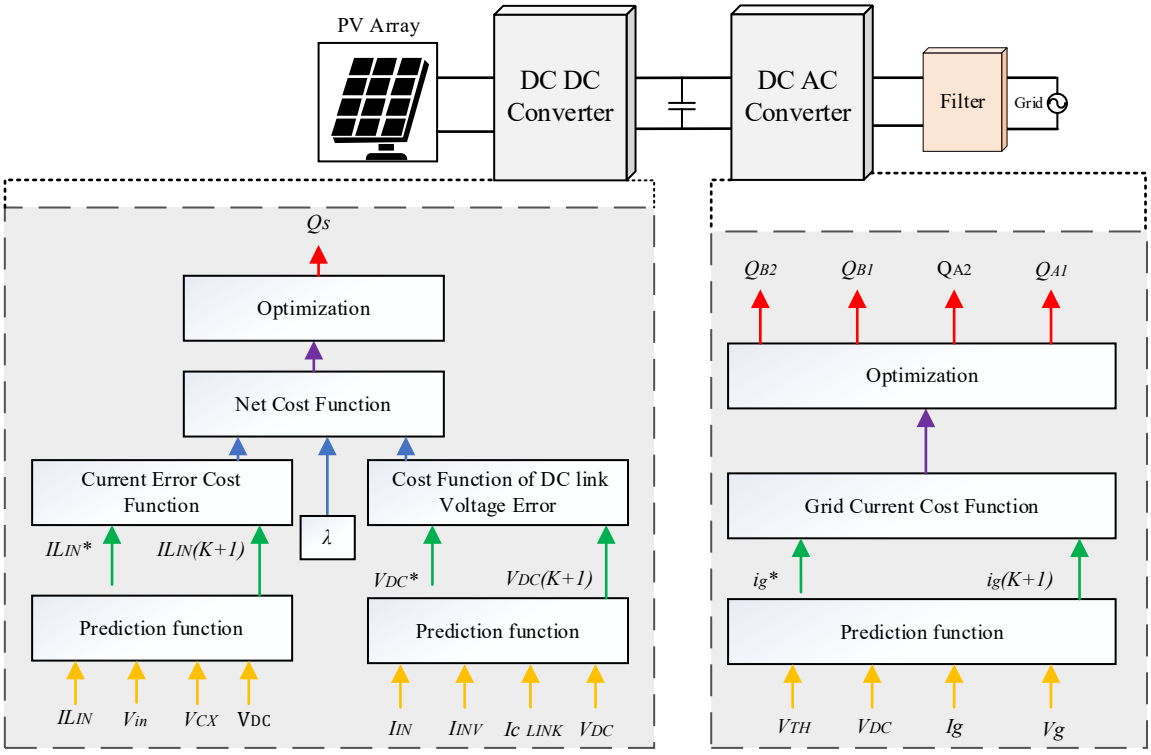

Figure 5.4 The block diagram of the MPC controlling structure of the SEPIC inverter.

The MPC techniques in a power electronic converter are usually a minimization optimization strategy to minimize the error between the actual value and the predicted value of the state variable. The grid-connected PV inverter with traditional MPC control suffers from large fluctuating ripples in the current output of the grid-tied inverter, resulting from the variable switching frequency associated with PC MPC. Therefore, operating the converter at a fixed

switching frequency can play a crucial role in minimizing ripples in the output current and enhancing power converter efficiency.

5.2.5 Simulation Results

The requirements related to the grid must be satisfied to prevent any problems on the distribution grid. The DC-AC inverter used in residential PV systems should incorporate a feedback control mechanism to effectively address variations and manage disturbances within the PV system. Typically, the primary focus in residential PV projects is on controlling the output current of the grid network. The transient phase exhibits fluctuations in grid current during the transient period; nevertheless, the system demonstrates an adequate settling time and a satisfactory level of stability.

The input current of the residential PV system should be pure DC with minimal fluctuations, which facilitates the function of the MPPT algorithm and improves the tracking process. Obtaining accurate MPP values leads to an increase in the converter efficiency and enhances power harvesting. Therefore, an additional PC MPC control system is necessary at the input side of the residential PV system. The primary objective of the current control system is to mitigate total harmonic distortion, with a particular emphasis on eliminating the second-order harmonic.

The study aims to evaluate the performance of the grid-connected PV system controller under sudden changes in irradiation levels. The grid current drops to 10 A at t = 0.28 sec as a result of the change in input current to examine the robustness of the control system. This situation has been investigated to observe the response of the MPC controller in changing the PV system dynamics. The microinverter controllers demonstrate a fast response to these changes and maintain the stability of the controlling system. The block diagram of the MATLAB/Simulink module of a single-module double-stage inverter is illustrated in Figure 5.5, and the response of the controlling system to these changes is displayed in Figure 5.6. It presents the behavior of the PV system when the grid current has a sudden drop. The controller demonstrates an effective response to such conditions, which leads to the absence of overshoot and a rapid settling time.

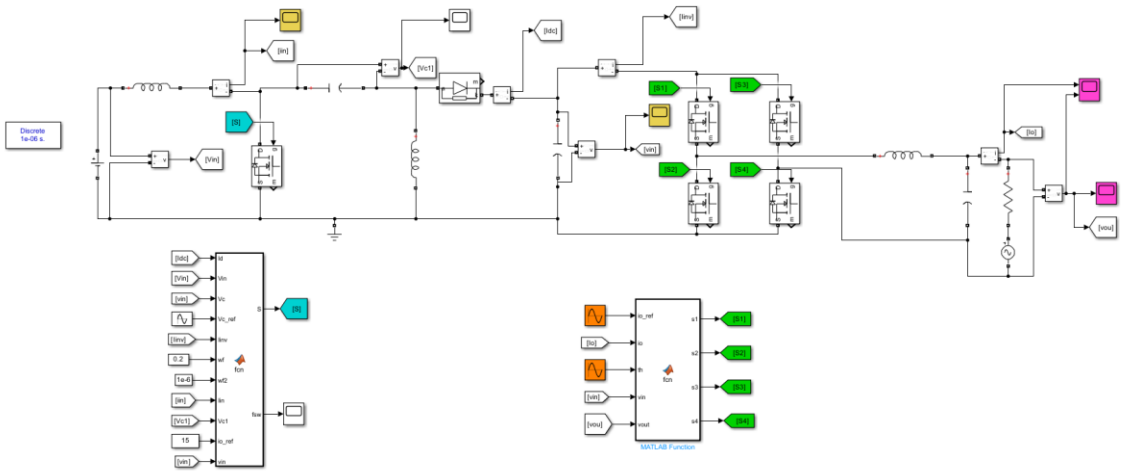

Figure 5.5 The Simulink block diagram of a single model two-stage inverter.

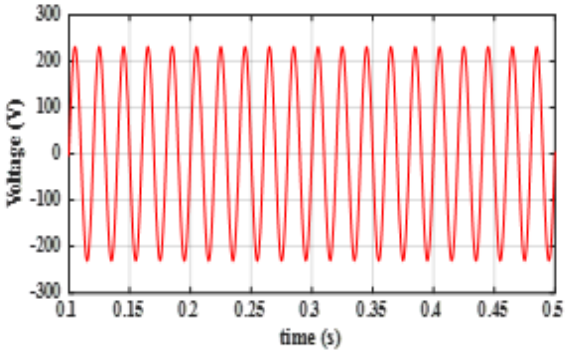

(a) Grid voltage

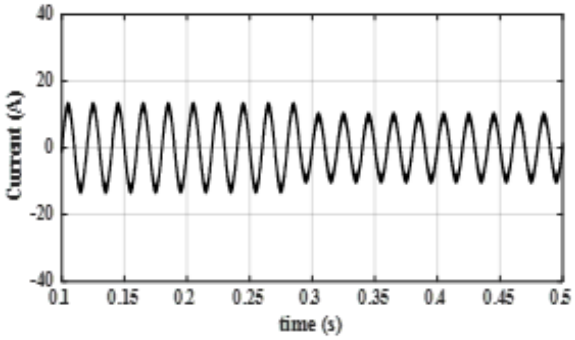

(b) grid current

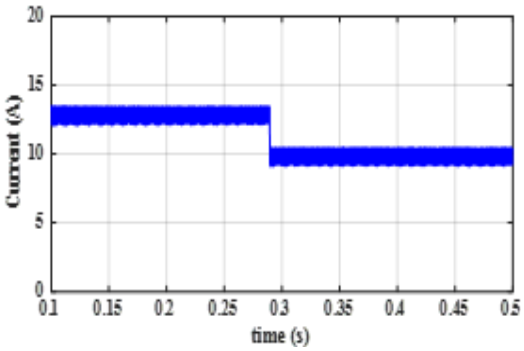

(C) Input current

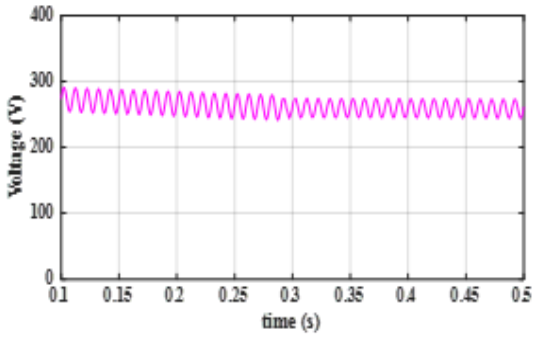

(d) Decoupling Capacitor voltage

Figure 5.6 The grid current and voltage waveforms with a sudden change in input current.

5.3 MPC Approach for Cascaded Electrical Configuration

The investigated electrical topology for grid-connected residential PV systems is illustrated in Figure 5.7. It represents a SEPIC-based grid-tied inverter where *n* subsystems are connected in series, with their output terminals linked to the electrical grid. Each subsystem is designed as a double-stage inverter, which consists of a DC-DC converter and a DC-AC inverter. A decoupling capacitor is placed between the two converters to perform the decoupling process. The subsystem in the proposed configuration contains a PV module and a battery system, designed to enhance the reliability of the grid-connected PV system.

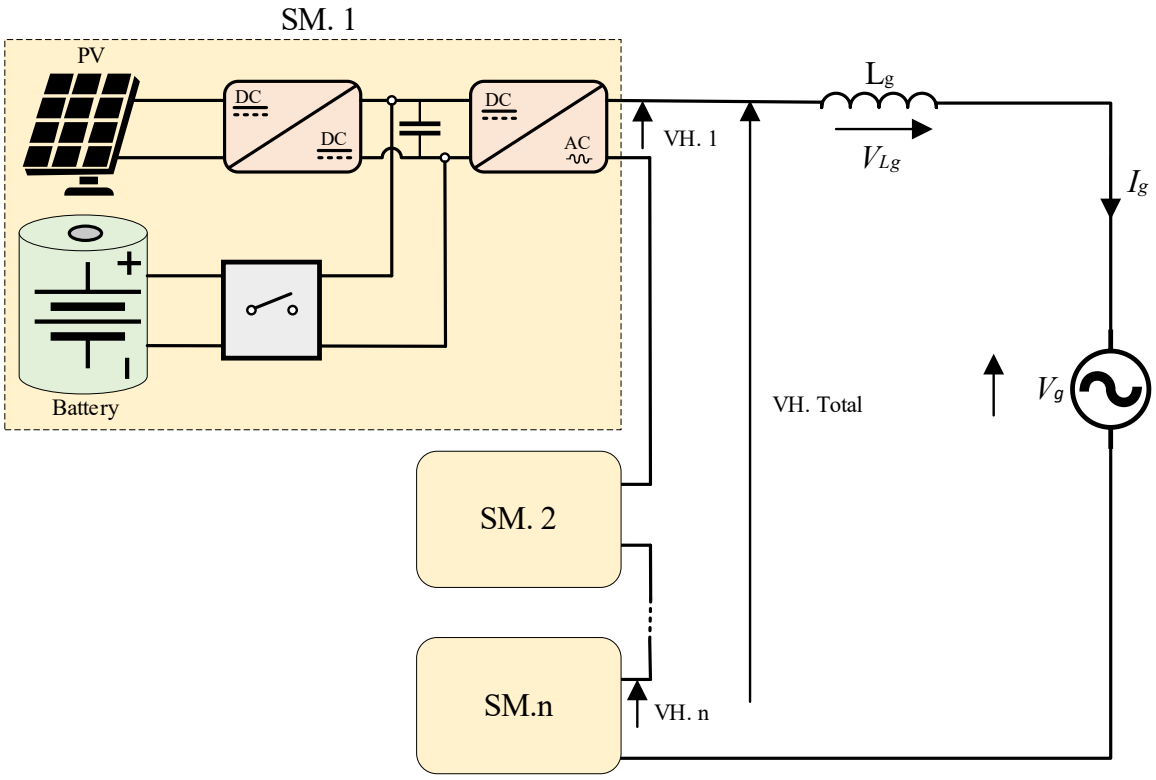

Figure 5.7 Block Diagram of the proposed cascaded electrical configuration.

5.3.1 Modular Level Operation

The first stage of the proposed system is a SEPIC DC-DC converter, which regulates the PV side and maintains a minimum ripple at the input current. The SEPIC DC-DC converter in the proposed electrical configuration operates at the MPP to enhance power production. The output power of the PV module is used to charge the battery or support the electrical grid. The battery of each subsystem is connected to the decoupling capacity by an SPDT and a single-direction diode. This configuration eliminates the need for an extra bidirectional converter, which is commonly associated with a significant loss. Figure 5.8 illustrates the internal structure of the subsystem that is used in the proposed electrical topology.

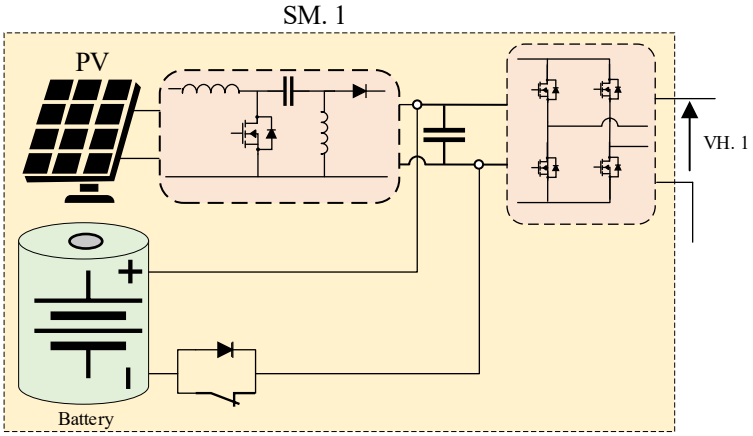

Figure 5.8 Complete view of the proposed cascaded configuration subsystem

5.3.2 The Proposed MPC Control System.

Operating the power electronic converters at a fixed switching frequency is crucial for maintaining the quality of the modulated signal and minimizing output signal ripples. In conventional PC MPC strategies, the power converters are operating at a variable switching frequency, resulting in large output ripples. In CC MPC approaches, this concern is solved; however, the control system becomes more complex, which reduces the performance of the PV system. Therefore, suggesting a practical PC MPC strategy that operates the power converter at a fixed switching frequency to improve output signal quality while maintaining the straightforward implementation of the controlling system is crucial.

A) Modular Level Control

Each inverter of the suggested cascaded electrical configuration has a modular controller, which maintains stable operation of the individual inverter. The modular control system consists of two parts to operate the DC-AC inverter effectively. The first part regulates the

input current from the PV module to harvest the maximum power while effectively trapping second-order harmonics in the DC link capacitor. The second part is responsible for regulating the output voltage of the module inverter. The mathematical formation is illustrated in the following subsections.

i) The DC-DC SEPIC Controller

The following equations are used to examine the different values of the duty ratio for the SEPIC converter to determine the optimal value.

The input current of the SEPIC converter can be calculated by the following differential equation:

$$\frac{d_{ilx}}{d_t} = \frac{1}{L_x}[\, vin\,.D\, - (v_{Ck} + v_o).(1 - D)] \tag{5.25}$$

In this context, *D* represents the power converter duty ratio, *Lx* is the inductor value, v_{in} is the voltage at the input side, v_{ck} is the voltage across the middle capacitor of the SEPIC converter, and v_o is the voltage at the output side.

The voltage at the DC link capacitor can be expressed by the following differential equation:

$$\frac{d_{vc_o}}{d_t} = \frac{1}{C_o}\left[\, i_D.(1 - D) - i_y\right] \tag{5.26}$$

The C_O is the value of the DC link capacitor, i_D is the current flowing through the diode, and i_y is the current passing to the VSI.

Euler's forward method is a common practical prediction method; therefore, it has been used to predict future values of the SEPIC input current and the DC link voltage.

The prediction equation for the input inductor current is expressed as:

$$i_{lx}(k+1) = \frac{T_S}{L_X}[\, vin\,.D - (vc_k + v_o).(1 - D)] + i_{lx}(k) \tag{5.27}$$

The minimization function of the input inductor current is described as:

$$g_a = |\, i^*_{lx}(k) - i_{lx}(k\ + 1)\,| \tag{5.28}$$

The prediction equation for the DC link voltage is expressed as:

$$v_{co}(k+1) = \frac{T_S}{C_O}[\, i_D(1-D) - i_o] + v_{co}(k) \quad 5.29$$

The minimization function of the DC link capacitor is described as:

$$g_b = |\, v_{co}^*(k) - v_{co}(k+1)\,| \quad 5.30$$

The optimization function for the PV system side can be expressed as follows:

$$g = |\, i_{lx}^*(k) - i_{lx}(k\ +1)\,| + \lambda_a\,|\, v_{co}^*(k) - v_{co}(k+1)\,| \quad 5.31$$

Where λ_a is the weighting factor obtained by the heuristic method in [154]

ii) The DC-AC VSI Controller

The following standard equation can calculate the optimal value of the duty ratio for the grid current:

$$v_{out} = L\frac{di}{dt} + R * i_{out} + v_{grid} \quad 5.32$$

The Euler's forward method is also used to forecast the future values of the grid current, as illustrated below:

$$i_{out}(K+1) = \frac{T_S}{L}\left[\left(\frac{L}{T_s} - R\right) i_{out}(k) + \left(v_{out}(K) - v_{grid}(k)\right)\right] \quad 5.33$$

Where:

$$v_{out} = v_{dc}.(2d\ -1\,) \quad 5.34$$

The optimization equation for the grid is expressed as follows:

$$g = |\, i_{out}^*(k) - i_{lout}(k\ +1)\,| \quad 5.35$$

The proposed control algorithm stabilizes the switching frequency by continuously assessing the duty ratios of the investigated PV inverter. The MPC algorithm begins by measuring the controlled variables of the grid-connected SEPIC inverter to perform the controlling actions. The algorithm examines different values of the duty ratio; this proposed method sticks to ten possible switching states to minimize the computational burden. Examining various duty ratio values can lead to better results; however, this approach is associated with implementation challenges for the DSP controller. The duty ratio with minimum error is sent

to the modulator to generate the gate signals for the converter switches. The proposed control algorithm stabilizes the switching frequency by continuously modifying the duty ratio of the investigated PV inverter. The proposed algorithm used to fix the switching frequency of a conventional PC MPC is illustrated in Algorithm II.

Algorithm (II): PV MPC Algorithm

Function (MPC SEPIC Inverter)

1: measure (Controlled values)

4: S_D = [***Possible Swiching State at Diffrent Values of Duty Ratio***]

5: $for\ j = 1, 2 \ldots . DO$

6: $Compute\ (5.27), (5.29), and\ (5.33)$

7: $Evaluate\ (5.31), and\ (5.35)$

8: $if\ g < g_{Optimal}$

9: $j_{optimal} = j$

10: $g_{Optimal} = g$

11: $end\ if$

12: $end\ for$

13: $Current\ Switch\ State = State(j_{optimal})$

14: $End\ Function$

B) System Level Control

The primary function of the grid-side control system is to send the extra active power from subsystems of the proposed configuration at unity power factor and high conversion efficiency to meet the grid-side requirements. The string current of the proposed cascaded configuration is common for all subsystems; thus, a single current controller is required to regulate the grid current. The subsystem voltages of the suggested electrical configuration become the controlling variables to equalize the output power of the subsystems during unbalanced power generation. The PR controller is commonly used to control the alternating signals because it can provide an infinite gain at the targeted frequency. In the proposed system, the resonant frequency of the PR is adjusted to match the grid frequency to reduce the steady-state error in the grid current. The controller that is used to effectively regulate the proposed cascaded electrical configuration is illustrated in Figure 5.9.

$$V_S = V_g + R_g I_g \sin(\omega t + \alpha) + \omega L_g I_g cos(\omega t + \alpha) \quad 5.36$$

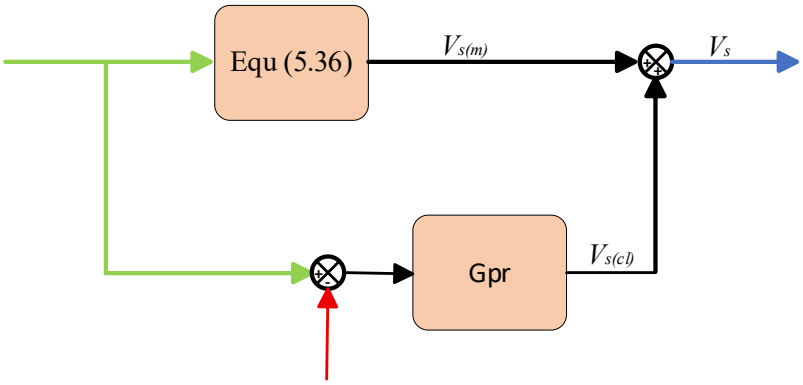

Figure 5.9 The controlling system of the cascaded electrical configuration

The block diagram illustrates the current controller employed to regulate the output voltage VS of the proposed electrical configuration, utilizing a PR feedforward controller. The measured grid current I_g feeds two paths, one passes to the equation (5.36) to calculate the cascaded module voltage $V_{s(m)}$. The second path compares the value of the current with the reference to generate the error signal. The error signal is fed to the PR controller, which is designed to minimize the error in grid current. The output of PR controller $V_{s(cl)}$, which adds to equation (5.36) to represent the corrected output voltage. The output voltage from the equation is often not accurate due to changes in system parameters. Therefore, the PR controller is employed to handle parameter variation issues.

5.3.3 Simulation Results

The proposed cascaded electrical configuration has been modeled and examined to confirm system functionality. MATLAB/Simulink software is used to simulate the proposed electrical topology and study the system's performance. The MATLAB/Simulink block diagram of the examined electrical configuration is illustrated in Figure 5.10, and the parameters used in the simulation are listed in Table 5.2. In simulation software, passive components are assumed to be ideal; therefore, the internal resistance of inductors, capacitors, and switches is neglected. The investigated electrical configuration has three cascaded inverters, each one integrated with a BESS that is connected to the DC link capacitor terminal. The output current of the three subsystems is the same since they are connected in series. Therefore, the voltage output of the subsystems becomes the controlling

objective. The power of the second inverter of the cascaded system is interrupted to investigate the robustness of the proposed configuration against disturbance.

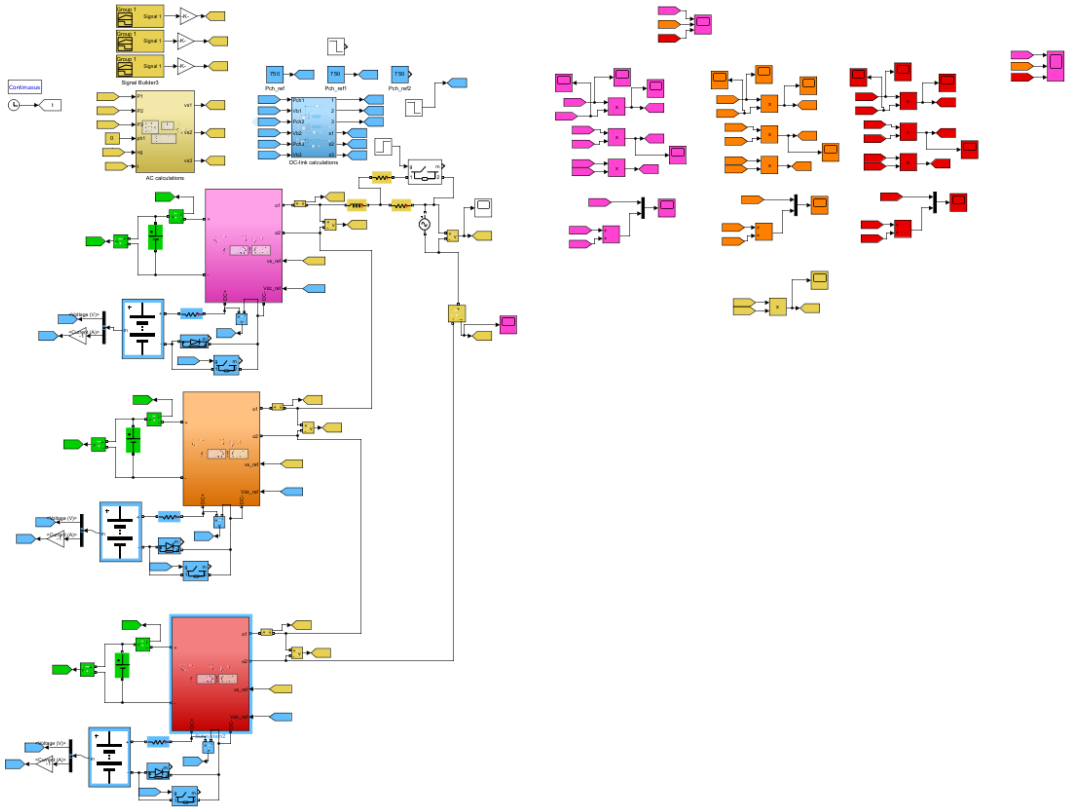

Figure 5.10 The MATLAB/Simulink block diagram of the cascaded electrical system

Table 5.2 Parameters of the MATLAB/Simulink model

Parameter	Value
No. of modules	3
SM rated power	2.5 kW
SM inductors	L_1 =1.5 mH and $L_{2=1}$ mH
SM capacitors	C1 =10 µF, C2= 10 µFand C_{dc} =100 µF
SM switching frequency	20 KHz
Transformer turns ratio	1
Battery pack voltage	100 V
Grid frequency	50 Hz

a) Case study I: Power Balancing

The power output of the first inverter of the proposed cascaded configuration starts with a rapid increase from zero and reaches its maximum power of 2500 W at 0.1 seconds, demonstrating a swift transit time. After that, the power reached a steady state condition, where it oscillates between 0 and its maximum power. Figure 5.11 illustrates the output power from the first double-stage inverter.

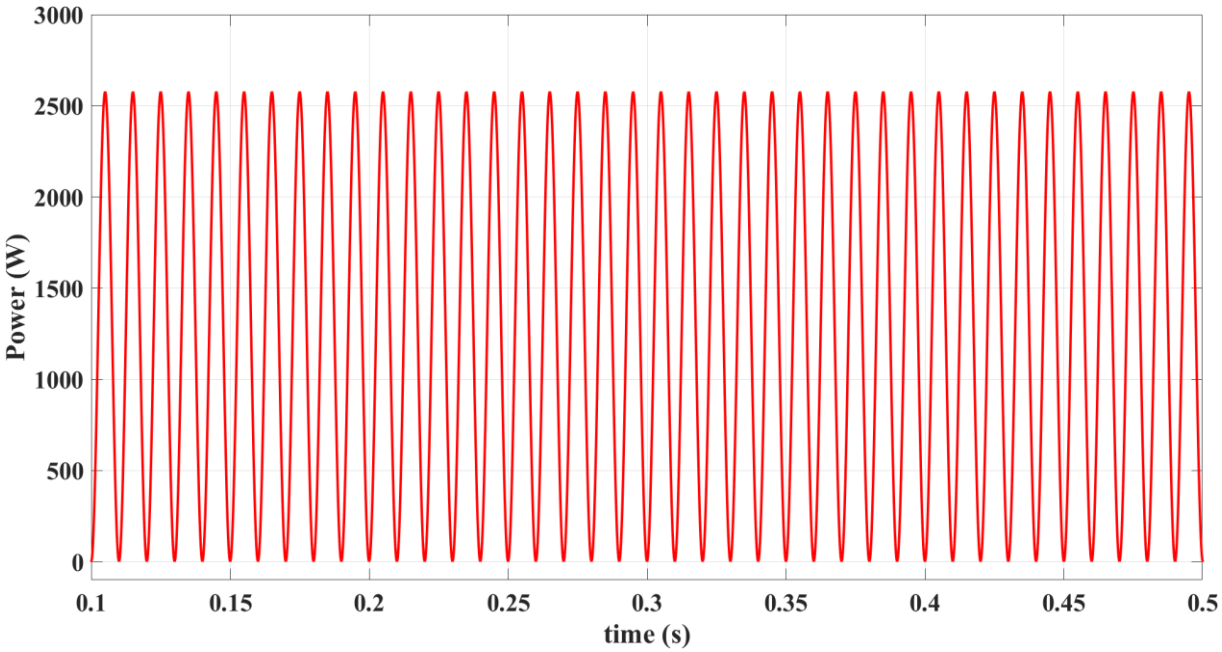

Figure 5.11 The output power from the 1st inverter in the cascaded electrical configuration.

The output power from the battery of the first inverter of the cascaded system is shown in Figure 5.12. The DC power from the battery system starts from 750 W and remains constant with time. The battery power is demonstrating a positive value, which means the electrical system is charging the battery.

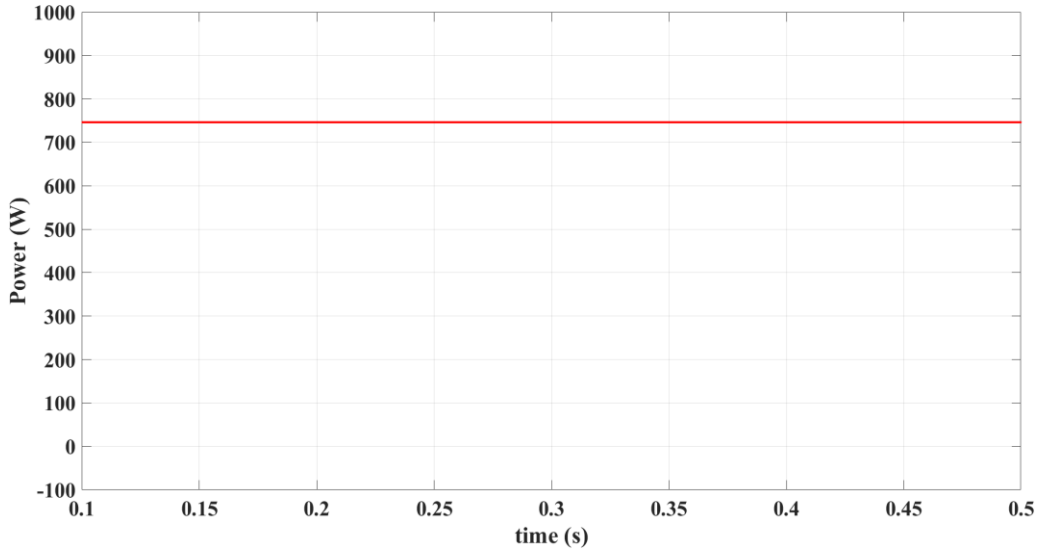

Figure 5.12 The battery power at the 1st inverter of the cascade system.

The power waveform of the second inverter of the cascaded electrical system is illustrated in Figure 5.13. The power waveform clearly shows three different operation regions. In the initial stage, the power begins from zero and rapidly reaches its maximum power. The output power drops after a few seconds to reach 1800 W to examine the robustness of the proposed system. After one second, the system was able to recover and reach its maximum power. In Figure 5.14, the DC power from the battery remains unchanged with a positive value, indicating that the battery is still charging and the system can recover without discharging the battery at the second inverter.

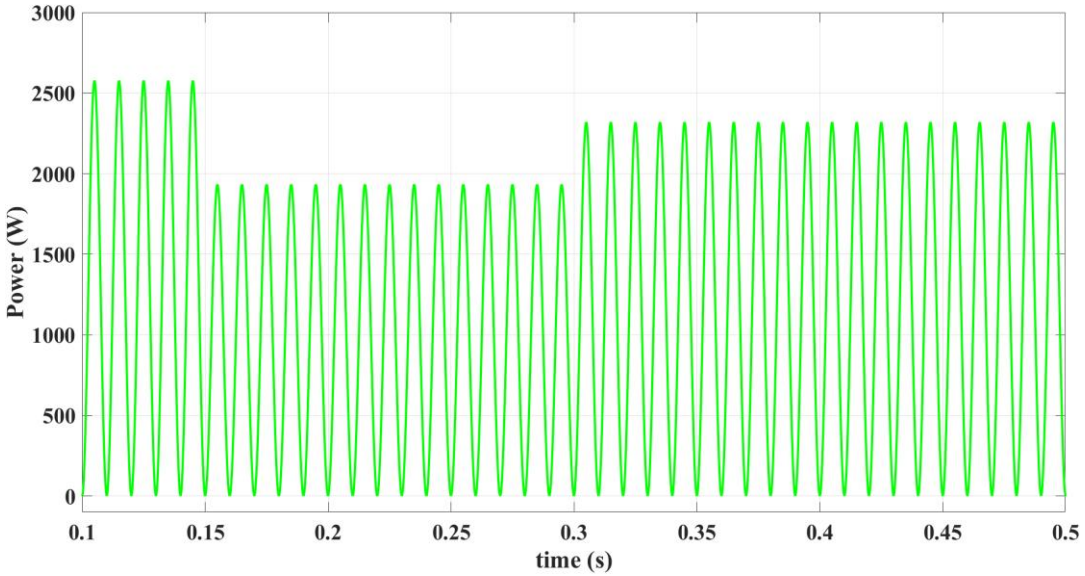

Figure 5.13 The output power from the 2nd inverter in the cascaded electrical configuration.

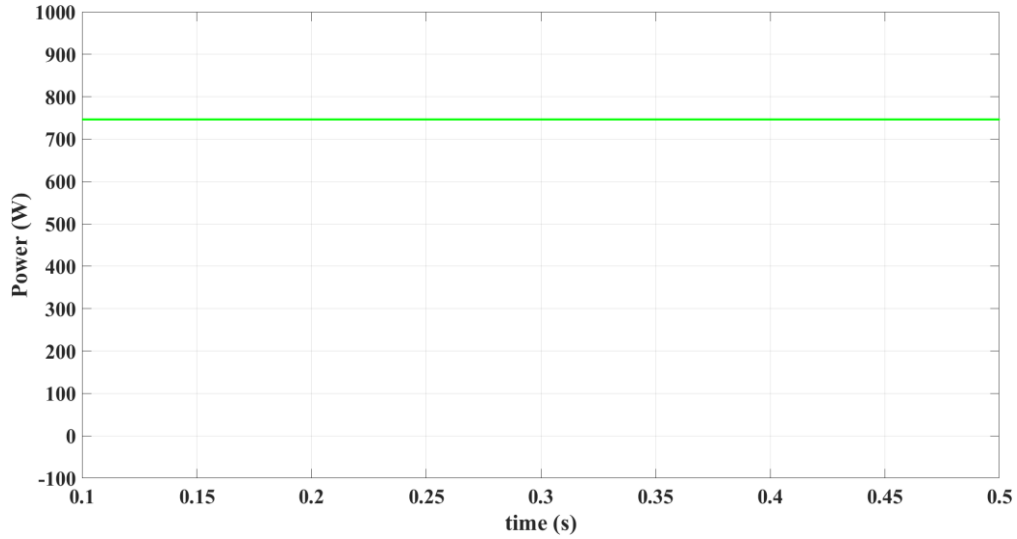

Figure 5.14 The battery power at the 2nd subsystem.

The power of the third inverter of the investigated cascaded electrical configuration is illustrated in Figure 5.15. This subsystem responds to sudden changes in power in the second cascaded inverter. The power starts to increase at 0.45 seconds, then returns to nominal power at 1 second. The power of the third cascaded inverter increased by increasing the voltage of the same inverter to resolve the voltage drop of the second inverter. Figure 5.16 illustrates the power of the battery of the third cascaded inverter. The battery starts charging before the power at the secondary two-stage inverter drops, then the battery begins discharging to maintain the normal operation of the investigated grid-connected electrical configuration.

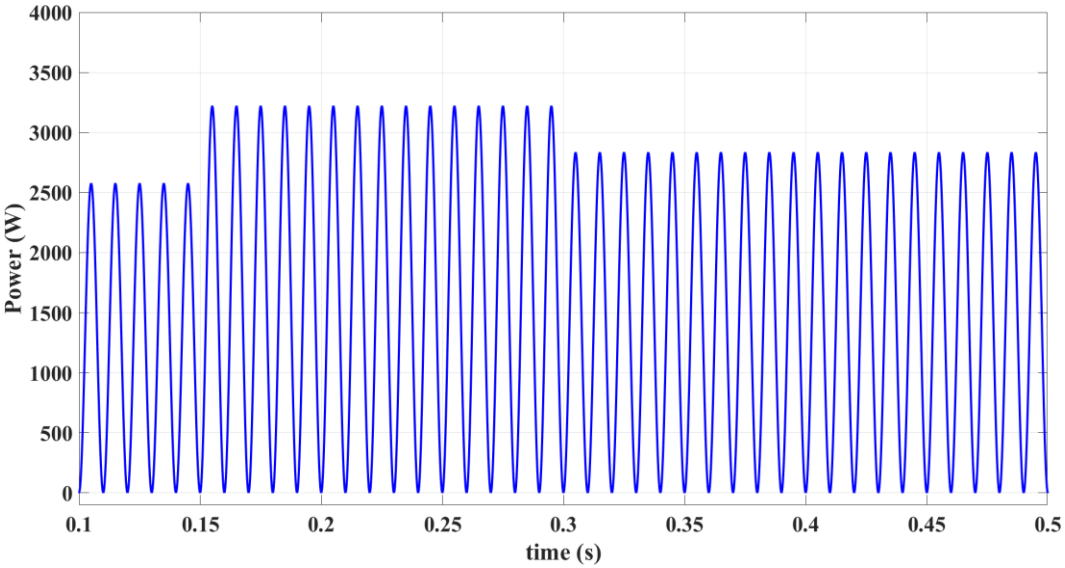

Figure 5.15 The output power from the 3rd inverter in the cascaded electrical configuration.

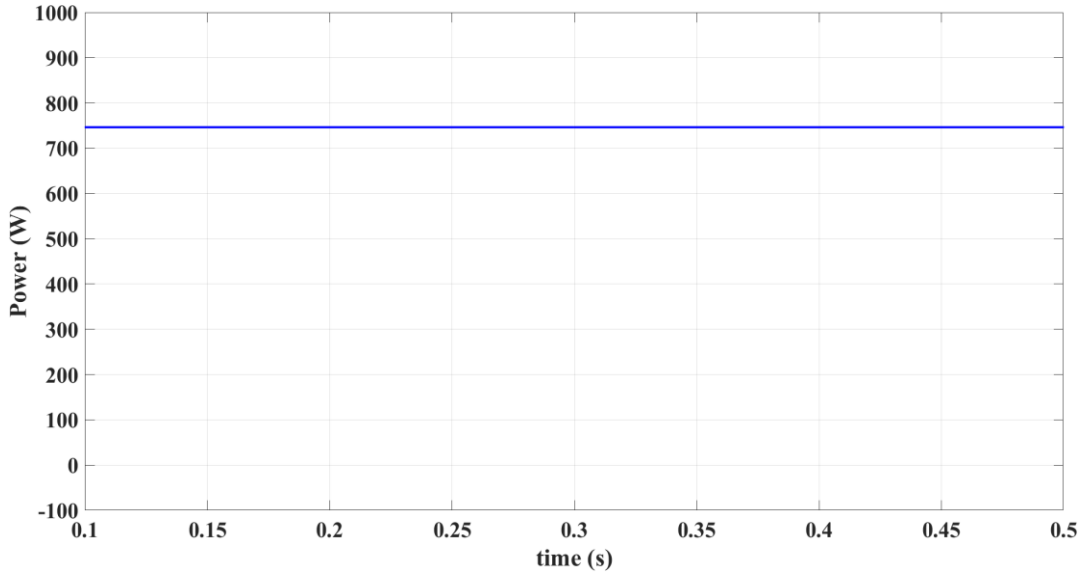

Figure 5.16 The output power of the battery at the 3rd subsystem

The output power at the grid should be the summation of the power from three cascaded inverters, as illustrated in Figure 5.17. The power starts from zero and reaches its maximum at 7,500 W, then continues to fluctuate without change, demonstrating the system's capability to handle sudden disturbances.

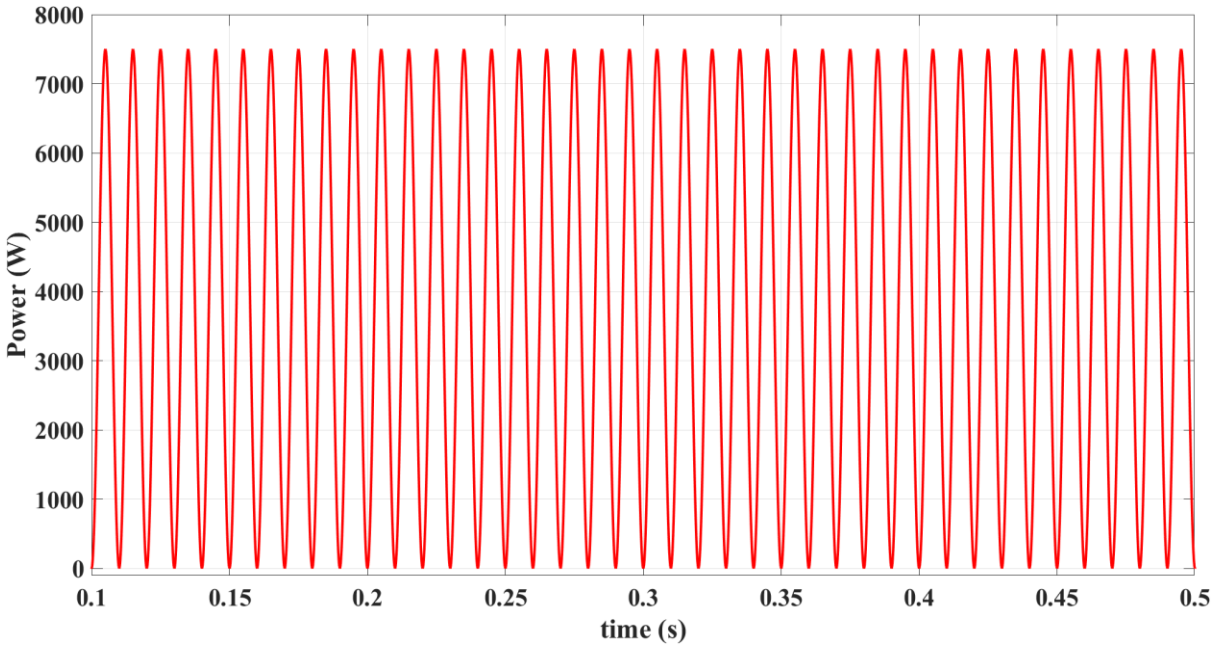

Figure 5.17 Total output power from the proposed cascaded electrical configuration.

b) Case study II: PS

In this scenario, the input power of the first SM drops by about 20% at t =0.5 sec, and the shading continues for the rest of the simulation as illustrated in Figure 5.18. The battery at the first SM responded to this change in the power and started discharging after the first second, as shown in Figure 5.19.

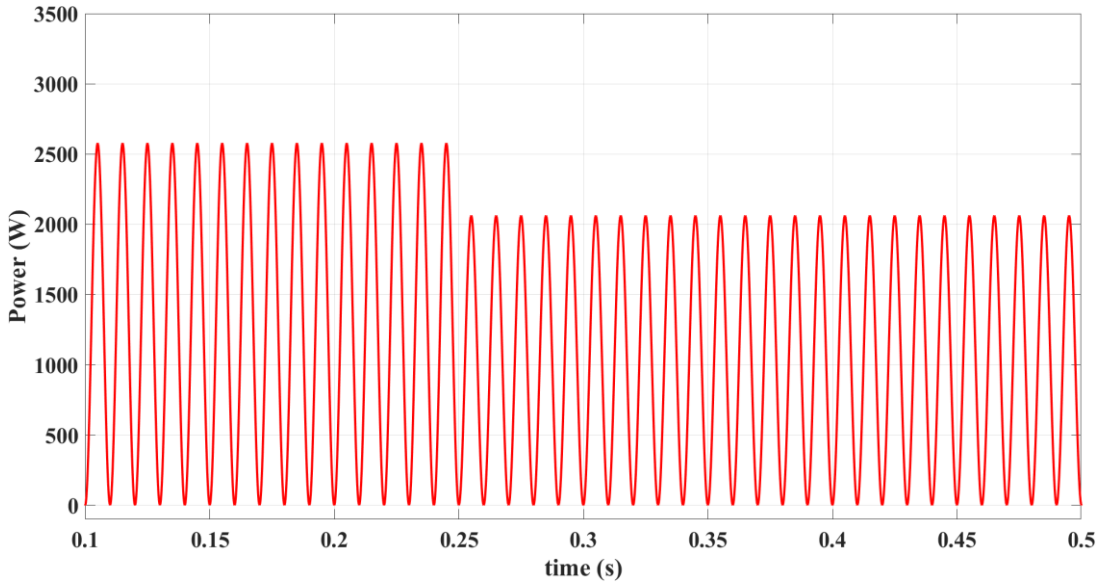

Figure 5.18 The power of the first SM under the effect of PS.

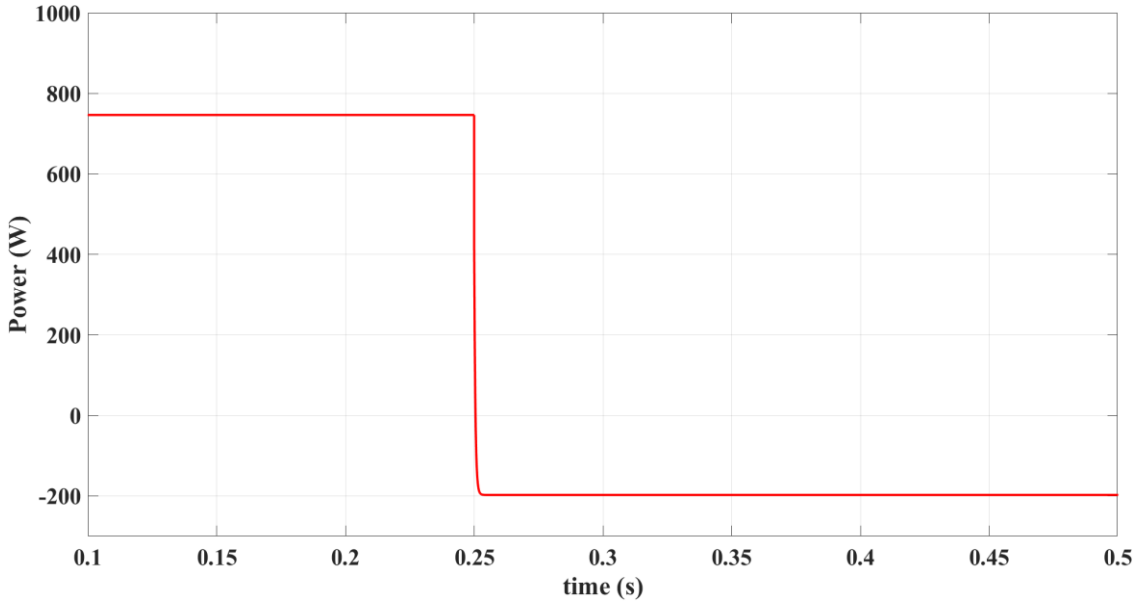

Figure 5.19 The battery power of the first SM under the effect of PS.

The second SM handles this drop and increases its power generation by 20 % at t = 1 sec. The battery at the second SM is continuously charging because the system can handle the change in power without discharging the battery. The change in the output power of the second SM is shown in Figure 5.20, and the battery charging power is illustrated in Figure 5.21.

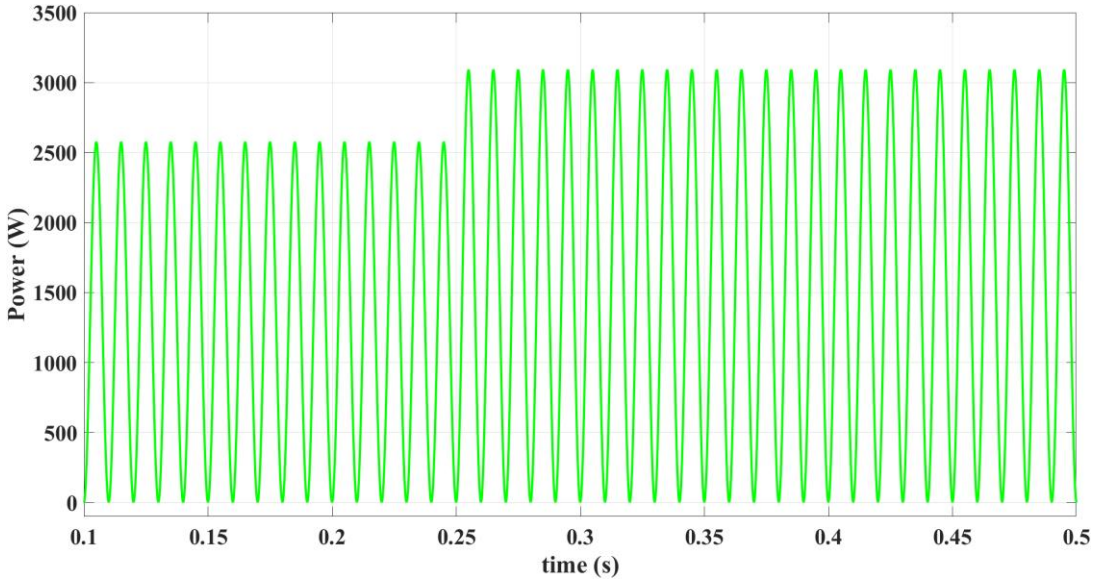

Figure 5.20 The second SM behavior under the effect of PS on the first SM.

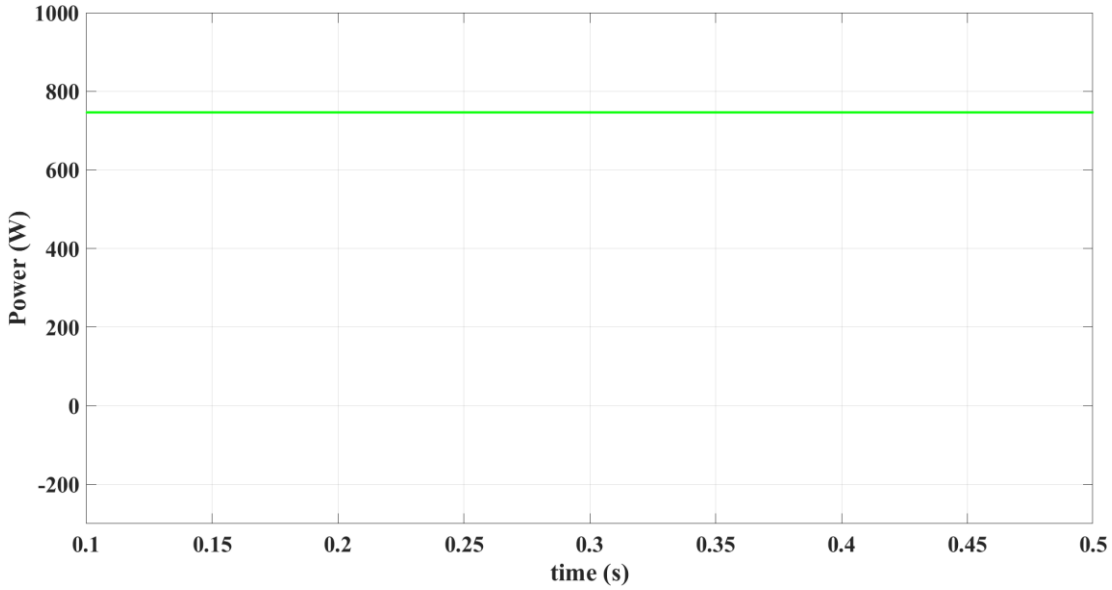

Figure 5.21 The battery power of the second SM when the first SM's power drops.

The power of the third SM of the investigated cascaded electrical configuration gradually increases until it reaches its maximum power of 2500 W, and then it enters the steady state

condition without any change in the power output. The battery at the third SM continues charging with 750W. Figure 5.22 shows the output power of the first SM, and Figure 5.23 illustrates the battery charging power.

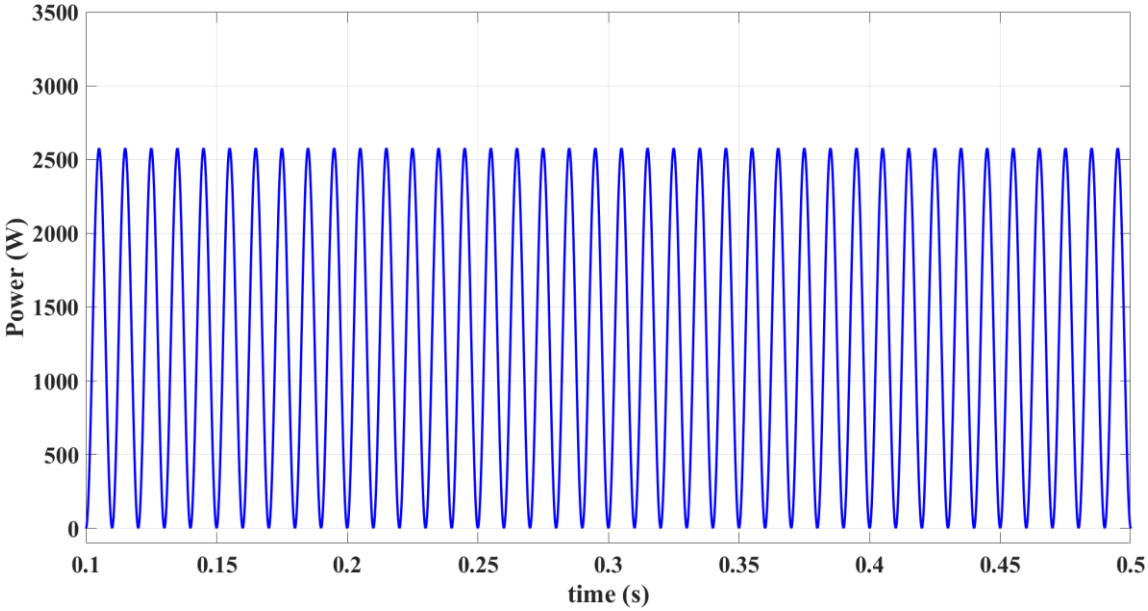

Figure 5.22 The third SM output power when the first SM is shaded.

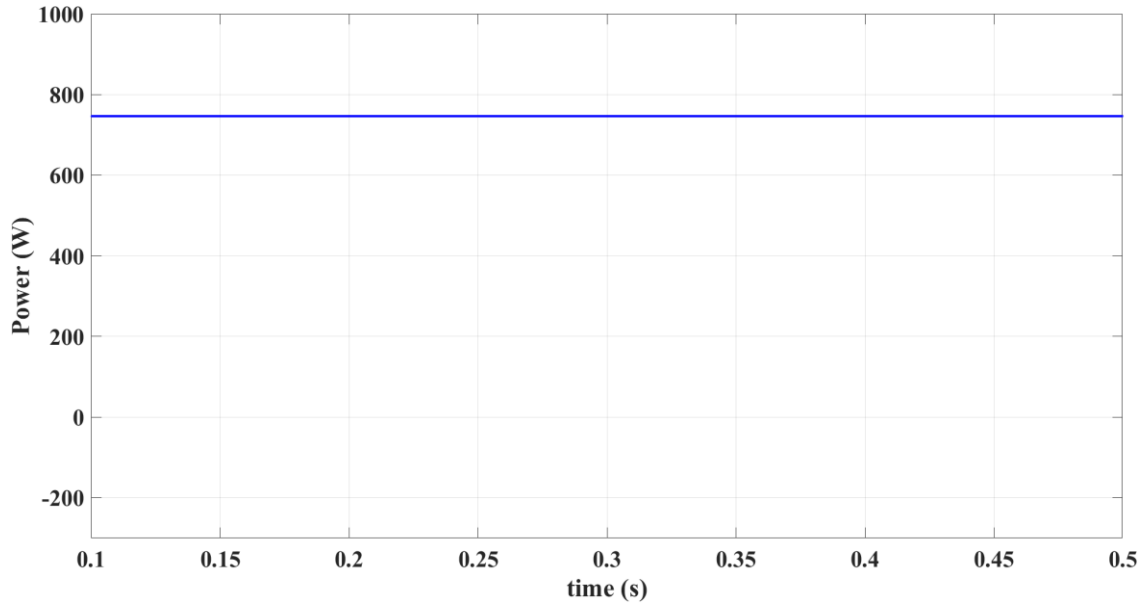

Figure 5.23 Battery power of the third SM when the first SM suffers from PS.

c) Case study III: Investigation of the system Controller

The block diagram in Figure 5.9 illustrates the current controller employed to regulate the output voltage V_S of the proposed electrical configuration, utilizing a PR feedforward controller. The measured grid current I_g feeds two paths; one sends to equation (5.36) to calculate the cascaded module voltage $V_{s(m)}$. The second path compares the value of the current with the reference to generate the error signal. The error signal is fed to the PR controller, which is designed to minimize the error in grid current. The output of PR controller $V_{s(cl)}$ adds to the output of equation (5.36) to represent the corrected output voltage. The output voltage from the equation is often not accurate due to changes in system parameters. Therefore, the PR controller is employed to handle parameter variation issues.

In normal operation, the open-loop calculation of the system parameters can be used to determine the voltage of the cascaded system, as demonstrated in equation (5.36). However, the system parameters, including grid resistance, may deviate due to several factors, such as increased temperature or variations in grid inductance. Therefore, incorporating a feedforward PR controller to handle these variations is crucial for maintaining the system's efficiency. The proposed PR controller in this study is designed to correct errors in the calculations and adjust the response according to the system requirements. Figure 5.24 illustrates the negative impact of changing system parameters on the output power of the proposed electrical system.

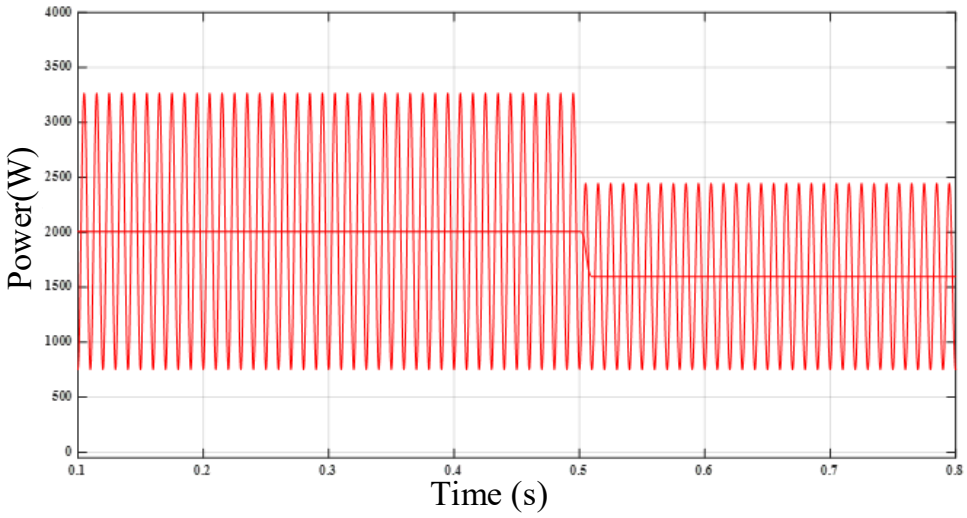

Figure 5.24 The drop in output power of the electrical configuration due to parameter changes.

The system parameters are interrupted by increasing the grid system resistance by 0.1 Ω to examine the controlling system functionality. Figure 5.25 illustrates the response of the system controller to a change in grid resistance. At t = 0.51 sec, the system interrupted, and the controller started responding to this error. The system takes 0.2 sec to resolve the issue and keep the grid current at its reference value.

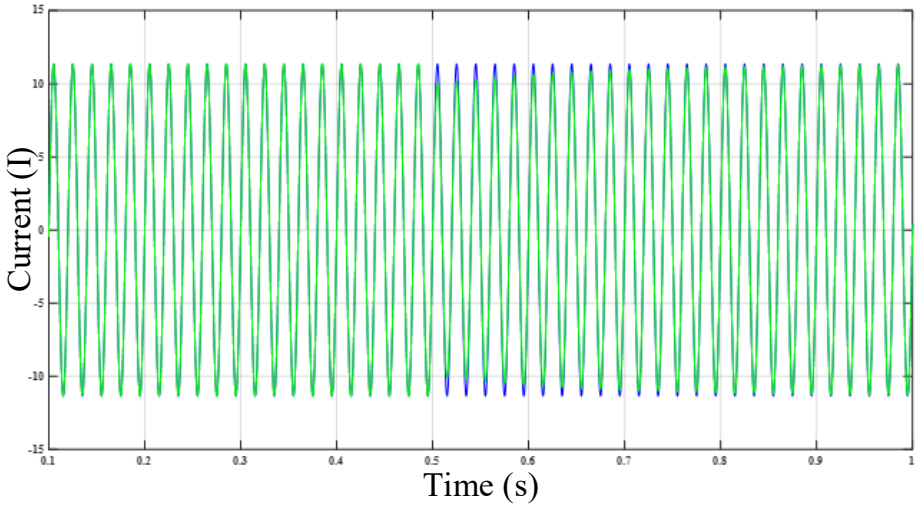

Figure 5.25 The response of the system controller.

The proposed feedforward PR controller is designed to maintain the normal operation of the electrical system. Therefore, the change in the controlled signal can be incremental or decremental according to the system's needs. Figure 5.26 illustrates the operation of the proposed PR controller. At the beginning, the system works correctly, thus there is no need for controlling action. At t = 0.51 sec, the controller is working to deal with the error in the grid current.

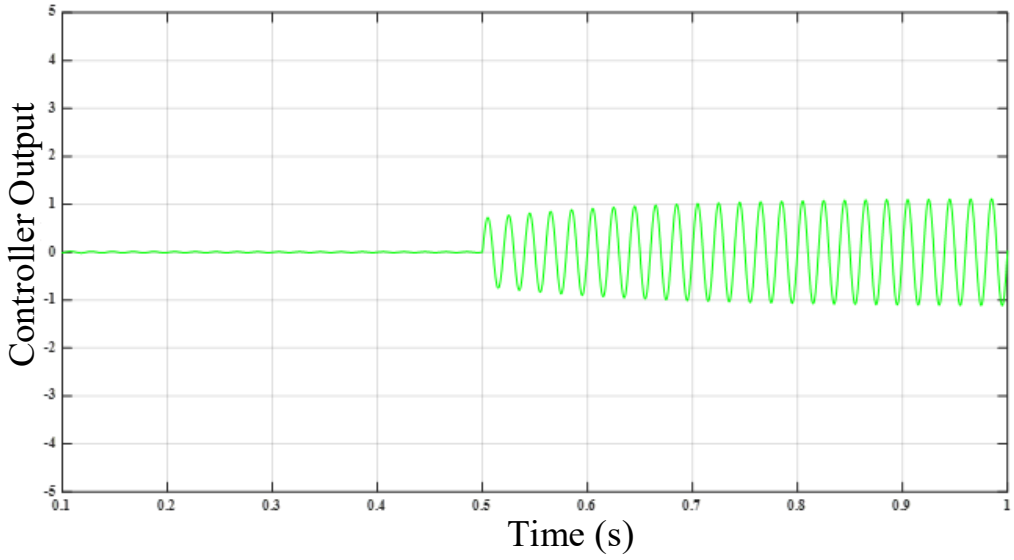

Figure 5.26 The PR controller output

5.3.4 Experimental Validation

The experimental validation and selection of the experiment components are explained in this section. A scale-down prototype of the proposed cascaded electrical configuration with integration with the utility grid is conducted to validate theoretical analysis and simulation results. Two cascaded inverters are cascaded to build the investigated electrical configuration. In this study, two DC voltage suppliers have been utilized to simulate PV modules.

The experimental setup for the investigated electrical configuration with the proposed control system is illustrated in Figure 5.27. It has been controlled by the TMS32028379 DSP with parameters in Table 5.3. DC sources were used in this study to represent the PV modules to examine the validity of the suggested electrical topology. Each subsystem was integrated with a battery energy system at the DC link point to enhance the reliability of the investigated system. The battery configuration is illustrated in Figure 5.28. The battery system is regulated by a battery regulation system that regularly monitors the battery parameters, including current, voltage, and temperature of the battery cells. This monitoring system is crucial for maintaining the safe operation of the electrical system in this study.

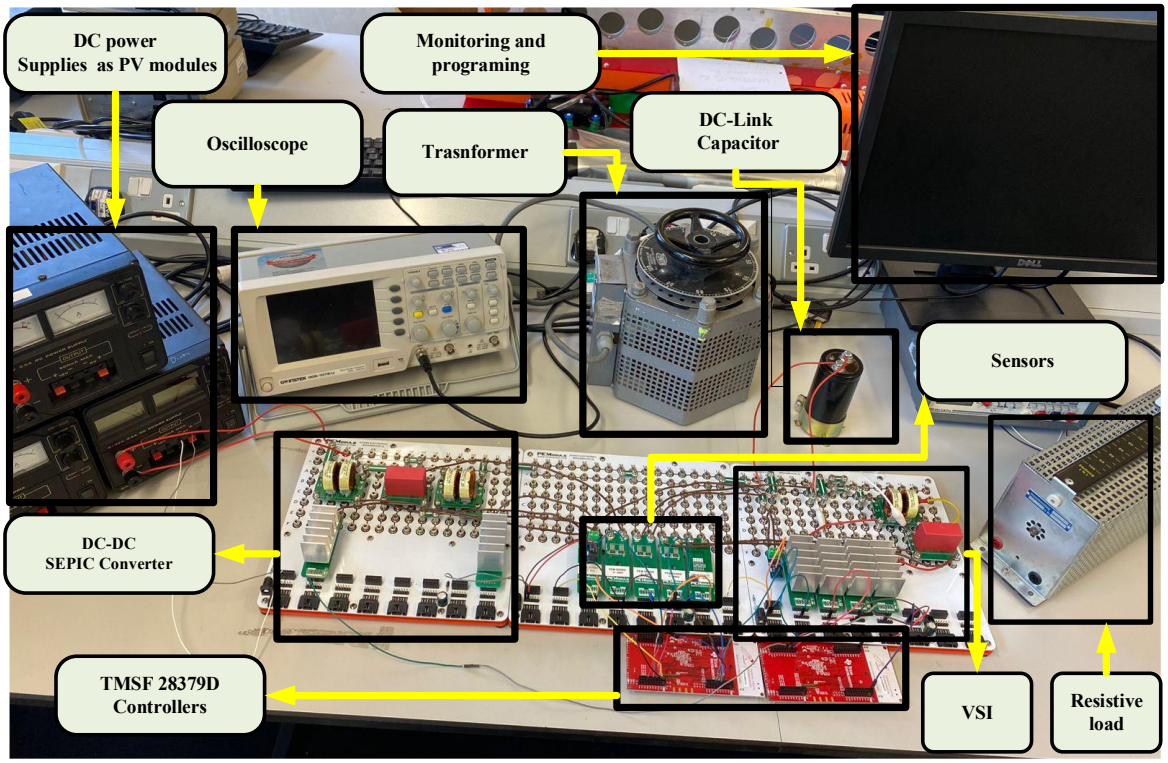

Figure 5.27 The experimental setup for the proposed electrical configuration.

Table 5.3 Parameter of the experimental model

Parameters	Value
Number of modules	$n = 2$
MI rated power	$p_{MI} = 250\ W$
MI inductors	$L_1 = L_2 = 0.5$ mH
MI capacitors	$C_1 = C_2 = 80$ µF - $C_o = 1$ µF
MI Switching frequency	$f_s = 50$ kHz
Transformer turns' ratio	$N = 1$
Charged battery voltage	V_{bat} = 12s x 4.1 V ≈ 49V
Grid voltage	325 V peak
Grid impedance	$L_g = 1$ mH, $r_g = 0.5\Omega$
Grid frequency	$f = 50$ Hz

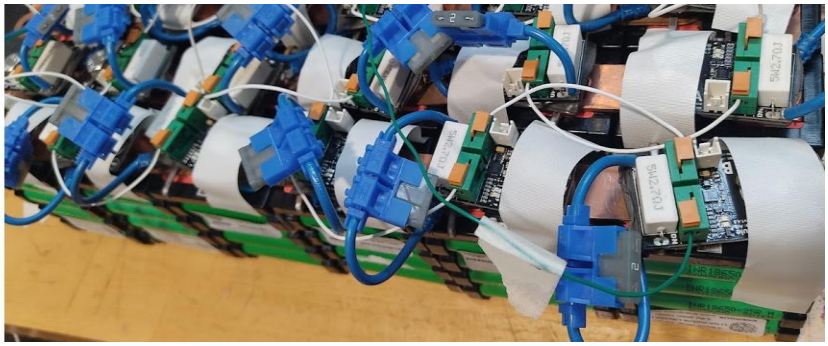

Figure 5.28 Battery parts.

In experimental validation, two SMs are cascaded to study the real scenarios of the investigated cascaded electrical configuration. Each SM is integrated with a battery that is connected to the DC link capacitor terminals. The two SMs are connected to the grid by a transformer to increase electrical system safety. Two different case studies have been conducted to examine the functionality of the proposed electrical system. The first scenario illustrates the system's behavior in normal operation conditions.

Figure 5.29 illustrates the output from various components of the proposed electrical topology. Figure 5.29 (a) illustrates the total output voltage from cascaded two SMs with about 400 V. Figure A1 (b) shows the input voltage from the PV module with about 100 V. Figure 5.29 (c) shows the input current from the PV module. Figure 5.29 (d) illustrates the voltages of the two batteries, which are approximately 200 V, connected to the DC link capacitors. Figure 5.29 (e) shows the battery current of the two SMs. Figure 5.29 (f) illustrates the voltage and current at the grid side.

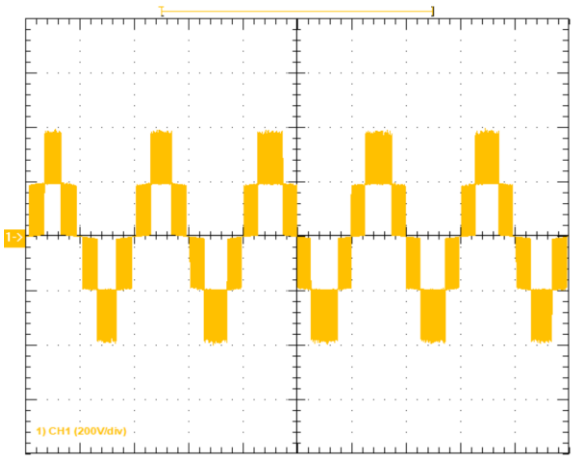

(a) Total output voltage from cascaded inverters
50 ms/div – 50 V/div

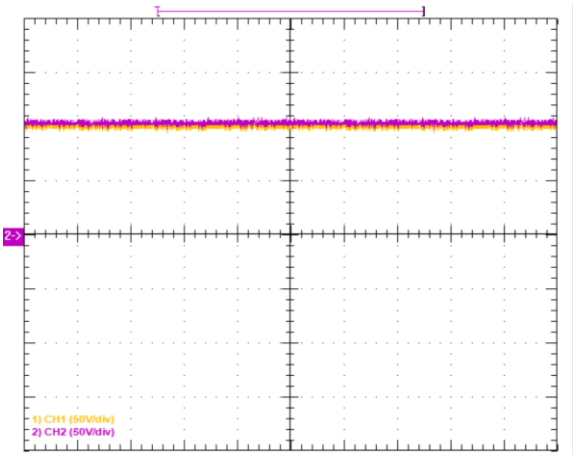

(b) Input (power supplies) voltages
50 ms/div – 50 V/div

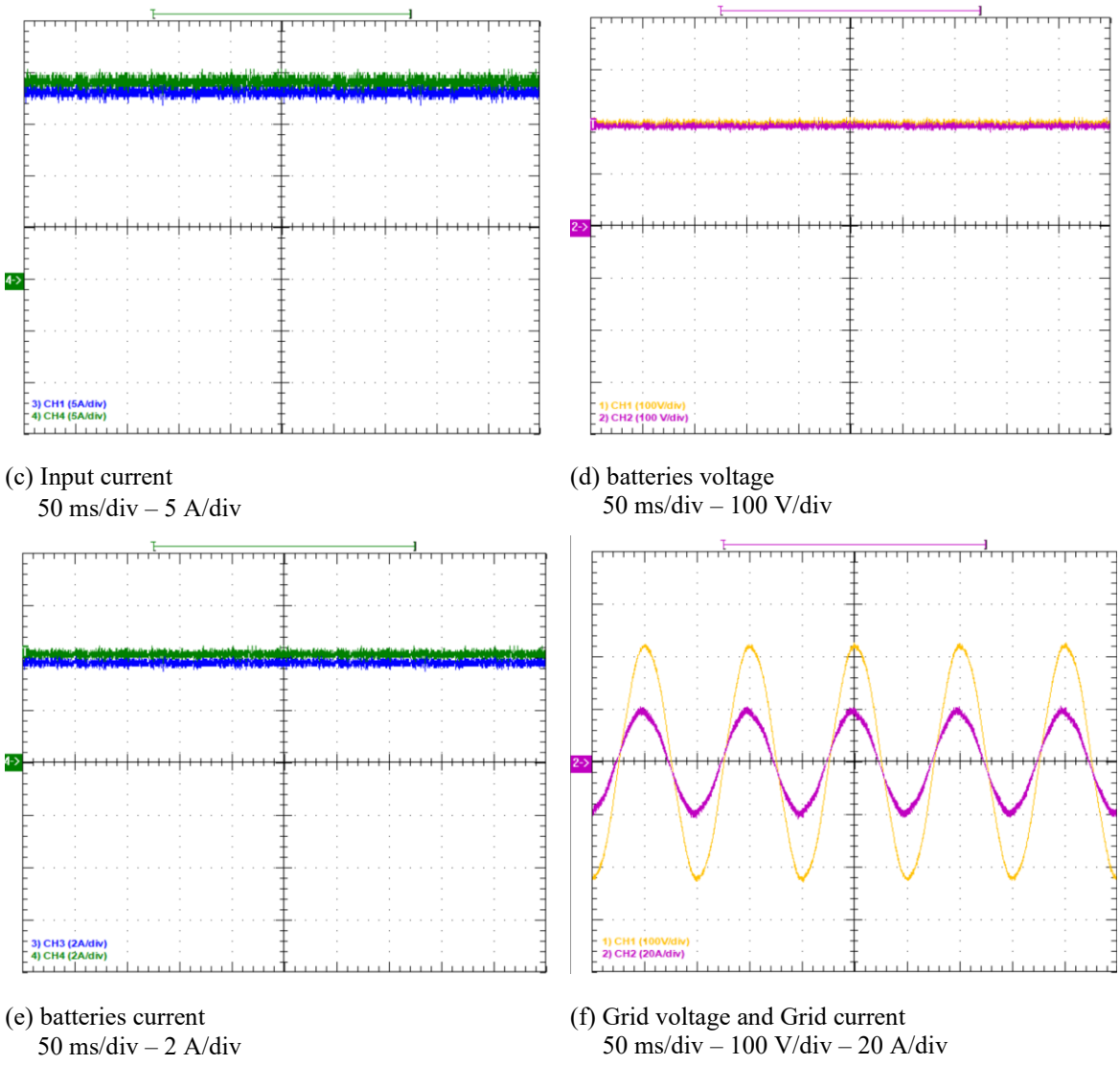

(c) Input current
50 ms/div – 5 A/div

(d) batteries voltage
50 ms/div – 100 V/div

(e) batteries current
50 ms/div – 2 A/div

(f) Grid voltage and Grid current
50 ms/div – 100 V/div – 20 A/div

Figure 5. 29 Experimental results of the electrical system in normal operation

The investigated electrical configuration has been interrupted to examine the system response to the disturbance and its robustness. The battery of the first SM continues charging while the battery at the second SM discharges to support the electrical configuration. The system's parameters have been affected due to this change during the transition to the new state. However, it continues operating normally without posing any issues to the grid.

Figure 5.30 shows the system response to changing the power direction at the second SM. Figure 5.30 (a) illustrates the total output voltage from cascaded two SMs with about 400 V, with a small effect at the transit time. Figure 5.30 (b) shows that changing the power direction at the second SM does not affect the input voltage. Figure 5.30 (c) illustrates the drop in the

input current at the second SM when the battery begins discharging. Figure 5.30 (d) shows that the voltage of the batteries is not significantly affected because the battery has enough power. Figure 5.30 (e) shows the battery current of the second SM, which changed from positive to negative because of the discharging process. Figure 5.30 (f) illustrates normal operation at the grid side without any significant changes in grid current or voltage.

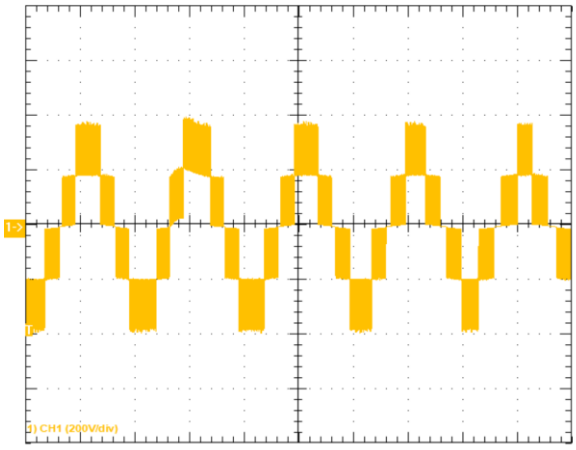

(a) Total output voltage from cascaded inverters
50 ms/div – 50 V/div

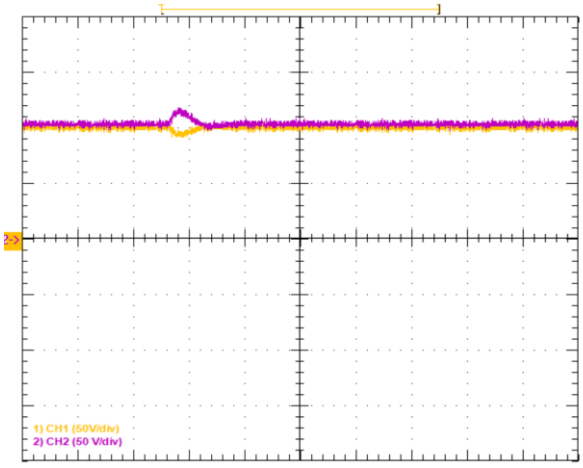

(b) Input (power supplies) voltages
50 ms/div – 50 V/div

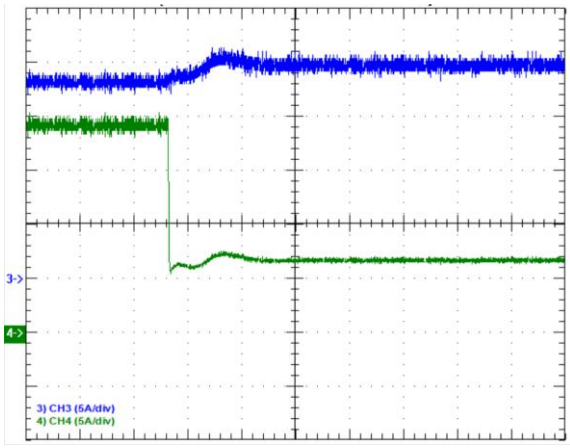

(c) Input current
50 ms/div – 5 A/div

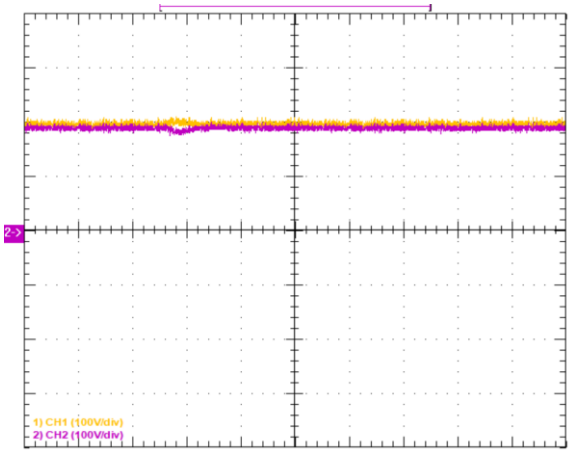

(d) batteries voltage
50 ms/div – 100 V/div

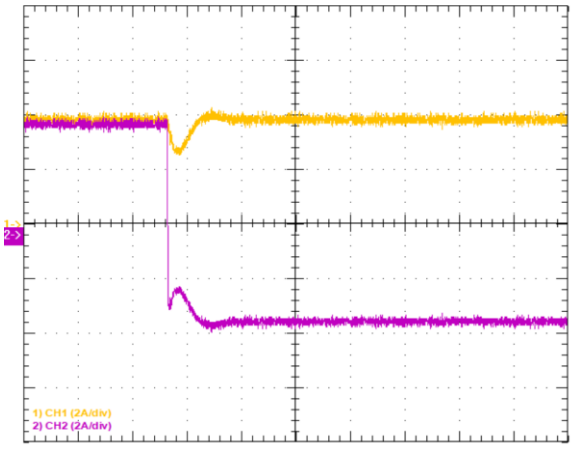

(e) batteries current
50 ms/div – 2 A/div

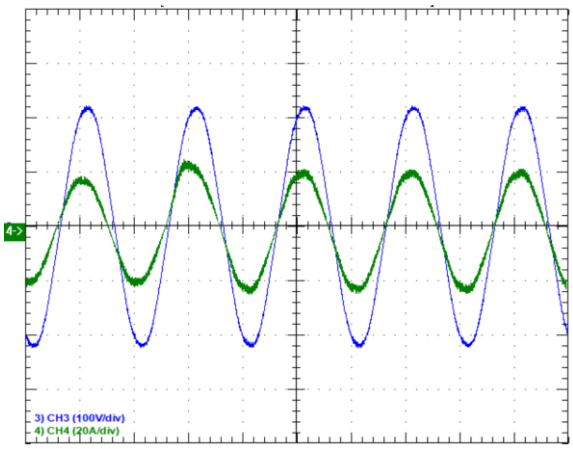

(f) Grid voltage and Grid current
50 ms/div – 100 V/div – 20 A/div

Figure 5.30 Experimental results of the electrical system during changing power flow

5.4 Chapter Conclusion

This chapter introduces MPC technology as an advanced control strategy for grid-tied PV applications. Recently, the MPC approach has been employed to regulate power converter circuits due to its ability to deal with dynamic operational modes and meet the requirements of the electrical grid. The chapter has also reviewed critical elements of the MPC system, including the MPC cost function, the tuning of weighting factors, and parameter selection, which are essential for constructing the MPC system. The advantages and limitations of the two main MPC types have been discussed, and their applications in grid-tied PV systems have been introduced. The chapter then presents the proposed PC MPC technique for a single-phase SEPIC inverter, which aims to operate the power converter at a fixed switching frequency using novel MPC techniques. It has confirmed effective coordination between the grid inverter stages and ensured grid synchronization. Simulation outcomes along with experimental results demonstrate the significance of the proposed method in enhancing dynamic response and improving the system efficiency of grid-connected PV systems. The future direction of utilizing MPC technology in grid-connected systems should continue to focus on developing practical control algorithms and enhancing hardware integration to further improve MPC technology.

Chapter 6

Conclusions and Future Research

This chapter concludes the work accomplished in investigating grid-connected PV systems, with a special focus on proposing a practical method to mitigate mismatch issues between PV modules and SMs. The presented work addresses the objectives of this thesis, as discussed in Chapter 1. The proposed strategies were described in detail, with an emphasis on the key outcomes. The chapter then presents the challenges and limitations of this study, followed by recommendations for future studies to provide further improvements.

6.1 Conclusion of Research

This PhD thesis has analyzed the various mismatch sources in residential PV systems and their impact on PV output power. Then, it presents multiple mitigation approaches for the mismatch concerns. Two new methods are presented in this thesis to mitigate mismatch concerns for residential PV systems, which effectively minimize mismatch issues and provide special advantages for recent residential PV systems. Additionally, the thesis explores the application of the PC MPC for grid-tied PV systems and its contributions to enhancing grid-tied PV applications.

The MCI is built of a well-designed series combination of multiple LV microinverters based on a Cuk circuit topology. This innovative design effectively eliminates the need for a central inverter, which is often associated with a large-value decoupling capacitor and high-cost semiconductor devices. The MCI topology significantly enhances the power extraction of LV PV systems by obtaining the maximum available power from each PV module within the PV system individually. The individual optimization of a PV module can mitigate mismatch concerns that arise between PV modules while significantly reducing power loss in the PV system. With this improvement, overall efficiency and energy harvesting have increased considerably.

The proposed advanced Cuk converter configuration provides continuous input and output current and eliminates the need for complex filtering circuits. The MCI enables stepping the output voltage up and down, which allows a broad range of voltage regulations. The novel

MCI design supports bidirectional operational modes, allowing the system to utilize PV energy to meet local demand and charge the battery from the utility grid. The integration with the electrical system enables sending excess power to the grid or charging the battery from the grid when necessary. Therefore, the overall performance and reliability of the PV system are significantly improved.

The MCI facilitates four different modes of operation: (1) providing power from PV modules to the utility AC grid, (2) discharging energy from the battery to the grid, (3) charging batteries via PV modules, and (4) charging batteries using the AC grid. This significantly improves energy management, particularly in the context of irregular load and generation scenarios.

The controlling system of the novel MCI has two controlling loops that efficiently regulate the MCI inverter. The inner loop focuses on regulating the input current from the PV system, with the essential purpose of minimizing the input current ripple, which facilitates the operation of MPPT system. The external control system regulates the AC grid current to meet the grid connection requirements. This control method is used to maintain the stability and reliability of the PV system across various operational modes, while enhancing overall efficiency and functionality.

A new multi-input single-output cascaded boost inverter topology is utilized to employ the distributed MPPT at the PV SM level, which can enhance the PV module power production and reduce the mismatch between PV SMs within a PV module. The proposed topology enables tracking the MPP for each SM on an individual basis, which can minimize power losses that arise from various mismatch issues, such as shading, soldering, or internal mismatches between PV SMs within a single PV module. Therefore, this approach significantly enhances overall system efficiency and performance, which makes it a suitable solution for modern residential PV applications.

The PV SM is connected to a separate boost converter to enhance power production from each PV SM and minimize mismatch losses. The three boost converters within a PV module are connected in series to improve the stepping-up capability of the grid-connected system. Therefore, the proposed dose does not require an external boosting circuit. A one-directional

diode is integrated between the PV side and the grid side to protect the PV modules from potential damage.

MPC methods can improve the performance of control systems in PV grid-connected applications, which mitigates mismatch issues and increases power extraction from the PV system. The MPC strategies offer several advantages compared to traditional PID controllers and can enhance the control design of PV grid-connected systems. The capability of the MPC to regulate multiple control objectives and the simple integration of the system constraints are the most important benefits of using the MPC for grid-tied applications. However, the MPC strategies have some significant challenges, including substantial computational requirements, which can pose a serious issue, especially in experimental validation. Operating the power inverter at different switching frequencies is another common issue of MPC, and it can lead to inconsistency in current and voltage ripples. Overcoming MPC-related challenges is important to achieve optimal system operation and effectively mitigate mismatch issues in a grid-connected PV system.

Chapter 2 This chapter presents a comprehensive review of the challenges that arise in grid-connected PV systems because of mismatch factors such as partial shading, dust, cell degradation, and manufacturing tolerances. The mismatch concerns can significantly decrease the output energy of the PV system and can cause it to operate away from its optimal power point. Additionally, the chapter conducts a review of distributed MPPT strategies implemented at the PV model and SM level, which aims to address mismatch issues and minimize power losses in grid-connected PV systems. The chapter studies different distributed MPPT methods, converter structures, and control techniques and demonstrates the advantages of using distributed MPPT at different levels of PV systems to increase energy harvesting. Furthermore, the chapter emphasizes associated concerns, including system complexity, installation costs, and control complications. The distributed MPPT strategies can improve the power production of PV systems compared to a centralized MPPT method. Nevertheless, further research on power electronics designs is required to improve the efficiency of grid-tied PV systems and maximize power production.

Chapter 3: The chapter introduces a novel grid-connected inverter integrated with energy storage systems (ESS) based on the Cuk converter configuration. The MCI enables the

connection of PV modules to battery storage units at the input stage of the utilized MIs. Given its bidirectional nature, each Cuk MI is designed to send power to the AC grid from the PV modules while simultaneously enabling the charging of battery packs from the AC grid. Furthermore, the chapter explained the control strategies for various operational modes of the Cuk MI functioning as a DC/DC converter, AC/DC rectifier, and DC/AC inverter. The control systems are designed to maintain a constant input current at the input side of the employed converter while ensuring that the AC side voltages and currents align with the grid frequency of 50 or 60 Hz. The passive components of the proposed MCI can effectively decouple the second-order harmonic in inverter or rectifier operation modes, which enhances the PV system efficiency and allows precise MPP tracking features. The proposed MCI has been designed to mitigate mismatch issues at the PV module level, increasing conversion efficiency and maximizing the overall PV power production. The bidirectional power flow characteristic of the MCI permits the connection of battery packs with the PV module, thus enabling the harvested energy to be stored during low-demand time rather than being wasted. Experimental evaluations of the 1 kW prototype have confirmed the functionality of the MCI with PV modules and battery packs. It employs four MIs, which are interfaced with the utility grid. These experimental findings have verified the proposed system's capability to maximize the extraction of available power from PV modules under normal and partially shaded conditions.

Chapter 4: This chapter presents a proposed micro-inverter topology that connects three DC-DC boost converters with a single-phase VSI to the electrical grid. The design of the proposed PV system addresses concerns regarding mismatch issues between PV SMs within a PV module. Utilizing the defined topology facilitates extracting the maximum available power from the individual strings of PV cells within a PV module by connecting a boost converter to each PV SM. The introduced LV micro-inverter introduces a series input configuration, eliminating the necessity for a considerable step-up voltage ratio. The proposed structure comprises two control systems to effectively operate the grid-connected PV system. The first controller regulates the grid-side current to meet the specifications of the distribution grid, while the second controller mitigates the input current ripple at the PV side. The effectiveness of the presented micro-inverter topology has been assessed through simulation and experimental methods. Experimental outcomes have demonstrated the

proposed design's ability to capture the maximum available power from the PV SM within a single PV module under standard operating conditions and scenarios characterized by mismatch effects.

Chapter 5: This chapter begins with an in-depth investigation of MPC control strategies for power converter circuits. It focuses on implementing the MPC strategies for grid-connected PV and highlights their critical role in recent PV systems. The MPC strategy is an effective control mechanism used to regulate power electronic converters by accurately capturing their dynamics. The MPC strategies have several advantages, including predictive features, fast dynamic response, and the ability to integrate various constraints within multivariable systems. Therefore, MPC approaches are a practical control option for power converters. The chapter then introduces the two MPC types with a special focus on the advantages and limitations of each category. Furthermore, it presents the fundamental components of MPC that are used for power converters, including the modulation of precise power converter circuits, the structure of objective functions and variables, and the optimization of parameters and weighting factors to achieve the desired control results. Building on this, a new PC MPC technique for controlling a grid-connected single-phase SEPIC inverter system is suggested. The proposed control system of the SEPIC-based structure offers a fixed switching feature to enhance the performance of the MPC control system. The new MPC method relies on introducing the future possible values of the duty ratio for the SEPIC converter. The optimal duty ratio is sent to the modulator to generate gate pulses for switches. The efficacy of the proposed method has been confirmed by experimental results, which demonstrate its capability to meet grid requirements.

6.2 Research Contributions

The primary goal of the research accomplished in this thesis is to develop a grid-connected DC-AC single-phase inverter for a residential PV system. It aims to tackle the associated mismatch issues of conventional PV designs. The focus has been on proposing novel, practical inverter topologies and employing the distributed MPPT at a finer level within the PV system (model and sub-model), aiming to mitigate mismatch issues and increase the power production of the PV system. The key achievements of the research are summarized as follows:

- The thesis presents a complete review of the mismatch factors, including shading, dust, and soldering issues. Mismatches in residential grid-connected PV systems are common and can significantly reduce power production. Distributed MPPT strategies are commonly employed to overcome the mismatch problems and enhance power production capabilities. Therefore, the project discusses implementing the decentralized MPPT at a finer level to enhance PV system power production.
- Develop a novel DC-AC inverter for low-voltage grid-connected PV applications based on the Cuk converter design. The Cuk-based MIs are series-connected, and each PV module is linked with a specific Cuk-based inverter, enabling individual MPPT systems for each PV module. Therefore, the suggested inverter significantly reduces the mismatch concerns caused by PS or degradation of PV modules and enhances the overall efficiency of the grid-tied inverter.
- Design a new multi-input, single-output microinverter configuration that offers scalable and efficient options for residential PV applications. The proposed structure employs boost converters for PV cell strings within a single PV module and applies a separate MPPT system for each PV SM. Thus, the mismatch issue of an individual PV model is mitigated significantly, leading to the maximum power production of the PV model. The design considers protecting the PV module under faulty scenarios by integrating a forward diode between the PV and the grid side. The distributed MPPT system, integration of practical control systems, and enhanced energy harvesting capabilities of the proposed structure result in reducing the mismatch issues between PV systems.
- Investigate MPC advanced control strategies and their applications in power electronic converters, with a special focus on PV grid-tied configurations. Proposing a modified PC MPC strategy for a single-phase SEPIC-based inverter, aiming to fix the switching frequency effectively and provide better control performance. The suggested method introduces several values for possible duty ratios and selects the optimal duty ratio that achieves minimum error.

6.3 Research Limitations

- The main objective of the thesis is to investigate the existing LV grid-connected PV applications, focusing on power converter design to propose more practical alternatives. The MPPT algorithm falls outside the scope of this thesis; therefore, the parameters for the PV modules will be obtained from the lookup table, with the current of the PV module adjusted by the voltage of that same PV module.
- Another limitation of the research is the lack of anti-islanding protection mechanisms. While the system focuses on optimizing power extraction and mitigating the mismatch issues, it does not adequately discuss islanding situations in which the inverter becomes faulty.

6.4 Future work

The thesis covered several essential aspects of grid-connected inverters for residential PV applications. However, some factors and challenges remain to be explored in future research. Some suggestions for future related research include the following points:

- Soft-switching techniques are commonly employed in the design of power electronic converters to reduce voltage and current stress on the power switches and enhance conversion efficiency. The future grid-connected topology should include new practical soft-switching techniques to improve system efficiency and increase power harvesting.
- The power electronic switch is a fundamental component in designing power electronic circuits; thus, selecting switches that demonstrate reduced switching and conduction losses can enhance power converter efficiency. Research has shown that power electronic switches based on GaN and SiC can provide superior efficiency and significantly reduce power losses. The drain-source on-state resistance of these switches is comparatively low, reducing the conduction losses during the ON state of the switch. Additionally, it is possible to operate at high switching frequencies with reduced switching losses.

- Anti-islanding protection is an additional feature that should be take into account in future structures; the strategies employed for detection errors should be both rapid and precise to effectively address power inverter failures.
- Exploring new MPPT algorithms is essential for maintaining a stable voltage level and ensuring the extraction of the maximum available power from the PV system. The expected MPPT systems should accurately track the MPPs under various operating scenarios, which results in a significant increase in power extraction.

Appendix A

A.1 Hardware Structure

The specific components used for the experimental configuration of the suggested module and SM topologies, along with the corresponding measurement and control units, are outlined in this section.

A.1.1 Digital Signal Processing (DSP)

The TMS320F28379D is a floating-point DSP controller from the TMS320C28X family, which was developed by Texas Instruments. The TMS320F28379D is illustrated in Figure A1. It offers several benefits, including precise results, an affordable price, and low power consumption, enabling users to create and implement applications in real-time.

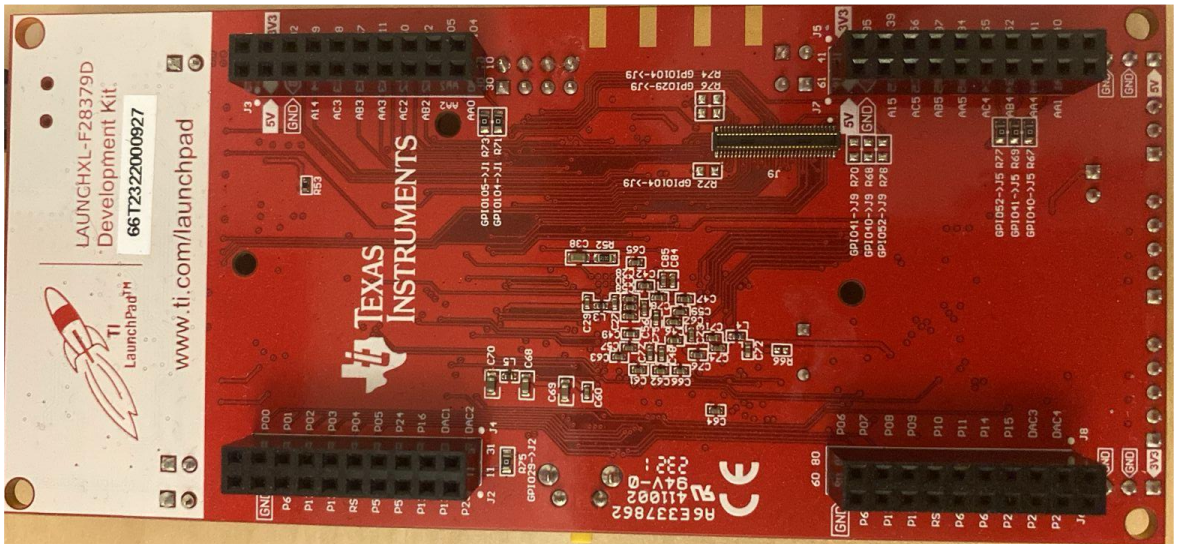

Figure A1. TMS320F28379D DSP Controller.

Components incorporated within the TMS320F28379D DSP controller are as follows:

- The TMS320F28379D offers a high-speed processing feature of 150 MHz.
- 32-bit floating-point units.
- 18 PWM high-resolution PWM outputs.
- 12-bit ADC with 16 channels.

The primary function of the TMS320F28379D DSP is to generate gate signals for the power converter circuits of the investigated MCI. The utilized DSP controller does not require supplementary interfacing circuits, which makes the control process straightforward. The Code Composer Studio programming software is also supplied and enables online monitoring of the proposed inverter's performance. This hardware/software combination facilitates integration with MATLAB Simulink, Real-Time Workshop, and an embedded target for the TI C2000 DSP. As a result, prototyping and editing the controller become fast and precise. The utilized control system not only ensures swift connectivity but also allows real-time monitoring by storing data within the microcontroller's RAM. The DSP is equipped with an analog-to-digital converter that has a 12-bit resolution, resulting in 4095 discrete values across the input control signal range of 0 to 3 volts. Each incremental step corresponds to a voltage change of 0.7 mV.

The TMS320F28379D DSP is programmable in C, C++, or MATLAB/Simulink. The corresponding support package facilitates the conversion of Simulink block diagrams into C code, allowing for the downloading of embedded code to the hardware board. In addition, the DSP is compatible with the CAN protocol, which enables its integration with CANalyzer devices. The CANalyzer Vector-XL tool is capable of transferring all variable data written in C code to the host personal computer through the CAN communication protocol.

Discretization and implementation of the PR controller can be obtained by using available DSP technology, removing the necessity for algebraic computations. The discrete formulation of the PR controller can be proficiently obtained through the use of the bilinear pre-normalized transformation, commonly known as the Tustin method, and is represented as follows:

$$s = \frac{2z - 1}{t_s z + 1} \qquad A.1$$

The transfer function GPR(z) of the PR controller, expressed in the discrete z-domain, is defined as follows:

$$G_{PR}(z) = \frac{k_r \frac{2z-1}{t_s z+1}}{\frac{4}{t_s^2}\frac{(z-1)^2}{(z+1)^2} + w^2} \qquad A.2$$

$$G_{PR}(z) = \frac{2t_s k_r (1-z^{-2})}{(4\ + w^2 t_s^2) + (2t_s^2 - 8)z^{-1} + (4\ + w^2 t_s^2)z^{-2}} \qquad A.3$$

, which can be expressed as follows:

$$G_{PR}(z) = \frac{a_0(1-z^{-2})}{b_0 + b_1 z^{-1} + b_2 z^{-2}} \qquad A.4$$

Where:

$a_0 = 2t_s k_r$

$b_0 = (4\ + w^2 t_s^2)$

$b_1 = (2t_s^2 - 8)$

$b_2 = (4\ + w^2 t_s^2)$

The PR controller configured in the z domain can be expressed in relation to the error signal e(z) and the output signal of the controller y(z) as follows:

$$G_{PR}(z) = \frac{y(z)}{e(z)} = k_p + \frac{a_0(1-z^{-2})}{b_0 + b_1 z^{-1} + b_2 z^{-2}} \qquad A.5$$

The next expression is used as the difference equation for the PR controller in the DSP board:

$$y(n) = \left[\frac{a_0\big(e(n) - e(n-2) - b_1 y(n-1) - b_2 y(n-2)\big)}{b_0}\right] + k_p e(n) \qquad A.6$$

A.1.2 PWM Gate Driver

To regulate the specified MCI parameters, the MOSFETs integrated within the converter must be activated by the PWM signal generated by the microcontroller. According to its specifications, the DSP F283379D is equipped with a maximum of 18 PWM channels, each capable of providing an amplitude of 3 volts; however, the gate of the MOSFET requires a minimum signal of approximately 5 volts. A PWM driver has been designed to step up the

PWM control signal from the DSP and ensure isolation from the power electronics, as illustrated in Figure A2.

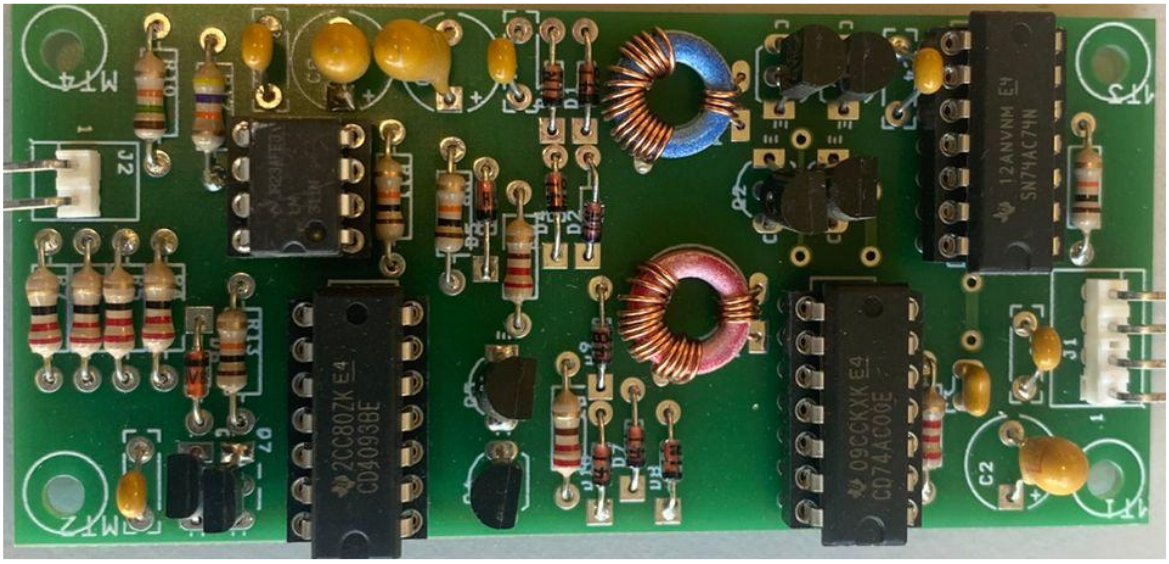

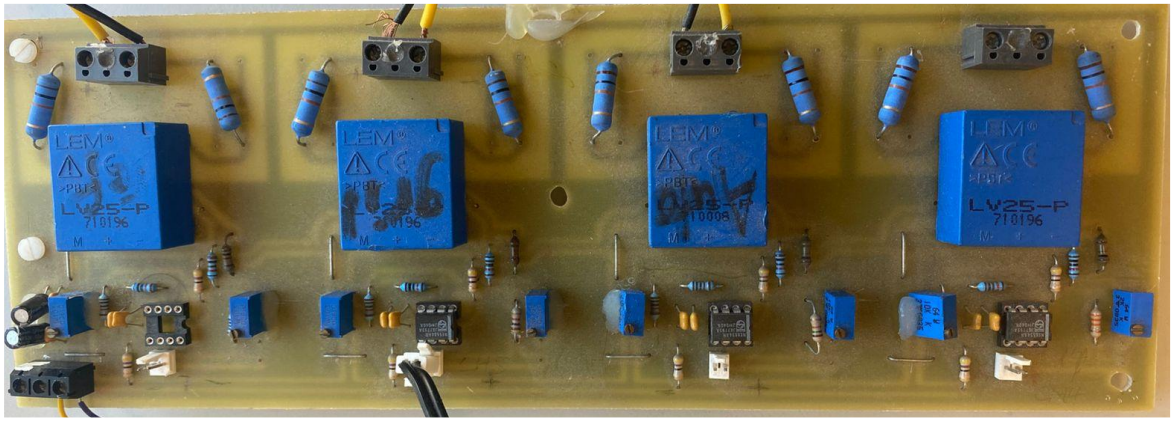

Figure A3. Voltage sensor board.

A.1.3.2 Current Measurement board

The current sensor selected for investigating MCI is LA55-P from the manufacturer LEM. Figure A.4 shows the current sensor board that employs LA55-P sensing instruments. The LA55-P sensor provides power isolation from the control signal by using the Hall Effect, offering current overload capability, and simple implementation. Therefore, it has been selected for experimental validation. The LA55-P sensors offer a broad measuring range from 0 to 50 A, along with a maximum bandwidth capability of 200 kHz.

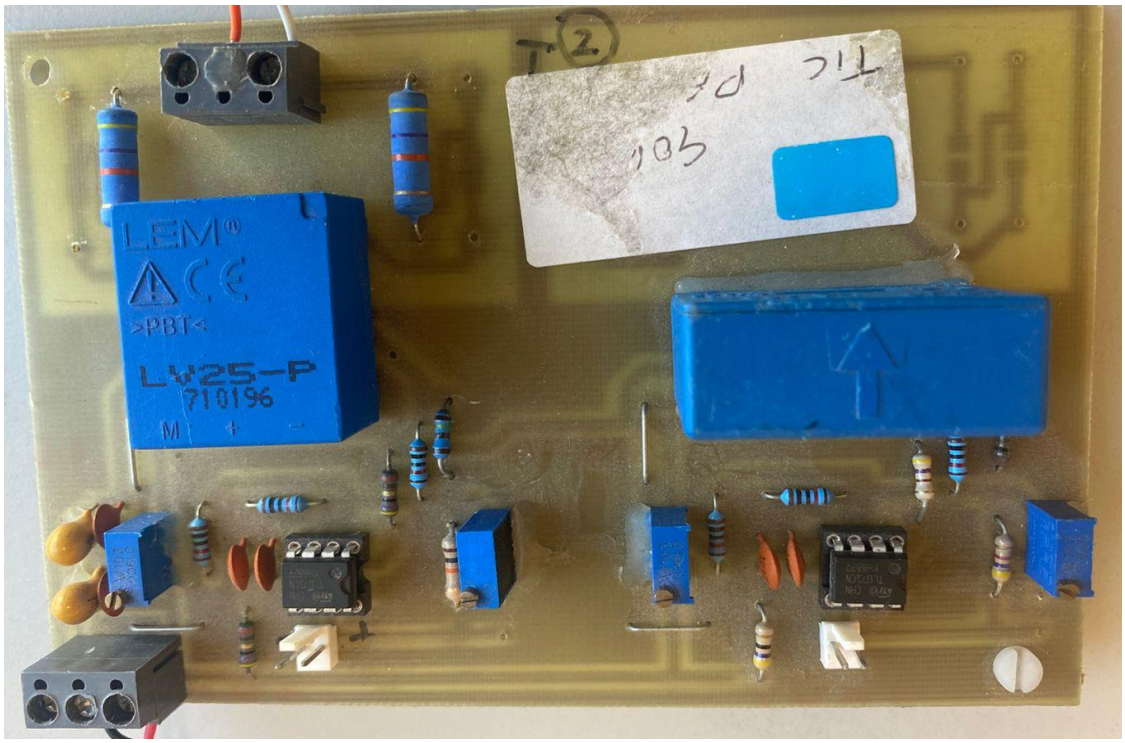

Figure A4. Current sensor board.

A.1.4 DC power supply

The DC power supplies have mimicked the operation of PV modules for simulating their operation during experimental evaluations. Therefore, two different power supplies are employed: one designated for the upper two series PV modules and the other for the two lower series PV modules, as illustrated in the schematic connection described in Figure A. The power supplies utilized, namely the EL300RT TRIPLE POWER SUPPLY.

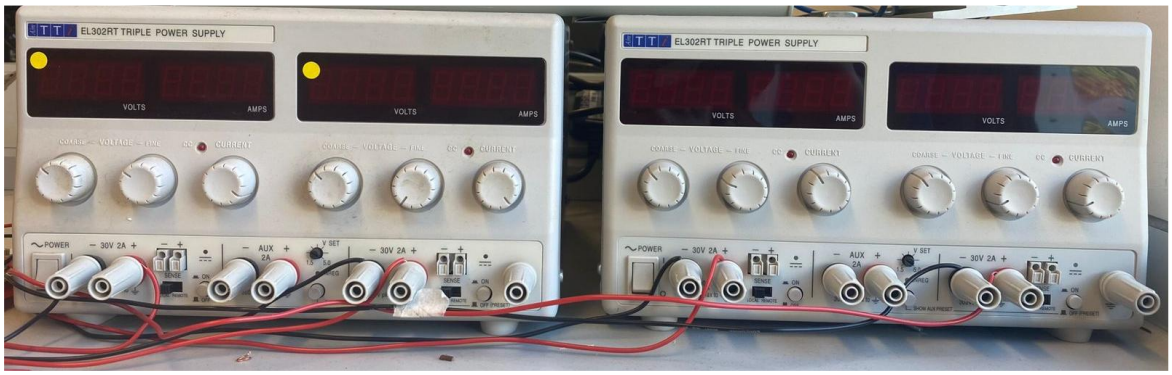

Figure A5. DC power supplies.

A.2 Component Selection for Cascaded Electrical Configuration

The Power Electronic Breadboard-XL from PE Modules, shown in Figure A6, is used to perform experimental validation of the electrical configurations proposed in the thesis. This electronic breadboard is designed to accommodate up to eight modular units simultaneously and can deal with electrical stresses of up to 800 V and 20 A, making it a practical platform for investigating both low- and high-power topologies. It allows designers to build various power electronic circuits by selecting different module combinations and wiring arrangements. The breadboard can be configured as a single- or three-phase inverter, a single- or three-phase rectifier, or implemented as a DC-DC converter circuit, including boost, buck, buck-boost, and other power electronic topologies. It also supports operation with or without feedback, enabling designers to explore both open-loop and close-loop control methods.

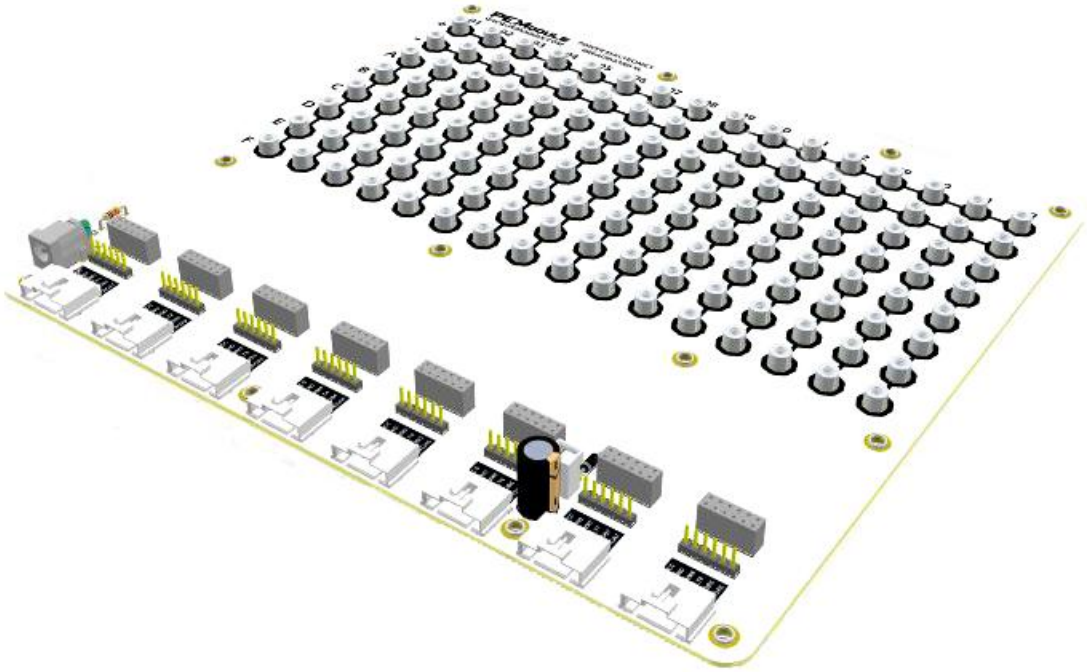

Figure A.6 Breadboard-XL model

The IGBT from the PEModuls company, shown in Figure A.7, is used as a switch in designing the investigated electrical topology. This high-performance IGBT module is integrated with a free-wheeling diode and can be used in most power electronic circuits that require fast switching and thermal management. The gate driver is integrated into the IGBT module, making circuit implementation straightforward. The saturation voltage of the IGBT module is very low, which helps minimize switching losses and enables fast operation. The free-wheeling diode in the IGBT module provides swift and soft recovery characteristics, reducing stress and minimizing EMI effects in the examined electrical topology. The module also ensures superior electrical safety by providing high electrical isolation. Furthermore, the active Miller Clamping feature in the IGBT module provides stable operation and protects the system against false turn-on or turn-off when operating at high switching frequencies

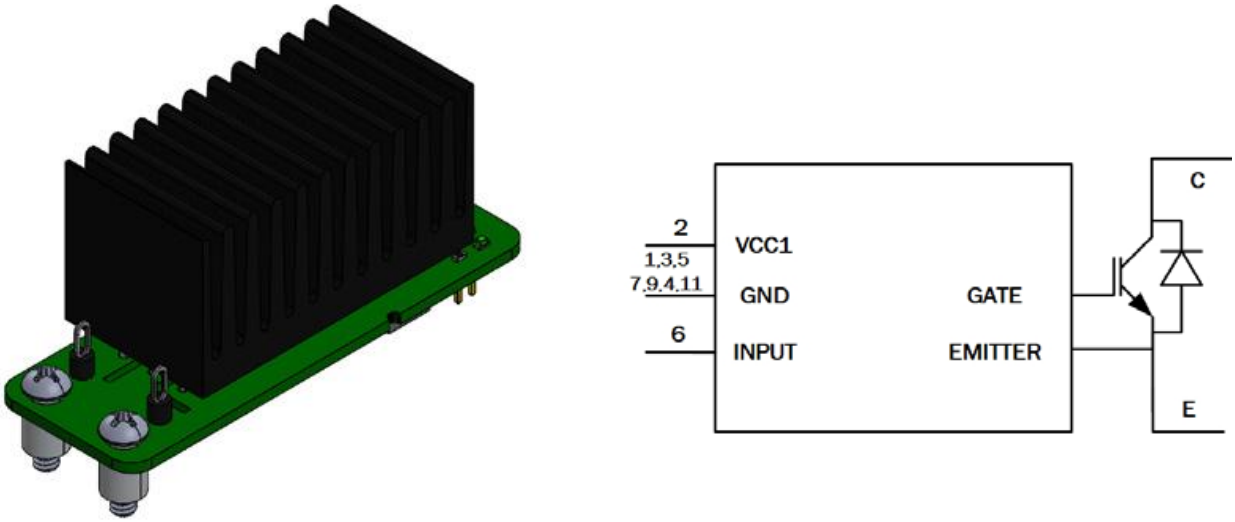

Figure A.7 Symbol and model of the IGBT switch.

The diode module from PEModules illustrated in Figure A.8 is a fast-recovery diode designed for investigating high-performance power electronic circuits. This module is suitable for fast-switching applications and offers high efficiency and reliability. It is integrated with an advanced thermal management system, ensuring stable operation and long service life. The diode's forward voltage drop and leakage current are very low, which significantly contributes to minimizing conduction losses. An isolation protection system is integrated into the diode module to protect the electrical system and improve overall efficiency. This module is well-suited for use in a wide range of power electronic circuits operating at different voltage levels.

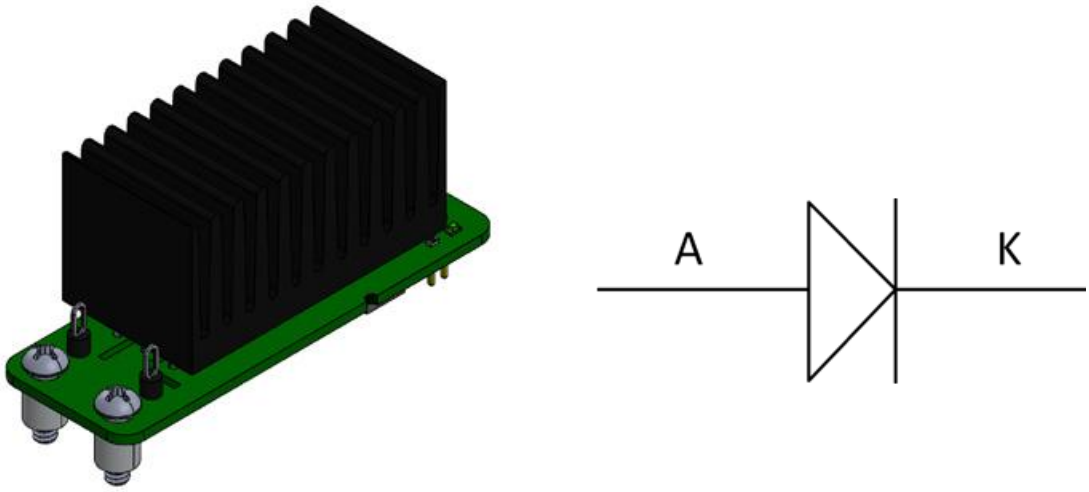

Figure A.8 The diode module.

The voltage sensor module from PEModules is illustrated in Figure A.9. It is a fully isolated voltage sensor that enables accurate measurement across a wide voltage range. This practical module is capable of measuring both DC and AC signals with a wide 200 kHz bandwidth. It provides excellent linearity of 0.5% and high gain accuracy of 1%. The module features a simple design with outstanding temperature stability of about 50 ppm/°C, eliminating the need for an external reference. It also provides a high isolation voltage of 3 kV, which significantly enhances protection and ensures safe operation. In addition, the module incorporates noise immunity features, making it a reliable choice for measuring voltages in a variety of power converter circuits, including motor drives, buck and boost converters, SMPS, UPS systems, and more.

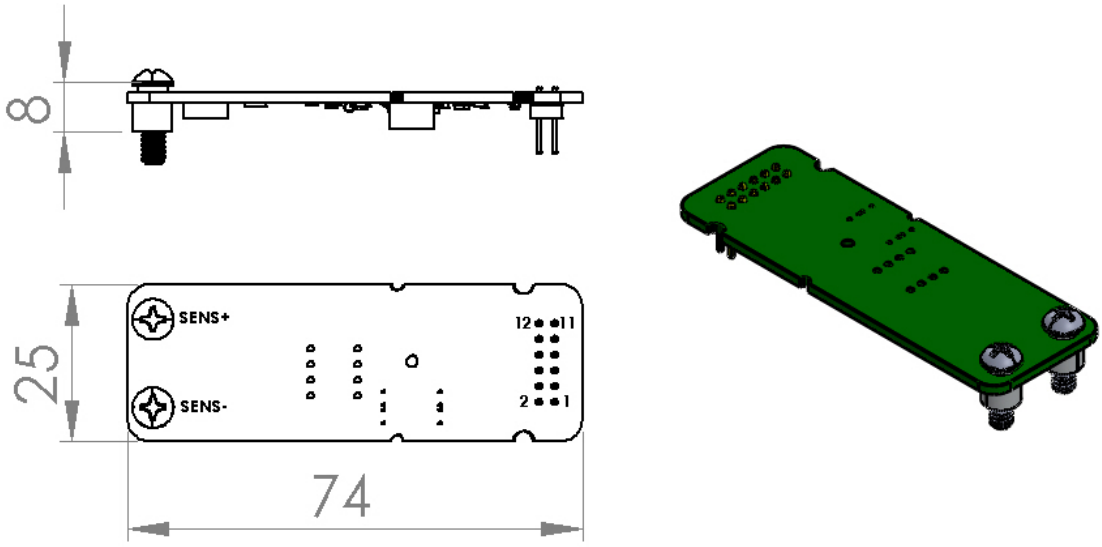

Figure A.9 Voltage sensor module.

The inductor series from PEModules is designed with a wide range of inductance and current ratings, making it suitable for most power electronic circuits. Figure A.10 illustrates the inductor module used in the experimental validation. The core structure of the inductors in this series incorporates a distributed air gap, which enhances their high energy storage capacity. Magnetic radiation is minimized through self-shielding design, making the series practical for applications that require low EMI and stable performance. These inductors are built with high current-carrying capability, ensuring consistent reliability under demanding operating conditions. In addition, the user-friendly design allows for straightforward installation and easy replacement, providing flexibility and convenience in designing the system.

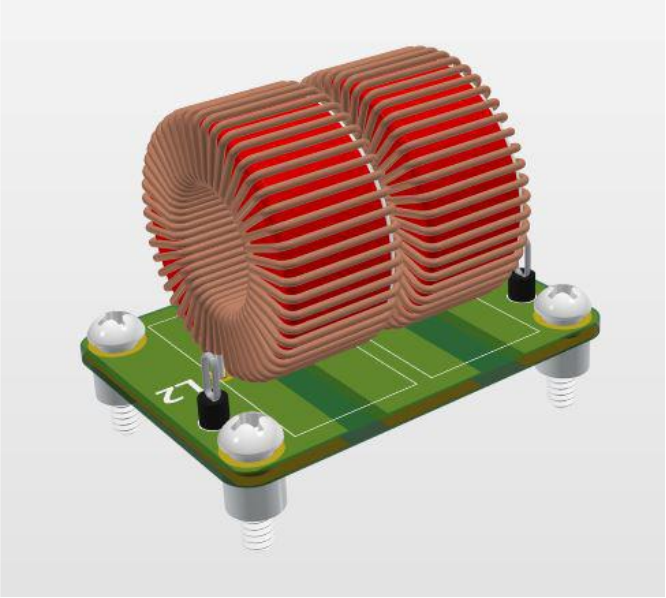

Figure A.10 Symbol and model of the inductor

The capacitor family from PEModules offers a wide range of capacitance values with different operating voltages, making it highly practical for power electronic applications. Figure A.11 illustrates one of the capacitors of the PEModules capacitor series. Designed with low ESR, these capacitors can handle high ripple currents effectively, contributing to improved system efficiency and enhanced stability. The series is engineered for long service life and reliable performance across a variety of operating environments. With a compact form factor, the capacitors are easy to install and replace, ensuring both convenience and flexibility in system integration.

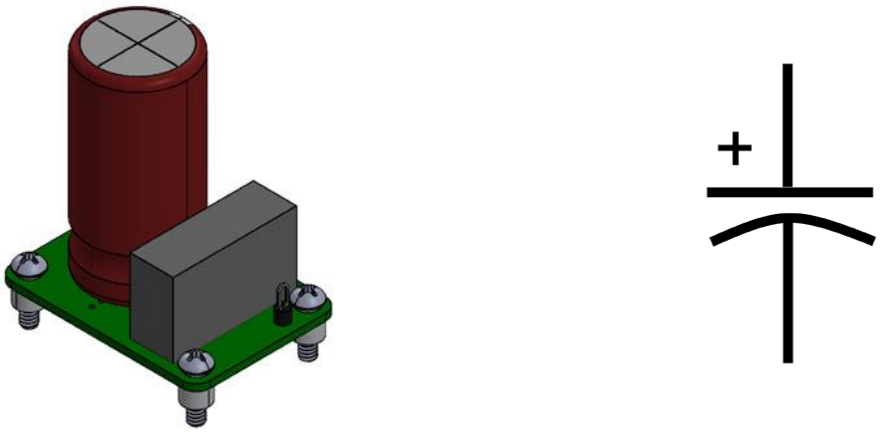

Figure A.11 Symbol and model of the capacitor.

A.2 Single-Phase Formulas Derivation

For single-phase AC, real power is:

$$P = V_{rms} I_{rms} \cos(\varphi)$$

$$P = (1/2)\, Vg\, Ig\, cos(\varphi)$$

$$Ig = 2\mathrm{P} / (Vg \cos(\varphi))$$

Using KVL in phasor form:

$$V = Vg - IgZg$$

Where:

$$Vg = Vg\angle 0 = Vg$$

$$Ig = Ig(cos\varphi - jsin\varphi)$$

$$Zg = rg + j\omega Lg$$

Multiply Ig*Zg

$$I_g Z_g = I_g(\cos(\varphi) - jsin(\varphi))(r_g + j\omega L_g)$$

$$= Ig[r_g \cos(\varphi) + \omega L_g \sin(\varphi) + j(\omega L_g \cos(\varphi) - r_g sin(\varphi))]$$

Real part

$$(I_g Z_g) = I_g r_g \cos(\varphi) + \omega L_g s$$

Imaginary part

$$(I_g Z_g) = I_g(\omega L_g \cos(\varphi) - r_g \sin(\varphi))$$

Real and Imaginary Parts of Load Voltage

$$V = V_g - I_g Z_g$$

Real part

$$V = V_g + r_g I_g \cos(\varphi) - \omega L_g I_g \sin(\varphi)$$

Imaginary part

$$V = r_g I_g \sin(\varphi) + \omega L_g I_g \cos(\varphi)$$

Voltage Angle

$$\theta = \tan^{-1} \left(\frac{V_{real}}{V_{imag}}\right)$$

$$\theta = \tan^{-1}\left[\frac{r_g I_g \sin(\varphi) + \omega L_g I_g \cos(\varphi)}{V_g + r_g I_g \cos(\varphi) - \omega L_g I_g \sin(\varphi)}\right]$$

Voltage Magnitude

$$V = \frac{V_{real}}{\cos(\theta)}$$

$$V = \left[\frac{V_g + r_g I_g \cos(\varphi) - \omega L_g I_g \sin(\varphi)}{\cos(\theta)}\right]$$

References

[1] S. Ahmad, U. K. Jhuma, M. Karimi, A. Pourdaryaei, S. Mekhilef, H. Mokhlis, and K. Kauhaniemi, "Direct power control based on point of common coupling voltage modulation for grid-tied AC microgrid PV inverter," *IEEE Access*, vol. 10, pp. 187–202, 2022.

[2] I. Jamal, M. F. Elmorshedy, S. M. Dabour, E. M. Rashad, W. Xu, and D. J. Almakhles, "A comprehensive review of grid-connected PV systems based on impedance source inverter," *IEEE Access*, vol. 10, pp. 89101–89123, Aug. 2022.

[3] H. Al-Rawashdeh, O. A. Al-Khashman, J. T. Al Bdour, M. R. Gomaa, H. Rezk, A. Marashli, L. M. Arrfou, and M. Louzazni, "Performance analysis of a hybrid renewable-energy system for green buildings to improve efficiency and reduce GHG emissions with multiple scenarios," *Sustainability*, vol. 15, no. 9, Art. no. 7529, May 2023.

[4] IEA-PVPS, *Trends in PV Applications 2020*, Int. Energy Agency Photovoltaic Power Systems Programme, 2020. [Online]. Available: https://iea-pvps.org/trends_reports/trends-in-pv-applications-2020/. [Accessed: May 6, 2025].

[5] IEA-PVPS, *Trends in PV Applications 2021*, Int. Energy Agency Photovoltaic Power Systems Programme, 2021. [Online]. Available: https://iea-pvps.org/trends_reports/trends-in-pv-applications-2021/. [Accessed: May 6, 2022].

[6] A. Poorfakhraei and M. Narimani, "A review of multilevel inverter topologies in electric vehicles: Current status and future trends," *IEEE Open J. Power Electron.*, vol. 2, pp. 155–170, 2021.

[7] T. E. K. Zidane, A. S. Aziz, Y. Zahraoui, and H. Kotb, "Grid-connected solar PV power plants optimization: A review," *IEEE Access*, vol. 11, pp. 79588–79608, 2023.

[8] A. Elnady, A. A. A. Ismail, M. AlShabi, and A. Noureldin, "A comprehensive review of centralized current/power control schemes for parallel inverters and AC microgrids," *IEEE Access*, vol. 10, pp. 125061–125085, 2022.

[9] C. G. Lee, W. G. Shin, J. R. Lim, G. H. Kang, and Y. C. Ju, “Analysis of electrical and thermal characteristics of PV array under mismatching conditions caused by partial shading and short circuit failure of bypass diodes,” *Energy*, vol. 220, Art. no. 119706, 2021.

[10] M. Li, H. Geng, and X. Zhang, “Distributed coordinated control for stabilization of multi-inverter power plant,” *IEEE Trans. Ind. Electron.*, vol. 70, no. 12, pp. 12421–12430, Dec. 2023.

[11] S. He and B. Liu, “Distributed carrier phase shifting control method for modular interleaved parallel inverters,” *IEEE Trans. Transp. Electrification*, vol. 9, no. 2, pp. 2497–2508, Jun. 2023.

[12] M. Talha, A. Amir, S. R. S. Raihan, and N. A. Rahim, “Grid-connected photovoltaic inverters with low-voltage ride through for a residential-scale system: A review,” *Int. Trans. Electr. Energy Syst.*, vol. 31, no. 10, 2021.

[13] M. A. Yagoub, A. A. Elserougi, and T. H. Abdelhamid, “Closed-loop string current control for string optimizer circuits-based PV system to enhance extracted PV power during partial shading conditions,” *Alexandria Eng. J.*, vol. 61, no. 12, pp. 11791–11803, Dec. 2022.

[14] S. N. Vodapally and M. H. Ali, “A comprehensive review of solar photovoltaic (PV) technologies, architecture, and its applications to improved efficiency,” *Energies*, vol. 15, no. 1, p. 3181, 2022.

[15] A. O. M. Maka and T. N. Chaudhary, “Performance investigation of solar photovoltaic systems integrated with battery energy storage,” *J. Energy Storage*, vol. 98, Art. no. 110784, Apr. 2024.

[16] X. Qi, Y. Wang, Y. Wang, and Z. Chen, “Optimization of centralized equalization systems based on an integrated cascade bidirectional DC–DC converter,” *IEEE Trans. Ind. Electron.*, vol. 69, no. 1, pp. 249–259, Jan. 2022.

[17] O. Abdel-Rahim, A. Chub, D. Vinnikov, and A. Blinov, “DC integration of residential photovoltaic systems: A survey,” *IEEE Access*, vol. 10, pp. 66974–66991, 2022.

[18] A. G. Yepes and J. Doval-Gandoy, “Simple carrier-based PWM for prolonged high DC-link utilization for symmetrical and asymmetrical-phase AC drives,” *IEEE Trans. Power Electron.*, vol. 36, no. 8, pp. 8696–8712, Aug. 2021.

[19] M. A. Perez, S. Ceballos, and G. Konstantinou, “Modular multilevel converters: Recent achievements and challenges,” *IEEE Open J. Ind. Electron. Soc.*, vol. 2, pp. 224–239, 2021.

[20] A. Kumar, M. Moradpour, M. Losito, and W. T. Franke, “Wide band gap devices and their application in power electronics,” *Energies*, vol. 15, no. 5, 2022.

[21] G. Iannaccone, C. Sbrana, I. Morelli, and S. Strangio, “Power electronics based on wide-bandgap semiconductors: Opportunities and challenges,” *IEEE Access*, vol. 9, pp. 139446–139456, 2021.

[22] J. Ballestín-Fuertes, J. Muñoz-Cruzado-Alba, et al., “Role of wide bandgap materials in power electronics for smart grids applications,” *Electronics*, vol. 10, no. 12, 2021.

[23] O. S. Chaudhary, M. Denaï, S. S. Refaat, and G. Pissanidis, “Technology and applications of wide bandgap semiconductor materials: Current state and future trends,” *Energies*, vol. 16, no. 2, 2023.

[24] A. Phillips, T. Cook, and B. West, “Gallium nitride efficacy for high-reliability forward converters in spacecraft,” *IEEE J. Emerg. Sel. Top. Power Electron.*, vol. 10, no. 5, pp. 5357–5370, Oct. 2022.

[25] H. Zitouni, A. Azouzoute, C. Hajjaj, and M. El Ydrissi, “Experimental investigation and modeling of photovoltaic soiling loss as a function of environmental variables: A case study of semi-arid climate,” *Sol. Energy Mater. Sol. Cells*, vol. 231, p. 110123, 2021.

[26] S. Nyamathulla, D. Chittathuru, and S. M. Muyeen, “An overview of multilevel inverters lifetime assessment for grid-connected solar photovoltaic applications,” *Electronics*, vol. 12, no. 4, 2023.

[27] A. Townsend and R. Gouws, “A comparative review of lead-acid, lithium-ion and ultra-capacitor technologies and their degradation mechanisms,” *Energies*, vol. 15, no. 10, 2022.

[28] C. D. Iweh, S. Gyamfi, E. Tanyi, and E. Effah-Donyina, “Distributed generation and renewable energy integration into the grid: Prerequisites, push factors, practical options, issues and merits,” *Energies*, vol. 14, p. 5375, 2021.

[29] E. Kandemir, N. S. Cetin, and S. Borekci, “A comprehensive overview of maximum power extraction methods for PV systems,” *Renew. Sustain. Energy Rev.*, vol. 78, pp. 93–112, 2017.

[30] S. B. Kjaer, J. K. Pedersen, and F. Blaabjerg, “A review of single-phase grid-connected inverters for photovoltaic modules,” *IEEE Trans. Ind. Appl.*, vol. 41, no. 5, pp. 1292–1306, 2005.

[31] A. Zahedi, “A review of drivers, benefits, and challenges in integrating renewable energy sources into electricity grid,” *Renew. Sustain. Energy Rev.*, vol. 15, no. 9, pp. 4775–4779, 2011.

[32] J. Lee, B. Chang, C. Aktas, and R. Gorthala, “Economic feasibility of campus-wide photovoltaic systems in New England,” *Renew. Energy*, vol. 99, pp. 452–464, 2016.

[33] E. Kabalcı, “Review on novel single-phase grid-connected solar inverters: Circuits and control methods,” *Sol. Energy*, vol. 198, pp. 247–274, 2020.

[34] R. A. Eshkaftaki and C. N. M. Ho, “Half-bridge current source inverter for grid-connected applications,” in *Proc. IEEE Energy Convers. Congr. Expo. (ECCE)*, Detroit, MI, USA, Oct. 9–13, 2022.

[35] F. Blaabjerg, Z. Chen, and S. B. Kjaer, “Power electronics as efficient interface in dispersed power generation systems,” *IEEE Trans. Power Electron.*, vol. 19, no. 5, pp. 1184–1194, 2004.

[36] M. A. Chowdhury, M. H. Rashid, and R. H. Ashique, “Inverter topologies, control strategies, and their applications in grid-tied photovoltaic systems: A review,” *Renew. Sustain. Energy Rev.*, vol. 158, p. 112124, 2022.

[37] H. A. Sher, A. F. Murtaza, and K. E. Addoweesh, “A survey on the performance improvement and control strategies of photovoltaic systems,” *Renew. Sustain. Energy Rev.*, vol. 92, pp. 698–714, 2018.

[38] A. D. Hansen, P. Sørensen, L. H. Hansen, and H. Bindner, "Models for a stand-alone PV system," *Risø National Laboratory*, Roskilde, Denmark, Tech. Rep. Risø-R-1219(EN), 2000.

[39] A. Safari and S. Mekhilef, "Simulation and hardware implementation of incremental conductance MPPT with direct control method using Cuk converter," *IEEE Trans. Ind. Electron.*, vol. 58, no. 4, pp. 1154–1161, Apr. 2011.

[40] N. Femia, G. Petrone, G. Spagnuolo, and M. Vitelli, "Optimization of perturb and observe maximum power point tracking method," *IEEE Trans. Power Electron.*, vol. 20, no. 4, pp. 963–973, Jul. 2005.

[41] A. K. Abdelsalam, A. M. Massoud, S. Ahmed, and P. Enjeti, "High-performance adaptive perturb and observe MPPT technique for photovoltaic-based microgrids," *IEEE Trans. Power Electron.*, vol. 26, no. 4, pp. 1010–1021, Apr. 2011.

[42] T. Esram and P. L. Chapman, "Comparison of photovoltaic array maximum power point tracking techniques," *IEEE Trans. Energy Convers.*, vol. 22, no. 2, pp. 439–449, Jun. 2007.

[43] N. D. Kaushika and A. K. Gautam, "Energy yield simulations of interconnected solar PV arrays," *IEEE Trans. Energy Convers.*, vol. 18, no. 1, pp. 127–134, Mar. 2003.

[44] A. A. Kulaksiz and R. Akkaya, "Training data optimization for ANN-based MPPT controller in photovoltaic systems," *Energy Convers. Manage.*, vol. 85, pp. 766–772, 2014.

[45] C. L. Trujillo, D. Velasco, and E. Figueres, "Reconfigurable control scheme for a PV system," *Renew. Energy*, vol. 36, no. 6, pp. 1611–1619, 2011.

[46] Y. Yang, F. Blaabjerg, and Z. Zou, "Benchmarking of grid fault ride-through and grid support requirements for wind turbine generators in China," *Renew. Sustain. Energy Rev.*, vol. 60, pp. 1316–1332, 2016.

[47] A. Yazdani and R. Iravani, *Voltage-Sourced Converters in Power Systems: Modeling, Control, and Applications*. Hoboken, NJ, USA: Wiley, 2010.

[48] D. N. Zmood and D. G. Holmes, “Stationary frame current regulation of PWM inverters with zero steady-state error,” *IEEE Trans. Power Electron.*, vol. 18, no. 3, pp. 814–822, May 2003.

[49] P. W. Lehn, “Exact modeling of the voltage source converter,” *IEEE Trans. Power Del.*, vol. 17, no. 1, pp. 217–222, Jan. 2002.

[50] Y. Khayat, J. Hossain, and F. Shahnia, *Power Quality in Microgrids*. Springer, 2020.

[51] A. Yazdani, M. Mojiri, and A. Bakhshai, “A fast and accurate synchronization technique for grid-connected power electronics converters,” *IEEE Trans. Power Electron.*, vol. 25, no. 3, pp. 517–522, Mar. 2010.

[52] S. Kouro, J. I. Leon, D. Vinnikov, and L. G. Franquelo, “Grid-connected photovoltaic systems: An overview of recent research and emerging PV converter technology,” *IEEE Ind. Electron. Mag.*, vol. 9, no. 1, pp. 47–61, Mar. 2015.

[53] P. Sanchis, J. López, A. Ursúa, and L. Marroyo, “On the testing, characterization, and evaluation of PV inverters and dynamic MPPT performance,” *Prog. Photovolt.: Res. Appl.*, vol. 19, no. 5, pp. 626–636, Aug. 2011.

[54] R. González, E. Gubía, J. López, and L. Marroyo, “Transformerless single-phase multilevel-based photovoltaic inverter,” *IEEE Trans. Ind. Electron.*, vol. 55, no. 7, pp. 2694–2702, Jul. 2008.

[55] M. Calais, J. Myrzik, T. Spooner, and V. G. Agelidis, “Inverters for single-phase grid connected photovoltaic systems—An overview,” in *Proc. IEEE PESC*, 2002, vol. 2, pp. 1995–2000.

[56] M. C. Cavalcanti, F. A. S. Neves, H. E. P. de Souza, G. M. S. Azevedo, and F. C. Camboim, “Comparative evaluation of power control strategies for single-phase grid-connected PV inverters,” *IEEE Trans. Power Electron.*, vol. 30, no. 6, pp. 3227–3237, Jun. 2015.

[57] L. F. Costa and J. A. Pomilio, “Simultaneous grid current and partial shading estimation for photovoltaic arrays,” *IEEE Trans. Ind. Electron.*, vol. 61, no. 3, pp. 1149–1157, Mar. 2014.

[58] A. M. Lienhardt, G. R. C. Mouli, M. Z. Camargo, and P. Bauer, “PV systems with enhanced power extraction capability under partial shading conditions,” *Energies*, vol. 14, no. 3, p. 780, 2021.

[59] D. Sera, T. Kerekes, R. Teodorescu, and F. Blaabjerg, “Improved MPPT algorithms for rapidly changing environmental conditions,” in *Proc. IEEE PESC*, 2006, pp. 2005–2010.

[60] J. M. A. Myrzik and M. Calais, “String and module integrated inverters for single-phase grid connected photovoltaic systems—A review,” in *Proc. IEEE Bologna Power Tech Conf.*, 2003, vol. 2, pp. 1–8.

[61] B. Yang, W. Li, Y. Zhao, and X. He, “Design and analysis of a grid-connected photovoltaic power system,” *IEEE Trans. Power Electron.*, vol. 25, no. 4, pp. 992–1000, Apr. 2010.

[62] S. Ghosh, S. K. Singh, and V. K. Yadav, "Experimental investigation of hotspot phenomenon in PV arrays under mismatch conditions," Solar Energy, vol. 253, pp. 219–230, 2023.

[63] H. Patel and V. Agarwal, “Maximum power point tracking scheme for PV systems operating under partially shaded conditions,” *IEEE Trans. Ind. Electron.*, vol. 55, no. 4, pp. 1689–1698, Apr. 2008.

[64] R. Kadri, J. P. Gaubert, and G. Champenois, “An improved maximum power point tracking for photovoltaic grid-connected inverter based on voltage-oriented control,” *IEEE Trans. Ind. Electron.*, vol. 58, no. 1, pp. 66–75, Jan. 2011.

[65] F. Liu, S. Duan, F. Liu, B. Liu, and Y. Kang, “A variable step size INC MPPT method for PV systems,” *IEEE Trans. Ind. Electron.*, vol. 55, no. 7, pp. 2622–2628, Jul. 2008.

[66] M. A. G. de Brito, L. Galotto, L. P. Sampaio, G. de Azevedo e Melo, and C. A. Canesin, “Evaluation of the main MPPT techniques for photovoltaic applications,” *IEEE Trans. Ind. Electron.*, vol. 60, no. 3, pp. 1156–1167, Mar. 2013.

[67] C. Hua and C. Shen, “Comparative study of peak power tracking techniques for solar storage system,” in *Proc. IEEE APEC*, 1998, vol. 2, pp. 679–685.

[68] J. Alonso, D. G. Lamar, S. Ortega, A. J. Calleja, and M. Rico-Secades, “Analysis and design of the integrated double buck–boost converter as a high-power-factor driver for power-LED lamps,” *IEEE Trans. Ind. Electron.*, vol. 59, no. 4, pp. 1689–1697, Apr. 2012.

[69] A. Pandey, N. Dasgupta, and A. K. Mukerjee, “High-performance algorithms for drift avoidance and fast tracking in solar MPPT system,” *IEEE Trans. Energy Convers.*, vol. 23, no. 2, pp. 681–689, Jun. 2008.

[70] S. Saravanan and N. R. Babu, “Maximum power point tracking algorithms for photovoltaic system – A review,” *Renew. Sustain. Energy Rev.*, vol. 57, pp. 192–204, May 2016.

[71] A. Mirzaei, H. Iman-Eini, and R. Rahimi, “Enhanced model predictive control for single-phase grid-connected converters,” *IEEE Trans. Power Electron.*, vol. 33, no. 12, pp. 10265–10275, Dec. 2018.

[72] R. Faranda and S. Leva, “Energy comparison of MPPT techniques for PV Systems,” *WSEAS Trans. Power Syst.*, vol. 3, no. 6, pp. 446–455, Jun. 2008.

[73] M. Veerachary, T. Senjyu, and K. Uezato, “Neural-network-based maximum-power-point tracking of coupled-inductor interleaved-boost-converter-supplied PV system using fuzzy controller,” *IEEE Trans. Ind. Electron.*, vol. 50, no. 4, pp. 749–758, Aug. 2003.

[74] J. L. Santos, F. Antunes, A. Chehab, and C. Cruz, “A maximum power point tracker for PV systems using a high performance boost converter,” *Sol. Energy*, vol. 80, no. 7, pp. 772–778, Jul. 2006.

[75] H. Patel and V. Agarwal, “MATLAB-based modeling to study the effects of partial shading on PV array characteristics,” *IEEE Trans. Energy Convers.*, vol. 23, no. 1, pp. 302–310, Mar. 2008.

[76] M. G. Villalva, J. R. Gazoli, and E. R. Filho, “Comprehensive approach to modeling and simulation of photovoltaic arrays,” *IEEE Trans. Power Electron.*, vol. 24, no. 5, pp. 1198–1208, May 2009.

[77] J. H. R. Enslin and D. B. Snyman, “Simplified feed-forward control of the maximum power point in PV installations,” *IEEE Trans. Ind. Electron.*, vol. 45, no. 1, pp. 158–162, Feb. 1998.

[78] D. Sera, R. Teodorescu, J. Hantschel, and M. Knoll, “Optimized maximum power point tracker for fast-changing environmental conditions,” *IEEE Trans. Ind. Electron.*, vol. 55, no. 7, pp. 2629–2637, Jul. 2008.

[79] A. Safari and S. Mekhilef, “Implementation of incremental conductance MPPT with direct control method using Cuk converter,” *IEEE Trans. Ind. Electron.*, vol. 58, no. 4, pp. 1154–1161, Apr. 2011.

[80] S. Armstrong and W. Hurley, “A new methodology to optimize the number of photovoltaic panels in a hybrid energy system,” *IEEE Trans. Energy Convers.*, vol. 21, no. 2, pp. 459–466, Jun. 2006.

[81] J. H. Lee, B. H. Cho, and F. Blaabjerg, “Design and control of isolated resonant converters for PV power systems,” *IEEE Trans. Power Electron.*, vol. 28, no. 3, pp. 1139–1149, Mar. 2013.

[82] A. Bidram, A. Davoudi, F. L. Lewis, and Z. Qu, “Secondary control of microgrids based on distributed cooperative control of multi-agent systems,” *IET Gener., Transm. Distrib.*, vol. 7, no. 8, pp. 822–831, Aug. 2013.

[83] L. Zhang, C. Y. Chung, and K. P. Wong, “Advanced wind power prediction based on wavelet neural network and Markov chain,” *IEEE Trans. Power Syst.*, vol. 25, no. 4, pp. 1788–1796, Nov. 2010.

[84] M. Ciobotaru, R. Teodorescu, and F. Blaabjerg, “Control of single-stage single-phase PV inverter,” in *Proc. IEEE PESC*, 2005, pp. 1397–1402.

[85] S. B. Kjaer, “Design and control of an inverter for photovoltaic applications,” Ph.D. dissertation, Inst. Energy Technol., Aalborg Univ., Aalborg, Denmark, 2005.

[86] F. Blaabjerg, M. Liserre, and K. Ma, “Power electronics converters for wind turbine systems,” *IEEE Trans. Ind. Appl.*, vol. 48, no. 2, pp. 708–719, Mar.–Apr. 2012.

[87] D. Meneses, F. Blaabjerg, O. Garcia, and J. A. Cobos, “Review and comparison of step-up transformerless topologies for photovoltaic AC-module application,” *IEEE Trans. Power Electron.*, vol. 28, no. 6, pp. 2649–2663, Jun. 2013.

[88] M. Islam, N. Mithulananthan, and K. Y. Lee, “Impact of large-scale rooftop solar PV system integration on the voltage profile of a distribution network,” *IEEE Trans. Sustain. Energy*, vol. 8, no. 1, pp. 145–154, Jan. 2017.

[89] Y. Yang, F. Blaabjerg, and H. Wang, “Low-voltage ride-through of single-phase transformerless photovoltaic inverters,” *IEEE Trans. Ind. Appl.*, vol. 50, no. 3, pp. 1942–1952, May–Jun. 2014.

[90] A. Sangwongwanich, Y. Yang, and F. Blaabjerg, “A sensorless power reserve control strategy for two-stage grid-connected PV systems,” *IEEE Trans. Power Electron.*, vol. 33, no. 10, pp. 8336–8349, Oct. 2018.

[91] G. Petrone, G. Spagnuolo, and M. Vitelli, “A multivariable perturb-and-observe maximum power point tracking technique applied to a single-stage photovoltaic inverter,” *IEEE Trans. Ind. Electron.*, vol. 58, no. 1, pp. 76–84, Jan. 2011.

[92] A. Sangwongwanich, Y. Yang, D. Sera, H. Wang, and F. Blaabjerg, “Delta power control strategy for multistring grid-connected PV inverters,” *IEEE Trans. Ind. Appl.*, vol. 33, no. 2, pp. 1213–1223, Mar. 2018.

[93] J. W. Kimball, B. T. Kuhn, and R. S. Balog, “A system design approach for unattended solar energy harvesting supply,” *IEEE Trans. Power Electron.*, vol. 24, no. 4, pp. 952–962, Apr. 2009.

[94] K. Ogimoto, “Future prospects of photovoltaic systems: The case of Japan,” *Sol. Energy Mater. Sol. Cells*, vol. 92, no. 11, pp. 1692–1696, Nov. 2008.

[95] N. S. M. N. Izam, Z. Itam, W. L. Sing, and A. Syamsir, "Sustainable development perspectives of solar energy technologies with focus on solar photovoltaic—A review," *Energies*, vol. 15, no. 8, p. 2790, 2022.

[96] M. M. R. Ahmed, S. Mirsaeidi, and M. A. Koondhar, "Mitigating uncertainty problems of renewable energy resources through efficient integration of hybrid solar PV/wind systems into power networks," *IEEE Access*, vol. 12, pp. 30311-30328, 2024.

[97] S. Manna, D. K. Singh, A. K. Akella, H. Kotb, and K. M. AboRas, "Design and implementation of a new adaptive MPPT controller for solar PV systems," *Energy Reports*, vol. 9, pp. 1818-1829, Dec. 2023.

[98] C. M. A. da Luz, E. M. Vicente, F. L. Tofoli, and E. R. Ribeiro, "Differential power processing architecture to increase energy harvesting of photovoltaic systems under permanent mismatch," *Solar Energy*, vol. 263, p. 111940, 2023.

[99] V. A. M. Lopez, H. Ziar, J. W. Haverkort, and M. Zeman, "Dynamic operation of water electrolyzers: A review for applications in photovoltaic systems integration," *Renewable and Sustainable Energy Reviews*, vol. 182, p. 113407, 2023.

[100] P. Kuznetsov, L. Yuferev, D. Voronin, and V. A. Panchenko, "Methods improving energy efficiency of photovoltaic systems operating under partial shading," *Applied Sciences*, vol. 11, no. 1, p. 64, 2021.

[101] H. Jiang, X. Zhang, L. Yao, N. Lu, et al., "High-resolution analysis of rooftop photovoltaic potential based on hourly generation simulations and load profiles," *Applied Energy*, vol. 348, p. 121553, 2023.

[102] S. Meunier, C. Protopapadaki, R. Baetens, and D. Saelens, "Impact of residential low-carbon technologies on low-voltage grid reinforcements," *Applied Energy*, vol. 297, p. 117057, 2021.

[103] A. Shawky, T. Takeshita, M. A. Sayed, and M. Aly, "Improved controller and design method for grid-connected three-phase differential SEPIC inverter," *IEEE Transactions on Industrial Electronics*, vol. 68, no. 3, pp. 2154-2164, 2021.

[104] A. I. M. Ali, Z. M. Alaas, M. A. Sayed, A. Almalaq, and A. Farah, "An efficient MPPT technique-based single-stage incremental conductance for integrated PV systems considering flyback central-type PV inverter," *Sustainability*, vol. 14, p. 12105, 2022.

[105] Y. Pan, A. Sangwongwanich, and Y. Yang, "Flexible active power control of distributed photovoltaic systems with integrated battery using series converter configurations," *IEEE Journal of Emerging and Selected Topics in Power Electronics*, vol. 10, no. 6, pp. 6891-6909, Dec. 2022.

[106] A. A. Hassan, O. Abdel-Rahim, M. Bajaj, and I. Zaitsev, "Power electronics for green hydrogen generation with focus on methods, topologies, and comparative analysis," *Scientific Reports*, vol. 14, p. 24767, 2024.

[107] A. Rashwan, A. Mikhaylov, M. Hemeida, and G. Pinter, "Two-stage grid-connected inverter topology with high frequency link transformer for solar PV systems," *Energy Reports*, vol. 9, pp. 123-134, 2023.

[108] M. N. Ali, K. Mahmoud, M. Lehtonen, and M. M. F. Darwish, "An efficient fuzzy-logic based variable-step incremental conductance MPPT method for grid-connected PV systems," *IEEE Access*, vol. 9, pp. 26420-26430, 2021.

[109] M. A. Yagoub and A. A. Elserougi, "Assessment of PV string optimizer circuit versus string and central inverters during partial shading conditions," in *Proc. 22nd Int. Middle East Power Syst. Conf. (MEPCON)*, Assiut, Egypt, pp. 14-19, 2021.

[110] U. Rafiq, A. F. Murtaza, H. A. Sher, and D. Gandini, "Design and analysis of a novel high-gain DC-DC boost converter with low component count," *Electronics*, vol. 10, no. 2, p. 176, 2021.

[111] A. Aslam, N. Ahmed, S. A. Qureshi, M. Assadi et al., "Advances in solar PV systems; A comprehensive review of PV performance, influencing factors, and mitigation techniques," Energies, vol. 15, pp 7595, 2022.

[112] M. E. Hossain and S. Biswas, "Feasibility study and design of a grid-tied low-cost solar system to replace IPS for a residential building," Journal of Energy & Technology (JET), Vol. 1, No. 2, 2021.

[113] A. C. Lazaroiu, “A comprehensive overview of photovoltaic technologies and their role in reducing greenhouse gas emissions,” *Sustainability*, vol. 15, no. 23, p. 16297, 2023.

[114] A. Zentani, A. Almaktoof, and M. T. Kahn, "A comprehensive review of developments in electric vehicles fast charging technology," Applied Sciences, vol. 14, pp 4728, 2024.

[115] S. Hollingworth, A. P. Fenny, S. Y. Yu, F. Ruiz, et al., "Health technology assessment in sub-Saharan Africa: a descriptive analysis and narrative synthesis," Cost Effectiveness and Resource Allocation, vol. 19, no. 1, 2021.

[116] E. Quiles, C. Roldán-Blay, G. Escrivá-Escrivá, and C. Roldán-Porta, "Accurate Sizing of Residential Stand-Alone Photovoltaic Systems Considering System Reliability," *Sustainability*, vol. 12, no. 3, art. no. 1274, Feb. 2020.

[117] S. R. Sanders, J. M. Noworolski, X. Z. Liu and G. C. Verghese, "Generalized averaging method for power conversion circuits," in *IEEE Transactions on Power Electronics*, vol. 6, no. 2, pp. 251-259, April 1991.

[118] N. S. Nise, Control Systems Engineering, 8th ed. Hoboken, NJ, USA: Wiley, 2020.

[119] I. A. Nassar and M. M. Abdella, "Impact of replacing thermal power plants by renewable energy on the power system," *Thermal Science and Engineering Progress*, vol. 5, pp. 506–515, 2018.

[120] M. Albadi and E. El-Saadany, "Comparative study on impacts of wind profiles on thermal units scheduling costs," *IET Renewable Power Generation*, vol. 5, no. 1, pp. 26–35, 2011.

[121] K. Ullah, M. A. Tunio, Z. Ullah, and M. T. Ejaz, "Ancillary services from wind and solar energy in modern power grids: A comprehensive review and simulation study," *Sustainable Energy*, vol. 16, no. 032701, 2024.

[122] J. Rodriguez, C. Garcia, and A. Mora, "Latest advances of model predictive control in electrical drives—Part I: Basic concepts and advanced strategies," *IEEE Trans. Power Electron.*, vol. 37, no. 4, pp. 3927–3942, Apr. 2022.

[123] H. Zhang, Y. Li, R. Xie, J. Song, and B. Liang, "Adaptive model predictive control of an interleaved boost converter using real-time updated model," *IEEE Trans. Power Electron.*, vol. 38, no. 2, pp. 1720–1731, Feb. 2023.

[124] I. Villanueva, N. Vázquez, J. Vaquero, C. Hernández, H. López, and R. Osorio, "L vs. LCL filter for photovoltaic grid-connected inverter: A reliability study," *Int. J. Photoenergy*, vol. 2020, pp. 1–10, Jan. 2020.

[125] N. F. Ibrahim, M. M. Mahmoud, and A. M. H. Al Thaiban, "Operation of grid-connected PV system with ANN-based MPPT and an optimized LCL filter using GRG algorithm for enhanced power quality," *IEEE Access*, vol. 11, pp. 106859–106876, 2023.

[126] Y. Wang, C. Wang, W. Zeng, and F. Bai, "Multifactorial prediction errors analysis and a feedback self-correction on model predictive control for the three-phase inverter," *IEEE Trans. Ind. Electron.*, vol. 66, no. 5, pp. 3647–3654, May 2019.

[127] Z. Zhang, Z. Li, M. P. Kazmierkowski, J. Rodriguez, and R. Kennel, "Robust predictive control of three-level NPC back-to-back power converter PMSG wind turbine systems with revised predictions," *IEEE Trans. Power Electron.*, vol. 33, no. 11, pp. 9588–9598, Nov. 2018.

[128] O. Babayomi, Z. Zhang, and Z. Li, "Robust predictive control of grid-connected converters: Sensor noise suppression with parallel-cascade extended state observer," *IEEE Trans. Ind. Electron.*, vol. 71, no. 4, pp. 3728–3740, Apr. 2024.

[129] H. Sartipizadeh, F. Harirchi, M. Babakmehr, and P. Dehghanian, "Robust model predictive control of DC-DC floating interleaved boost converter with multiple uncertainties," *IEEE Trans. Energy Convers.*, vol. 36, no. 2, pp. 1403–1412, Jun. 2021.

[130] D. Pérez-Estévez and J. Doval-Gandoy, "A model predictive current controller with improved robustness against measurement noise and plant model variations," *IEEE Open J. Ind. Appl.*, vol. 2, pp. 131–142, Apr. 2021.

[131] Y. Han, H. Sun, B. Huang, and S. Qin, "Discrete-time domain modal analysis of oscillatory stability of renewables integrated power systems," *IEEE Trans. Power Delivery*, vol. 37, no. 5, pp. 4248–4260, Oct. 2022.

[132] D. Yan, C. Yang, L. Hang, Y. He, and P. Luo, "Review of general modeling approaches of power converters," *Chinese Journal of Electrical Engineering*, vol. 7, no. 1, pp. 27–36, Mar. 2021.

[133] J. T. Betts, “Survey of numerical methods for trajectory optimization,” *AIAA J. Guid., Control, Dyn.*, vol. 21, pp. 193–207, 1998.

[134] D. Celestini, D. Gammelli, and T. Guffanti, “Transformer-based model predictive control: Trajectory optimization via sequence modeling,” *IEEE Robotics and Automation Letters*, vol. 9, no. 11, pp. 9820–9827, Nov. 2024.

[135] B. Aljafari, K. Rameshkumar, and V. Indragandhi, “A novel single-phase shunt active power filter with a cost function based model predictive current control technique,” *Energies*, vol. 15, p. 4531, 2022.

[136] M. A. Zamani, N. Wrathall, and R. Beresh, “A review of the latest voltage and frequency ride-through requirements in Canadian jurisdictions,” in *Proc. IEEE Elect. Power Energy Conf.*, Nov. 2014.

[137] S. Xu, Y. Xue, and L. Chang, “Review of power system support functions for inverter-based distributed energy resources—Standards, control algorithms, and trends,” *IEEE Open J. Power Electronics*, vol. 2, pp. 88–105, 2021.

[138] R. Morales-Caporal and E. Bonilla-Huerta, “Finite-control-set model predictive control for single-phase CHB 5-level inverter as an active power filter with discrete-time FO-PI DC-link controller,” *IEEE Access*, vol. 12, pp. 57478–57491, 2024.

[139] L. Du, H. Cao, Z. Saadatizadeh, and Y. Zhao, “A simple switching-event dependent high-frequency sampling method for power conversion system,” *IEEE Trans. Power Electron.*, vol. 38, no. 6, pp. 6880–6885, Jun. 2023.

[140] I. A. Acosta, A. L. Cedeño, and G. Carvajal, “DNN-based long prediction horizon finite control set MPC with switching effort penalization,” in *Proc. IECON 2024 - 50th Annu. Conf. IEEE Ind. Electron. Soc.*, Chicago, IL, USA, 2024, pp. 1–6.

[141] R. Cagienard, P. Grieder, E. Kerrigan, and M. Morari, “Move blocking strategies in receding horizon control,” *Journal of Process Control*, vol. 17, no. 6, pp. 563–570, 2007.

[142] T. Geyer, “Generalized model predictive direct torque control: Long prediction horizons and minimization of switching losses,” in *Proc. 48th IEEE Conf. Decision and*

Control (CDC) jointly with 28th Chinese Control Conf., Shanghai, China, 2009, pp. 6799–6804.

[143] S. A. Davari, D. A. Khaburi, and R. Kennel, "An improved FCS–MPC algorithm for an induction motor with an imposed optimized weighting factor," *IEEE Trans. Power Electron.*, vol. 27, no. 3, pp. 1540–1551, Mar. 2012.

[144] M. Uddin, S. Mekhilef, M. Mubin, M. Rivera, and J. Rodriguez, "Model predictive torque ripple reduction with weighting factor optimization fed by an indirect matrix converter," *Electr. Power Compon. Syst.*, vol. 42, no. 10, pp. 1059–1069, Jun. 2014.

[145] T. Li, X. Sun, G. Lei, Y. Guo, and Z. Yang, "Finite-control-set model predictive control of permanent magnet synchronous motor drive systems—An overview," *IEEE/CAA Journal of Automatica Sinica*, vol. 9, no. 6, pp. 1027–1040, 2022.

[146] T. He, M. Wu, R. P. Aguilera, D. D. C. Lu, Q. Liu, and S. Vazquez, "Low computational burden model predictive control for single-phase cascaded H-bridge converters without weighting factor," *IEEE Trans. Ind. Electron.*, vol. 70, no. 3, pp. 2396–2406, Mar. 2023.

[147] E. F. Camacho and C. Bordons, *Model Predictive Control*, 2nd ed. London, U.K.: Springer, 2007.

[148] S. Vazquez et al., "An artificial intelligence approach for real-time tuning of weighting factors in FCS-MPC for power converters," *IEEE Trans. Ind. Electron.*, vol. 69, no. 12, pp. 11987–11998, Dec. 2022.

[149] M. E. Albira and M. A. Zohdy, "Adaptive model predictive control for DC-DC power converters with parameters' uncertainties," *IEEE Access*, vol. 9, pp. 135121–135131, 2021.

[150] A. Rashwan, A. Mikhaylov, M. Hemeida, G. Pinter, and D. S. Osheba, "Two-stage grid-connected inverter topology with high frequency link transformer for solar PV systems," *Energy Reports*, vol. 10, pp. 1864–1874, 2023.

[151] X. Zhang, H. Liu, P. Wheeler, and F. Wu, "Research on power decoupling and parameter mismatch of three-port isolated resonant DC–DC converter applied switch-controlled capacitor," *IEEE Trans. Ind. Electron.*, vol. 70, no. 8, pp. 8098–8107, Aug. 2023.

[152] S. Vazquez, J. Rodriguez, M. Rivera, L. G. Franquelo, and M. Norambuena, “Model predictive control for power converters and drives: Advances and trends,” *IEEE Trans. Ind. Electron.*, vol. 64, no. 2, pp. 935–947, Feb. 2017.

[153] R. Suzuki, F. Kawai, H. Ito, C. Nakazawa, Y. Fukuyama, and E. Aiyoshi, “Automatic tuning of model predictive control using particle swarm optimization,” in *Proc. IEEE Swarm Intelligence Symp.*, Honolulu, HI, USA, pp. 221–226, 2007.

[154] S. Vazquez *et al*., "An Artificial Intelligence Approach for Real-Time Tuning of Weighting Factors in FCS-MPC for Power Converters," in *IEEE Transactions on Industrial Electronics*, vol. 69, no. 12, pp. 11987-11998, Dec. 2022.